Preparation of Polyaniline-Based Nanocomposites for Photocatalytic Degradation of Pollutants and Hydrogen Production

A Thesis Submitted in Fulfillment of the Requirements for the Award of the Degree of

DOCTOR OF PHILOSOPHY

in

Chemistry

Submitted By

PRITAM HAIT

(Regd. No.: 902209003)

Under the Supervision of

Dr. Soumen Basu
Professor
Department of Chemistry and Biochemistry
TIET, Patiala

Dr. Rajeev Mehta
Professor
Department of Chemical Engineering
TIET, Patiala

THAPAR INSTITUTE OF ENGINEERING & TECHNOLOGY, PATIALA, PUNJAB

January, 2026

DECLARATION

I, Pritam Hait hereby declare that the work presented in this thesis entitled ***Preparation of Polyaniline-Based Nanocomposites for Photocatalytic Degradation of Pollutants and Hydrogen Production*** in fulfillment of the requirement for the award of degree of Doctor of Philosophy submitted at Department of Chemistry and Biochemistry, Thapar Institute of Engineering and Technology, Patiala is an authentic record of work carried out under supervision of Dr. Soumen Basu, Professor, Department of Chemistry and Biochemistry, Thapar Institute of Engineering and Technology, Patiala, India and Dr. Rajeev Mehta, Professor, Department of Chemical Engineering, Thapar Institute of Engineering and Technology, Patiala, India from August,2022 to January,2026. The matter presented in this has not been submitted either in part or full to any other university or institute for the award of any other degree.

Date: 19/08/2026

Pritam Hait

(Pritam Hait)

(Regd. No.: 902209003)

CERTIFICATE

It is certified that the work contained in the thesis titled ***Preparation of Polyaniline-Based Nanocomposites for Photocatalytic Degradation of Pollutants and Hydrogen Production*** by Pritam Hait [902209003] has been carried out under our supervision and that this work has not been submitted elsewhere for any other degree.

(Dr. Soumen Basu)

(Professor)

Department of Chemistry and Biochemistry

Thapar Institute of Engineering and Technology

Date: 19/08/2026

(Dr. Rajeev Mehta)

(Professor)

Department of Chemical Engineering

Thapar Institute of Engineering and Technology

Date: 19/08/2026

Acknowledgements

First and foremost, I express my deepest gratitude to **God Almighty** for bestowing me with the strength, perseverance, and wisdom required to complete this research work.

I would like to express my sincere and heartfelt gratitude to my Ph.D. supervisors, **Prof. Soumen Basu** and **Prof. Rajeev Mehta**, for their invaluable guidance, constant encouragement, and insightful suggestions throughout the course of this research. Their academic excellence, constructive criticism, and unwavering support played a pivotal role in shaping this thesis.

I am sincerely thankful to the members of my **Doctoral Advisory Committee**, **Prof. Bonamali Pal**, **Prof. Bhaskar Chandra Mohanty**, and **Dr. Banibrata Maity**, for their valuable time, expert advice, and constructive feedback, which significantly improved the quality of my research work.

I would like to extend my gratitude to the **Head of the Department, Prof. Manmohan Chhibber**, for providing the necessary research facilities and a supportive academic environment during my doctoral studies.

I sincerely acknowledge **Dr. Akanksha Mehta**, **PR Testing Facility**, and **IIT Roorkee** for their valuable support in carrying out **XPS analysis** for different research publications associated with this work.

I acknowledge **Panjab University** for providing HRTEM and LC-MS analysis facilities. I am grateful to the **Department of Physics and Materials Science** for providing XRD, FESEM, and Raman analysis facilities, and to the **SAI Laboratory** for SEM analysis support.

I extend my sincere appreciation to my lab seniors-**Dr. Surbhi Sharma, Dr. Shelly Singla, Dr. Neeraj Shoal, Dr. Ranjeet Kumar Jha, Dr. Anushka Garg, Dr. Aayushi Kundu, Dr. Divya Monga, Dr. Shagun Kainth, and Dr. Piyush Sharma**-for their continuous support, valuable discussions, and guidance during my research work.

I am grateful to my friends and colleagues **Mr. Vikash Ranjan** and **Mr. Abhishek Chandel** for their cooperation and encouragement. I would also like to thank my labmate **Ms. Ramandeep Kaur** for her assistance and camaraderie in the laboratory.

I sincerely acknowledge the support and encouragement of my friends **Mr. Animesh Pal (BITS Pilani, Hyderabad)**, **Mr. Srijib Das (CSIR–CMERI)**, **Mr. Pintu Ghosh (IIEST Shibpur)**, and **Mr. Krishna Kanta Samanta (IIT Kharagpur)** for their constant motivation and helpful discussions.

Above all, I owe my deepest gratitude to my beloved family. I am immensely thankful to my **father, Mr. Krishna Pada Hait**, **mother, Mrs. Namita Hait**, and **brother, Mr. Pegus Hait**, for their unconditional love, sacrifices, patience, and unwavering faith in me throughout this journey. I also extend my heartfelt thanks to **all my family members and relatives** for their continuous encouragement, moral support, and blessings.

Finally, I extend my heartfelt thanks to everyone who directly or indirectly contributed to the successful completion of this thesis. Their support and encouragement made this journey both enriching and memorable.

TABLE OF CONTENTS

CHAPTER 1

Introduction and Literature Survey

CHAPTER 2

Solar-Powered Pollutant Degradation and H_2 Production via PANI/BiOCl/GO

CHAPTER 3

Ultrafast Charge Separation in PANI/GO/MoO_3 for Visible-Light Dye Degradation and H_2 Generation

CHAPTER 4

PANI/GO/MoS_2 Nanocomposites for Efficient Photocatalytic Pollutant Degradation and H_2 Generation

CHAPTER 5

Multifunctional PANI–LDH for Dye Mineralization and Hydrogen Production

CHAPTER 6

Conclusions and Future Perspectives

List of Figures

Figures No. **Title**

Chapter 3

Chapter 4

Chapter 5

List of Schemes

Scheme No. **Title**

List of Tables

Fig. No. **Title**

Table of Abbreviations

a.u.	Arbitrary unit
B. E.	Binding energy
BET	Brunauer-Emmett-Teller
BJH	Barrett-Joyner-Halenda
BOD	Biochemical oxygen demand
COD	Chemical oxygen demand
CR	Cango red
CVD	Chemical vapor deposition
DRS	Diffuse reflectance spectroscopy
EDS	Energy dispersive X-ray spectroscopy
EIS	Electrochemical impedance spectroscopy
FESEM	Field emission scanning electron microscopy
GC-MS	Gas chromatography-mass spectrometry
LC-MS	Liquid chromatography-mass spectrometry
HRTEM	High resolution transmission electron microscopy
JCPDS	Joint committee on powder diffraction standards
MO	Methyl orange
min	Minute
PL	Photoluminescence
ppm	Parts per million
pzc	Point of zero charge
Rh-B	Rhodamine B

SEM	Scanning electron microscopy
TOC	Total organic carbon
UV- Vis	Ultraviolet-visible
XPS	X-ray photoelectron spectroscopy
XRD	X-ray diffraction

Table of Abbreviations

%	Percentage
%D	Percent degradation or degradation efficiency
Å	Angstrom
A0	Initial absorbance of pollutant
At	Absorbance of pollutant at a certain time
C_0	Initial concentration of pollutant
cm^3/g	Centimeter cube per gram
Ct	Concentration of pollutant at a certain time
E_g	Band gap energy
g	Gram
g/L	Gram per litre
h	Planck constant
k	Pseudo-first order rate constant, min^{-1}
M	Molar
mg	Milligram
mL	Millilitre
mM	Millimolar
nm	Nanometer
°	Degree

R^2	Regression coefficient
S_{BET}	BET surface area, m^2/g
t	Time, min
V	Total pore volume, cm^3/g
α	Absorption coefficient
θ	Theta
λ	Wavelength
ν	Light frequency

Abstracts

Chapter 1:

Nanotechnology allows us to work with materials that are extremely small—about one-billionth of a meter. At this tiny scale, materials behave differently and can show special abilities. One important use of such materials is in photocatalysis, a process where sunlight helps break down harmful chemicals in water or produce clean fuel like hydrogen.

This thesis focuses on creating new photocatalyst materials made by combining polyaniline (a conducting polymer) with different metal-based nanoparticles. Polyaniline can absorb visible light and help move electrical charges more efficiently, making the overall material work better under visible light. The goal of this research is twofold:

i) To remove harmful dyes and pollutants from wastewater using sunlight, and
ii) To generate hydrogen gas, a clean and renewable fuel, using the same sunlight-driven process.

The materials developed in this work are tested using different scientific tools to understand their structure, how they absorb light, and how well they perform. The results show that these newly designed nanocomposites can clean polluted water more effectively and also produce hydrogen in a more efficient and eco-friendly way. In simple terms, this research aims to turn sunlight into a powerful tool—for cleaner water and cleaner energy.

Chapter 2:

Recently, polyaniline-based photocatalysts have gained great attention due to their narrow band gap (E = 1.77 eV), which enables them to absorb a significant amount of visible light (~ 43%) in the solar spectrum. In this study, we have synthesized a ternary nanocomposite (PANI/BiOCl/GO) through an oxidative polymerization approach, incorporating polyaniline (PANI), graphene oxide (GO), and bismuth oxychloride (BiOCl). Different weight percentages of composites (GO/BiOCl: 0.5%, 1%, 2.5%, and PANI: 99.5%, 99%, 97.5%) were prepared and named as 0.5PBG, 1PBG, and 2.5PBG, respectively. The ternary nanocomposite's successful development, crystallinity, purity, porosity, and optical properties were evaluated through several spectroscopic and surface analysis techniques, including UV-Vis-DRS, PL, XRD, XPS, BET, and EDS analysis. FESEM and HRTEM images unveiled the porous

characteristics of PANI, the morphology of exfoliated GO layers, and the nanoplate-like structure of BiOCl. The ternary nanocomposite was finally tested for its ability to degrade an organic dye, rhodamine-b (Rhb), and in the process also generate solar-light-driven green hydrogen by water half-splitting. The composite achieved about 90% detoxification (assigned from GC-TCD by analyzing the evolved CO_2 gas after degradation) and 96% color removal of Rhb dye within 120 minutes. The degradation of Rhb by 1PBG displayed a first-order reaction, featuring a rate constant 7.25 times higher than that observed for pure PANI, 3.8 times higher than for pure GO, and 3.9 times higher than for pure BiOCl. Thus, the ternary composites achieve a good amount of synergy. Significantly, this reaction rate constant is 4.7 times greater than the rate observed with commercially used TiO_2-P25 photocatalyst. Various reaction parameters including solution pH, different illumination areas, catalyst dosage, and the study of scavengers were investigated to understand their effects on the degradation reaction. The photocatalyst's reusability effectiveness was evaluated over 6 cycles, and its stability was subsequently confirmed through XRD and ICP-OES analysis. The LC-MS study revealed the identification of various intermediates and end products following the degradation reaction. The nanocomposite also produced 1000 ppm of hydrogen gas with an apparent quantum efficiency (AQE) of 17.97% when CH_3OH was used as a sacrificial agent, 500 ppm (AQE of 9.69%) in the acidic conditions, and 600 ppm (AQE of 11.63%) in the basic conditions. In a broader perspective, this endeavor paves the way for exploring fresh opportunities in the utilization of this ternary nanocomposite. Its potential extends beyond accelerating dye degradation to encompass diverse solar-driven applications as well.

Chapter 3:

Polyaniline-based photocatalysts have attracted attention due to their favourable bandgap (2.7 eV) and significant visible light absorption (~43%). In this study, a novel ternary nanocomposite, PANI/GO/MoO_3, synthesized via oxidative in-situ polymerization, combining polyaniline (PANI), graphene oxide (GO), and molybdenum trioxide (MoO_3) was presented with different wt./wt. %. Comprehensive characterization using XRD, BET, EDS, XPS, PL, and UV-Vis-DRS revealed crystallinity, porosity, and superior optical properties, respectively. FESEM image confirmed the porous morphology of PANI, exfoliated GO layers, and MoO_3 nanorods (60-80 nm). Among the composites, 2.5PGMO (GO-MoO_3: 2.5 wt.% and PANI: 97.5 wt.%) exhibited the highest electron lifetime (0.612 ms), significantly outperforming

individual components like PANI (0.0495 ms), GO (0.023 ms), and MoO_3 (0.022 ms). Photocatalytic activity was validated through both methyl orange (MO) degradation and solar-driven hydrogen production via water splitting. The 2.5PGMO composite achieved 98% MO removal and 70% detoxification within 120 minutes, with a reaction rate surpassing traditional photocatalysts. Optimal conditions, such as pH, catalyst dosage, and scavenger presence, enhanced performance. The composite shows 85% degradation of the pollutant over five cycles and stability of the nanocomposite was confirmed by XRD and ICP-OES. In solar hydrogen production, it delivered an apparent quantum efficiency (AQE) of 30.76% using CH_3OH as a sacrificial agent, with nearly 28% AQE across varying pH conditions. This study underscores the PANI/GO/MoO_3 nanocomposite as a promising multifunctional photocatalyst for simultaneous environmental remediation and sustainable hydrogen production, paving the way for advanced solar-driven technologies.

Chapter 4:

This study focused on creating a ternary nanocomposite (PANI/GO/MoS_2) using an oxidative polymerization technique. The composite incorporated polyaniline (PANI), graphene oxide (GO), and molybdenum disulfide (MoS_2) in different weight ratios. Comprehensive characterizations were performed using UV-Vis-DRS, PL, XRD, XPS, BET, and EDS to evaluate the material's crystallinity, purity, porosity, and optical properties. FESEM imaging revealed the porous nature of PANI, the exfoliated structure of GO, and the nanosphere morphology of MoS_2 (35-55 nm in diameter). This composite was tested for its effectiveness in degrading methyl orange (MO) dye and generating green hydrogen via visible-light-driven water splitting. Within 120 minutes, it achieved around 81.23% detoxification and 99% removal of MO dye. The degradation process adhered to first-order kinetics with a rate constant 7.1 times higher than pure PANI, 22 times higher than GO, 6.35 times higher than MoS_2, and 9.26 times greater than the commercial TiO_2-P25 photocatalyst, indicating strong synergy among the components. The study also examined the impact of various reaction parameters like pH, illumination area, catalyst dosage, and scavengers on the degradation process. Reusability of the photocatalyst was assessed over six cycles, maintaining 80% stability, as confirmed by XRD analysis. GC-MS identified the intermediates and final degradation products. The nanocomposite achieved hydrogen production with an apparent quantum efficiency (AQE) of 26% using CH_3OH as a sacrificial agent, and AQEs of 22%, 19%, and

15% under acidic, basic, and neutral conditions, respectively. This research highlights the potential of ternary nanocomposites for diverse applications beyond dye degradation, including various solar-driven technologies.

Chapter 5:

In this study, a binary nanocomposite comprising polyaniline (PANI) and nickel–aluminium layered double hydroxide (Ni-Al LDH) was synthesized via an oxidative polymerization method, with varying LDH loadings (2, 5, and 7 wt%). Comprehensive physicochemical characterization including UV-Vis DRS, photoluminescence (PL), XRD, XPS, BET, and EDS was employed to investigate the optical, structural, compositional, and textural attributes of the materials. From FESEM the porous morphology of PANI and the hierarchical, flower-like morphology of LDH were observed. The photocatalytic performance of the composite was evaluated for Congo red (CR) dye degradation and photocatalytic hydrogen evolution under visible light irradiation. After 120 minutes, the system achieved 98% dye removal and approximately 50% mineralization, as confirmed by total organic carbon analysis. Kinetic studies indicated pseudo-first-order behaviour, with the rate constant exceeding those of pristine PANI, LDH, and TiO_2-P25 by factors of 6, 8, and 9, respectively, evidencing a pronounced synergistic interaction. Operational parameters such as pH, catalyst loading, illumination area, and the presence of scavengers significantly influenced activity. The composite maintained ~70% catalytic efficiency over six consecutive cycles. HRMS enabled identification of intermediate and final degradation products. Under methanol-assisted conditions, the composite exhibited a hydrogen evolution AQE of 20%, with AQEs of 18%, 21%, and 16% in acidic, basic, and neutral media, respectively. These results underscore the composite's bifunctionality for environmental remediation and solar-driven energy conversion.

Chapter 1

Introduction and Literature Survey

1.1. Introduction in nanotechnology:

Physicist Richard Feynman introduced the term nanotechnology in 1959. In his influential lecture, "There's Plenty of Room at the Bottom," he underscored the potential inherent in exploring and controlling structures at the molecular level, thus laying the conceptual foundation for the field. In contemporary scientific literature, nanotechnology is conceptualized as a multidisciplinary domain focused on the controlled design and application of materials and phenomena occurring at sub-100-nanometer scales. Nanoscience is concerned with exploring and manipulating materials at the atomic to macromolecular levels, where their behaviours and characteristics deviate markedly from those observed at larger dimensions[1]. Complementarily, nanotechnology focuses on the engineering, synthesis, and practical deployment of nanoscale structures and systems achieved by regulating their size and shape at the nanometer range. These systems hold considerable promise for enhancing numerous areas of study and real-world application. The term nanometer (nm) defines a dimensional unit equivalent to 1×10^{-9} meters. At nanometer dimensions, materials may display altered properties, which can be explained by two principal underlying causes. The primary factor is that nanomaterials display a significantly enlarged surface-to-volume ratio in contrast to bulk materials of equal mass, thereby increasing their reactivity and potentially altering their structural strength. A further factor is the emergence of quantum effects at very small sizes, which can strongly modify the optical, structural, and magnetic responses of nanomaterials. These materials can exist in several dimensional regimes, ranging from one-dimensional ultra-thin coatings to two-dimensional nanowires and nanotubes, and even three-dimensional nanoparticles. Central to nanotechnology is the principle of reducing structures to nanoscale dimensions[2].

1.2. Critical Role of Materials at the Nanoscale:

Nanoscale materials possess exceptional optical, magnetic, electrical, and other characteristics that originate from their reduced particle dimensions. Once particle sizes drop below 100 nm, the system experiences a pronounced increase in surface-to-volume ratio and specific surface area. The total surface energy grows with expanding surface area, a relationship that is strongly

governed by the dimensionality of the material. Such heightened energy states contribute to the persistence and stabilization of metastable structures at the nanoscale. Nanostructures differ from their bulk counterparts in a manner that induces a relaxation of the standard crystalline lattice, thereby influencing the physical and chemical properties of the material. Nanostructures differ from their bulk counterparts in a manner that induces a relaxation of the standard crystalline lattice, thereby influencing the physical and chemical properties of the material[3]. The capacity to modulate the properties of materials by manipulating this factor is critical for various advanced technological applications. The population of atomic vacancies, existing inherently at thermal equilibrium, represents another significant consideration in the study of nanostructures. In nanostructured systems, the presence of atomic vacancies and other lattice defects plays a crucial role in determining numerous physical properties. The introduction of linear strain exhibits an inverse relationship with particle dimensions, causing a decrease in the lattice constant or interatomic distances in nanoscale materials[4].

1.3. Effects of Nanoscale Confinement on Material Optical Properties:

From an electronic perspective, metals are characterized by partially filled conduction bands. In contrast, semiconductors have a completely filled valence band separated from an almost empty conduction band by an energy gap E_g, which corresponds to the HOMO-LUMO gap in molecular systems. Insulators share the same fundamental electronic structure as semiconductors but differ mainly by possessing a significantly wider bandgap, as illustrated in **Fig 1.1**. Typically, materials with a bandgap below about 0.1 eV behave as metals, those with bandgaps in the range of 0.5–3.5 eV are classified as semiconductors, and substances with bandgaps of approximately 4 eV or higher are considered insulators. When the dimensions of an inorganic crystalline solid are reduced to the nanometer scale, the material can exhibit distinctive optical and electronic behaviours that are not seen in its bulk form. Semiconducting materials that are confined to dimensions of roughly 1–10 nm in all directions are commonly known as quantum dots or semiconductor nanocrystals. At these extremely small scales, the electrons display pronounced quantum-mechanical behaviour[4], [5], [6], [6], [7].

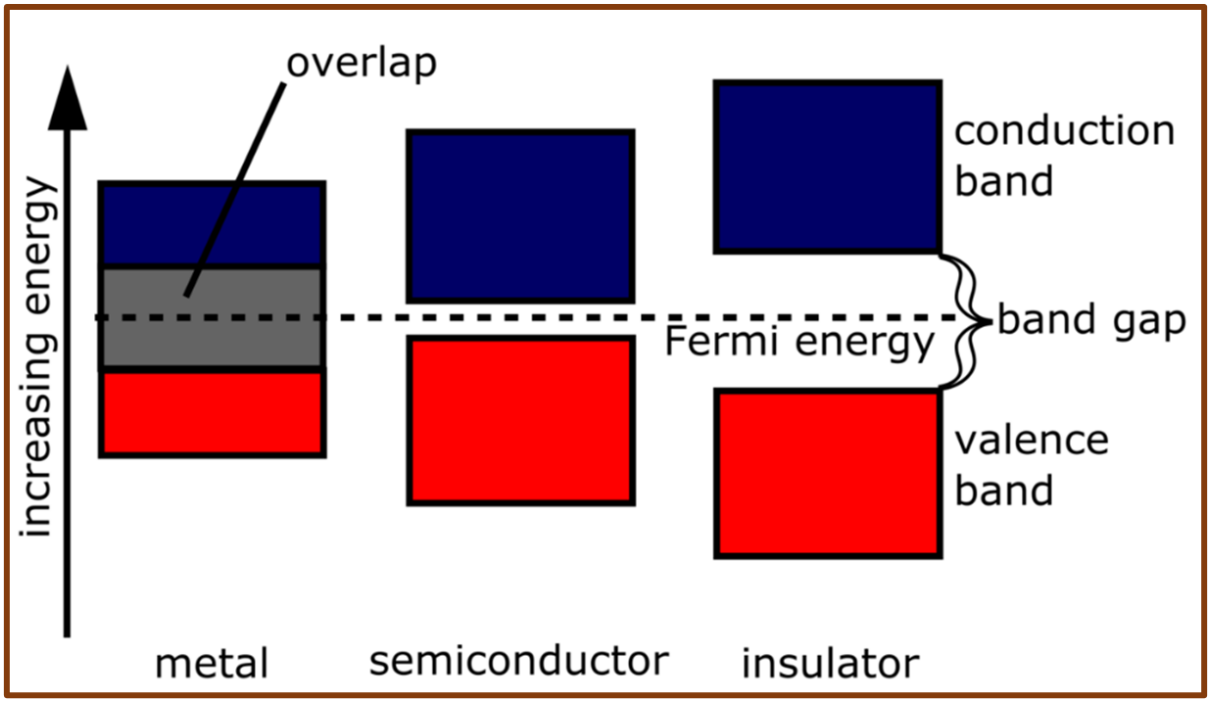

Fig 1.1: Comparative energy band structures of metals, semiconductors, and insulators.[4]

In semiconductor nanocrystals, the behaviour of optical absorption and photoluminescence differs distinctly from that observed in traditional molecular systems. When a semiconductor absorbs a photon, an electron from the valence band is excited into the conduction band, creating a corresponding hole in the valence band. After excitation, the electron in the conduction band rapidly settles into its lowest available energy level, while the hole simultaneously migrates to the uppermost state of the valence band. The buildup of holes in the highest valence-band levels facilitates the downward relaxation of valence electrons into lower-energy states. Emission via photoluminescence is produced by electron–hole recombination: a conduction-band electron fills a valence-band hole, converting the pair's energy into a photon and removing both excitations. Within the framework of solid-state physics, the coupled electron-hole pair is regarded as a unified object, since the absence of one would violate charge balance. This quasi-particle, called an exciton, consists of an electron and a hole whose opposite charges generate a strong Coulomb attraction, thereby restricting their motion to a nanoscale volume within the crystal. For a particular material, the exciton's effective volume can be evaluated. When the dimensions of a nanocrystal shrink to the scale of its Bohr radius, quantum confinement effects begin to dominate. Using the modified Bohr model described in **Equation 1.1**, it is possible to determine the effective spatial separation between an electron and its associated hole, collectively known as an exciton.

$$r = \frac{\varepsilon h^2}{\pi m_r e^2} \quad \textbf{(1.1)}$$

Here, r indicates the radius that characterizes the 3D spacing between the electron and hole. The term ε stands for the dielectric constant of the semiconductor, m_r refers to the reduced electron-hole mass, while h and e correspond to Planck's constant and the electron's charge, respectively.

Ion cyclotron resonance studies have provided values for electron and hole effective masses in many semiconductors, revealing that they commonly lie between 0.1 m_e and 3 m_e. For most semiconductor materials, their characteristic dielectric constants lead to estimated electron-hole pair spacings of approximately 1 to 10 nm. When excitons are generated at this size scale, the nanocrystal's physical boundaries restrict their motion in a manner reminiscent of the particle-in-a-box model. Thus, effects such as energy level quantization are theoretically observable at the nanoscale. One can regard the electronic structure of a nanoparticle as

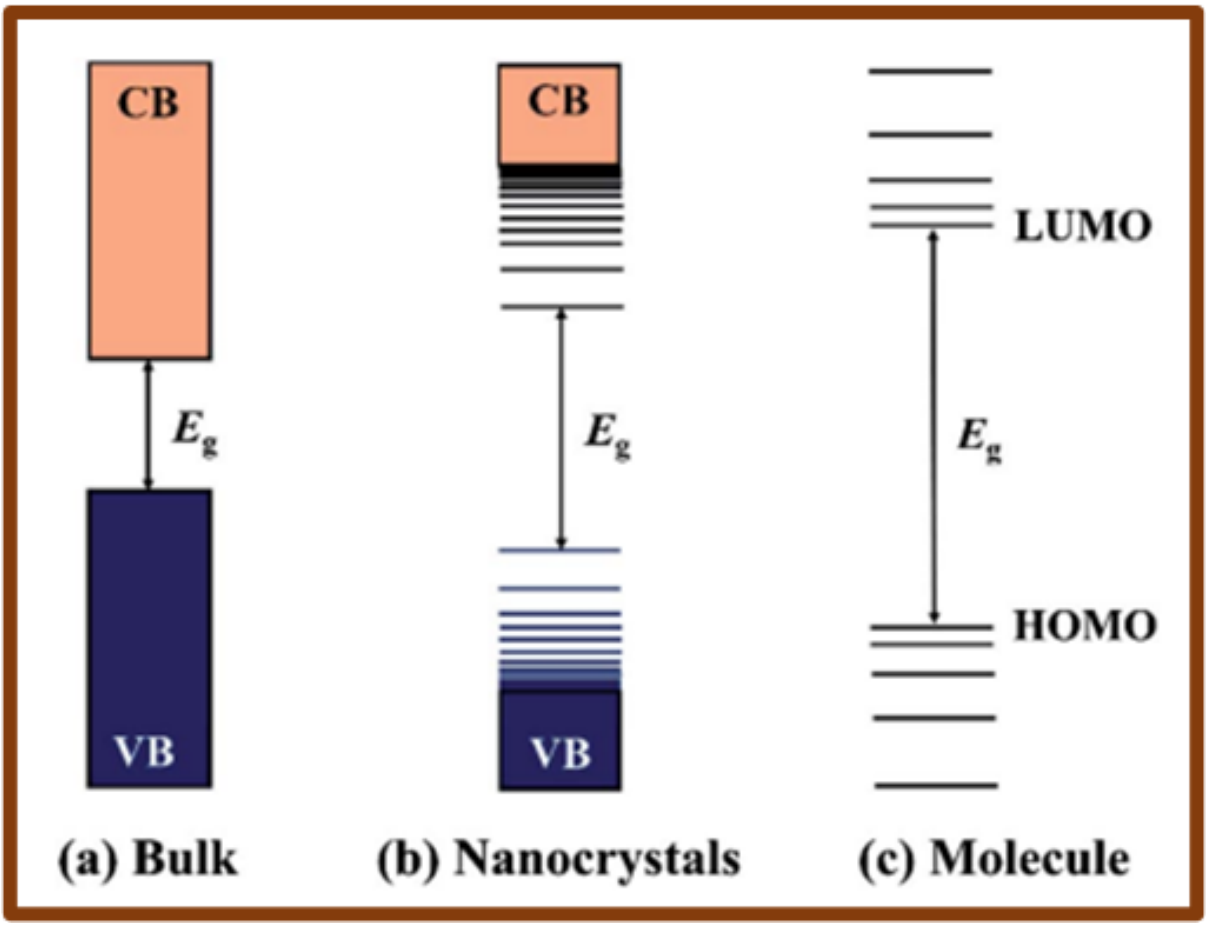

Fig 1.2: Energy Level Diagrams of Bulk, Nanocrystal, and Molecular Systems.[5]

transitional between continuum band states and discrete molecular orbitals (illustrated in **Fig 1.2**). This intermediate nature causes the energy gap E_g to be size-dependent: reducing particle dimensions produce an increase in E_g. The effective-mass model of Brus provides the theoretical framework that relates bandgap enlargement to particle size[8], [9].

1.4. Introduction of photocatalysis:

With energy scarcity and environmental degradation becoming critical global issues, significant research initiatives have focused on mitigating fossil fuel depletion and persistent pollution by developing sustainable energy systems and green technological solutions[10][11][12][13]. Within this framework, photocatalysis emerges as an appealing strategy, utilizing a semiconductor-based photocatalyst and harnessing solar energy as its only power input. Particularly, photocatalysis holds great promise for hydrogen and oxygen generation through water splitting and for the photocatalytic reduction of CO_2 into hydrocarbon fuels[14][15][16]. Beyond energy applications, photocatalysis offers considerable potential in the decomposition of dyes and volatile organic compounds (VOCs), in bacterial inactivation, and in directing selective organic syntheses[17]. Photocatalytic activity on semiconductor catalysts generally involves four major steps:

(1) photoexcitation leading to electron–hole pair formation,

(2) their separation and migration to active surface sites,

(3) engagement of these carriers in oxidation–reduction reactions, and

(4) eventual carrier recombination within the bulk phase or at the catalyst surface.

The interrelated nature of these steps means that the thermodynamic feasibility and kinetic rates of the individual processes collectively dictate the efficiency of a photocatalyst[18][19].

1.5. Challenges in photocatalyst:

The seminal work of Fujishima and Honda on TiO_2-mediated photoelectrochemical hydrogen evolution has prompted broad research into diverse semiconductor photocatalysts[20]. Nevertheless, the modest performance of the synthesized photocatalysts continues to constrain their practical implementation[21][22][23]. An important challenge is minimizing the rapid

electron–hole recombination that occurs under illumination. This process is strongly promoted by the Coulomb attraction between the charges, comparable to how gravity pulls a person back to the ground after a jump **(Fig 1.3(a–b))**[24]. Another limitation of single-material photocatalysts is that achieving both robust redox potential and an extended light-harvesting range is difficult, as these characteristics generally do not coexist effectively. To supply the required oxidative or reductive force for a particular surface reaction, a single-component catalyst must possess a sufficiently high bandgap, because greater bandgap energies enhance redox potential[25]. On the other hand, efficient solar-energy utilization calls for a decreased bandgap because materials with lower bandgaps can capture a wider portion of the solar spectrum. Consequently, creating simple yet efficient methods to address these issues is essential for boosting the overall performance of photocatalysts.

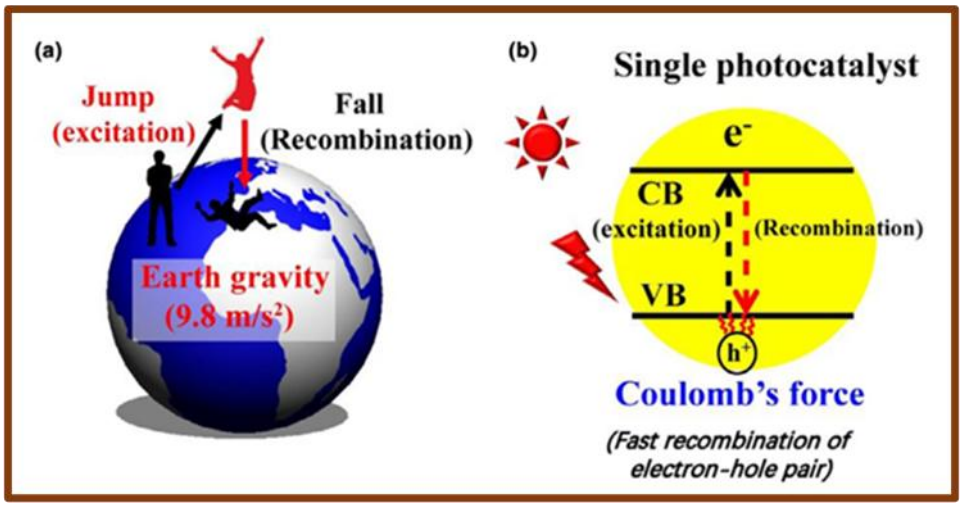

Fig 1.3: (a) how gravity affects a human jumping off the surface, and (b) the process by which electrons and holes reunite in a lone photocatalyst material[24].

1.6. Strategies for Overcoming Challenges:

Until now, a wide range of strategies and studies have been implemented to tackle these issues[24]. Of the strategies explored, heterojunction structures stand out for their ability to decouple photogenerated electrons and holes and to synergistically integrate the favourable properties of each component[26]. Typically constructed from two semiconductors that present a staggered band alignment, these heterojunctions facilitate the Type-II photocatalytic mechanism, as depicted in **Fig 1.4a**. Under sufficient photoexcitation, both photocatalysts form electron–hole pairs; the excited electrons in PC-I, which possesses a higher conduction-band edge, preferentially transfer to the conduction band of PC-II where the energy is lower[27].

Conversely, the holes produced under light excitation in both semiconductor components drift in the reverse direction relative to the electron flow. Consequently, light-induced electrons are retained by PC II for reductive processes, whereas holes are sequestered on PC I for oxidative reactions[18]. Such enforced spatial separation minimizes charge recombination and substantially boosts the heterojunction's energy conversion performance[18][23]. Despite these advantages, Type-II heterojunctions may weaken the redox potentials of photogenerated carriers, limiting their photocatalytic activity. Therefore, the Z-scheme strategy is preferred as it preserves stronger redox potentials while maintaining efficient charge separation. Although its band alignment resembles that of a Type-II heterojunction, the charge-transfer mechanism is distinctly different, as shown in **Fig. 1.4b**. In a direct Z-scheme, the highly energetic CB electrons of PC I and VB holes of PC II are retained, while the less energetic carriers recombine. Thus, Z-scheme photocatalysts combine strong redox ability with effective charge separation and can improve solar-light utilization through the use of narrow-bandgap semiconductors.[28].

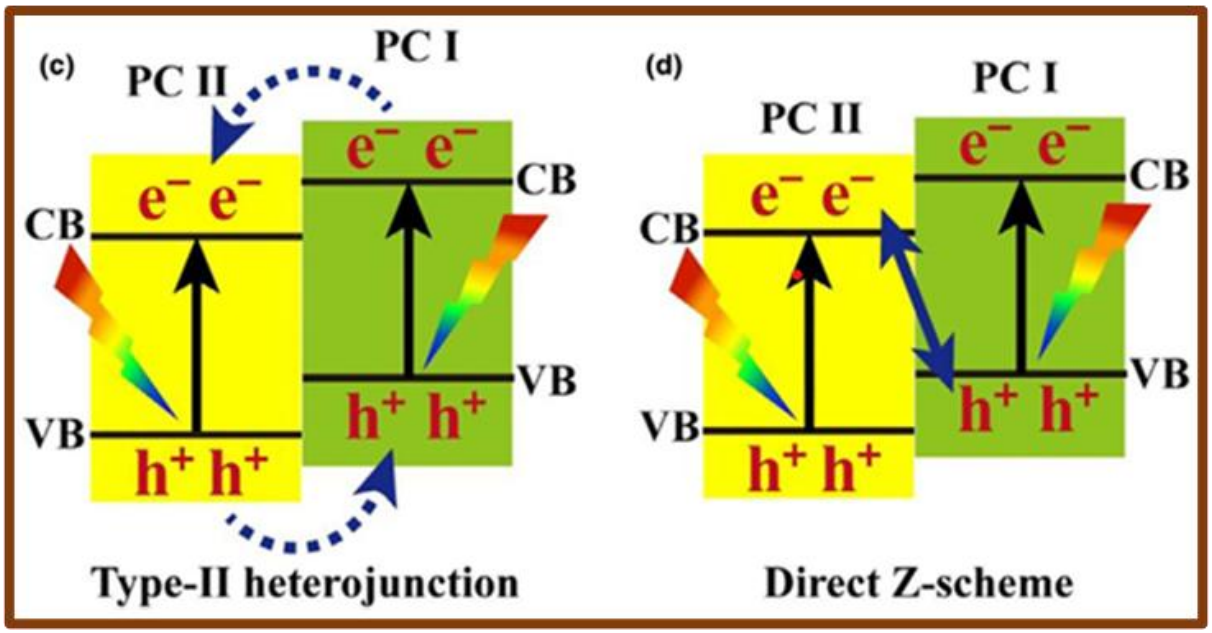

Fig 1.4: (a) Schematic of a Type-II heterojunction and (b) a direct Z-scheme heterojunction. CB and VB represent the conduction and valence bands, and PC I / PC II refer to the two photocatalyst components.[28]

1.7.Polyaniline as a photocatalyst:

Over the past decade, intensified efforts to develop efficient photocatalytic materials have been driven by their prospective contributions to sustainable energy and environmental protection. Notably, polyaniline-based nanocomposites exhibit a combination of desirable attributes, including strong stability, high conductivity, and tunable optical/electronic properties, that make them attractive for advanced applications[29].

As a conductive polymer with exceptional physicochemical traits, polyaniline (PANI) has been widely explored for applications ranging from electronic components and sensor platforms to various energy-storage systems[30]. The addition of PANI to nanocomposites has enabled the creation of materials with improved characteristics, including greater surface area, enhanced catalysis, and more effective light absorption[31]. Polyaniline-based nanocomposites demonstrate significant potential in areas like photocatalytic breakdown of contaminants and the production of hydrogen[32]. In photocatalytic degradation, illumination triggers chemical reactions that convert harmful pollutants into safer compounds. In contrast, the production of hydrogen utilizes photocatalytic materials to decompose water molecules, yielding hydrogen and oxygen that serve as a clean, renewable form of energy[33]. Both fields have emerged as key areas of study, largely due to their promise in overcoming pressing environmental problems and fulfilling future energy requirements[34]. The degradation of dyes through photocatalysis, where semiconductor materials facilitate the breakdown of hazardous organic pollutants has gained recognition as a sustainable and efficient technique for managing industrial wastewater. At the same time, the photocatalytic generation of hydrogen, relying on the same class of semiconductor catalysts to drive water-splitting, has attracted attention as a promising approach to clean, renewable energy production. Emerging evidence shows that photocatalytic dye degradation and hydrogen evolution can be coupled within one multifunctional setup, where pollutant breakdown is accompanied by the generation of hydrogen as a beneficial by-product[35]. The integration of dye degradation and hydrogen production within a single photocatalytic system offers an exceptional opportunity to confront environmental contamination and renewable-energy requirements concurrently, supporting the transition toward sustainability[33]. In recent times, a substantial body of work has examined the

fabrication and detailed characterization of polyaniline-derived nanocomposites for their photocatalytic degradation performance and hydrogen-generation capability. Collectively, these studies demonstrate that PANI-based nanocomposites deliver notable catalytic performance, long-term stability, and favourable energy-conversion efficiencies[36]. Integration of these nanocomposites into photocatalytic processes promises a cost-effective, environmentally benign strategy for pollutant abatement and concurrent H_2 production, supporting sustainable energy applications[37]. Overall, polyaniline-based nanocomposites show great promise for photocatalytic degradation and hydrogen production; continued development of these materials is likely to yield important strides in environmental cleanup and sustainable energy solutions.

1.8. Importance of the proposed investigation:

1. The current endeavour aims to reduce the volume and toxicity of wastewater produced by the textile industry.

2. The proposed study will employ a cost-effective and non-toxic method for the photocatalytic degradation of textile dyes and the production of green hydrogen using solar light.

3. The development of a selective photocatalyst material will enable the efficient degradation of organic pollutants and the production of hydrogen energy by half-water splitting.

4. A more dependable photocatalyst design that can be activated by both UV-visible and solar light is being pursued.

5. Analytical methods will be employed to identify useful end products and transfer technical knowledge to collaborative textile industries.

6. The efficiency of textile dye degradation through photocatalysis will be compared under solar and UV irradiation, and possibilities for a cost-effective approach to significantly improve efficiency will be explored.

1.9. Literature Review:

1.9.1. Photocatalytic degradation of organic pollutants:

There are a very large of studies on the photocatalytic degradation of organic pollutants. Herein, a few studies are discussed when in PANI composites has been used for degradation of dye.

Jumat et al. (2017) [38] prepared in situ, a spherical dispersed TiO_2 anchored on the polymeric chain was successfully synthesized using PANI-TiO_2 as a catalyst with a 4% dosage, exhibiting excellent photocatalytic performance for the degradation of methylene blue (MB) under Vis-lamp irradiation. Characterization techniques such as SEM and TEM revealed the presence of uniformly dispersed TiO_2 particles on the polymer chain, while XRD analysis confirmed a crystallite size of 16.27 nm. Additionally, UV-visible spectroscopy measurements demonstrated a significantly lowered band gap of 3.15 eV. This catalyst achieved an impressive 99% degradation efficiency of MB by 4 hours of irradiation.

Chauhan et al. (2013) [39] using an in-situ approach, in which a pinstriped and spherical particle of PANI, along with small agglomerated TiO_2, was successfully deposited on cotton fibers, and the morphology was characterized by SEM and TEM. The photocatalytic performance of the PANI/TiO_2-modified cotton was evaluated under irradiation from a 300 W Xenon arc lamp, achieving 87.7% degradation efficiency of Rhd-B dye by 3 hours irradiation at a concentration of 1.0×10^{-5} M. Further analysis by FT-IR indicated a higher intensity of –OH groups on the modified cotton, while XPS analysis identified a higher binding energy, suggesting enhanced interactions between the PANI/TiO_2 particles and the cotton fiber.

Song et al. (2020) [40] by employing self-assembly techniques to fabricate and characterised PVA/PANI/TiO_2 hydrogels were successfully fabricated and characterized using SEM, revealing the presence of open channels within the structure. The photocatalytic performance of these hydrogels was evaluated under irradiation from a 100 W mercury lamp, showcasing an impressive 78.7% degradation efficiency of MB dye at concentrations of 10 mg and 25 mg L^{-1}. Notably, the addition of PANI resulted in the identification of intense and broad peaks, indicating its successful incorporation into the hydrogel matrix.

Koysuren et al. (2019) [41], prepared PANI/Fe–TiO_2 composite and investigated for its photocatalytic activity against MB dye under irradiation from a 30 W UV lamp, resulting in a 28% degradation efficiency in 2.5 hours irradiation time at a concentration of 10 mg L^{-1}. The microstructural analysis using SEM and TEM unveiled the presence of well-ordered aggregation of TiO_2 and Fe–TiO_2 onto the polymeric network, indicating a highly crystalline structure. Furthermore, FT-IR analysis provided evidence of bonding linkages between Fe and

TiO_2 as well as PANI–Fe, confirming the successful incorporation of Fe into the composite material.

Liu et al. (2014) [42] using an in-situ method, prepared spherical TiO_2 and SiO_2 nano fibers coated with PANI powder. The photocatalytic activity of the PANI/TiO_2/SiO_2 composite was evaluated under irradiation from a 500 W Xenon arc lamp, exhibiting an impressive 87% degradation efficiency of MO dye at a concentration of 1.5 mg L^{-1}. Additionally, XRD analysis indicated an increased peak intensity upon the addition of SiO_2, suggesting improved crystallinity and enhanced structural properties of the composite material.

Maruthapandi et al. (2020) [43] utilizing Sonochemical synthesis, flake-like SiO_2 particles were successfully anchored onto the PANI network. The photocatalytic performance of the PANI/SiO_2 composite was evaluated for the degradation of MB dye at a concentration of 50 mg and pH 6.7, resulting in a significant 74% degradation efficiency. Notably, XRD analysis revealed that the addition of SiO_2 led to a narrowing of the broader peak of PANI, indicating improved crystallinity and enhanced structural properties of the composite material.

Table 1. Degradation of the organic contaminants with the various PANI- based photocatalysts.

S.no.	Polymeric composite	Synthesis technique	Pollutant dye	Time (hours)	Experimental conditions	Dye removal (%)	Ref.
1	PANI-TiO_2	*In-situ*	MB	2	10 mg, 10 mg L^{-1}	89.7	[38]
2	PANI/TiO_2/Cotton	*In-situ*	Rhb	3	1.0 x 10^{-5}	87.7	[39]
3	PVA/PANI/TiO_2	Self-assembly	MB	2	10 mg, 25 mg L-1	78.7	[40]
4	PANI/Fe-TiO_2	Mixing	MB	2.5	10 mg L-1	28	[41]
5	PANI/TiO_2/SiO_2	Mixing	MO	2	1.5 mg L-1	87	[42]

6	PANI/SiO_2	Sonochemical	MB	2	50 mg, pH 6.7	74	[43]
7	Ag-ZnO/PANI	*In-situ*	MG	2	0.2 g L-1, 0.2 g, pH 8	98.6	[44]
8	Cu_2O/ZnO-PANI	*In-situ*	CR	30	0.05 g L-1, 100 mg, pH 6	95	[45]

1.9.2. Photocatalytic hydrogen production:

Lee et al. (2019) [46] the synthesized PANI/g-TiO_2 composite, which under the irradiation of a 300 W Xenon lamp, demonstrated remarkable photocatalytic performance for methanol degradation with a conversion rate of 1790 mmol $g^{-1}h^{-1}$. In this process, methanol acts as a sacrificial agent, providing electrons to the PANI/g-TiO_2 composite, thereby facilitating the generation of reactive species that efficiently degrade the methanol molecules, resulting in the high conversion rate observed.

Ma et al. (2020) [47] the PANI-TiO_2/RGO composite, when exposed to the irradiation of a 300 W Xenon lamp, displayed impressive photocatalytic activity for the degradation of a sacrificial agent, triethanolamine, with a high conversion rate of 806 mmol g^{-1} h^{-1}. In this process, triethanolamine serves as a sacrificial agent by providing electrons to the PANI-TiO_2/RGO composite, enabling the generation of reactive species that effectively degrade the triethanolamine molecules, resulting in the observed high conversion rate. The synergistic combination of PANI-TiO_2 and RGO in the composite enhances the photocatalytic performance by promoting electron transfer and increasing the active surface area, leading to improved efficiency in the photocatalytic water splitting.

Wirth et al. (2011) [48] studied the adsorption and splitting of water molecules on a rutile ruthenium dioxide anode using periodic density functional calculations. The structure of adsorbed H_2O molecules and radicals involved in the splitting process ($O^{\bullet}$, $OH^{\bullet}$,$^{\bullet}OOH$) were determined and compared with available experimental results. On the basis of these electronic structure calculations, a method was used to calculate the stability of the reaction intermediates and conclude on the thermodynamical possibility of the water splitting reaction at the surface.

Results showed that a moderate overpotential of 0.64V is required for the reaction to take place at the RuO_2 (110) surface.

Table 2. Hydrogen production rate of different photocatalysts.

S.no.	Photocatalyst	Light source	Sacrificial agent	H_2 rate ($\mu mol.h^{-1}. g^{-1}$)	Reference
1	PANI/g-TiO_2	300 W Xe	Methanol	1790	[46]
2	PANI-TiO_2/RGO	300 W Xe	Triethanolamine	806	[47]
3	PANI/TiO_2	UV-LEDs	Methanol	3083	[49]
4	Ppy/TiO_2	UV-LEDs	Methanol	2090	[49]
5	PEDOT/TiO_2	UV-LEDs	Methanol	1370	[49]

1.10. The rationale of the present study:

The development of modern textile dyes has led to the creation of dyes that possess strong structural integrity and color stability. These dyes are primarily composed of aromatic compounds, which contribute to their robustness and durability. Consequently, they have found widespread usage in various industries and applications [50].

However, a significant concern arises from the potential unintended release of these dyes into the environment, particularly through wastewater. When textile dyes are discharged into water bodies without proper treatment, they can pose significant risks to both human health and ecological systems [51].

The release of toxic textile dyes into the environment can have adverse effects on human health. Direct exposure to these dyes can lead to various health issues, whether through contact with contaminated water or consumption of affected aquatic organisms. These may include skin

irritation, respiratory problems, and even more severe conditions such as carcinogenic or mutagenic effects [52].

Furthermore, the ecological impact of textile dye pollution should not be overlooked. When these dyes enter water bodies, they can cause extensive damage to aquatic ecosystems. The vibrant and persistent colors of the dyes hinder sunlight penetration, disrupting photosynthesis and ultimately affecting the balance of the ecosystem. Additionally, the toxic nature of the dyes can harm aquatic organisms, leading to a decline in biodiversity and ecological imbalance [42].

Given these risks, it becomes crucial to prioritize the effective removal of toxic textile dyes from wastewater[53]. Implementing proper treatment methods to eliminate or minimize the presence of these dyes is essential to mitigate the potential harm they can cause. Various techniques such as advanced oxidation processes, adsorption, and biological treatments can be employed to remove or degrade textile dyes effectively [54].

By addressing the issue of textile dye pollution and implementing appropriate wastewater treatment measures, we can safeguard both human health and the integrity of ecological systems[55]. It is essential for industries, regulatory bodies, and society as a whole to recognize the importance of responsible dye usage and invest in sustainable practices that minimize the environmental impact of textile dyes [56].

Due to the increasing levels of greenhouse gas emissions resulting from human energy consumption through the combustion of fossil fuels, human-induced climate change has become an urgent and critical concern[57]. This has led to various environmental changes, including the melting of land ice and rising sea levels caused by ocean thermal expansion, contributing to global warming. As the most significant environmental, social, and economic crisis worldwide, numerous statutory and voluntary initiatives have been implemented to reduce greenhouse gas emissions and mitigate the impact of global warming by decreasing the use of fossil fuels[58].

One potential solution to address these issues is the utilization of a water-splitting process to produce hydrogen. Hydrogen is considered a reliable energy source as it significantly reduces pollution. However, the water-splitting reaction requires a high potential of about 237 J/mol, making it thermodynamically unfavorable. In reality, due to the high stability of water, hydrogen evolution cannot occur without a catalyst and an external energy source. The

electrochemical reduction process, which involves the delivery of electrical energy between two electrodes, is a promising method for hydrogen production under moderate conditions. However, further development is necessary to make it economically viable on an industrial scale, as it currently incurs high operational costs, largely reliant on fossil fuel combustion for electricity generation [47].

Therefore, solar energy, which is abundant, renewable, and environmentally friendly, is recommended as a method for water splitting to generate hydrogen. Sunlight contains a broad spectrum of energy, including UV, visible (VIS), and infrared (IR) radiation, which can facilitate the splitting of water molecules. Although the current photo-conversion efficiencies are generally impractical for large-scale operations, solar irradiation holds great potential. The incorporation of catalysts to enhance the reaction rate enables energy-efficient, rapid, and highly selective hydrogen generation. However, the efficacy of photocatalysts is limited by factors such as high recombination rates, susceptibility to photo corrosion, and insufficient charge migration capabilities [59].

Studies suggest that the prevention of photo corrosion and recombination can be achieved by creating an equal number of electrons and holes in the photocatalyst. One common approach is catalyst pairing, which facilitates multiple proton-electron excitation pathways through a physical contact cascade or z scheme. Therefore, there is a need to explore highly efficient and reusable 2D nanocomposites that respond to sunlight, forming heterojunctions, to overcome these limitations in the field of solar-driven water splitting for hydrogen production.

1.11. Research gaps:

i. Semiconductor photocatalysts such as TiO_2, ZnO, WO_3, MoS_2, BiOCl, and g-C_3N_4 have been extensively investigated for photocatalytic degradation. However, their practical application is still limited by poor visible-light utilization and rapid charge-carrier recombination. Developing efficient PANI-based composite photocatalysts with enhanced visible-light absorption and charge separation remains a significant challenge.

ii. Although several PANI-based binary and ternary photocatalysts have been reported, studies on lesser-explored PANI-based composite systems for the degradation of dyes, pharmaceuticals, and pesticides are limited. Moreover, mechanistic investigations on charge transfer and reactive species generation are still scarce.

iii. Solar-driven photocatalytic water splitting has been widely studied; however, hydrogen evolution using the specific PANI-based binary and ternary nanocomposites proposed in this work has been reported only to a limited extent. Their structure–property relationship and photocatalytic performance under natural sunlight require further investigation.

1.12. Objectives

The main objectives of the present study are:

1. Preparation of polyaniline (PANI)-based binary/ternary nanocomposites with GO, BiOCl, MoO_3, MoS_2, and LDH for enhanced physiochemical properties.
2. Study the photocatalytic activity of these as-prepared nanocomposites towards application in pollutants degradation and hydrogen production through water splitting under light irradiation.

References:

[1] C. M. Lieber, "Nanoscale Science and Technology: Building a Big Future from Small Things," *MRS Bull.*, vol. 28, no. 7, pp. 486–491, Jul. 2003, doi: 10.1557/mrs2003.144.

[2] "The Feynman principle for a Fermi system," *Proc. R. Soc. London. Ser. A. Math. Phys. Sci.*, vol. 251, no. 1267, pp. 543–549, Jun. 1959, doi: 10.1098/rspa.1959.0127.

[3] F. Caruso, "Nanoengineering of Particle Surfaces," *Adv. Mater.*, vol. 13, no. 1, pp. 11–22, Jan. 2001, doi: 10.1002/1521-4095(200101)13:1<11::AID-ADMA11>3.0.CO;2-N.

[4] G. Cao and Y. Wang, *Nanostructures and Nanomaterials*, vol. 2. in World Scientific Series in Nanoscience and Nanotechnology, vol. 2. WORLD SCIENTIFIC, 2011. doi: 10.1142/7885.

[5] P. E. Lippens and M. Lannoo, "Calculation of the band gap for small CdS and ZnS crystallites," *Phys. Rev. B*, vol. 39, no. 15, pp. 10935–10942, May 1989, doi: 10.1103/PhysRevB.39.10935.

[6] L. E. Brus, "Electron–electron and electron-hole interactions in small semiconductor crystallites: The size dependence of the lowest excited electronic state," *J. Chem. Phys.*, vol. 80, no. 9, pp. 4403–4409, May 1984, doi: 10.1063/1.447218.

[7] H. Weller, "Colloidal Semiconductor Q-Particles: Chemistry in the Transition Region

Between Solid State and Molecules," *Angew. Chemie Int. Ed. English*, vol. 32, no. 1, pp. 41–53, Jan. 1993, doi: 10.1002/anie.199300411.

[8] H. Weller, "Quantized Semiconductor Particles: A novel state of matter for materials science," *Adv. Mater.*, vol. 5, no. 2, pp. 88–95, Feb. 1993, doi: 10.1002/adma.19930050204.

[9] S. V. Gaponenko, *Optical Properties of Semiconductor Nanocrystals*. Cambridge University Press, 1998. doi: 10.1017/CBO9780511524141.

[10] A. Kubacka, M. Fernández-García, and G. Colón, "Advanced Nanoarchitectures for Solar Photocatalytic Applications," *Chem. Rev.*, vol. 112, no. 3, pp. 1555–1614, Mar. 2012, doi: 10.1021/cr100454n.

[11] J. Fu, J. Yu, C. Jiang, and B. Cheng, "g-C_3N_4 -Based Heterostructured Photocatalysts," *Adv. Energy Mater.*, vol. 8, no. 3, Jan. 2018, doi: 10.1002/aenm.201701503.

[12] H. Khojasteh, M. Salavati-Niasari, H. Safajou, and H. Safardoust-Hojaghan, "Facile reduction of graphene using urea in solid phase and surface modification by N-doped graphene quantum dots for adsorption of organic dyes," *Diam. Relat. Mater.*, vol. 79, pp. 133–144, Oct. 2017, doi: 10.1016/j.diamond.2017.09.011.

[13] H. Haghjoo, F. S. Sangsefidi, and M. Salavati-Niasari, "Synthesis of $PbSiO_3$ nanoparticles in the presence of proteins as a greencapping agent and their application as photocatalyst," *J. Mol. Liq.*, vol. 247, pp. 345–353, Dec. 2017, doi: 10.1016/j.molliq.2017.10.029.

[14] C. Ye *et al.*, "Protonated Graphitic Carbon Nitride with Surface Attached Molecule as Hole Relay for Efficient Photocatalytic O_2 Evolution," *ACS Catal.*, vol. 6, no. 12, pp. 8336–8341, Dec. 2016, doi: 10.1021/acscatal.6b02664.

[15] Z. Tong, D. Yang, Y. Sun, Y. Nan, and Z. Jiang, "Tubular g-C_3N_4 Isotype Heterojunction: Enhanced Visible-Light Photocatalytic Activity through Cooperative Manipulation of Oriented Electron and Hole Transfer," *Small*, vol. 12, no. 30, pp. 4093–4101, Aug. 2016, doi: 10.1002/smll.201601660.

[16] F. Xu, W. Xiao, B. Cheng, and J. Yu, "Direct Z-scheme anatase/rutile bi-phase nanocomposite TiO_2 nanofiber photocatalyst with enhanced photocatalytic H_2 -

production activity," *Int. J. Hydrogen Energy*, vol. 39, no. 28, pp. 15394–15402, Sep. 2014,

[17] M. Abbadi, A. Laghzizil, and D. Robert, "La-CeO_2/ZnO nanocomposites for photocatalytic mineralization of diclofenac under solar irradiation," *J. Photochem. Photobiol. A Chem.*, vol. 457, p. 115861, Dec. 2024, doi: 10.1016/j.jphotochem.2024.115861.

[18] S. Bai, J. Jiang, Q. Zhang, and Y. Xiong, "Steering charge kinetics in photocatalysis: intersection of materials syntheses, characterization techniques and theoretical simulations," *Chem. Soc. Rev.*, vol. 44, no. 10, pp. 2893–2939, 2015, doi: 10.1039/C5CS00064E.

[19] A. L. Linsebigler, G. Lu, and J. T. Yates, "Photocatalysis on TiO_2 Surfaces: Principles, Mechanisms, and Selected Results," *Chem. Rev.*, vol. 95, no. 3, pp. 735–758, May 1995, doi: 10.1021/cr00035a013.

[20] A. FUJISHIMA and K. HONDA, "Electrochemical Photolysis of Water at a Semiconductor Electrode," *Nature*, vol. 238, no. 5358, pp. 37–38, Jul. 1972, doi: 10.1038/238037a0.

[21] K. Qi, B. Cheng, J. Yu, and W. Ho, "A review on TiO_2-based Z-scheme photocatalysts," *Chinese J. Catal.*, vol. 38, no. 12, pp. 1936–1955, Dec. 2017, doi: 10.1016/S1872-2067(17)62962-0.

[22] H. Najafian, F. Manteghi, F. Beshkar, and M. Salavati-Niasari, "Efficient degradation of azo dye pollutants on $ZnBi_{38}O_{58}$ nanostructures under visible-light irradiation," *Sep. Purif. Technol.*, vol. 195, pp. 30–36, Apr. 2018, doi: 10.1016/j.seppur.2017.11.076.

[23] M. Mahdiani, F. Soofivand, F. Ansari, and M. Salavati-Niasari, "Grafting of $CuFe_{12}O_{19}$ nanoparticles on CNT and graphene: Eco-friendly synthesis, characterization and photocatalytic activity," *J. Clean. Prod.*, vol. 176, pp. 1185–1197, Mar. 2018, doi: 10.1016/j.jclepro.2017.11.177.

[24] J. Low, J. Yu, M. Jaroniec, S. Wageh, and A. A. Al-Ghamdi, "Heterojunction Photocatalysts," *Adv. Mater.*, vol. 29, no. 20, May 2017, doi: 10.1002/adma.201601694.

[25] P. García-Muñoz, A. Abega, A. Hernández-Zanoletty, D. Robert, S. Malato, and N.

Keller, "Scaling-up the use of macroscopic photo-CWPO $La_{1-x}Ti_xFeO_3$/SiC alveolar foam catalyst for solar water treatment against micropollutants," *Chem. Eng. J.*, vol. 498, p. 155750, Oct. 2024, doi: 10.1016/j.cej.2024.155750.

[26] G. Gao, Y. Jiao, E. R. Waclawik, and A. Du, "Single Atom (Pd/Pt) Supported on Graphitic Carbon Nitride as an Efficient Photocatalyst for Visible-Light Reduction of Carbon Dioxide," *J. Am. Chem. Soc.*, vol. 138, no. 19, pp. 6292–6297, May 2016, doi: 10.1021/jacs.6b02692.

[27] Z. Zhang *et al.*, "Graphitic carbon nitride nanosheet for photocatalytic hydrogen production: The impact of morphology and element composition," *Appl. Surf. Sci.*, vol. 391, pp. 369–375, Jan. 2017, doi: 10.1016/j.apsusc.2016.05.174.

[28] L. Liu, Y. Qi, J. Hu, Y. Liang, and W. Cui, "Efficient visible-light photocatalytic hydrogen evolution and enhanced photostability of core@shell Cu_2O@g-C_3N_4 octahedra," *Appl. Surf. Sci.*, vol. 351, pp. 1146–1154, Oct. 2015, doi: 10.1016/j.apsusc.2015.06.119.

[29] R. Kumar *et al.*, "Facile route to a conducting ternary polyaniline@TiO_2/GN nanocomposite for environmentally benign applications: photocatalytic degradation of pollutants and biological activity," *RSC Adv.*, vol. 6, no. 112, pp. 111308–111317, 2016, doi: 10.1039/C6RA24079H.

[30] Q. Wang *et al.*, "Photodegradation of methyl orange with PANI-modified BiOCl photocatalyst under visible light irradiation," *Appl. Surf. Sci.*, vol. 283, pp. 577–583, Oct. 2013, doi: 10.1016/j.apsusc.2013.06.149.

[31] A. Kumar, R. Kumar, and G. Pandey, "Synthesis, Characterization of Titania/Polyaniline/GO Nanocomposites, and Its Photocatalytic Activity Under UV-Visible Light," *Macromol. Symp.*, vol. 379, no. 1, Jun. 2018, doi: 10.1002/masy.201600192.

[32] P. Ahuja, S. K. Ujjain, I. Arora, and M. Samim, "Hierarchically Grown NiO-Decorated Polyaniline-Reduced Graphene Oxide Composite for Ultrafast Sunlight-Driven Photocatalysis," *ACS Omega*, vol. 3, no. 7, pp. 7846–7855, Jul. 2018, doi: 10.1021/acsomega.8b00765.

[33] C.-C. Hu and H. Teng, "Gallium Oxynitride Photocatalysts Synthesized from Ga(OH)

$_3$ for Water Splitting under Visible Light Irradiation," *J. Phys. Chem. C*, vol. 114, no. 47, pp. 20100–20106, Dec. 2010, doi: 10.1021/jp1070083.

[34] A. Kudo and Y. Miseki, "Heterogeneous photocatalyst materials for water splitting," *Chem. Soc. Rev.*, vol. 38, no. 1, pp. 253–278, 2009, doi: 10.1039/B800489G.

[35] T.-F. Yeh, J. Cihlář, C.-Y. Chang, C. Cheng, and H. Teng, "Roles of graphene oxide in photocatalytic water splitting," *Mater. Today*, vol. 16, no. 3, pp. 78–84, Mar. 2013, doi: 10.1016/j.mattod.2013.03.006.

[36] V. Etacheri, G. Michlits, M. K. Seery, S. J. Hinder, and S. C. Pillai, "A Highly Efficient $TiO_{2-x}C_x$ Nano-heterojunction Photocatalyst for Visible Light Induced Antibacterial Applications," *ACS Appl. Mater. Interfaces*, vol. 5, no. 5, pp. 1663–1672, Mar. 2013, doi: 10.1021/am302676a.

[37] M. Atarod, M. Nasrollahzadeh, and S. Mohammad Sajadi, "Euphorbia heterophylla leaf extract mediated green synthesis of Ag/TiO_2 nanocomposite and investigation of its excellent catalytic activity for reduction of variety of dyes in water," *J. Colloid Interface Sci.*, vol. 462, pp. 272–279, Jan. 2016, doi: 10.1016/j.jcis.2015.09.073.

[38] N. A. Jumat, P. S. Wai, J. J. Ching, and W. J. Basirun, "Synthesis of Polyaniline-TiO_2 Nanocomposites and Their Application in Photocatalytic Degradation," *Polym. Polym. Compos.*, vol. 25, no. 7, pp. 507–514, Sep. 2017, doi: 10.1177/096739111702500701.

[39] N. P. S. Chauhan, N. K. Jangid, and P. B. Punjabi, "Synthesis and Characterization of Conducting Polyanilines via Catalytic Oxidative Polymerization," *Int. J. Polym. Mater.*, vol. 62, no. 10, pp. 550–555, May 2013, doi: 10.1080/00914037.2012.761625.

[40] X. Song *et al.*, "Efficient construction and enriched selective adsorption-photocatalytic activity of PVA/PANI/TiO_2 recyclable hydrogel by electron beam radiation," *J. Appl. Polym. Sci.*, vol. 137, no. 13, Apr. 2020, doi: 10.1002/app.48516.

[41] O. Koysuren and H. N. Koysuren, "Photocatalytic activity of polyaniline/Fe-doped TiO_2 composites by in situ polymerization method," *J. Macromol. Sci. Part A*, vol. 56, no. 3, pp. 267–276, Mar. 2019, doi: 10.1080/10601325.2019.1565548.

[42] Z. Liu *et al.*, "Flexible polyaniline-coated TiO_2/SiO_2 nanofiber membranes with enhanced visible-light photocatalytic degradation performance," *J. Colloid Interface Sci.*, vol. 424, pp. 49–55, Jun. 2014, doi: 10.1016/j.jcis.2014.03.009.

[43] M. Maruthapandi, L. Eswaran, J. H. T. Luong, and A. Gedanken, "Sonochemical preparation of polyaniline@TiO_2 and polyaniline@SiO_2 for the removal of anionic and cationic dyes," *Ultrason. Sonochem.*, vol. 62, p. 104864, Apr. 2020, doi: 10.1016/j.ultsonch.2019.104864.

[44] F. Habtamu, S. Berhanu, and T. Mender, "Polyaniline Supported Ag-Doped ZnO Nanocomposite: Synthesis, Characterization, and Kinetics Study for Photocatalytic Degradation of Malachite Green," *J. Chem.*, vol. 2021, pp. 1–12, Sep. 2021, doi: 10.1155/2021/2451836.

[45] A. M. Mohammed, S. S. Mohtar, F. Aziz, M. Aziz, and A. Ul-Hamid, "Cu_2O/ZnO-PANI ternary nanocomposite as an efficient photocatalyst for the photodegradation of Congo Red dye," *J. Environ. Chem. Eng.*, vol. 9, no. 2, p. 105065, Apr. 2021, doi: 10.1016/j.jece.2021.105065.

[46] S. Xu *et al.*, "Fabrication of polyaniline sensitized grey-TiO_2 nanocomposites and enhanced photocatalytic activity," *Sep. Purif. Technol.*, vol. 184, pp. 248–256, Aug. 2017, doi: 10.1016/j.seppur.2017.04.025.

[47] J. Ma, J. Dai, Y. Duan, J. Zhang, L. Qiang, and J. Xue, "Fabrication of PANI-TiO_2/rGO hybrid composites for enhanced photocatalysis of pollutant removal and hydrogen production," *Renew. Energy*, vol. 156, pp. 1008–1018, Aug. 2020, doi: 10.1016/j.renene.2020.04.104.

[48] J. Wirth, S. Monturet, T. Klamroth, and P. Saalfrank, "Adsorption and (photo-) electrochemical splitting of water on rutile ruthenium dioxide," *EPL (Europhysics Lett.*, vol. 93, no. 6, p. 68001, Mar. 2011, doi: 10.1209/0295-5075/93/68001.

[49] H. M. El-Bery, M. R. Salah, S. M. Ahmed, and S. A. Soliman, "Efficient non-metal based conducting polymers for photocatalytic hydrogen production: comparative study between polyaniline, polypyrrole and PEDOT," *RSC Adv.*, vol. 11, no. 22, pp. 13229–13244, 2021, doi: 10.1039/D1RA01218E.

[50] G. Cravotto, E. Borretto, M. Oliverio, A. Procopio, and A. Penoni, "Organic reactions in water or biphasic aqueous systems under sonochemical conditions. A review on catalytic effects," *Catal. Commun.*, vol. 63, pp. 2–9, Mar. 2015, doi: 10.1016/j.catcom.2014.12.014.

[51] J. Kröger *et al.*, "Interfacial Engineering for Improved Photocatalysis in a Charge Storing 2D Carbon Nitride: Melamine Functionalized Poly(heptazine imide)," *Adv. Energy Mater.*, vol. 11, no. 6, p. 2003016, Feb. 2021, doi: 10.1002/aenm.202003016.

[52] A. Li, W. Zhu, C. Li, T. Wang, and J. Gong, "Rational design of yolk–shell nanostructures for photocatalysis," *Chem. Soc. Rev.*, vol. 48, no. 7, pp. 1874–1907, 2019, doi: 10.1039/C8CS00711J.

[53] M. Pahuja *et al.*, "Dual-action photocatalyst: MnO_2/CuO decorated 3D porous carbonaceous matrix as reusable photocatalyst for rapid removal of industrial dyes and antibiotics from contaminated-water," *J. Environ. Chem. Eng.*, vol. 13, no. 3, p. 116502, Jun. 2025, doi: 10.1016/j.jece.2025.116502.

[54] L. Dashairya, A. Mehta, P. Saha, and S. Basu, "Visible-light-induced enhanced photocatalytic degradation of Rhodamine-B dye using $Bi_xSb_{2-x}S_3$ solid-solution photocatalysts," *J. Colloid Interface Sci.*, vol. 561, pp. 71–82, Mar. 2020, doi: 10.1016/j.jcis.2019.11.118.

[55] S. K. Shah *et al.*, "Photocatalytic degradation of 2,4-dichlorophenol and parathion using gel-like carbon dots under simulated solar irradiation," *Colloids Surfaces A Physicochem. Eng. Asp.*, vol. 731, p. 138987, Feb. 2026, doi: 10.1016/j.colsurfa.2025.138987.

[56] Y. Fu and X. Wang, "Magnetically Separable $ZnFe_2O_4$ –Graphene Catalyst and its High Photocatalytic Performance under Visible Light Irradiation," *Ind. Eng. Chem. Res.*, vol. 50, no. 12, pp. 7210–7218, Jun. 2011, doi: 10.1021/ie200162a.

[57] D. Rathore, A. Banerjee, and S. Pande, "Bifunctional Tungsten-Doped $Ni(OH)_2$ /NiOOH Nanosheets for Overall Water Splitting in an Alkaline Medium," *ACS Appl. Nano Mater.*, vol. 5, no. 2, pp. 2664–2677, Feb. 2022, doi: 10.1021/acsanm.1c04359.

[58] S. Rej, M. Bisetto, A. Naldoni, and P. Fornasiero, "Well-defined Cu_2O photocatalysts for solar fuels and chemicals," *J. Mater. Chem. A*, vol. 9, no. 10, pp. 5915–5951, 2021, doi: 10.1039/D0TA10181H.

[59] N. A. Jumat, P. S. Wai, J. J. Ching, and W. J. Basirun, "Synthesis of Polyaniline-TiO_2 Nanocomposites and Their Application in Photocatalytic Degradation," *Polym. Polym. Compos.*, vol. 25, no. 7, pp. 507–514, Sep. 2017, doi: 10.1177/096739111702500701.

Chapter 2

Solar-Powered Pollutant Degradation and H_2 Production via PANI/BiOCl/GO

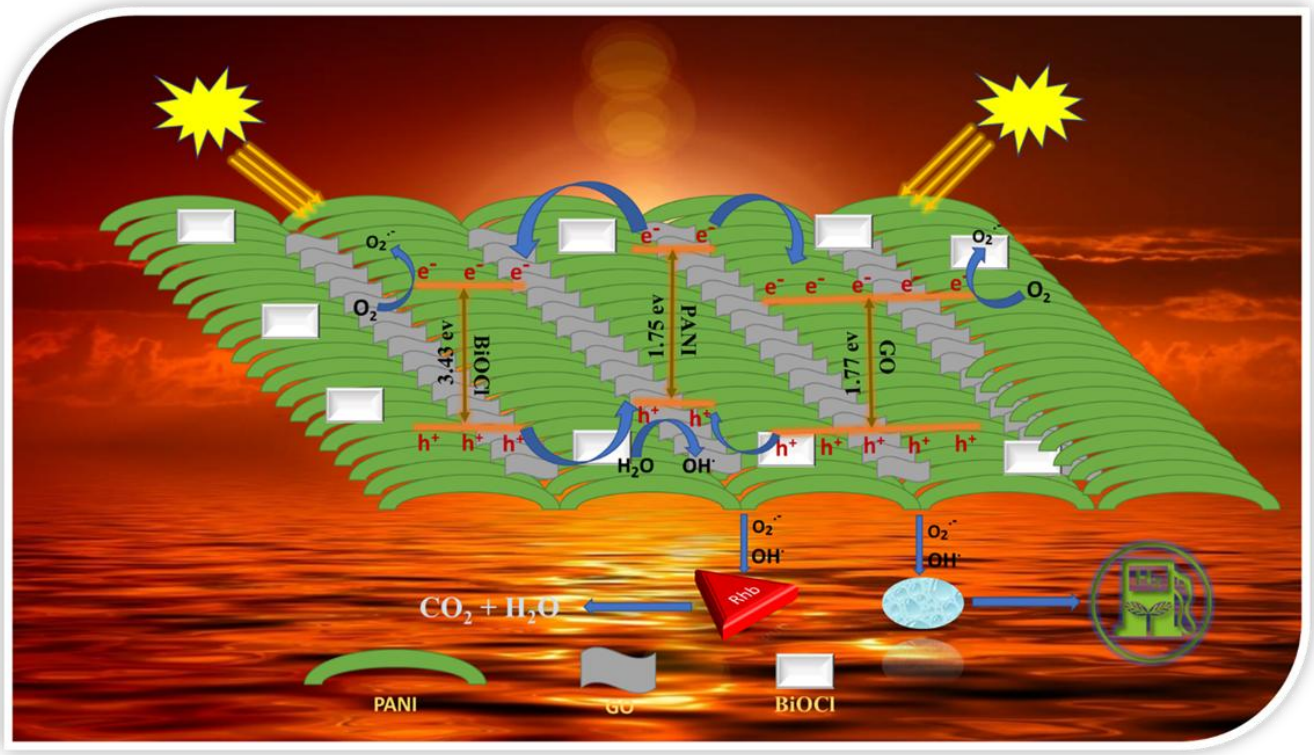

Highlights

- Fabrication of different mole ratios of Polyaniline/BiOCl/GO Ternary nanocomposite.
- Photocatalysts efficacy tested by degradation of Rhb and H_2 production from water splitting.
- Photocatalytic elimination of Rhb (96 %, rate constant~ 0.015 min^{-1}) was observed under sunlight.
- The nanocomposite produced 1000 ppm of hydrogen gas with AQE of 17.97%.

2.1. Introduction:

Water pollution caused by the release of dye sewage from various industrial sources such as paper, leather, and nylon have a significant impact on aquatic life [1][2]. Therefore, eliminating dyes from water is crucial. Chemical and physical elimination methods are two types of processes used for this purpose[3][4]. Chemical elimination methods include oxidation, electrochemical disintegration, Fenton reaction, ozonolysis, and photocatalytic degradation, while physical elimination methods include adsorption, agglomeration-precipitation, ion exchange, membrane separation, and reverse osmosis [5][6]. Solar-powered hydrogen evolution from water is a promising solution to environmental issues and the worldwide energy crisis caused by fuel production[7]. Hydrogen gas is an efficient energy carrier with a high energy capacity and does not release harmful pollutants [8][9]. As a result, there is an urgent need for an effective and fast photocatalytic method for hydrogen production. Three primary methods of hydrogen evolution powered by solar energy exist heterogeneous photocatalysis, photovoltaic-driven electrolysis, and photoelectrochemical cells [10]. Among these, heterogeneous photocatalysis is expected to be more cost-effective than the other two [9]. However, the efficiency of solar-assisted hydrogen evolution using heterogeneous photocatalysis is currently low. Several approaches, such as architectural and flaw engineering, plasmon-mediated effects, and elemental impregnation, have been deliberated to enhance the photonic absorption and light-induced electron transfer and transport of photocatalysts, yet there is still room for improvement [11][8].

In the recent past, the development of efficient photocatalytic materials has gained substantial focus owing to their prospective applications in various fields, including energy and the environment. One such promising material is polyaniline-based nanocomposites, which possess unique properties such as high stability, excellent conductivity, and tuneable optical and electronic properties. Polyaniline (PANI) is a conducting polymer that has attracted considerable attention in wide array of applications, comprising electronic apparatus, sensors, and energy warehousing systems, owing to its excellent physicochemical properties [12]. The incorporation of PANI into nanocomposites has led to the development of new materials with enhanced properties, such as increased surface area, improved catalytic activity, and enhanced light absorption [13].

Different metal oxides such as ZnO, NiO, TiO_2, BiOCl, etc. have been widely used to investigate their photocatalytic activity but there has a major drawback is a wide band gap [14][15]. To reduce the band gap of metal oxides, various methods, such as doping with metal or non-metal ions, making composites with carbon nanotubes, activated carbon, graphene, or coupling with conducting polymers, have been used [16]. Graphene oxide (GO) is a useful co-catalyst that reduces the recombination rate of bismuth oxychloride and shows good performance in photocatalytic degradation [17]. BiOCl is a conspicuous photocatalyst for many researchers because of its layered crystal-type structure in a tetragonal shape, where the bismuth atom is coordinated with four chlorine atoms, generating an intramural electric field that separates photogenerated electron(e^-) and hole(h^+) [18]. Noble metals, such as Pt, Rh, and Ru, can also be used as co-catalysts to increase the photocatalytic activity of BiOCl. However, they are expensive and only introduce active sites for the smooth segregation of charges [19]. Taking all these factors into consideration, graphene oxide (GO) can be used due to its sp^2 hybridized layered structure, which provides a high surface area of nearly 2630 m^2g^{-1} and demonstrates tremendous electronic mobility of nearly 200000 $cm^2\ V^{-1}s^{-1}$ for a p-conjugated structure [20]. Additionally, oxygenated functional groups such examples as epoxy, alcohol, and acid treatment on the surface of GO attract dye molecules for degradation. All of these characteristics make GO a useful co-catalyst in reducing the recombination rate of bismuth oxychloride and promoting good performance in photocatalytic degradation [9]. Overall, the synergistic effect of the ternary composite can increase the photocatalytic activity of the nanocomposite and make them a prominent one as a photocatalyst.

Wang et al. prepared a composite of 7 W% of PANI/BiOCl, which degraded only 67% of MO dye in 210 min [21]. Zhang et al. synthesized a composite of poly (3,4-ethylene dioxythiophene) with MnO_2 and graphene, it degrades methylene blue (MB) dye in 7 hours [22]. Kumar et al. developed PANI/TiO_2/GN photocatalyst which degrades MB in 180 min [23]. Pendiselvi et al. prepared a ternary nanocomposite of gold doped in graphene/TiO_2 and degraded MB in 250 min [24]. El-Bery and colleagues conducted a synthesis of a PANI-TiO_2 composite for the degradation of organic pollutants. However, the composite exhibited a degradation efficiency of 89.7% over a duration of 120 minutes, indicating relatively low effectiveness [25]. In a similar vein, Ma et al. developed a PANI/TiO_2/Cotton photocatalyst, achieving a degradation rate of 87.7% for Rhb within a three-hours period, which is also

considered to be of limited efficiency [26]. Likewise, Li et al. designed a PANI/TiO_2/SiO_2 catalyst, demonstrating the degradation of an organic dye by 87% within two hours [27]. However, this level of catalytic activity is not notably efficient. In a different approach, Kroger et al. fabricated a PANI/Fe-TiO_2 photocatalyst, yet the degradation achieved was merely 28% in 2.5 hours, signifying a significantly poor photocatalytic performance [28]. In all the conducted studies, the prepared catalysts exhibited relatively low degradation percentages of organic dyes, requiring prolonged periods of light irradiation.

In this study, we have synthesized a ternary composite of PANI/BiOCl/GO to investigate its effectiveness in the photocatalytic mineralization of Rhb dye exposed to solar irradiation. The synthesized ternary composites were thoroughly characterized (XRD, XPS, FTIR, FESEM, TEM, UV-DRS, etc.), and various photocatalytic properties (catalyst dose, effective illumination area, solution pH, scavenger studies, etc.) were studied. The degraded final products and intermediates are identified by LC/MS. Additionally, we examined the possible mechanisms of photocatalytic degradation to gain a deeper understanding of the process. The photocatalyst also exemplifies the ability to produce green hydrogen gas by water splitting photo catalytically. Hydrogen evolution reactions were studied with a sacrificial agent, acidic condition, and basic condition. The apparent quantum yield (AQE%) of water photochemical splitting was calculated in these three conditions. This process involves the absorption of photons by the target material, leading to chemical reactions that ultimately result in the degradation of organic pollutant into smaller, less harmful components and promote reactions that split water molecules into hydrogen and oxygen. The generated hydrogen gas may be used as a clean and sustainable energy source**.**

2.2. Materials and reagents:

2.2.1. Materials:

The following chemicals were used for the synthesis of the materials: graphite fine powder (98%, LOBA CHEMIE), aniline (99%, LOBA CHEMIE), hydrochloric acid (36%, LOBA CHEMIE), ammonium persulfate (98%, SDFCL), potassium chloride (99.5%-100%, LOBA CHEMIE), bismuth nitrate pentahydrate (98%, LOBA CHEMIE), potassium permanganate (99%, LOBA CHEMIE), sodium nitrite (97%, LOBA CHEMIE), and hydrogen peroxide (30% solution, RANKEM). Rhodamine b was purchased from CDH Chemical.

2.2.2. Synthesis of polyaniline (PANI):

In a 70mL solution of 2M HCl, approximately 4.5 mL of aniline (with a density of 1.020-1.025 g/mL) was added and subjected to sonication for half an hour. After 30 minutes, approximately 11.5 g of ammonium persulfate ($(NH_4)_2S_2O_8$) was added in a dropwise manner with continuous swirling. The polymerization reaction was left to continue for 4 hours ambient temperature. Subsequently, the reaction mixture was centrifuged at 5000 rpm for 10 minutes and purified thrice with 2 M HCl and distilled water. Finally, it was dried for 24 hours at 60°C in a hot air chamber, resulting in the collection of green-colored powder as the final product [29].

2.2.3. Synthesis of BiOCl and graphene oxide:

A total of 485 mg of bismuth nitrate pentahydrate (Bi $(NO_3)_3.5H_2O$) was mixed in to 200 mL of water, and then 2 mL nitric acid (HNO_3) was mixed in to dissolve the bismuth nitrate. The mixture was ultrasonicated for 30 minutes, and then 74 mg of potassium chloride (KCl) was mixed in. The solution was continuously swirled for 4 hours. The final solution was centrifuged, followed by washing with distilled water and ethanol three times. The procured white powder was dried at 60°C for 24 hours [30]. Graphene oxide (GO) was synthesized using a modified Hummer method [31].

2.2.4. Synthesis of ternary composite:

To begin, a 1:1 GO/BiOCl composite was prepared using the precursor of BiOCl through an in-situ process. Next, different weight percentages of the 1:1 GO/BiOCl composite were used to prepare a ternary composite via the oxidative polymerization method. Initially, 1:1 GO/BiOCl and aniline were added to a 2M HCl solution and stirred for one hour before being sonicated for an additional hour. Then, ammonium persulfate (APS) was added dropwise and stirred overnight for polymerization. Afterward, the resultant solution was washed repeatedly with 2M HCl and water before being dried at 60°C for 24 hours. In this way, the different weight ratio (1, 0.5, 2.5) of PANI/BiOCl/GO composite was prepared and given named 1PBG, 0.5 PBG, and 2.5 PBG respectively.

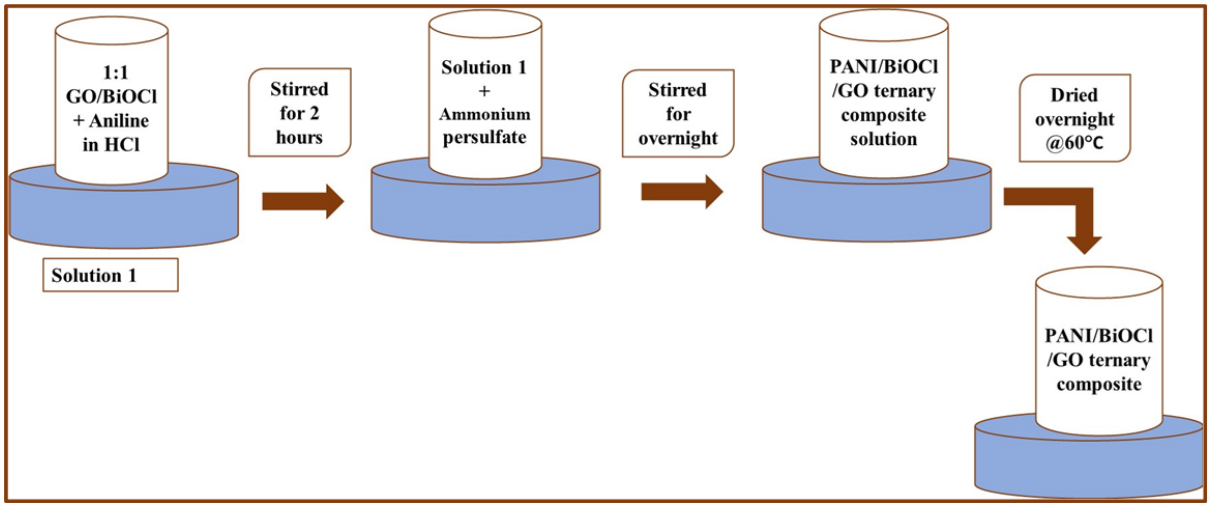

Scheme 2.1: Schematic diagram for the preparation of ternary nanocomposite.

2.3. Results and discussion:

2.3.1. Characterization of the synthesized photocatalyst:

The as-prepared nanocomposites were characterized by various characterization techniques. The ultraviolet-visible absorption spectra of the synthesized materials were measured utilizing a UV-vis spectrophotometer instrument (Shimadzu UV 2600). Photoluminescence spectra were recorded utilizing a spectrofluorometer instrument (Shimadzu RF-6000). The shape and dimensions of the prepared composite were analysed using transmission electron microscopy (TEM, FEI Tecnai G2 F20) and field emission scanning electron microscopy (FESEM, JEOL). The functional groups present in the materials were identified using Fourier transform infrared (FTIR) spectroscopy (Shimadzu IRTracer-100). The X-ray Photoelectron Microscopy (XPS) analysis was performed using a monochromatic aluminium source, specifically Al ka radiation, on an Omicron ESCA instrument with an energy of 1486.7 eV. Brunauere-Emmette-Teller (BET) method and Barrette-Joynere-Halenda (BJH) method were done by autosorb, Quantachrome instrument. The degraded products and possible Intermediate by products of the degradation product were analysed by Liquid Chromatography Mass Spectrometry (LCMS, Alliance 2795, Q-TOF Micromass Mass Spectrometer). The amount of CO_2 released after photocatalytic degradation and the amount of hydrogen produced by photocatalytic water splitting was measured using GC-TCD (Centurion Scientific).

2.3.1.1. Morphological characterization:

FESEM analysis anticipates for the understanding of the structural belongings of the prepared composite. FESEM images of synthesized BiOCl, PANI, GO, and 1PBG composite are illustrated in **Fig 2.1(a-d)**. From the FESEM image of BiOCl, it can be shown that it forms a rectangular platelet and the width of the platelet is within the span of 30-60 nm whereas, FESEM image of PANI also confirms the formation of fibrous morphology with porous nature. Well-agglomerated and exfoliated layers of GO were seen in **Fig 2.1a**. Exfoliation of GO occurred because of the existence of oxygenated functional groups atop the surface of the layers. Finally, in the nanocomposite, GO is agglomerated with the PANI due to the fibrous nature of the polymer. The nanoplates of BiOCl are clearly seen in in the composite (**Fig 2.1d**). The FESEM image of the nanocomposite confirms occurrence of polyaniline, GO and BiOCl which further approve the successful formation of heterojunction structures. The stoichiometric constitution of the synthesized nanocomposites was evaluated by energy dispersive spectroscopy (EDS) (**Fig 2.2**). From EDS analysis, it was confirmed that C, N, Bi, O, and Cl are simultaneously present in the synthesized nanocomposite. Moreover, the elemental color mapping of the nanocomposite confirms the homogeneous distribution of all the elements which affect the enhanced photocatalytic property.**Fig 2.1(e-f)** illustrates the TEM image of the synthesized nanocomposite, where we can see agglomerated particles in the nanocomposite. The TEM image (**Fig 2.1f**) distinguishes three different types of lattice fringes corresponding to the (102), (100), and (003) planes, having d-spacing of 0.266, 0.213, and 0.350 nm for BiOCl (2Θ = 33.611°), GO (2Θ = 42.364°), and PANI (2Θ = 25.39°), respectively.

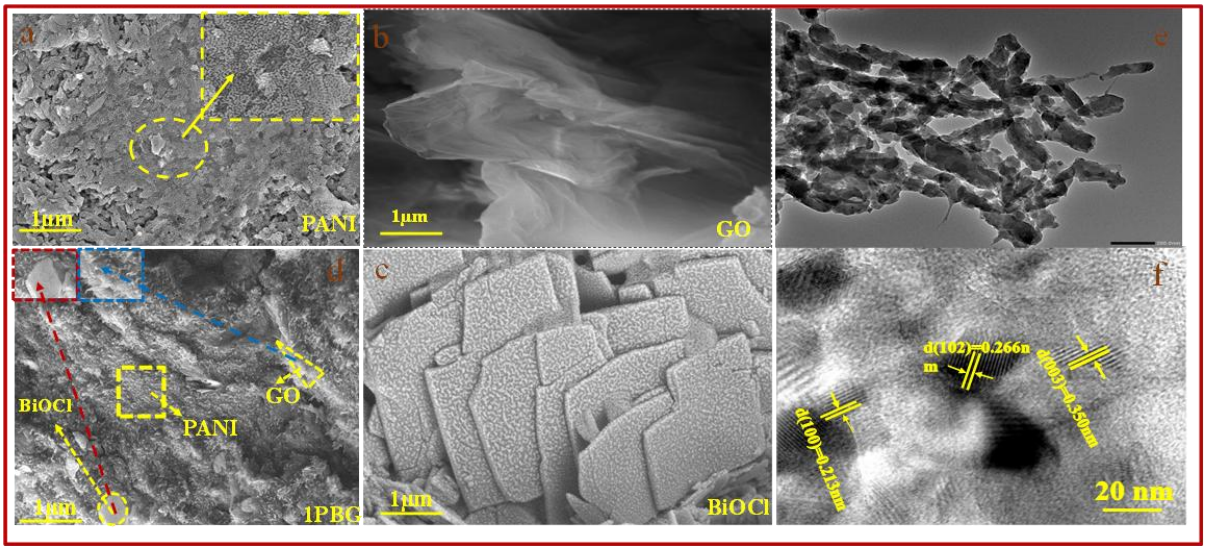

Fig 2.1: FESEM image of (a) PANI, (b) GO, (c) BiOCl, (d) 1PBG and (e, f) HRTEM image of 1PBG at different magnification.

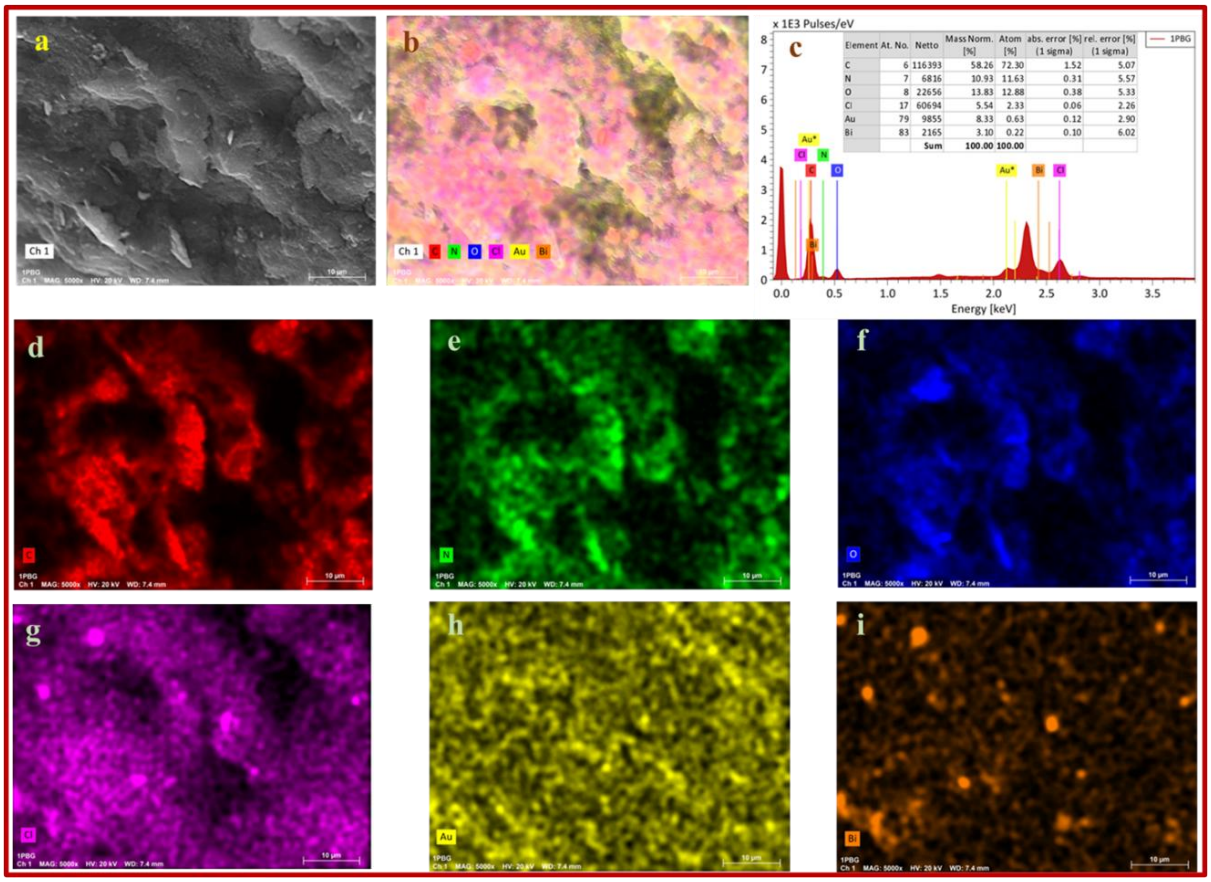

Fig 2.2: (a) FESEM image of 1PBG, (c) EDS spectrum of 1PBG and (b, d-e) is the elemental mapping of its constituents.

2.3.1.2. Surface properties:

BET analysis was performed to measure the total surface area, average pore size, and total pore volume of both the bare materials and the composites as shown in **Fig 2.3** and **Fig 2.4** and in **Table 2.1**. The type IV isotherm was observed for both bulk materials and composites, indicating the formation of multimolecular adsorbed layers of the molecules and the condensation of some of the molecules within the narrow capillary pores of the adsorbent. The BJH plot shows that all materials are mesoporous, with a pore size of less than 5nm. The total pore volume of all composites was higher than that of the bulk materials. PANI and BiOCl had very low surface areas compared to the composites and GO, indicating that GO played a dominant role in enhancing the surface area in the composites, which is favourable for efficient adsorption.

Table 2.1: BET surface area, average pore size, and total pore volume.

Photocatalyst	Surface Area (m^2/g)	Average pore size (nm)	Total pore Volume (cc/g)
PANI	1.56	3.19	2.49×10^{-2}
GO	30.36	2.76	2.099×10^{-2}
BiOCl	1.11	3.69	1.02×10^{-3}
0.5 PBG	37.87	3.88	3.68×10^{-2}
1PBG	32.63	4.37	3.56×10^{-2}
2.5 PBG	37.87	4	3.57×10^{-2}

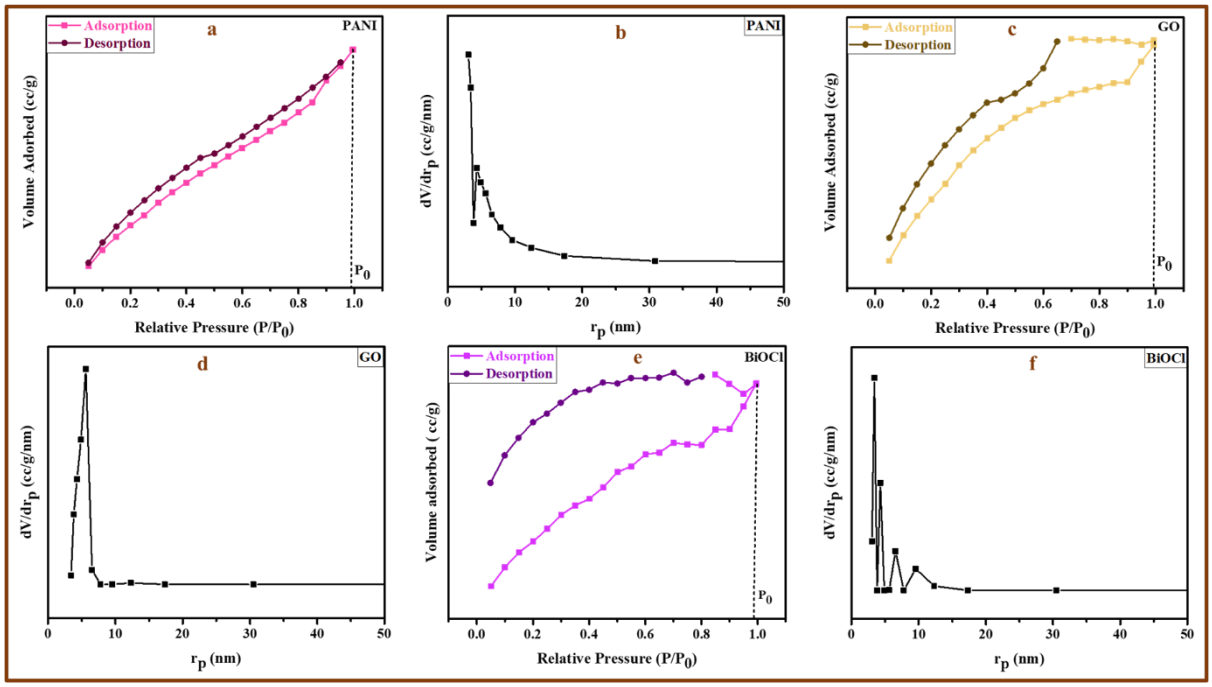

Fig 2.3: (a), (c), and (e) are adsorption-desorption curves of PANI, GO, and BiOCl respectively, whereas (b), (d), and (f) are BJH plots of PANI, GO, and BiOCl respectively.

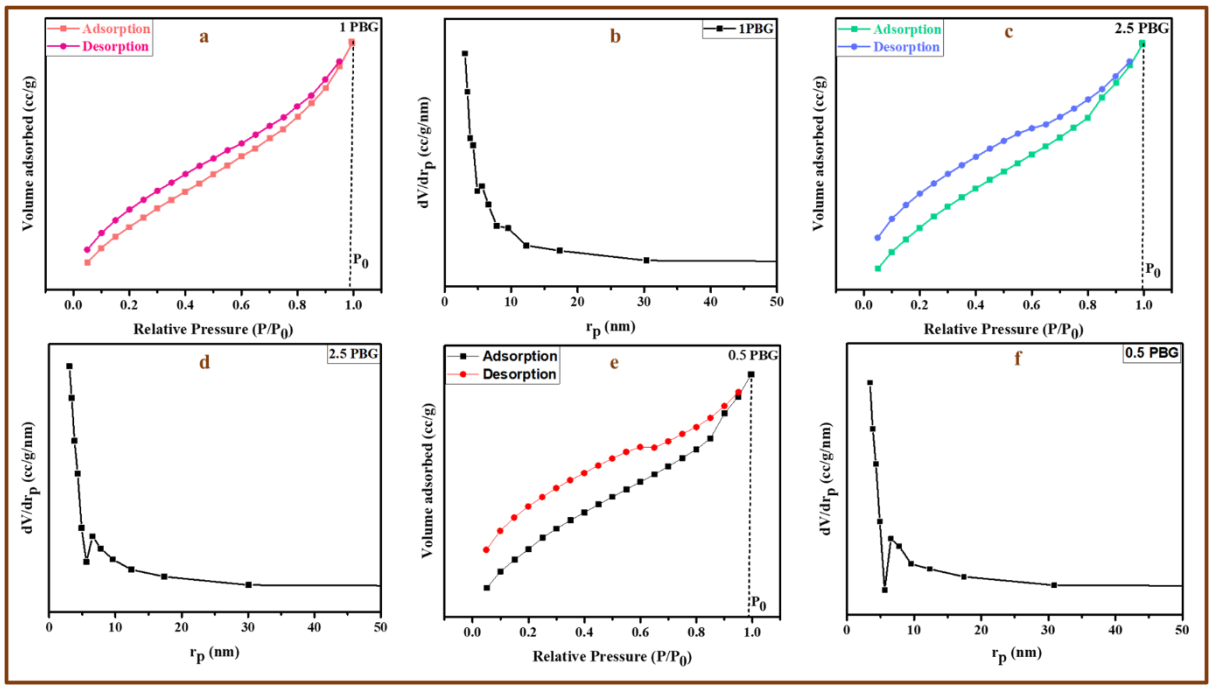

Fig 2.4: (a), (c), and (e) are adsorption-desorption curves 1PBG, 2.5 PBG, and 0.5 PBG Respectively, whereas (b), (d), and (f) are BJH plots of 1PBG, 2.5 PBG, and 0.5 PBG respectively.

2.3.1.3. Spectral characterisation:

The X-ray diffraction (XRD) pattern of the bare photocatalysts and nanocomposites is shown in **Fig 2.5a**. The peaks at 2Θ = 11.99°, 24.1195°, 25.866°, 32.54°, 33.46°, 36.52°, 40.90°, 46.67°, 49.71°, 55.06°, 58.63° correspond to d(001), d(002), d(101), d(110), d(102), d(003), d(112), d(200), d(201), d(004), d(104), d(212) and confirm the formation of BiOCl nanoplates with tetragonal unit cell (JCPDS NO.: 06-0249) [32]. The peaks at 2Θ = 14.84° (121), 20.63° (310), and 25.26° (003) confirm the formation of polyaniline (PANI) and it is amorphous in nature, while the peak at 25.26° (003) indicates the polymeric nature of PANI [33]. The peak at 11.16° (002) and 42.15° (100) indicates the formation of graphitic graphene oxide, which is amorphous in nature [34]. The peaks of BiOCl, g-GO, and PANI in the nanocomposites 0.5PBG, 1PBG, and 2.5PBG confirm the potential of the catalysts. The average crystallite sizes of BiOCl, PANI, g-GO, and 1PBG were calculated using the Scherrer equation, which is

$$\mathbf{D} = \frac{k\lambda}{\beta Cos\beta\theta} \qquad \textbf{(2.1)}$$

where D is the crystallite size (nm), K is the Scherrer constant, λ is 0.15406 nm (dependent on x-ray sources), β is the full-width half-maxima (FWHM) (in radians), and Θ is the peak position (in radians). The calculated average crystallite sizes of BiOCl, PANI, g-GO, and 1PBG are 76.006 nm, 135.465 nm, 109.97 nm, and 60.797 nm, respectively.

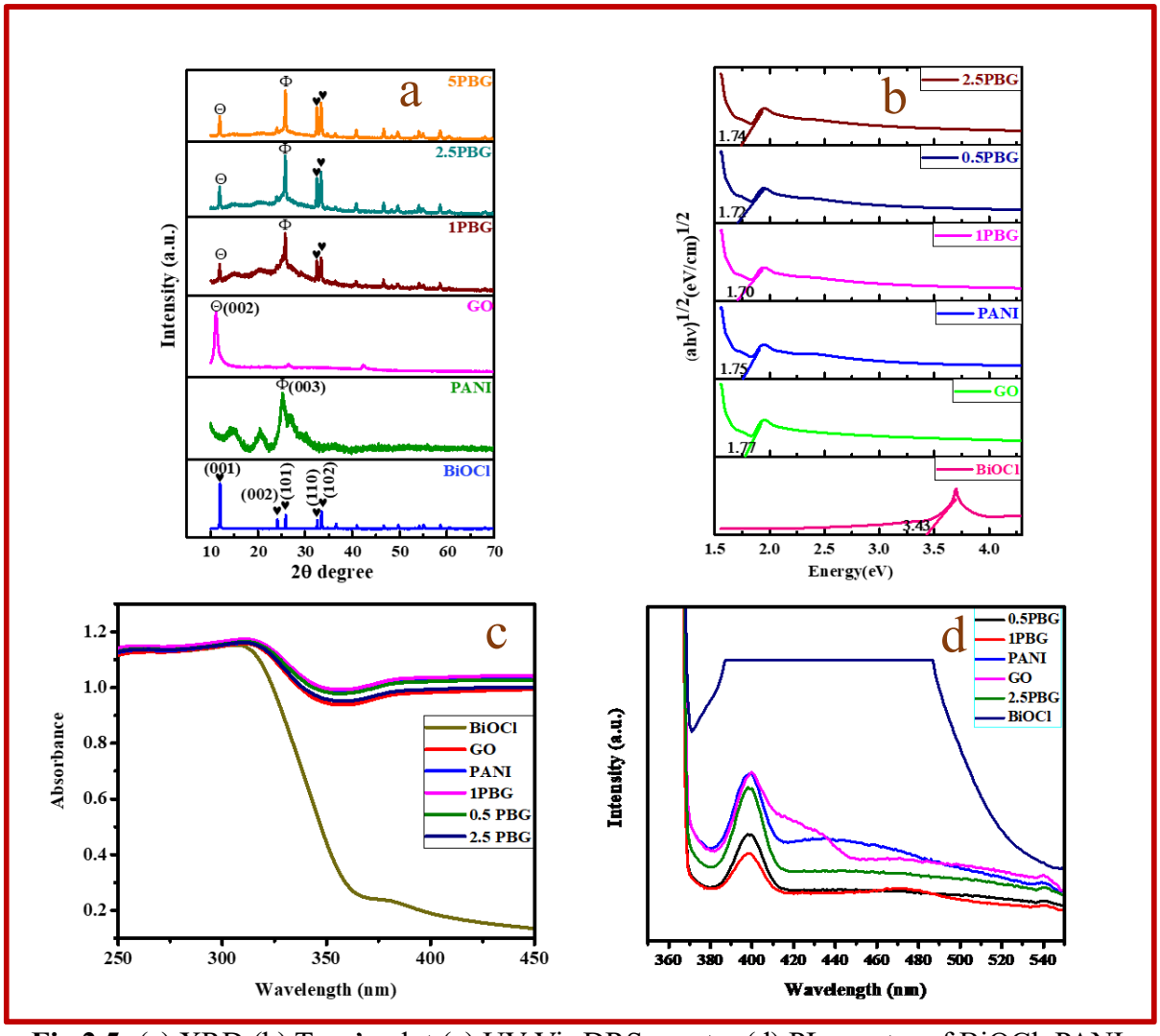

Fig 2.5: (a) XRD (b) Tauc'c plot (c) UV-Vis DRS spectra (d) PL spectra of BiOCl, PANI, GO, 1PBG, 2.5 PBG, 5 PBG.

XPS was undertaken to investigate the atomic valence state of the elements present in the synthesized ternary composite (1PBG). The XPS survey spectrum (**Fig 2.6a**) of the ternary composite confirmed existence of Bi, C, N, O, and Cl elements. The elemental spectra of Bi

4f, C 1s, N 1s, O 1s, and Cl 2p were deconvoluted by Gaussian fitting of the spectra. The photoemission peaks for Bi 4f were observed at 158.73 eV, 164 eV, and 167.67 eV (**Fig 2.6 b**). Specifically, the peak at 158.73 eV corresponded to Bi $4f_{5/2}$, the binding energy of 164 eV corresponded to Bi $4f_{7/2}$ of Bi_2O_3, and the binding energy of 167.67 eV corresponded to Bi $4f_{7/2}$ of BiOCl [35],[36]. In **Fig 2.6c**, three different binding energies of the C1s spectrum were observed for three different types of carbon bonding: the peak at 283.75 eV for non-oxygenated carbon (C-H/C=C/C-C), 288.32 eV for oxygenated carbon (O-C=O/C-O/C=O), and 285.13 eV for nitrogenous carbon (C=N, C-N) [37], [38]. The N 1s spectrum (**Fig 2.6d**) showed three different peaks for three different types of nitrogen environments: the peaks at 398.59 eV, 398.95 eV, and 400.58 eV occurred due to the quinoid amine, benzenoid amine, and nitrogen cationic radical ($N^{+\cdot}$), respectively [39]. In **Fig 2.6e**, the peak at 530.90 eV and 532.92 eV for the O1s spectrum was attributed to the Bi-O bonds in the $(BiO)_2^{2+}$ layered structure in BiOCl and the surface hydroxyl group on the composite[40]. The peaks at 196.66 eV and 198.94 eV indicated Cl $2p_{3/2}$ and Cl $2p_{1/2}$, respectively, for the Cl^- ion in the composite (**Fig 2.6f**)[41].

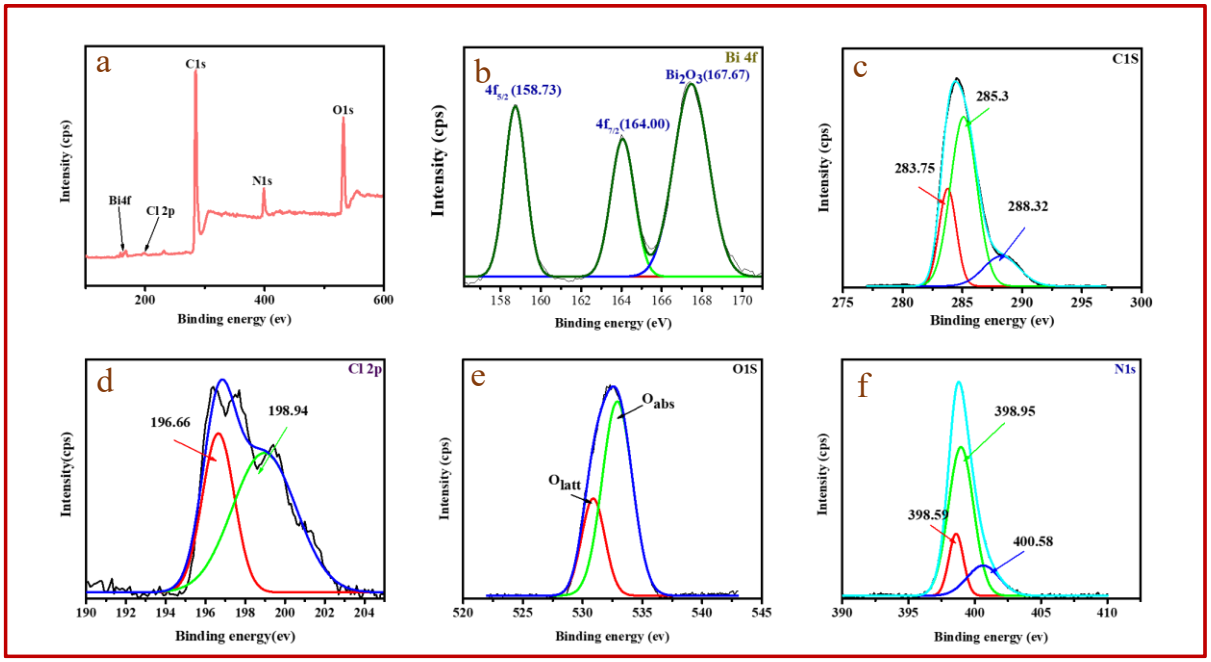

Fig 2.6: XPS spectrum of 1PBG (a) survey spectrum (b) Bi 4f core level spectrum (c) C 1s core level spectrum (d) Cl 2p core level spectrum (e) O 1s core level spectrum (f) N 1s core level spectrum.

The FTIR spectrum of PBG composites in **Fig 2.7**. confirms existence of several functional groups present on the surface of the nanocomposite. The sharp absorption peak at 502.34 cm^{-1} confirms the formation of the Bi-O bond in the metal oxide [43]. The peak at 1537 cm^{-1} corresponds to the C=C stretching vibration mode of the benzenoid ring, while the peak at 1396 cm^{-1} corresponds to the C-N stretching frequency of the benzenoid ring. The peak at 1230 cm^{-1} corresponds to the protonated C-N group. The absorption peak at 783 cm^{-1} indicates electron delocalization in the conducting polymer [44],[45]. The peak at 3503 cm^{-1} corresponds to the O-H stretching vibration of GO, while the peak at 1718 cm^{-1} corresponds to the C=O stretching of carboxylic groups. The peak at 1617 cm^{-1} corresponds to the O-H bending and aromatic C=C stretching frequency, while the peak at 1389 cm^{-1} corresponds to the tertiary C-OH bond. The absorption peak at 1227 cm^{-1} corresponds to the epoxy C-O groups [46],[47],[48],[49]. The absorption peaks of various functional groups of the nanocomposite are observed with some shifting in the wavenumber, confirming the successful synthesis of the nanocomposites.

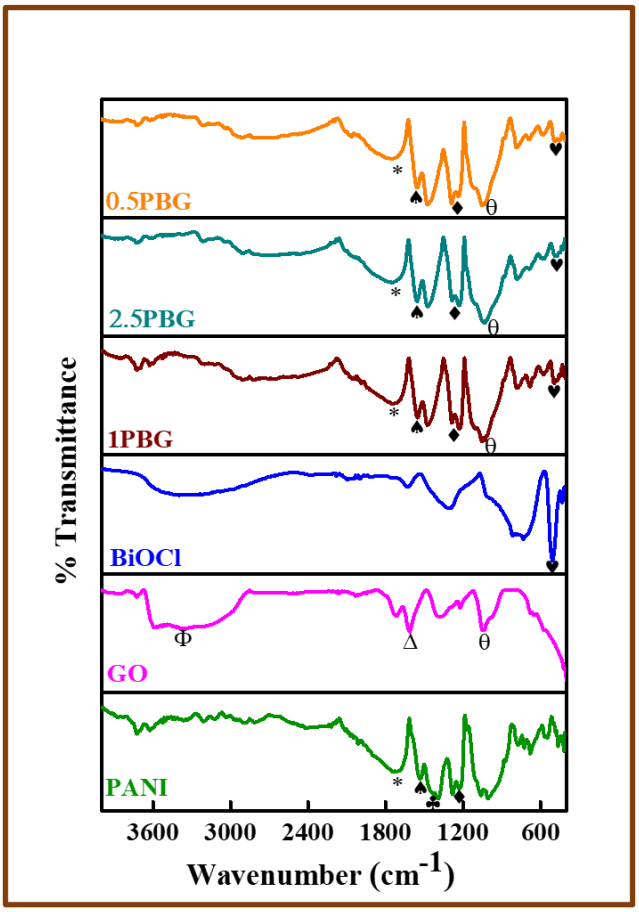

Fig 2.7: FTIR spectra of PANI, GO, BiOCl, 1PBG, 2.5 PBG, and 0.5 PBG.

The UV-DRS of BiOCl, GO, PANI, 1PBG, 0.5PBG, and 2.5PBG photocatalysts are shown in **Fig 2.5c**. BiOCl absorbs in the ultraviolet region, but after the preparation of a composite with GO and PANI, its absorption range shifted to the visible region. The band edge energies of all the materials were calculated using Tauc's equation:

$$(\alpha h\nu)^{1/2} = h\nu - E_g \quad (2.2)$$

Here α, h, ν, and Eg represent the absorption coefficient, Planck's constant, frequency of light, and band edge energy respectively. The linear approximation line meeting the x-axis of Tauc's plot indicates the band gap of the respective materials. The band edges of BiOCl, GO, PANI, 1PBG, 0.5PBG, and 2.5PBG photocatalysts were found to be 3.43, 1.77, 1.75, 1.70, 1.72, and 1.74 eV respectively (**Fig 2.5b**).

The values of the valence band (VB) and conduction band (CB) of BiOCl were calculated using the following equations:

$$E_{VB} = X - E_e + 0.5\, E_g \quad (2.3)$$

$$E_{CB} = E_{VB} - E_g \quad (2.4)$$

Here, E_{CB} and E_{VB} represent the energy of the conduction band (CB) and valence band (VB) respectively, X is the total electronegativity of the compound, and Ee is the electron energy in reference to hydrogen which has a fixed value of 4.5 eV [50]. By putting all the values assigned to the equations above, the value of the VB and CB of BiOCl was recognized as 2.47 eV and -0.96 eV respectively. Due to the decreasing band gap of the ternary nanocomposite, it is effective for sunlight utilization. Mitra et al. have made similar observations, incorporating reduced graphene oxide into polyaniline [51]. The resulting photocatalyst composite demonstrates light absorption within the visible spectrum. Similarly, Ahuja et al. successfully synthesized a PANI/rGO/NiO composite, which also exhibits activity under visible light [33].

The catalytic efficiency of a photocatalyst strongly depends on the rate of recombination of charges. The low PL spectral intensity of the photocatalytic materials is attributed to the high separation of photogenerated electron-hole pairs. The light emission spectra of the synthesized materials were studied with the incident wavelength of 350 nm. The PL intensity of the

prepared nanocomposites were found to be inferior to that of the bulk BiOCl, PANI, and GO, indicating higher efficiency of the nanocomposites over the bulk materials (**Fig 2.5d**). The formation of heterojunctions between PANI, BiOCl, and GO facilitates electron transfer, improving charge separation. This brings about a decrease in the PL intenseness of the nanocomposites. Additionally, 1PBG exhibits the lowest PL intensity, resulting in the highest photocatalytic efficacy.

2.3.2. Photocatalytic activity:

The photoactivity of 1PBG was evaluated by investigating its ability to catalytically degrade the organic dye (Rhb). The reactions were conducted using a 20 mL solution containing contaminants, with a catalyst concentration of 0.6 g/L for 5 ppm Rhb. Initially, a dark adsorption process was carried out for 120 minutes to achieve adsorption-desorption equilibrium. Subsequently, a solar light reaction was conducted for a total duration of two hours in the month of August 2022, and the effect of illumination area experiment was conducted using a 45 W Philips lamp with a radiant flux of 100 W/m^2. A gap of approximately 10 cm was upheld between the light bulb and the surface layer of the solution. Additionally, the reaction performed without light (lamp OFF) for 120 minutes using the same catalyst concentration. Every investigation was repeated three times, and error indicators representing approximately 5% of the data were included in each plot. Using a UV-visible spectrophotometer, the photodegradation of Rhb was observed at its respective maximum absorption wavelengths 555 nm, and the percentage degradation (%D) was determined using Equation (6). The optimum concentration of the catalyst was determined by varying its catalyst dosage from 0.1g/L to 0.7g/L under sunlight. The mineralization efficacy gradually increased from 0.1 to 0.6g/L and remained almost constant for 0.7g/L. This saturation was caused by a decrease in dye solution transparency that blocked the active sites of the photocatalyst.

$$\textbf{Degradation efficiency (\%D)} = \frac{C_0 - C_f}{C_0} * 100 \qquad (2.5)$$

Where C_0 and C_f are the primary concentration, and concentration after the degradation respectively.

To determine the kinetics of the reaction, the experiment was carried out using a 0.6g/L catalyst concentration. Initially, the solution was allowed to agitate in the dark for 120 min to absorb the maximum amount of dye, after which it was irradiated in sunlight for 120 min for photodegradation. To compare the efficiency of the ternary composite, the same experiment was performed with PANI, GO, BiOCl, PB, GB, TiO_2 P25 (commercial photocatalyst), 1PBG, 0.5PBG, and 2.5PBG. The experimental results showed that the ternary composites exhibited better efficiency with an elevated rate constant (1PBG = 0.015 min^{-1}, 0.5 PBG = 0.008 min^{-1}, 2.5 PBG = 0.009 min^{-1}) than the bare PANI (0.002 min^{-1}), GO(0.003 min^{-1}), BiOCl(0.004 min^{-1}), TiO_2-P25(0.003 min^{-1}), and binary composites (1PB = 0.007 min^{-1}, 11GB = 0.007 min^{-1} where, 1PB is 1 weight percent of BiOCl in PANI/BiOCl, and 11GB = 1:1 GO/BiOCl composite) **(Fig 2.8c)**. The synergy obtained by the combination of PANI, GO, and BiOCl was calculated using the synergy factor (R), which was determined by the following equation:

$$\mathbf{R}= \frac{K_{PANI+GO+BiOCl}}{K_{PANI}+ K_{GO}+K_{BiOCl}} \quad \textbf{(2.6)}$$

Here, $K_{PANI+GO+BiOCl}$, $K_{PANI}, K_{GO}, and\ K_{BiOCl}$ are the photodegradation rate constants of the PANI/GO/BiOCl ternary composite, pure PANI, pure GO, and pure BiOCl, respectively. The synergy factor of 1PBG, 0.5PBG, 2.5PBG, 1PB, and 11GB was found to be 1.52, 0.82, 0.98, 1.16, and 1, respectively. So, among all the nanocomposites, 1PBG has the highest synergy factor which is responsible for the highest photocatalytic degradation efficiency and the highest rate constant of 0.015 min^{-1}.

2.3.2.1. Impact of solution pH:

The photocatalyst's ability to absorb pollutants on the composite surface is highly dependent on the pH level of dye solution, that impacts the degradation efficiency [29]. To analyze the impact of solution pH on the Rhb dye removal process, solutions of varying pH were prepared using 0.1 N HCl and 0.1 N NaOH solutions. A concentration of 0.6 g/L catalyst to dye solutions of different pH was prepared, and the pH value before and after degradation was measured. **Fig 2.8b** shows that 1PBG has a point of zero charge (pzc) around pH 5.8. Since Rhb is an acidic dye, it shows higher degradation efficiency above the pzc value. From pH 1 to 5, the degradation effectiveness gradually decreases up to the pzc. In basic solutions, the degradation effectiveness gradually increases, and the highest degradation effectiveness is achieved at pH

8 (**Fig 2.8d**). At extremely basic solutions, the degradation efficiency gradually decreases due to the formation of metal hydroxide precipitation on the catalyst's interface.

2.3.2.2. Impact of illumination area:

The study successfully investigated the role of the effective illumination area using 1PBG composite as a photocatalyst under visible light [52]. A photocatalyst with a catalyst dosage of 0.6 g/L was stirred with a 5 ppm Rhb dye solution under visible light for 120 minutes. The surface area of the reaction was varied by using vessels with different diameters while maintaining a constant distance of 8 cm from the visible lamp. The results showed that there was an enhancement in degradation efficiency with an enhancement in the exposed surface of the reaction mixture. The higher the open area of the reaction mixture, the greater the irradiation of light, which increased the photocatalytic degradation of the pollutants and resulted in the highest degradation efficiency (**Fig 2.8e**).

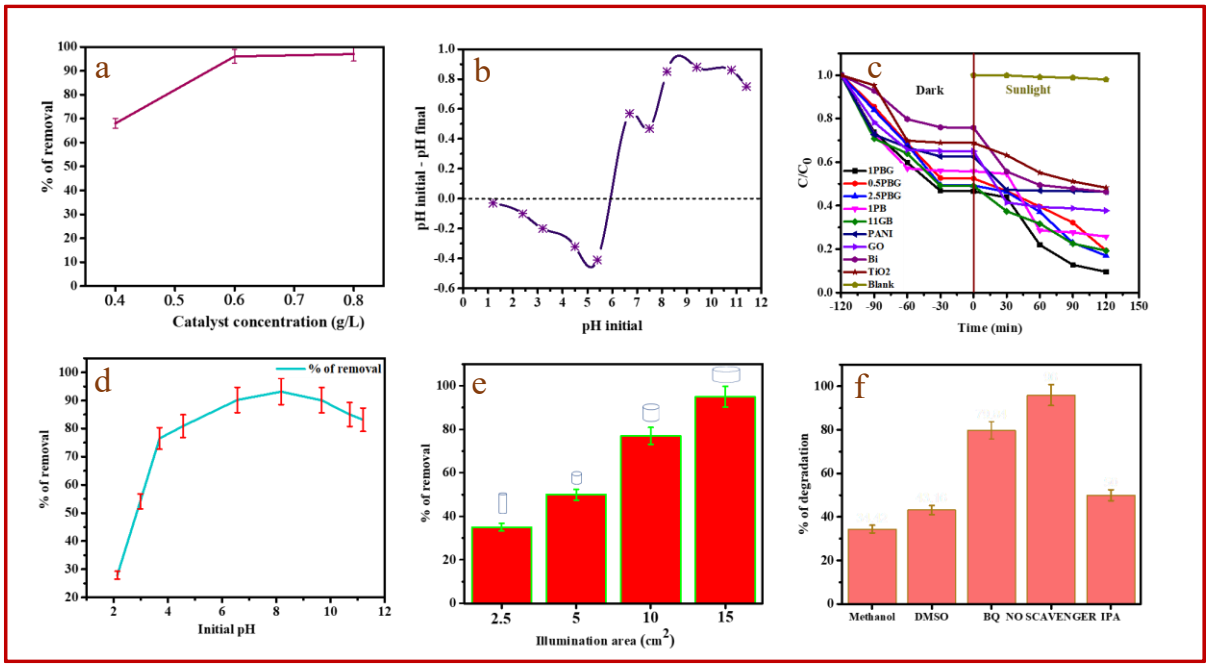

Fig 2.8: (a) effect of catalyst concentration (b) pzc studies (c) kinetic studies (d) effect of pH on Rhb solution (e) effect of illumination area (f) scavenger studies.

2.3.2.3. CO_2 generation study:

The photo-mineralization study was conducted by analyzing the GC-TCD data. A solution containing 5 ppm of dye in 20 mL of solvent was exposed to sunlight for 120 minutes. After mineralization, the evolved CO_2 was quantified. The mineralization process resulted in the

formation of some low molecular weight organic compounds, which were identified by LC-MS analysis. It is well reported that from one molecule of Rhb dye, twenty-seven molecules of CO_2 were formed[53]. In our study, 3.422*10^20 molecules of CO_2 were formed from 1.25*10^20 molecules of RhB. This suggests, 90% detoxification of Rhb by 1PBG under sunlight irradiation.

2.3.2.4. Probable photocatalytic reaction pathway of Rhb under sunlight:

To identify the intermediates produced during the photodegradation of organic dyes, it is important to measure the total organic carbon (TOC) and chemical oxygen demand (COD) in the solution during irradiation [54]. After 120 minutes of sunlight irradiation, the reduction efficiencies of TOC and COD for Rhb is 95% and 78%, respectively. From **Fig. 2.12d** it can be suggested that the solutions almost completely mineralized and contained intermediates with low mineralization potential.

The possible photocatalytic reaction pathway of Rhb under sunlight was determined using LC-MS. Previous research by Li et al. (2007) showed that Rhb degradation occurs mainly via two pathways: N-de-ethylation and destructed structure [55]. In **Fig 2.10** four main steps were identified for the complete degradation of Rhb: N-de-ethylation, chromophore cleavage, ring opening, and mineralization. In the first step, N, N-diethyl-N'-ethyl-rhodamine was observed at a retention time of 5.435 min and (E)-N-(9-(2-carboxyphenyl)-6-(ethylamino)-3H-xanthen-3-ylidene) ethanaminium [m/z = 387.17] was observed at a retention time of 4.959 min due to N-de-ethylation of Rhb. For chromophore cleavage of the products formed in the N-de LC/MS spectrum mainly showed 3- hydroxybenzoic acid (m/z = 138), Phthalic anhydride (m/z = 148), benzoic acid (m/z = 122), etc. After N-de-ethylation and chromophore cleavage, xanthene ring opening occurred and LC/MS showed the presence of oxalic acid (m/z= 90), malonic acid (m/z = 104), succinic acid (m/z = 118), etc [56]. GC-TCD confirmed that about 90% of mineralization had occurred.

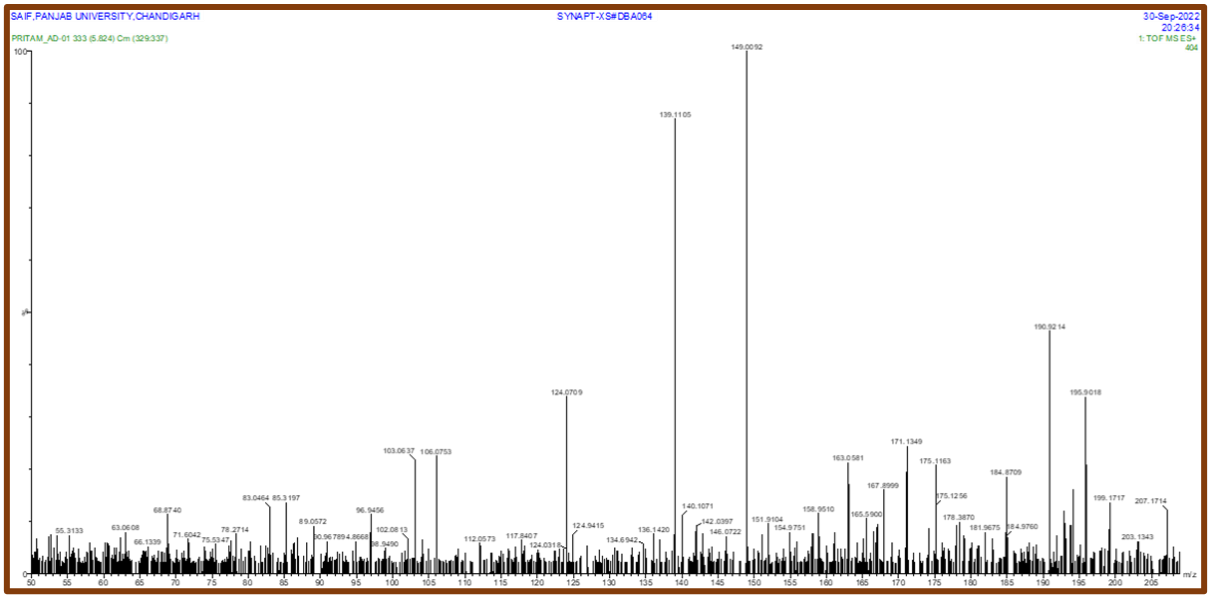

Fig 2.9: LC-MS data after degradation of Rhb.

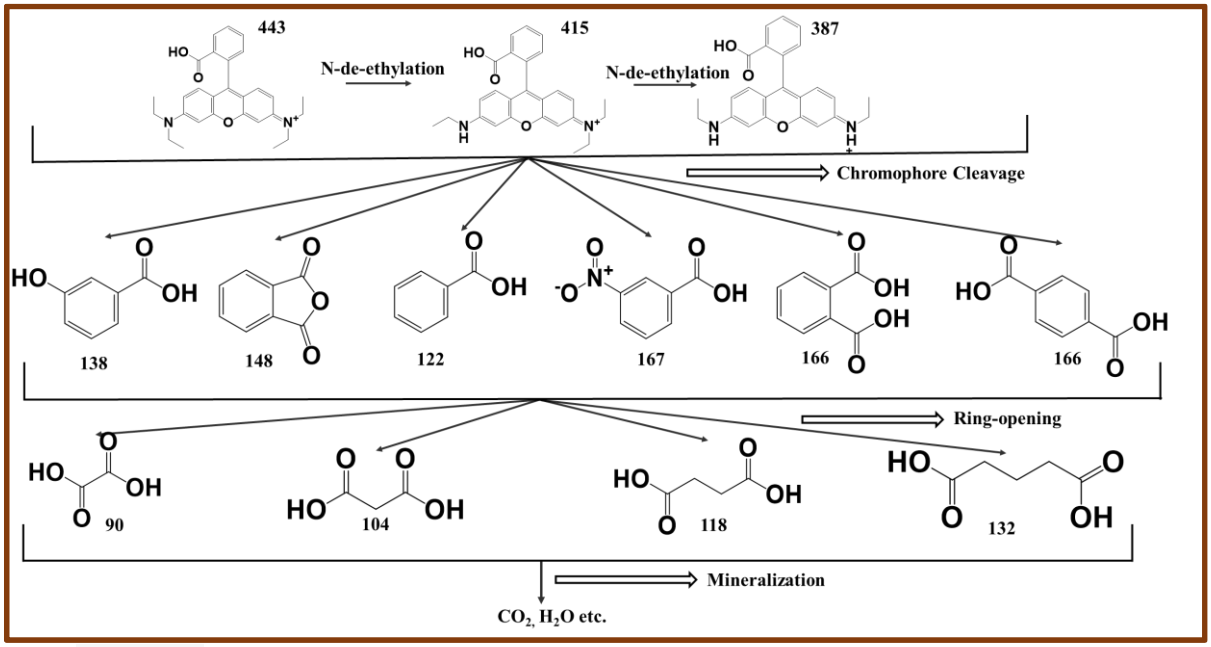

Fig 2.10: Possible photocatalytic reaction pathway of Rhb by 1PBG photocatalyst.

2.3.2.5. Effect of scavenger and possible charge transfer mechanism:

The degradation process involves mainly electrons in the CB, holes in the VB, superoxide radicals, and hydroxyl radicals, which play a major role [30]. To determine which species plays a major role in the degradation process, a scavenger study was conducted. Various scavengers, such as isopropyl alcohol (IPA), Dimethyl sulfoxide (DMSO), benzoquinone (BQ), and methanol, were used to trap hydroxyl radicals ($OH^{\cdot}$), electrons (e^{-}), superoxide radicals ($O_2^{\cdot}$),

and holes (h^+), respectively [57]. The $O^{2\bullet-}$ radical serves as a reductive agent and engages with BQ to produce hydroquinone. The involvement of DMSO also yields a significant impact, indicating that $^{\bullet}OH$ radicals also possess a pivotal function [58]. The unbound electron pairs located on the oxygen atoms within DMSO molecules facilitate electron transfer and establish hydrogen bonding with the hydrogen from $^{\bullet}OH$ radicals [54]. From **Fig 2.8f**, it can be observed that the degradation reaction is highly affected by methanol, IPA, and DMSO. This indicates that holes, hydroxyl radicals, and electrons are the superior species in the degradation mechanism. The supercilious activity of the PBG composite is delineated by enhancing the charge separation due to the addition of GO and BiOCl in the polyaniline matrix. To explain the mechanism of the intensified photocatalyst PBG, the relative band positions of PANI, GO, and BiOCl were studied [59], [60]. As mentioned in the **Fig 2.11**, when the PBG composite is irradiated in sunlight, PANI gets excited and light-induced electrons (e^-) and holes (h^+) are generated. Electrons in the CB of PANI move to the valence band of GO and BiOCl, which influences the decrease of the electron-hole recombination rate. Both GO and BiOCl have enhanced reduction potential than $O_2/\cdot O^{2-}$ (+ 0.07 eV) [61]. Electrons residing on the surface of GO and BiOCl can certainly form a reaction with the solubilized oxygen molecule to generate superoxide radical anion ($\cdot O^{2-}$). As the valence band of PANI is situated at a lower elevation than oxidation potential of $H_2O/OH\cdot$ (+ 2.32 eV) [61], holes present in the VB of PANI can positively react with the water molecule to produce hydroxide radicals ($OH\cdot$). Based on the above discussion, the proposed mechanism of Rhb degradation is mentioned in **Fig 2.11** and the following **equations (2.7-2.14)** [51]:

$$PANI \longrightarrow h^+(VB) + e^-(CB) \quad \textbf{(2.7)}$$

$$(e^-CB)\ PANI \longrightarrow GO(CB)(e^-) + BiOCl(CB)(e^-) \quad \textbf{(2.8)}$$

$$GO(CB)(e^-) + BiOCl(CB)(e^-) + O_2 \longrightarrow \cdot O_2^- \quad \textbf{(2.9)}$$

$$H_2O + \cdot O_2^- \longrightarrow \cdot OOH + OH^- \quad \textbf{(2.10)}$$

$$\cdot OOH + H_2O \longrightarrow \cdot OH + H_2O_2 \quad \textbf{(2.11)}$$

$$H_2O_2 + (h^+_{VB})\ PANI \longrightarrow \cdot OOH + H^+ \quad \textbf{(2.12)}$$

$$H_2O_2 + \cdot OOH \longrightarrow \cdot OH + H_2O + O_2 \quad \textbf{(2.13)}$$

$$\cdot OH + \cdot O_2^- + dye \longrightarrow CO_2 + H_2O \quad \textbf{(2.14)}$$

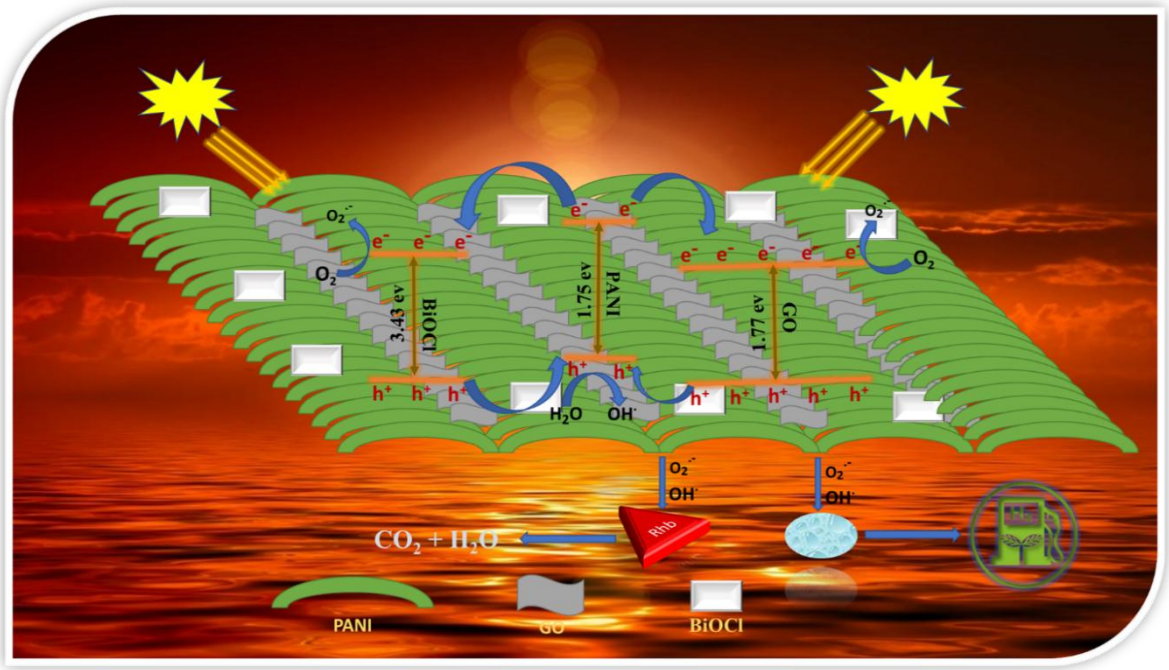

Fig 2.11: Possible Charge Transfer Mechanism of photocatalytic degradation and hydrogen generation.

2.3.2.6. Reusability studies:

Photocatalyst permanence is a crucial parameter for the continued use of the composite in environmental remediation. Therefore, it is indispensable to study the robustness of photocatalysis composite after multiple cycles of photodegradation. To investigate this, the degradation of Rhb was carried out using the same catalyst for six cycles. The results showed that the 1PBG composite exhibited high photostability even after six cycles, with a degradation efficiency of 86-96% for Rhb, as illustrated in the photodegradation plots in **Fig 2.12a**. After six cycles nanocomposite was characterized by XRD analysis, where it was seen that there is a slide decrease in the intensity of the peek due to the absorption of the dye molecule on the catalyst surface but there is no change in the XRD pattern of the catalyst (**Fig 2.12b**). This implies the durable stability and intactness of the photocatalyst.

The 1PBG photocatalyst underwent a comparison with other materials that have been documented in the literature for the purpose of photocatalytic detoxification of Rhb. The results were organized in **Table 2.2**. From the analysis, it is apparent that a reduced concentration of catalyst is a successful approach in treating persistent organic pollutants.

Table 2.2: Comparison of different photocatalyst materials for the degradation of Rhb.

Photocatalyst	Catalyst amount (mg)	% degradation	Time (min)	References
PANI-TiO_2	10	89.7	120	[25]
PANI/TiO_2/Cotton	-	87.7	180	[26]
PANI/TiO_2/SiO_2	-	87	120	[27]
PANI/Fe-TiO_2	-	28	150	[28]
Ag-Ag_2O/TiO_2@PPY	100	100	175	[23]
PEDOT/GO/MnO_2	20	92.7	420	[62]
RGO/mesoTiO_2/AuNP	10	-	240	[63]
PANI@GN/TiO_2	50	87	180	[64]
Ag_2O/TiO_2@PPY	50	100	240	[65]
PANI/BiOCl/GO (1%)	6	96	120	Present work

2.3.2.7. Photocatalytic H_2 generation study:

Photocatalytic hydrogen generation from water splitting was performed using three different water solutions under sunlight for 48 hours. In the first solution, 1 ml of methanol (sacrificial agent) was diluted with 19 ml of water. In the second solution, 1 ml of HCl was diluted with 19 ml of water to make an acidic solution, while in the third solution, 1 ml of NaOH was diluted with 19 ml of water to form a basic solution.

In the presence of methanol, approximately 1000 ppm of hydrogen gas was evolved (**Fig 2.12c**). Methanol acts as a hole scavenger and a sacrificial donor, resulting in the formation of intermediate byproducts such as formic acid (HCOOH) or formaldehyde (HCHO) [66]. These intermediate products partially participate in the photocatalytic reduction of hydrogen ions (H^+)

that are produced during the water-splitting reaction. In an acidic condition, around 500 ppm of hydrogen gas was generated, and in a basic condition, around 600 ppm of hydrogen gas was generated (**Fig 2.12c**). The apparent quantum efficiency (AQE) with the sacrificial agent was about 18%, 10% in the acidic solution, and 12% in the basic solution.

$$\text{AQE}\ (\%) = \frac{n * \Delta G}{W * S * T} * 100 \qquad \textbf{(2.15)}$$

Where n denotes the moles of H_2 produced (moles/L), ΔG is the total Gibbs free energy of water splitting (237 KJ/mol), W stands for the sun radiation (637 W/m^2), S is the surface area of the reaction tube (m^2), and T is the time of the reaction (s).

The redox reaction is carried out by the electron-hole pairs in the CB and VB, as mentioned below **(equation 2.16-2.19)** [67], [68]:

In acidic condition:

Oxidation:

$$2H_2O\ (l) + 4h^+ \longrightarrow O_2\ (g) + 4H^+\ (aq) \qquad \textbf{(2.16)}$$

$$E^0_{oxidation} = -1.23\ V$$

Reduction

$$2H^+ + 2e^- \longrightarrow O_2\ (g) + 2H_2\ (g) \qquad \textbf{(2.17)}$$

$$E^0_{reduction} = 0\ V$$

In basic condition:

Oxidation:

$$2OH^-\ (aq) \longrightarrow \frac{1}{2} O_2\ (g) + H_2O\ (l) + 2e^- \qquad \textbf{(2.18)}$$

Reduction:

$$2H_2O\ (l) + 2e^- \longrightarrow H_2\ (g) + 2OH^- \qquad \textbf{(2.19)}$$

Based on the scavenger study, it was observed that the photocatalytic activity is attributed to both holes and electrons. As a result, a significant amount of hydrogen was generated in both acidic and basic conditions

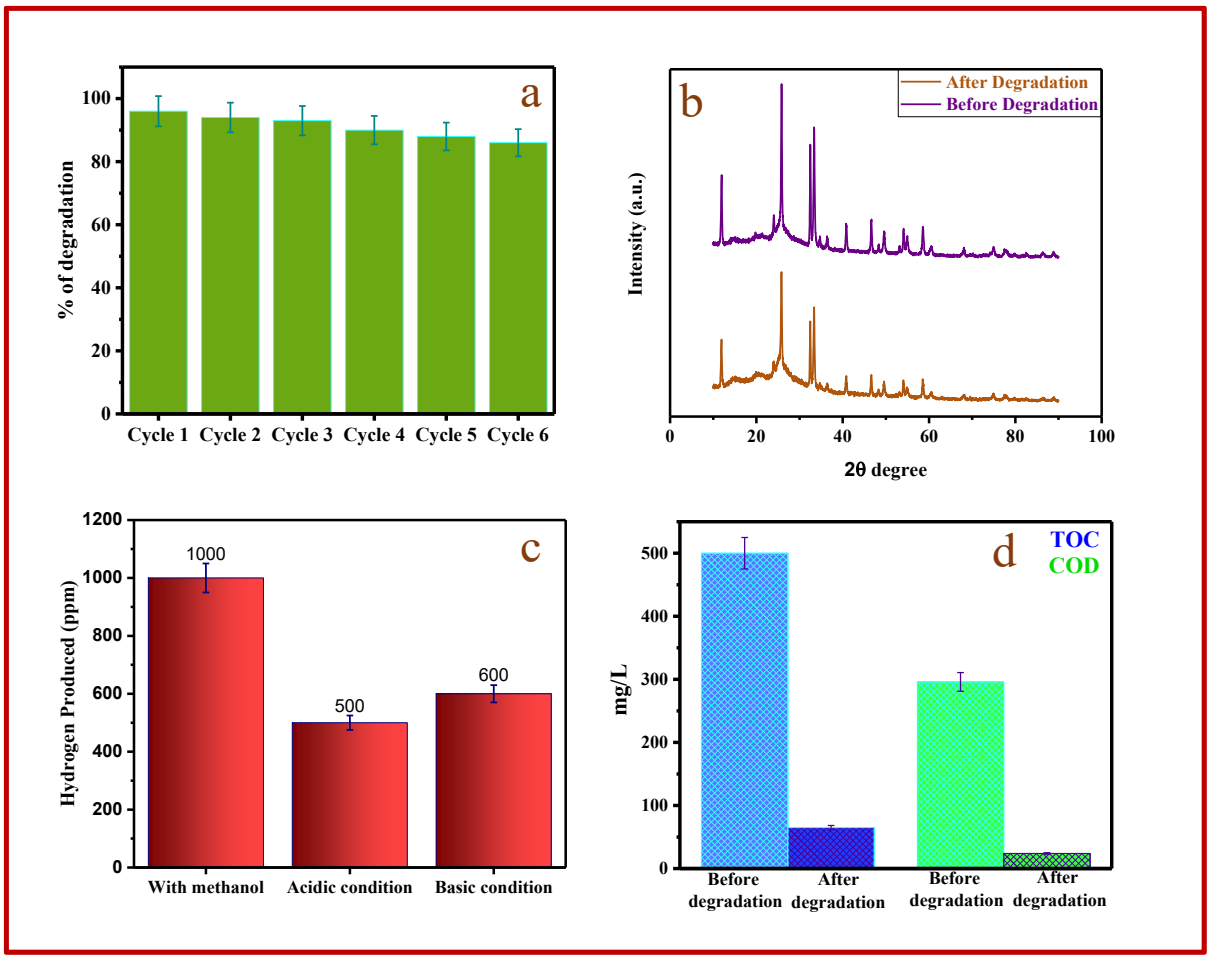

Fig 2.12: (a) reusability studies (b) XRD of 1PBG before and after degradation (c) H_2 production studies (d) TOC and COD of Rhb before and after degradation.

References

[1] J. Abdi, M. Vossoughi, N. M. Mahmoodi, and I. Alemzadeh, "Synthesis of metal-organic framework hybrid nanocomposites based on GO and CNT with high adsorption capacity for dye removal," *Chem. Eng. J.*, vol. 326, pp. 1145–1158, Oct. 2017, doi: 10.1016/j.cej.2017.06.054.

[2] Z. Peng *et al.*, "Facile Synthesis of 'Boron-Doped' Carbon Dots and Their Application in Visible-Light-Driven Photocatalytic Degradation of Organic Dyes," *Nanomaterials*, vol. 10, no. 8, p. 1560, Aug. 2020, doi: 10.3390/nano10081560.

[3] M. Tavakkoli Yaraki, B. Liu, and Y. N. Tan, "Emerging Strategies in Enhancing Singlet Oxygen Generation of Nano-Photosensitizers Toward Advanced Phototherapy," *Nano-Micro Lett.*, vol. 14, no. 1, p. 123, Dec. 2022, doi:

10.1007/s40820-022-00856-y.

[4] B. Shi, G. Li, D. Wang, C. Feng, and H. Tang, "Removal of direct dyes by coagulation: The performance of preformed polymeric aluminum species," *J. Hazard. Mater.*, vol. 143, no. 1–2, pp. 567–574, May 2007, doi: 10.1016/j.jhazmat.2006.09.076.

[5] S. Wang and E. Ariyanto, "Competitive adsorption of malachite green and Pb ions on natural zeolite," *J. Colloid Interface Sci.*, vol. 314, no. 1, pp. 25–31, Oct. 2007, doi: 10.1016/j.jcis.2007.05.032.

[6] A. Sheikhmohammadi, E. Asgari, and J. Yeganeh, "Application of the Fe_3O_4@activated carbon magnetic nanoparticles for the adsorption of metronidazole from wastewater: optimization, kinetics, thermodynamics and equilibrium studies," *Desalin. WATER Treat.*, vol. 222, pp. 354–365, 2021, doi: 10.5004/dwt.2021.27101.

[7] M. Pahuja *et al.*, "Harvesting Green Hydrogen from the Deep Blue: Seawater-Compatible SnSe-P Decorated Graphene-CNTs Based Electrocatalyst Under Universal pH," *Small*, vol. 20, no. 49, Dec. 2024, doi: 10.1002/smll.202406113.

[8] A. Kudo and Y. Miseki, "Heterogeneous photocatalyst materials for water splitting," *Chem. Soc. Rev.*, vol. 38, no. 1, pp. 253–278, 2009, doi: 10.1039/B800489G.

[9] T.-F. Yeh, J. Cihlář, C.-Y. Chang, C. Cheng, and H. Teng, "Roles of graphene oxide in photocatalytic water splitting," *Mater. Today*, vol. 16, no. 3, pp. 78–84, Mar. 2013, doi: 10.1016/j.mattod.2013.03.006.

[10] J. Wang, T. van Ree, Y. Wu, P. Zhang, and L. Gao, "Metal oxide semiconductors for solar water splitting," in *Metal Oxides in Energy Technologies*, Elsevier, 2018, pp. 205–249. doi: 10.1016/B978-0-12-811167-3.00008-0.

[11] T. Preethi, B. Abarna, K. N. Vidhya, and G. R. Rajarajeswari, "Sol–gel derived cobalt doped nano-titania photocatalytic system for solar light induced degradation of crystal violet," *Ceram. Int.*, vol. 40, no. 8, pp. 13159–13167, Sep. 2014, doi: 10.1016/j.ceramint.2014.05.020.

[12] U. Riaz and S. M. Ashraf, "Microwave-Assisted Solid State in Situ Polymerization and

Intercalation of Poly(carbazole) between Bentonite Layers: Effect of Microwave Irradiation and Gallery Confinement on the Spectral, Fluorescent, and Morphological Properties," *J. Phys. Chem. C*, vol. 116, no. 22, pp. 12366–12374, Jun. 2012, doi: 10.1021/jp303060p.

[13] U. Riaz and S. M. Ashraf, "Synergistic effect of microwave irradiation and conjugated polymeric catalyst in the facile degradation of dyes," *RSC Adv.*, vol. 4, no. 88, pp. 47153–47162, 2014, doi: 10.1039/C4RA06698G.

[14] E. Asgari, A. Esrafili, A. Jonidi Jafari, R. R. Kalantary, and M. Farzadkia, "Synthesis of TiO_2/polyaniline photocatalytic nanocomposite and its effects on degradation of metronidazole in aqueous solutions under UV and visible light radiation," *Desalin. WATER Treat.*, vol. 161, pp. 228–242, 2019, doi: 10.5004/dwt.2019.24291.

[15] B. Abarna, T. Preethi, and G. R. Rajarajeswari, "Single-pot solid-state synthesis of ZnO/chitosan composite for photocatalytic and antitumour applications," *J. Mater. Sci. Mater. Electron.*, vol. 30, no. 24, pp. 21355–21368, Dec. 2019, doi: 10.1007/s10854-019-02512-5.

[16] C.-C. Hu and H. Teng, "Gallium Oxynitride Photocatalysts Synthesized from $Ga(OH)_3$ for Water Splitting under Visible Light Irradiation," *J. Phys. Chem. C*, vol. 114, no. 47, pp. 20100–20106, Dec. 2010, doi: 10.1021/jp1070083.

[17] G. Tian *et al.*, "Hierarchical flake-like Bi_2MoO_6/TiO_2 bilayer films for visible-light-induced self-cleaning applications," *J. Mater. Chem. A*, vol. 1, no. 23, p. 6961, 2013, doi: 10.1039/c3ta10511c.

[18] B. Pare, B. Sarwan, and S. B. Jonnalagadda, "The characteristics and photocatalytic activities of BiOCl as highly efficient photocatalyst," *J. Mol. Struct.*, vol. 1007, pp. 196–202, Jan. 2012, doi: 10.1016/j.molstruc.2011.10.046.

[19] M. D. Stoller, S. Park, Y. Zhu, J. An, and R. S. Ruoff, "Graphene-Based Ultracapacitors," *Nano Lett.*, vol. 8, no. 10, pp. 3498–3502, Oct. 2008, doi: 10.1021/nl802558y.

[20] X. Du, I. Skachko, A. Barker, and E. Y. Andrei, "Approaching ballistic transport in suspended graphene," *Nat. Nanotechnol.*, vol. 3, no. 8, pp. 491–495, Aug. 2008, doi:

10.1038/nnano.2008.199.

[21] Q. Wang *et al.*, "Photodegradation of methyl orange with PANI-modified BiOCl photocatalyst under visible light irradiation," *Appl. Surf. Sci.*, vol. 283, pp. 577–583, Oct. 2013, doi: 10.1016/j.apsusc.2013.06.149.

[22] W. Zhang *et al.*, "In situ preparation of cubic Cu_2O-RGO nanocomposites for enhanced visible-light degradation of methyl orange," *Nanotechnology*, vol. 27, no. 26, p. 265703, Jul. 2016, doi: 10.1088/0957-4484/27/26/265703.

[23] R. Kumar, R. El-Shishtawy, and M. Barakat, "Synthesis and Characterization of Ag-Ag_2O/TiO_2@polypyrrole Heterojunction for Enhanced Photocatalytic Degradation of Methylene Blue," *Catalysts*, vol. 6, no. 6, p. 76, May 2016, doi: 10.3390/catal6060076.

[24] K. Pandiselvi, H. Fang, X. Huang, J. Wang, X. Xu, and T. Li, "Constructing a novel carbon nitride/polyaniline/ZnO ternary heterostructure with enhanced photocatalytic performance using exfoliated carbon nitride nanosheets as supports," *J. Hazard. Mater.*, vol. 314, pp. 67–77, Aug. 2016, doi: 10.1016/j.jhazmat.2016.04.035.

[25] H. M. El-Bery, M. R. Salah, S. M. Ahmed, and S. A. Soliman, "Efficient non-metal based conducting polymers for photocatalytic hydrogen production: comparative study between polyaniline, polypyrrole and PEDOT," *RSC Adv.*, vol. 11, no. 22, pp. 13229–13244, 2021, doi: 10.1039/D1RA01218E.

[26] J. Ma, J. Dai, Y. Duan, J. Zhang, L. Qiang, and J. Xue, "Fabrication of PANI-TiO_2/rGO hybrid composites for enhanced photocatalysis of pollutant removal and hydrogen production," *Renew. Energy*, vol. 156, pp. 1008–1018, Aug. 2020, doi: 10.1016/j.renene.2020.04.104.

[27] A. Li, W. Zhu, C. Li, T. Wang, and J. Gong, "Rational design of yolk–shell nanostructures for photocatalysis," *Chem. Soc. Rev.*, vol. 48, no. 7, pp. 1874–1907, 2019, doi: 10.1039/C8CS00711J.

[28] J. Kröger *et al.*, "Interfacial Engineering for Improved Photocatalysis in a Charge Storing 2D Carbon Nitride: Melamine Functionalized Poly(heptazine imide)," *Adv. Energy Mater.*, vol. 11, no. 6, p. 2003016, Feb. 2021, doi: 10.1002/aenm.202003016.

[29] A. Kumar, R. Kumar, and G. Pandey, "Synthesis, Characterization of Titania/Polyaniline/GO Nanocomposites, and Its Photocatalytic Activity Under UV-Visible Light," *Macromol. Symp.*, vol. 379, no. 1, p. 1600192, Jun. 2018, doi: 10.1002/masy.201600192.

[30] A. Kundu, S. Sharma, and S. Basu, "Modulated BiOCl nanoplates with porous g-C_3N_4 nanosheets for photocatalytic degradation of color/colorless pollutants in natural sunlight," *J. Phys. Chem. Solids*, vol. 154, p. 110064, Jul. 2021, doi: 10.1016/j.jpcs.2021.110064.

[31] Z. B. Siddique, S. Basu, and P. Basak, "Effect of Graphene Oxide Dispersed Natural Ester Based Insulating Oil on Transformer Solid Insulation," *IEEE Trans. Dielectr. Electr. Insul.*, vol. 29, no. 2, pp. 378–385, Apr. 2022, doi: 10.1109/TDEI.2022.3157926.

[32] M. Guan *et al.*, "Vacancy Associates Promoting Solar-Driven Photocatalytic Activity of Ultrathin Bismuth Oxychloride Nanosheets," *J. Am. Chem. Soc.*, vol. 135, no. 28, pp. 10411–10417, Jul. 2013, doi: 10.1021/ja402956f.

[33] P. Ahuja, S. K. Ujjain, I. Arora, and M. Samim, "Hierarchically Grown NiO-Decorated Polyaniline-Reduced Graphene Oxide Composite for Ultrafast Sunlight-Driven Photocatalysis," *ACS Omega*, vol. 3, no. 7, pp. 7846–7855, Jul. 2018, doi: 10.1021/acsomega.8b00765.

[34] H. Shin *et al.*, "Efficient Reduction of Graphite Oxide by Sodium Borohydride and Its Effect on Electrical Conductance," *Adv. Funct. Mater.*, vol. 19, no. 12, pp. 1987–1992, Jun. 2009, doi: 10.1002/adfm.200900167.

[35] N. Kumada, M. Hosoda, and N. Kinomura, "Preparation of Alkaline Earth Bismuth Pyrochlores Containing Bi^{5+} by Low Temperature Hydrothermal Reaction," *J. Solid State Chem.*, vol. 106, no. 2, pp. 476–484, Oct. 1993, doi: 10.1006/jssc.1993.1307.

[36] B. Begemann and M. Jansen, "Bi_4O_7, das erste definierte binÄre Bismut(III, V)-oxid," *J. Less Common Met.*, vol. 156, no. 1–2, pp. 123–135, Dec. 1989, doi: 10.1016/0022-5088(89)90412-8.

[37] H. Liu, Y. Su, Z. Chen, Z. Jin, and Y. Wang, "Graphene sheets grafted three-dimensional BiOBr0.2I0.8 microspheres with excellent photocatalytic activity under visible light," *J. Hazard. Mater.*, vol. 266, pp. 75–83, Feb. 2014, doi: 10.1016/j.jhazmat.2013.12.013.

[38] S. Shahabuddin, N. M. Sarih, F. H. Ismail, M. M. Shahid, and N. M. Huang, "Synthesis of chitosan grafted-polyaniline/Co_3O_4 nanocube nanocomposites and their photocatalytic activity toward methylene blue dye degradation," *RSC Adv.*, vol. 5, no. 102, pp. 83857–83867, 2015, doi: 10.1039/C5RA11237K.

[39] K. Zhang, L. L. Zhang, X. S. Zhao, and J. Wu, "Graphene/Polyaniline Nanofiber Composites as Supercapacitor Electrodes," *Chem. Mater.*, vol. 22, no. 4, pp. 1392–1401, Feb. 2010, doi: 10.1021/cm902876u.

[40] Z. Liu *et al.*, "Decoration of BiOI quantum size nanoparticles with reduced graphene oxide in enhanced visible-light-driven photocatalytic studies," *Appl. Surf. Sci.*, vol. 259, pp. 441–447, Oct. 2012, doi: 10.1016/j.apsusc.2012.07.063.

[41] G. Cheng, J. Xiong, and F. J. Stadler, "Facile template-free and fast refluxing synthesis of 3D desertrose-like BiOCl nanoarchitectures with superior photocatalytic activity," *New J. Chem.*, vol. 37, no. 10, p. 3207, 2013, doi: 10.1039/c3nj00413a.

[42] G. Cheng, J. Xiong, and F. J. Stadler, "Facile template-free and fast refluxing synthesis of 3D desertrose-like BiOCl nanoarchitectures with superior photocatalytic activity," *New J. Chem.*, vol. 37, no. 10, p. 3207, 2013, doi: 10.1039/c3nj00413a.

[43] Y. Chou *et al.*, "BiOCl nanosheets immobilized on electrospun polyacrylonitrile nanofibers with high photocatalytic activity and reusable property," *Appl. Surf. Sci.*, vol. 285, pp. 509–516, Nov. 2013, doi: 10.1016/j.apsusc.2013.08.085.

[44] A. Abdolahi, E. Hamzah, Z. Ibrahim, and S. Hashim, "Synthesis of Uniform Polyaniline Nanofibers through Interfacial Polymerization," *Materials (Basel).*, vol. 5, no. 8, pp. 1487–1494, Aug. 2012, doi: 10.3390/ma5081487.

[45] G. Gaikwad, P. Patil, D. Patil, and J. Naik, "Synthesis and evaluation of gas sensing properties of PANI based graphene oxide nanocomposites," *Mater. Sci. Eng. B*, vol.

218, pp. 14–22, Apr. 2017, doi: 10.1016/j.mseb.2017.01.008.

[46] T. Szabó, E. Tombácz, E. Illés, and I. Dékány, "Enhanced acidity and pH-dependent surface charge characterization of successively oxidized graphite oxides," *Carbon N. Y.*, vol. 44, no. 3, pp. 537–545, Mar. 2006, doi: 10.1016/j.carbon.2005.08.005.

[47] Y. Fu and X. Wang, "Magnetically Separable $ZnFe_2O_4$ –Graphene Catalyst and its High Photocatalytic Performance under Visible Light Irradiation," *Ind. Eng. Chem. Res.*, vol. 50, no. 12, pp. 7210–7218, Jun. 2011, doi: 10.1021/ie200162a.

[48] C.-M. Chen, Q. Zhang, M.-G. Yang, C.-H. Huang, Y.-G. Yang, and M.-Z. Wang, "Structural evolution during annealing of thermally reduced graphene nanosheets for application in supercapacitors," *Carbon N. Y.*, vol. 50, no. 10, pp. 3572–3584, Aug. 2012, doi: 10.1016/j.carbon.2012.03.029.

[49] P. Wang *et al.*, "One-step synthesis of easy-recycling TiO_2-rGO nanocomposite photocatalysts with enhanced photocatalytic activity," *Appl. Catal. B Environ.*, vol. 132–133, pp. 452–459, Mar. 2013, doi: 10.1016/j.apcatb.2012.12.009.

[50] D. Monga and S. Basu, "Tuning the photocatalytic/electrocatalytic properties of MoS_2 /$MoSe_2$ heterostructures by varying the weight ratios for enhanced wastewater treatment and hydrogen production," *RSC Adv.*, vol. 11, no. 37, pp. 22585–22597, 2021, doi: 10.1039/D1RA01760H.

[51] M. Mitra *et al.*, "Polyaniline/Reduced Graphene Oxide Composite-Enhanced Visible-Light-Driven Photocatalytic Activity for the Degradation of Organic Dyes," *ACS Omega*, vol. 4, no. 1, pp. 1623–1635, Jan. 2019, doi: 10.1021/acsomega.8b02941.

[52] S. Sharma and S. Basu, "Fabrication of centimeter-sized Sb_2S_3/SiO_2 monolithic mimosa pudica nanoflowers for remediation of hazardous pollutants from industrial wastewater," *J. Clean. Prod.*, vol. 280, p. 124525, Jan. 2021, doi: 10.1016/j.jclepro.2020.124525.

[53] L. Dashairya, A. Mehta, P. Saha, and S. Basu, "Visible-light-induced enhanced photocatalytic degradation of Rhodamine-B dye using $Bi_xSb_{2-x}S_3$ solid-solution photocatalysts," *J. Colloid Interface Sci.*, vol. 561, pp. 71–82, Mar. 2020, doi:

10.1016/j.jcis.2019.11.118.

[54] H. Alamgholiloo *et al.*, "Facile fabrication of Z-scheme TiO2/ZnO@MCM-41 heterojunctions nanostructures for photodegradation and bioactivity performance," *J. Mol. Liq.*, vol. 364, p. 119990, Oct. 2022, doi: 10.1016/j.molliq.2022.119990.

[55] J. Li, X. Zhang, Z. Ai, F. Jia, L. Zhang, and J. Lin, "Efficient Visible Light Degradation of Rhodamine B by a Photo-Electrochemical Process Based on a Bi_2WO_6 Nanoplate Film Electrode," *J. Phys. Chem. C*, vol. 111, no. 18, pp. 6832–6836, May 2007, doi: 10.1021/jp070694z.

[56] C. Chen, W. Zhao, P. Lei, J. Zhao, and N. Serpone, "Photosensitized Degradation of Dyes in Polyoxometalate Solutions Versus TiO_2 Dispersions under Visible-Light Irradiation: Mechanistic Implications," *Chem. - A Eur. J.*, vol. 10, no. 8, pp. 1956–1965, Apr. 2004, doi: 10.1002/chem.200305453.

[57] S. Singla, S. Sharma, and S. Basu, "MoS_2/WO_3 heterojunction with the intensified photocatalytic performance for decomposition of organic pollutants under the broad array of solar light," *J. Clean. Prod.*, vol. 324, p. 129290, Nov. 2021, doi: 10.1016/j.jclepro.2021.129290.

[58] H. Alamgholiloo, E. Asgari, S. Nazari, A. Sheikhmohammadi, N. Noroozi Pesyan, and B. Hashemzadeh, "Architecture of bimetallic-MOF/silicate derived Co/NC@$mSiO_2$ as peroxymonosulfate activator for highly efficient ciprofloxacin degradation," *Sep. Purif. Technol.*, vol. 300, p. 121911, Nov. 2022, doi: 10.1016/j.seppur.2022.121911.

[59] T. Guo, L. Wang, D. G. Evans, and W. Yang, "Synthesis and Photocatalytic Properties of a Polyaniline-Intercalated Layered Protonic Titanate Nanocomposite with a p−n Heterojunction Structure," *J. Phys. Chem. C*, vol. 114, no. 11, pp. 4765–4772, Mar. 2010, doi: 10.1021/jp9055413.

[60] T. Lv, L. Pan, X. Liu, T. Lu, G. Zhu, and Z. Sun, "Enhanced photocatalytic degradation of methylene blue by ZnO-reduced graphene oxide composite synthesized via microwave-assisted reaction," *J. Alloys Compd.*, vol. 509, no. 41, pp. 10086–10091, Oct. 2011, doi: 10.1016/j.jallcom.2011.08.045.

[61] P. S. Rao and E. Hayon, "Redox potentials of free radicals. IV. Superoxide and

hydroperoxy radicals $\cdot O^{2-}$ and $\cdot HO_2$," *J. Phys. Chem.*, vol. 79, no. 4, pp. 397–402, Feb. 1975, doi: 10.1021/j100571a021.

[62] L. Zhang, R. Jamal, Q. Zhao, M. Wang, and T. Abdiryim, "Preparation of PEDOT/GO, PEDOT/MnO_2, and PEDOT/GO/MnO_2 nanocomposites and their application in catalytic degradation of methylene blue," *Nanoscale Res. Lett.*, vol. 10, no. 1, p. 148, Dec. 2015, doi: 10.1186/s11671-015-0859-6.

[63] Y. Yang, Z. Ma, L. Xu, H. Wang, and N. Fu, "Preparation of reduced graphene oxide/meso-TiO_2 /AuNPs ternary composites and their visible-light-induced photocatalytic degradation n of methylene blue," *Appl. Surf. Sci.*, vol. 369, pp. 576–583, Apr. 2016, doi: 10.1016/j.apsusc.2016.02.078.

[64] R. Kumar *et al.*, "Facile route to a conducting ternary polyaniline@TiO_2 /GN nanocomposite for environmentally benign applications: photocatalytic degradation of pollutants and biological activity," *RSC Adv.*, vol. 6, no. 112, pp. 111308–111317, 2016, doi: 10.1039/C6RA24079H.

[65] R. Kumar, "Mixed phase lamellar titania-titanate anchored with Ag_2O and polypyrrole for enhanced adsorption and photocatalytic activity," *J. Colloid Interface Sci.*, vol. 477, pp. 83–93, Sep. 2016, doi: 10.1016/j.jcis.2016.05.039.

[66] R. A. Rather, S. Singh, and B. Pal, "Core–shell morphology of Au-TiO_2 @graphene oxide nanocomposite exhibiting enhanced hydrogen production from water," *J. Ind. Eng. Chem.*, vol. 37, pp. 288–294, May 2016, doi: 10.1016/j.jiec.2016.03.039.

[67] T. Jafari, E. Moharreri, A. Amin, R. Miao, W. Song, and S. Suib, "Photocatalytic Water Splitting-The Untamed Dream: A Review of Recent Advances," *Molecules*, vol. 21, no. 7, p. 900, Jul. 2016, doi: 10.3390/molecules21070900.

[68] A. A. Murashkina, T. V. Bakiev, Y. M. Artemev, A. V. Rudakova, A. V. Emeline, and D. W. Bahnemann, "Photoelectrochemical Behavior of the Ternary Heterostructured Systems CdS/WO_3/TiO_2," *Catalysts*, vol. 9, no. 12, p. 999, Nov. 2019, doi: 10.3390/catal9120999.

Chapter 3

Ultrafast Charge Separation in PANI/GO/MoO_3 for Visible-Light Dye Degradation and H_2 Generation

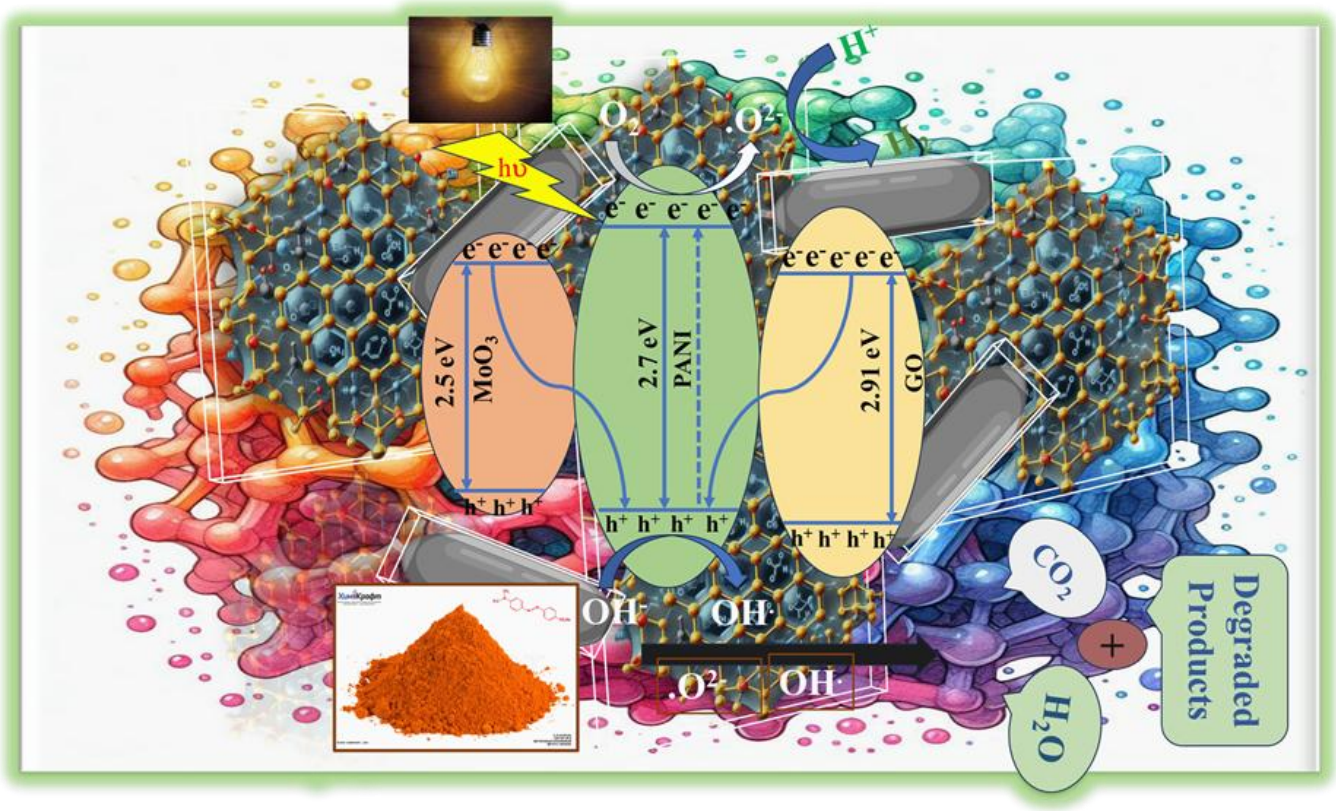

Highlights

- Fabrication of different mole ratios of Polyaniline/GO/MoO_3 ternary nanocomposite.
- Photocatalysts efficacy tested by degradation of methyl orange and H_2 production from water splitting.
- Photocatalytic elimination of methyl orange (98 %, rate constant~ 0.0299 min^{-1}) was observed under LED light.
- The nanocomposite produced 26468.4 ppm of hydrogen gas in the presence of a sacrificial agent (MeOH) with an AQE of 17.97%.

3.1. Introduction:

In the present era, semiconductor-based photocatalysis is essential in addressing the pressing challenges of energy scarcity and environmental pollution[1]. By harnessing solar energy as a clean, abundant, and renewable source, this technology offers several advantages, including high efficiency, eco-friendliness, and cost-effectiveness[2] [3] [4]. To date, the majority of efforts have been concentrated on inorganic semiconductors, including TiO_2 and various metal oxides, sulfides, and nitrides [5]. However, titanium dioxide (TiO_2) has limitations, such as a low quantum yield and sensitivity only to UV light around 4% of solar energy due to its wide band gap of roughly 3.2 eV[6][7]. Additionally, TiO_2 is known tohave a carcinogenic nature[8]. Hence, there is an imminent demand for the advancement of novel and enhanced visible-light-driven photocatalysts to maximize solar energy exploitation[9] [10] [11].

In the field of photocatalytic applications for photo-generated fuel production and pollutant degradation, organic semiconductors are still relatively underexplored [12]. In recent developments, conductive polymers featuring extensively delocalized π-conjugated electron systems-such as polypyrrole (PPy), polythiophene (PT), and polyaniline (PANI)-have demonstrated promising capabilities in electron transfer mechanisms[13][14]. These polymers exhibit notable characteristics such as high mobility of charge carriers, exceptional stability, effective hole-transport abilities, significant absorption of visible light, and reduced rates of charge recombination [15][16][17]. The intriguing properties of PANI have attracted considerable attention among researchers, prompting an exploration of its unique characteristics and potential applications[18]. Polyaniline (PANI) exhibits a unique conjugation mechanism in which benzenoid and quinoid rings dynamically interact, leading to three distinct oxidation states that function as versatile ensembles adaptable to various situations[19]. This conjugation phenomenon underscores PANI's commercial viability, transcending laboratory settings to emerge as a promising candidate for real-world applications across industries[20]. Noteworthy attributes include its high absorption coefficient within the visible spectrum, positioning PANI as a potential star in diverse industrial sectors where efficient energy absorption is crucial[21]. PANI's remarkable protonation reversibility, resembling a dynamic toggling between charged and uncharged states, enhances its versatility and utility in various contexts[22][23]. Furthermore, PANI's excellent redox properties enable proficient electron handling, rendering it advantageous for catalyzing chemical reactions

effectively[24]. Additionally, PANI exhibits notable sensitivity as a photocatalyst, particularly in facilitating organic dye interactions, while its superior light and thermal stability contribute to the sustained photocatalytic activity, promoting cleaner and more sustainable processes[25]. In summary, PANI's multifaceted properties, including its unique conjugation mechanism, high absorption coefficient, reversible protonation, redox capabilities, environmental stability, and photocatalytic sensitivity, collectively position it as a compelling material for further scientific exploration and practical applications across diverse sectors.

The scientific and engineering communities have been captivated by graphene oxide, It is composed of carbon atoms arranged in a hexagonal lattice resembling a honeycomb structure [26]. Its exceptional attributes can be delineated as follows: (i) High Surface Area: Graphene oxide exhibits an extraordinarily large surface area despite its nearly two-dimensional structure, providing an expansive platform for chemical reactions to occur[27]; (ii) Electron Acceptor: graphene oxide readily accepts electrons, thereby impeding the recombination of photogenerated charge carriers and sustaining their activity[28]; (iii) Synergistic Hybridization: when PANI and graphene oxide are present together, their hybrid structure, often in conjunction with inorganic materials or transition-metal oxides, enhances degradation rates by mitigating electron recombination losses[29]. In summary, the synergistic partnership between PANI and graphene oxide constitutes a formidable alliance, facilitating efficient degradation processes through their coordinated actions. While PANI and GO composites show enhanced photocatalytic activity compared to individual components, their performance may still fall short of expectations, especially when compared to other advanced photocatalytic materials, that's why it is necessary to introduce a metal oxide to form a ternary composite[30]. Much research has verified that enhancing the photocatalytic activity of semiconductor photocatalysts (such as $Bi_2O_2CO_3$, ZnO, TiO_2, CdS, and $Bi_{12}O_{17}C_{l2}$) by sensitizing them with PANI leads to improved reactivity in photocatalysis[22][23][31][32][33]. In the present study, molybdenum trioxide (MoO_3) is used because of its non-toxicity, thermal stability, cost-effectiveness, and rich oxygen vacancies[34]. Due to its large specific surface area and numerous active sites, it demonstrates outstanding photo-assisted degradation properties. MoO_3 is an n-type semiconductor characterized by a bandgap energy ranging from 2.5 to 3.2 eV[35]. This material exhibits remarkable light-absorbing capacity in both the visible and UV regions. Moreover,

MoO_3 acts as a photocatalyst, demonstrating an impressive adsorption capacity for organic dyes in photocatalytic processes.

In recent decades, substantial research has investigated the photocatalytic properties of titanium dioxide (TiO_2), cadmium oxide (CdO), cadmium selenide (CdSe), zinc oxide nanoparticles (ZnO NPs), and their combinations with conductive polymers (CPs). Researchers have proposed various mechanisms to explain the synergistic effects observed between CPs and metal oxide NPs, such as π to π^* transition of electrons from highest occupied molecular orbital (HOMO) to lowest unoccupied molecular orbital (LUMO), increased phase space separation between charge carriers, elevated concentration of hydroxyl free radicals, and enhanced photo-activity under ordinary light[36]. Our main hypothesis of this work is threefold: firstly, presence of rod shaped MoO_3 helps in better dispersion of 2D GO, with a reduction in the number of its stacked layers, and secondly, this will lead to a synergistic improvement in electron lifetime of the ternary composite of PANI/GO/MoO_3. Thirdly, increased electron life time would lead to better dye degradation and greater solar energy hydrogen production via water splitting[37] [38].

This study centers on the fabrication of a novel ternary composite comprising polyaniline (PANI), molybdenum trioxide (MoO_3), and graphene oxide (GO) **(Scheme 3.1)** to assess its efficacy in the breakdown of methyl orange (MO) dye through photocatalysis under LED light exposure. The synthesized ternary composites underwent comprehensive characterization using techniques such as X-ray diffraction (XRD), X-ray photoelectron spectroscopy (XPS), Fourier-transform infrared spectroscopy (FTIR), field-emission scanning electron microscopy (FESEM), electrochemical impedance spectroscopy (EIS), and UV-visible diffuse reflectance spectroscopy (UV-DRS). The study examined several photocatalytic features, such as the amount of catalyst used, the area effectively lit, the pH of the solution, and the impact of scavengers. Analysis of intermediates and ultimate products that have degraded was performed using gas chromatography-mass spectrometry (GC-MS). Furthermore, potential mechanisms of photocatalytic degradation were explored to enhance comprehension of the procedure. Moreover, the photocatalyst demonstrated the capability to generate green hydrogen gas through photocatalytic water splitting. We assessed various conditions such as sacrificial agent presence, acidic, basic, and neutral environments for the hydrogen evolution process. The apparent quantum yield (AQE%) for photochemical water splitting was then determined under

these conditions. This process entails the catalyst absorbing photons, which initiates chemical processes that break down organic contaminants into less hazardous substances and enable water to split into hydrogen (H_2) and oxygen (O_2).

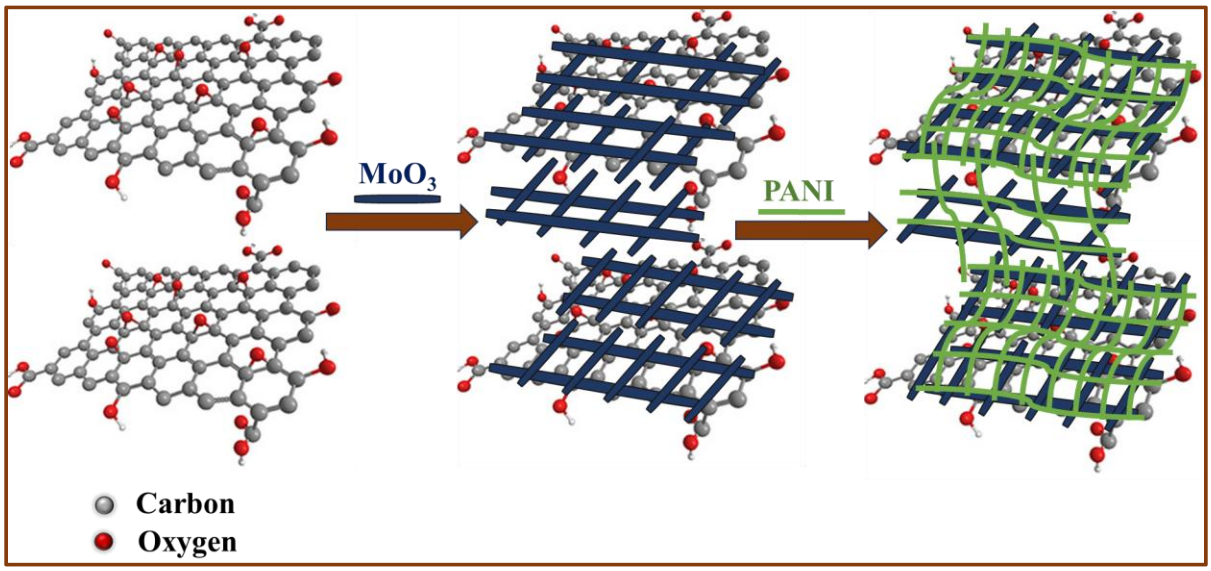

Scheme 3.1: Dispersion of graphene oxide layers and MoO_3 nanorods, and *in-situ* polymerisation of PANI.

3.2. Experimental section:

The following chemicals were used for the synthesis of the materials: graphite fine powder (98%, LOBA CHEMIE), aniline (99%, LOBA CHEMIE), hydrochloric acid (36%, LOBA CHEMIE), ammonium persulfate (98%, SDFCL), potassium chloride (99.5%-100%, LOBA CHEMIE), Ammonium Molybdate (98%, LOBA CHEMIE), potassium permanganate (99%, LOBA CHEMIE), sodium nitrite (97%, LOBA CHEMIE), and hydrogen peroxide (30% solution, RANKEM). Methyl Orange was purchased from CDH Chemical.

3.2.1.1. Preparation of MoO_3 and GO:

MoO_3 nanoparticles were prepared by dissolving 0.2 M ammonium molybdate in 10 ml of distilled water, then adding 5 ml of concentrated HNO_3. The mixture was subsequently placed into a Teflon-lined stainless-steel autoclave and kept at 150°C for 12 hrs. Afterward, the precipitates were separated, washed, and subjected to vacuum drying at 70°C for another 12 hrs[39]. Graphene oxide was synthesized from graphite precursor by the modified hummers method[40].

3.2.1.2. Preparation of ternary nanocomposite:

To commence the process, a composite of GO-MoO_3 in a 1:1 ratio was synthesized through an in-situ procedure utilizing the precursor of MoO_3. Subsequently, various weight percentages of the resulting 1:1 GO-MoO_3 composites were employed to fabricate ternary composites using the oxidative polymerization method. The procedure involved introducing 1:1 GO-MoO_3 and aniline into a 2M hydrochloric acid solution, followed by stirring for one hour and additional sonication for another hour. Subsequently, ammonium persulphate (APS) was gradually added, initiating an overnight stirring process for polymerization. The ensuing solution underwent thorough washing with 2M hydrochloric acid and water, then dried at 60°C for 24 hrs (**Scheme 3.2**)[21]. This method facilitated the preparation of a PANI/GO/MoO_3 composite with distinct weight ratios (1, 2.5, 4), each labeled as 1PGMO, 2.5 PGMO, and 4PGMO, respectively.

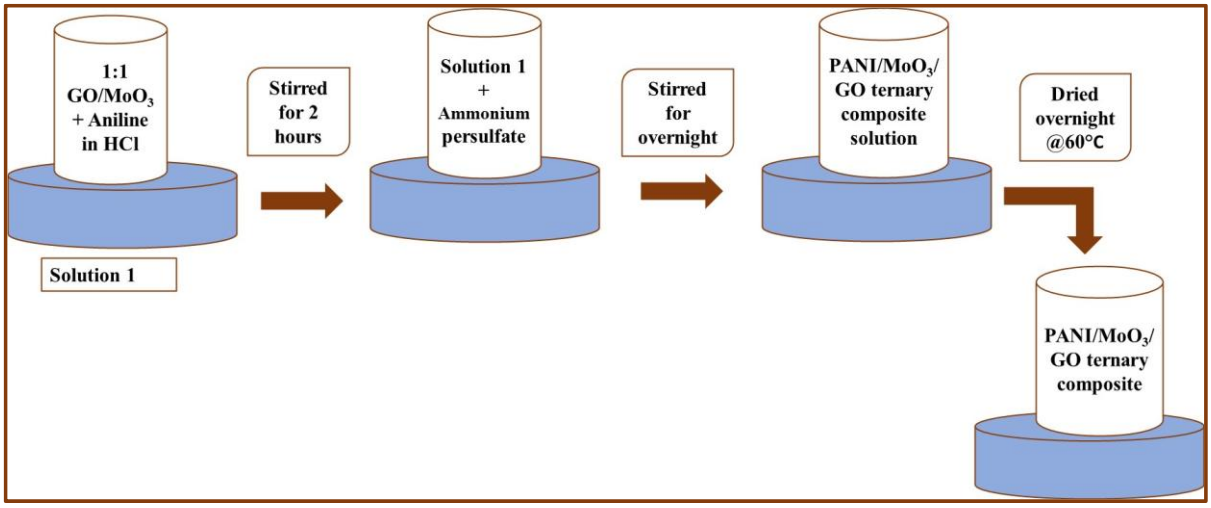

Scheme 3.2: Synthesis procedure of ternary nanocomposite.

3.2.2. Characterization methods:

The as-prepared nanocomposites were characterized by various characterization techniques. The ultraviolet-visible absorption spectra of the synthesized materials were measured utilizing a UV-vis spectrophotometer instrument (Shimadzu UV 2600). Photoluminescence spectra were recorded utilizing a spectrofluorometer instrument (Shimadzu RF-6000). The shape of the prepared composite was analyzed using field emission scanning electron microscopy (FESEM,

JEOL). The functional groups present in the materials were identified using Fourier transform infrared (FTIR) spectroscopy (Shimadzu IRTracer-100). The X-ray Photoelectron Microscopy (XPS) analysis was performed using a monochromatic aluminium source, specifically Al ka radiation, on an Omicron ESCA instrument with an energy of 1486.7 eV. Brunauere-Emmette-Teller (BET) method and Barrette-Joynere-Halenda (BJH) method were done by Belsorp Mini II instrument. The degraded products and possible Intermediate by-products of the degradation product were analysed by Gas Chromatography Mass Spectrometry (GCMS, Bruker SHS-40). The amount of CO_2 released after photocatalytic degradation and the amount of hydrogen produced by photocatalytic water splitting was measured using GC-TCD (nucon 5765). Electrochemical studies were carried out in BioLogic SP 300 Potentiostat instrument.

3.2.3. Experiments involving photocatalysis:

3.2.3.1. Test for evaluating the efficacy of photocatalytic degradation activity:

To assess the photocatalytic degradation capability, methyl orange (MO) was chosen as the test compound. In a standard procedure, 4 mg of the photocatalyst was introduced into a 20 mL methyl orange aqueous solution (20 ppm). The suspension was kept in darkness for 120 min to reach an adsorption-desorption equilibrium. Utilizing a photocatalytic reactor powered by a 40W LED lamp (Phillips) as the light source, the system was agitated using a magnetic stirrer throughout the entire photocatalytic process. The UV–vis spectrophotometer was employed to measure the remaining concentrations of MO. The percentage (%) of MO degradation was determined using the **equation 2.5 (Chapter 2)**.

The extent of mineralization was determined using the equation:

$$\textbf{Mineralization (\%)} = \frac{TOC_{initial} - TOC_{final}}{TOC_{initial}} * 100 \qquad \textbf{(3.1)}$$

In this context, "TOC $_{initial}$" denotes the initial total organic carbon (TOC) concentration of MO (measured in mg/L) prior to the degradation process, while "TOC $_{final}$" signifies the concentration of total organic carbon (TOC) in MO after 120 min of degradation.

Moreover, the identification of the degradation MO products utilized a GC-MS system. Chemical structures were deduced from their m/z values, with 'm' indicating the molecular mass and 'z' denoting the charge number of the product. Mobile phases for analysis consisted of aqueous solutions containing 0.1% dichloromethane (DCM).

3.2.3.2. Photocatalytic hydrogen production:

The photocatalyst, weighing 2 mg, was evenly distributed in a 20 mL aqueous solution. The solution contained one mL of MeOH as a sacrificial agent. The experiment was conducted under four different conditions: without any sacrificial agent, under acidic conditions, under basic conditions, and with a sacrificial agent in an environment saturated with nitrogen gas. The container was sealed tightly with an airtight cap. Using a photocatalytic reactor equipped with a 40 W LED lamp (Phillips) as the light source, the generated H_2 photoproduct was analyzed using gas chromatography (GC) with a thermal conductivity detector (TCD) and nitrogen as the carrier gas. During the photocatalytic process, the system was stirred continuously using a magnetic stirrer. The formula form **equation 2.15 (Chapter 2)** was used to calculate the apparent quantum efficiency (AQE).

3.3. Results and discussion:

3.3.1. Characterisation of the prepared photocatalyst:

3.3.1.1. Spectral characterization:

The X-ray diffraction (XRD) pattern presented in **Fig 3.1a** illustrates the characteristics of both the pure bulk nanomaterials and their nanocomposites. Examining the peaks at 2Θ values of 12.8°, 25.77°, and 39.09° reveals the corresponding lattice plan of d(100), d(210), and d(310), d(110) of MoO_3. These peaks confirm the formation of pure MoO_3 nanomaterials with a hexagonal unit cell (JCPDS NO.: 21-0569)[39]. Additionally, the XRD analysis identifies peaks at 2Θ = 14.78° (121), 20.45° (310), and 25.08° (003), providing evidence for the presence of PANI. The occurrence of the peak at 25.08° (003) further signifies the polymeric characteristics of PANI[41]. Moreover, the peaks at 11.23° (002) and 42.16° (100) indicate the existence of graphitic graphene oxide[42]. By examining the XRD patterns of the nanocomposites 1PGMO, 2.5PGMO, and 4PGMO, it becomes evident that the peaks corresponding to MoO_3, GO, and PANI persist, confirming the successful incorporation of these components into the nanocomposite structures. In the nanocomposite, the amorphous

peak at 2Θ = 13.1° may be marched with d (121) of PANI and d (002) of GO, and there is one crystalline peak in the amorphous nanocomposite at 2Θ = 32.55° due to crystalline MoO_3. This analysis underscores the potential of the 1PGMO, 2.5PGMO, and 4PGMO catalysts, as their composition aligns with the identified characteristics of MoO_3, graphene oxide, and polyaniline. We used the Scherrer equation to determine the average crystallite sizes of MoO_3, PANI, g-GO, and 2.5PGMO. Applying Scherrer equation allows for the determination of the "D" of MoO_3, PANI, g-GO, and 2.5PGMO, which are 60.005, 132.235, 102.65, and 101.34 nm, respectively.

The investigation into the atomic oxidation states of elements within the ternary composite (2.5PGMO) involved XPS. The XPS survey spectrum revealed (**Fig 3.1b**), that the presence of Mo, C, N, and O elements in the ternary composite was conclusively confirmed. To delve deeper into the elemental composition and chemical states, Gaussian fitting was applied to deconvolute the elemental spectra of Mo 3d, C 1s, N 1s, and O 1s. Further, analyzing the Mo 3d spectrum (**Fig 3.1c**) revealed the distinct photoemission peaks at 236.4 eV and 232.5 eV correspond to Mo^{+6} $3d_{3/2}$, and Mo^{+6} $3d_{5/2}$ [43][44]. Examining the C 1s spectrum in **Fig 3.1f** revealed three distinct binding energies representing different carbon bonding states. The peak at 283.98 eV corresponds to carbon atoms bonded to hydrogen (C–H), carbon-carbon bonds (C—C), and carbon-carbon single bonds (C–C), indicating non-oxygenated carbon. The peak at 284.23 eV represents carbon atoms bonded to oxygen (O–C), carbon-oxygen bonds (C—O), and carbon-oxygen single bonds (C–O), indicating oxygenated carbon. Lastly, the peak at 285.15 eV indicates carbon atoms bonded to nitrogen (C—N) and carbon-nitrogen bonds (C–N), indicating nitrogenous carbon[45][46]. Three distinct peaks were observed in the N 1s spectrum **(Fig 3.1e)**, each representing different nitrogen environments. The peak at 398.98 eV indicates the presence of the quinoid amine, while the peak at 399.08 eV is associated with the benzenoid amine. Lastly, the peak at 399.83 eV is attributed to the nitrogen cationic radical ($N^{+\cdot}$). [47]. This spectral analysis offers valuable insights into the diverse chemical configurations of nitrogen within the synthesized ternary composite (2.5PGMO), shedding light on its molecular structure and potential functionalities. Turning attention to the O 1s spectrum depicted in **Fig 3.1d** two prominent peaks were identified at 531 and 532.2 eV. These peaks were associated with the Mo–O bonds present in the MoO_3 hexagonal structure and the hydroxyl group located on the surface of the composite material. [48]. This observation

underscores the significance of oxygen in the bonding network of the composite material, highlighting its role in facilitating interactions and structural stability.

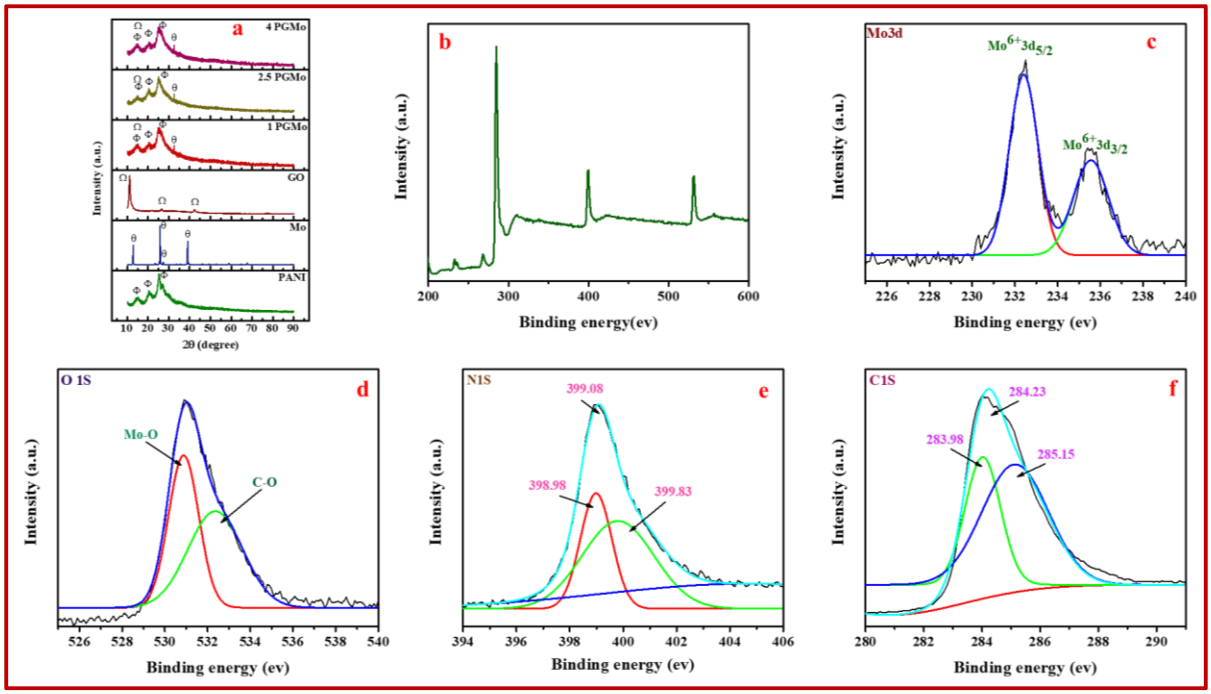

Fig 3.1: (a) XRD pattern, (b) XPS survey spectrum of 2.5PGMO, (c) Mo 3d core level spectrum, (d) O 1s core level spectrum, (e) N 1s core level spectrum and (f) C 1s core level spectrum.

The FTIR spectral analysis reveals distinct absorption peaks corresponding to specific vibrational modes and chemical groups within the materials. At 1540 cm^{-1}, the peak signifies the benzenoid ring exhibits a C=C stretching vibration mode, at a frequency of 1395 cm^{-1}, the peak represents the stretching of the C-N bond within the ring structure. Furthermore, the 1267 cm^{-1} signal indicates the existence of the protonated C-N group. Within the context of conducting polymers, the detection of a peak in absorption around 775 cm^{-1} signifies the spread of electrons throughout the polymer matrix [49][50]. Regarding graphene oxide (GO), distinctive peaks are observed in the spectrum. The peak at 3500 cm^{-1} is attributed to the stretching vibration of the O-H bond in GO, while at 1715 cm^{-1}, the peak represents the carboxylic groups' C=O stretching. Furthermore, the identified peak at 1613 cm^{-1} represents the frequency associated with O–H bending and aromatic C=C stretching. Additionally, the peak at 1383 cm^{-1} indicates the presence of tertiary C–OH bonds. Finally, the peak observed at 1221 cm^{-1} provides evidence for the existence of epoxy C–O groups[51][52],[53],[51],[54].

The distinctive pattern includes a notable small intensity peak, followed by a subsequent high-intensity peak at 838.5 cm^{-1} and 982.9 cm^{-1}, characteristic of the u_s (Mo=O) stretching vibrations associated with the hexagonal phase. Notably, these features in the spectrum are indicative of the specific vibrational modes inherent to the hexagonal crystalline structure. The absorption peaks observed in the 476.2 cm^{-1} relate to the vibration of the Mo–O bond. This spectral region captures the unique characteristics of the chemical bonds within the hexagonal MoO_3 structure[55]. The detailed vibrational analysis of other synthesized samples is presented in **Fig 3.2,** enhancing our understanding of the bonding configurations of the material, and providing valuable insights into its structural properties. The successful synthesis of the nanocomposites is confirmed by observing absorption peaks associated with various functional groups. The presence and modified positions of these absorption peaks offer concrete evidence of the effective formation of the desired nanocomposite, providing valuable insights into its chemical composition and structural characteristics.

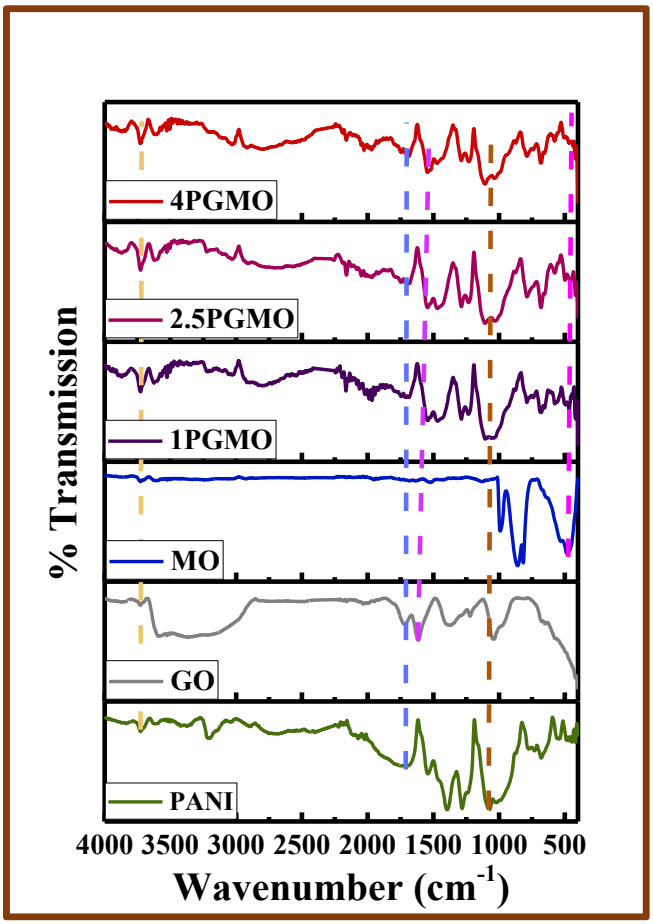

Fig 3.2: FTIR of PANI, GO, MoO_3, 1PGMO, 2.5PGMO, and 4PGMO.

The ability of photocatalysts to absorb light is crucial for their photocatalytic activity. In **Fig 3.3a**, the UV–vis absorption spectra of the obtained photocatalysts are presented. MoO_3 nanorods exhibit intense absorption in the ultraviolet spectrum (250−400 nm). However, the ternary nanocomposites (PGMO) demonstrate a broader absorption in the UV as well as visible region. This broader absorption is attributed to the presence of the PANI, which acts as a sensitizer for visible light. Moreover, the hue of the photocatalysts shifts from white for MoO_3 to dark green for ternary nanocomposites, which indicates the successful incorporation of PANI into the composite structure and reflects its visible light-absorption properties. Consequently, it is anticipated that the ternary nanocomposites will exhibit superior photocatalytic performance compared to pure MoO_3 under visible-light irradiation, owing to their enhanced light-absorption capabilities facilitated by the PANI component.

The energy gap of a semiconductor can be calculated using Tauc's formula. In this study, the bandgap energy (E_g) was derived from graphs showing $(\alpha h\nu)^2$ versus E_g. As illustrated in **Fig 3.3b**, the Eg of MoO_3 is calculated to be 2.5 eV, while for 2.5PGMO composites, the E_g value is 2.4 eV, for 1PGMO is 2.7 eV, and for 4PGMO is 2.64 eV. The decrease in E_g for the 2.5PGMO nanocomposite suggests a significant broadening of the range responsive to visible light after PANI modification. That's why, we use 2.5PGMO for photocatalytic studies. This broadening of responsive to visible light range indicates that the incorporation of PANI is advantageous for improving the efficiency of photocatalysis of MoO_3 for 2.5PGMO composite.

Typically, photoluminescence (PL) spectra are utilized to assess the effectiveness of processes such as photo-generated carrier capturing, movement, transport, isolation, and recombination. **Fig 3.3c** depicted the PL emission spectra for both MoO_3, PANI, GO, and the PGMO composites. These spectra reveal a luminous peak at approximately 450 nm for photocatalysts. Interestingly, when comparing the PL emission intensity of pure MoO_3, PANI, and GO with that of the PGMO composites, a significant decrease in fluorescence intensity is observed in the latter. This decrease in fluorescence suggests the effective isolation of electron-hole pairs generated by light within the composite structure. The efficient separation of the effective management of electron-hole pairs is essential for enhancing the degradation through photocatalysis performance of materials. This separation prevents preventing the recombination of electron-hole pairs, enabling more efficient use of these carriers in photocatalytic reactions.

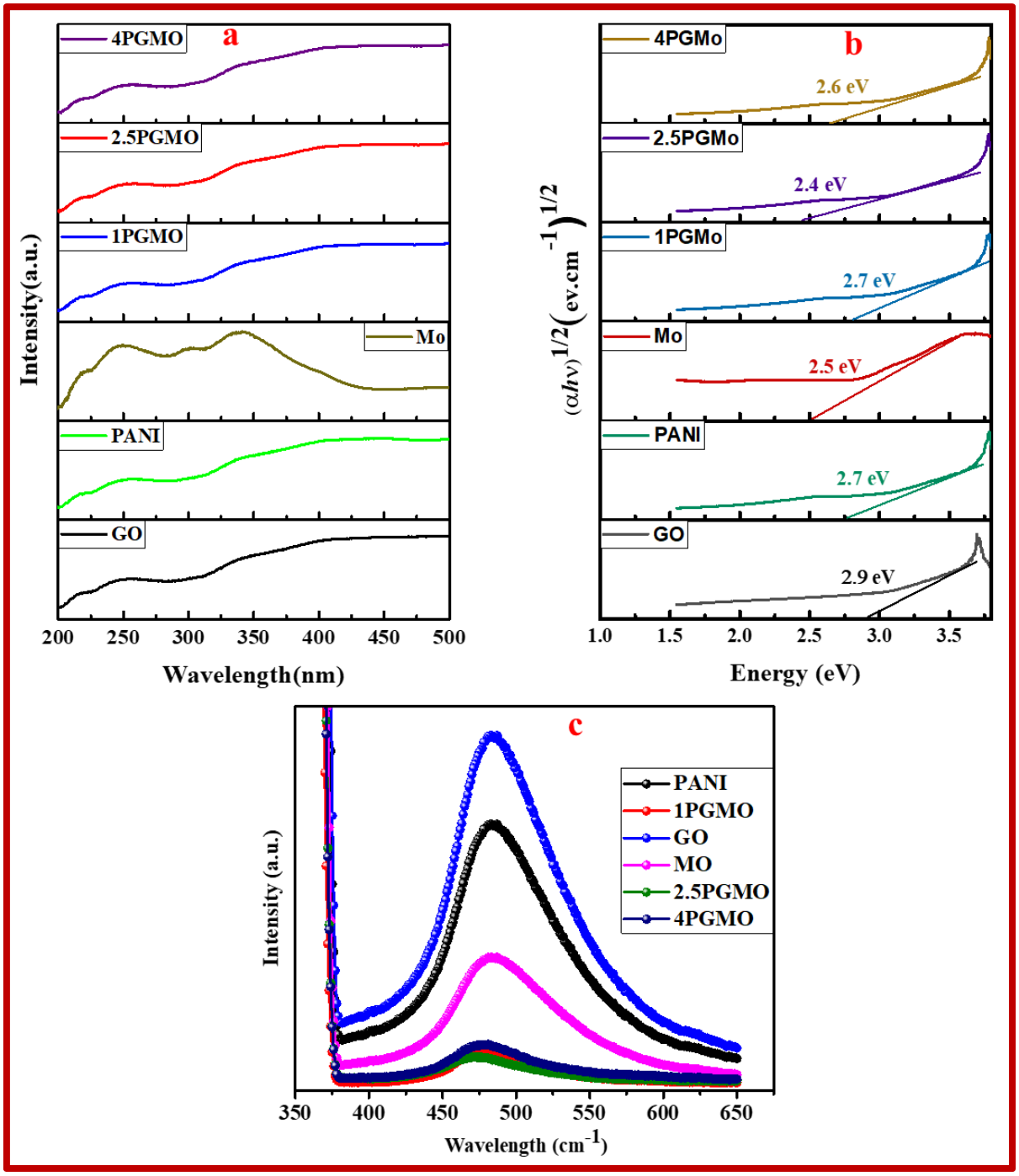

Fig 3.3: (a) UV-Vis DRS spectra, (b) Tauc's plot, and (c) PL spectra of GO, PANI, MO, 1PGMO, 2.5PGMO, and 4PGMO.

3.3.1.2. Surface properties:

The BET study was conducted to assess the overall surface area, mean pore size, and total volume of pore for the individual materials and their composites. This analysis is depicted in **Fig 3.4** and summarized in **Table 3.1**. For both pure substances and composites of materials, a

type IV isotherm was observed, demonstrating the creation of multiple molecular adsorption layers and the process of particles condensing within tiny capillary pores. Furthermore, the BJH plot suggested each material displayed mesoporous attributes, with pore diameters below 5 nm. Interestingly, the composite materials exhibited a higher pore volume compared to the bulk materials. Specifically, GO and MoO_3 exhibited much lower surface areas in comparison to the composites and PANI. These findings suggest that PANI plays a pivotal role in augmenting the surface area within the composites. This increased surface area is advantageous for efficient adsorption processes. In summary, the BET analysis offers vital information on the structural characteristics of the materials and emphasizes the notable impact of PANI in improving the overall surface area of the composite materials.

Table 3.1: BET surface area, total pore volume, and average pore diameter.

Photocatalyst	**Surface Area (m^2/g)**	**Total Pore Volume (cm^3/g)**	**Average Pore Diameter (nm)**
PANI	17.3	0.020	4.7
GO	8.9	0.0172	5
MO	7.4	0.007	3.9
1PGMO	18.9	0.025	3.5
2.5PGMO	29.6	0.034	3.6
4PGMO	27.9	0.022	3.1

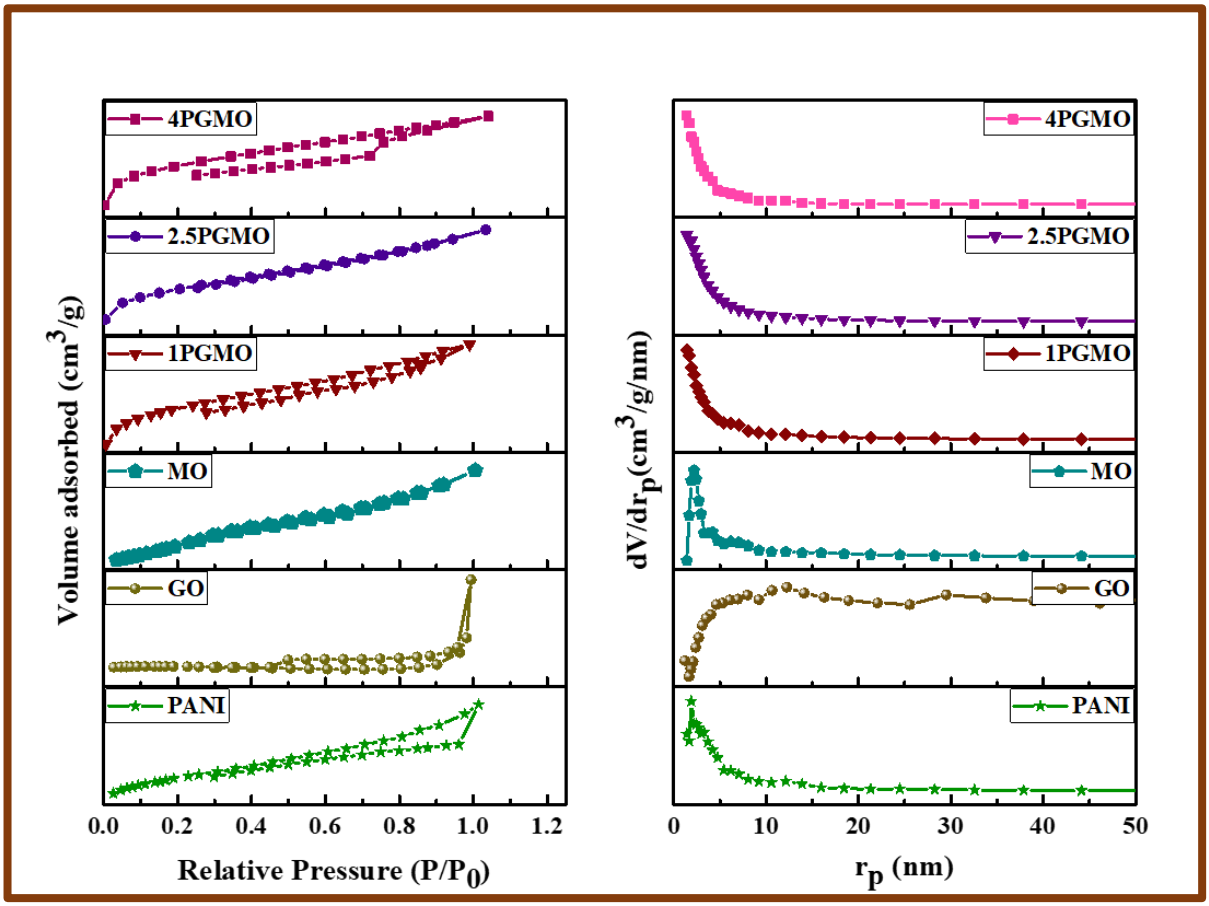

Fig 3.4: (a) Adsorption-Desorption curves of PANI, GO, MoO_3,1PGMO,2.5PGMO,4PGMO

(b) BJH plot of PANI, GO, MoO_3,1PGMO,2.5PGMO,4PGMO.

3.3.1.3. Morphological properties:

FESEM analysis (**Fig 3.5a-3.5d**) offers valuable insights into the structural features of the prepared composite. The FESEM image of MoO_3 reveals long nanorods with diameters ranging from 60 to 80 nm. Similarly, The FESEM image of Polyaniline (PANI) validates the existence of a fibrous structure characterized by a porous texture. In **Fig 3.5b**, well-agglomerated and scrubbed layers of graphene oxide (GO) are visible, indicating effective dispersion and separation of GO layers. The exfoliation of GO can be attributed to the existence of oxygen-containing functional groups on its surface layers. The nanocomposite forms agglomerates of GO with PANI as a result of the fibrous characteristics of the polymer. The FESEM image of the nanocomposite material (**Fig 3.5c**) provides evidence for the simultaneous existence of polyaniline, GO, and MoO_3 nanorods, thereby verifying the successfully forming heterojunction structures. The harmonious composition of the produced nanocomposites was

determined by the use of EDS (**Fig 3.6**). The EDS analysis verified the concurrent existence of carbon (C), nitrogen (N), molybdenum (Mo), and oxygen (O) in the produced nanocomposite. Furthermore, the element color mappings of the nanocomposite material verify the even dispersion of all elements, a critical factor in improving the photocatalytic characteristics of the composite. Overall, the FESEM and EDS analyses provide comprehensive structural and elemental information, essential for understanding the composition and properties of the synthesized nanocomposites.

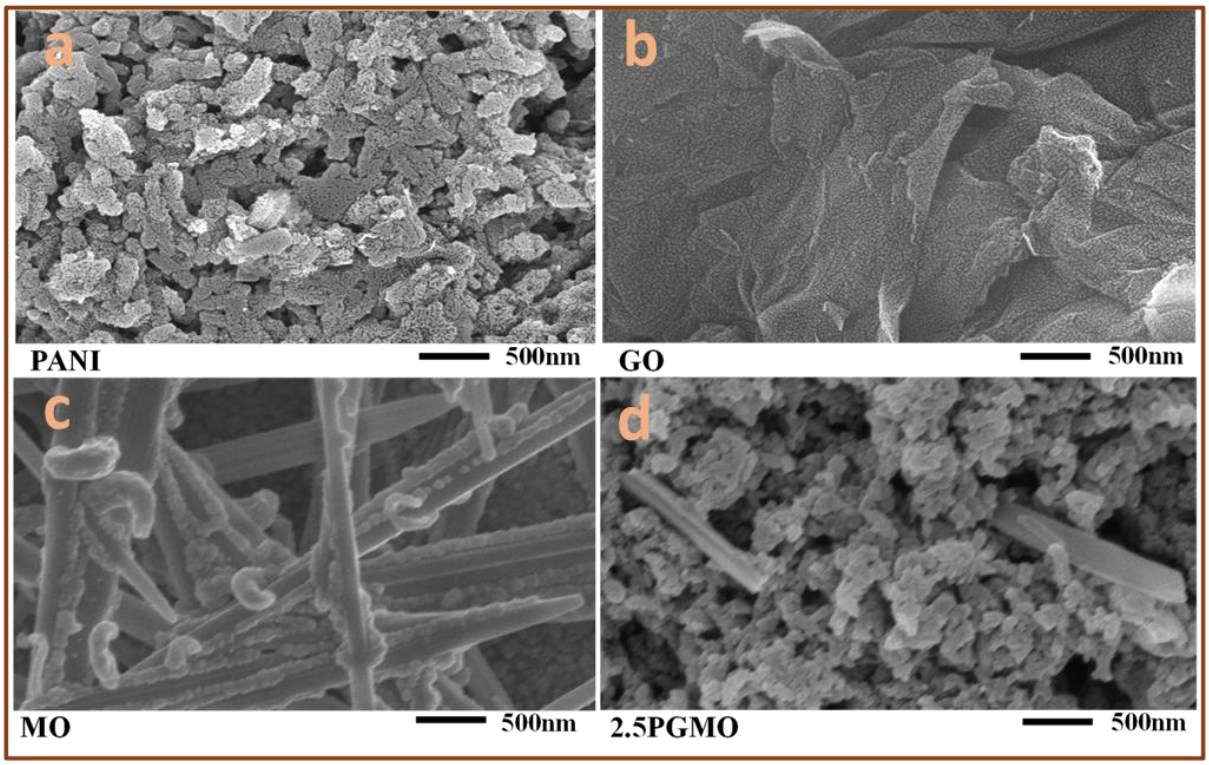

Fig 3.5: FESEM image of (a) PANI, (b) GO, (c) MO, and (d) 2.5 PGMO.

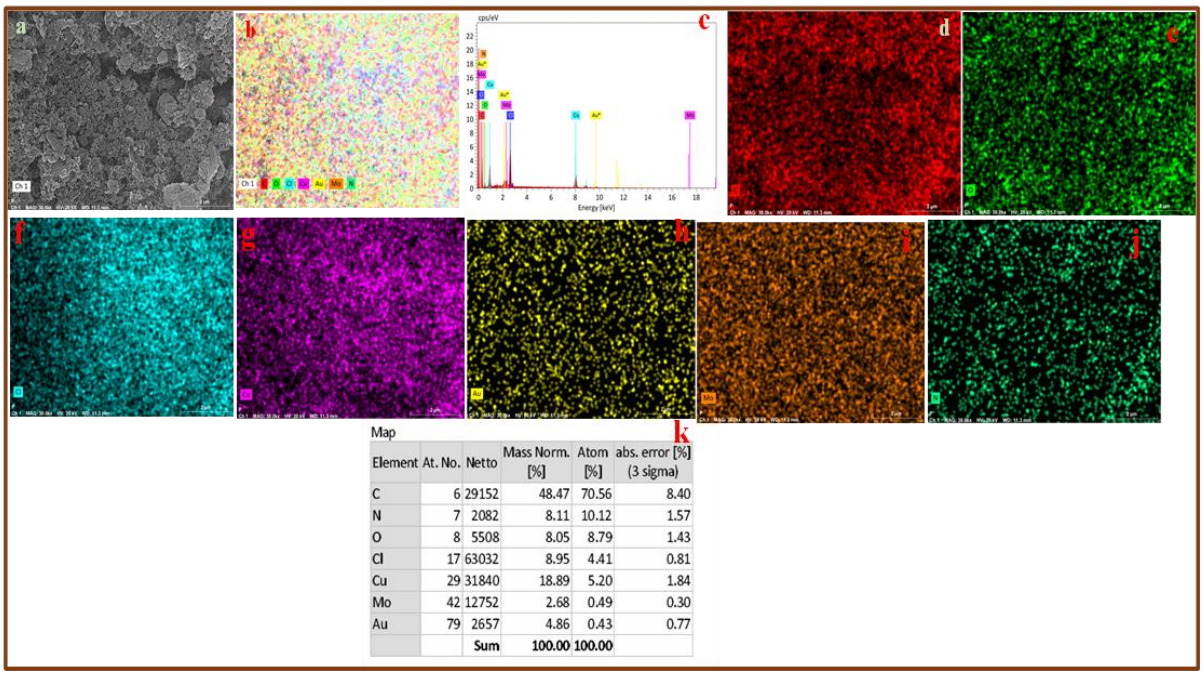

Fig 3.6: (a) FESEM image of 2.5PGMO (c,k) EDS spectrum of 2.5PGMO and (b,d-j) is the elemental mapping of its constituents.

3.3.1.4.Photoelectrochemical measurements:

To investigate the photo-electrocatalytic performance, photoelectrochemical measurements were conducted. Employing EIS, a significant tool for studying charge transfer processes at the electrode-electrolyte interface, was instrumental. This method is commonly employed to assess the efficacy of charge separation in photo-induced reactions. The EIS results, illustrated in **Fig 3.7a-3.7d**, depict a representative impedance spectrum of the prepared samples. For a more in-depth analysis, an equivalent circuit (inset in **Fig 3.7a-3.7d**) was applied to interpret the impedance spectra, and EC-Lab software facilitated fitting. In this circuit, R1 represents the system's series resistance. The high-frequency semi-circle indicates the charge-transfer resistance (R2) at the Pt counter electrode/electrolyte interface, while the middle-frequency semi-circle corresponds to the charge-transfer resistance (R2) at the anode/electrolyte interface of the sample prepared. In this context, R3 denotes the charge transfer resistance within the Helmholtz layer, 'C' denotes chemical capacitance, and 'W' denotes Warburg impedance. The semi-circular Nyquist plot in **Fig 3.7** further confirms that the 2.5PGMO composite electrode exhibits a smaller arc radius than pure PANI, GO, and MoO_3 when exposed to visible light. This indicates that the 2.5PGMO photo-electrode demonstrates a more efficient division of light-induced charge carriers and accelerated interfacial charge transfer. In **Fig 3.8**, the

characteristic peak of PANI, GO, MoO_3, and 2.5PGMO shows a frequency of 3214.77, 6689.46, 7236.66, and 259.9 Hz respectively. This shift to a lower frequency for 2.5PGMO implies a faster process for electron transfer. The relationship between frequency (f) and the duration (τ) of injected electrons' lifespan, as per the equation $\tau \approx 1/(2\pi f)$, suggests that the electron lifetime of 2.5PGMO (0.612 ms) is approximately 12-fold increase compared to pure PANI (0.0495 ms), 25-fold increase compared to pure GO (0.023 ms), and 28-fold increase compared to pure MoO_3 (0.022 ms). This substantial increase indicates a longer injected electron lifetime, effectively inhibiting charge recombination in the 2.5PGMO photo-electrode. As a result, this improves charge separation efficiency and boosts photo-electrocatalytic performance.

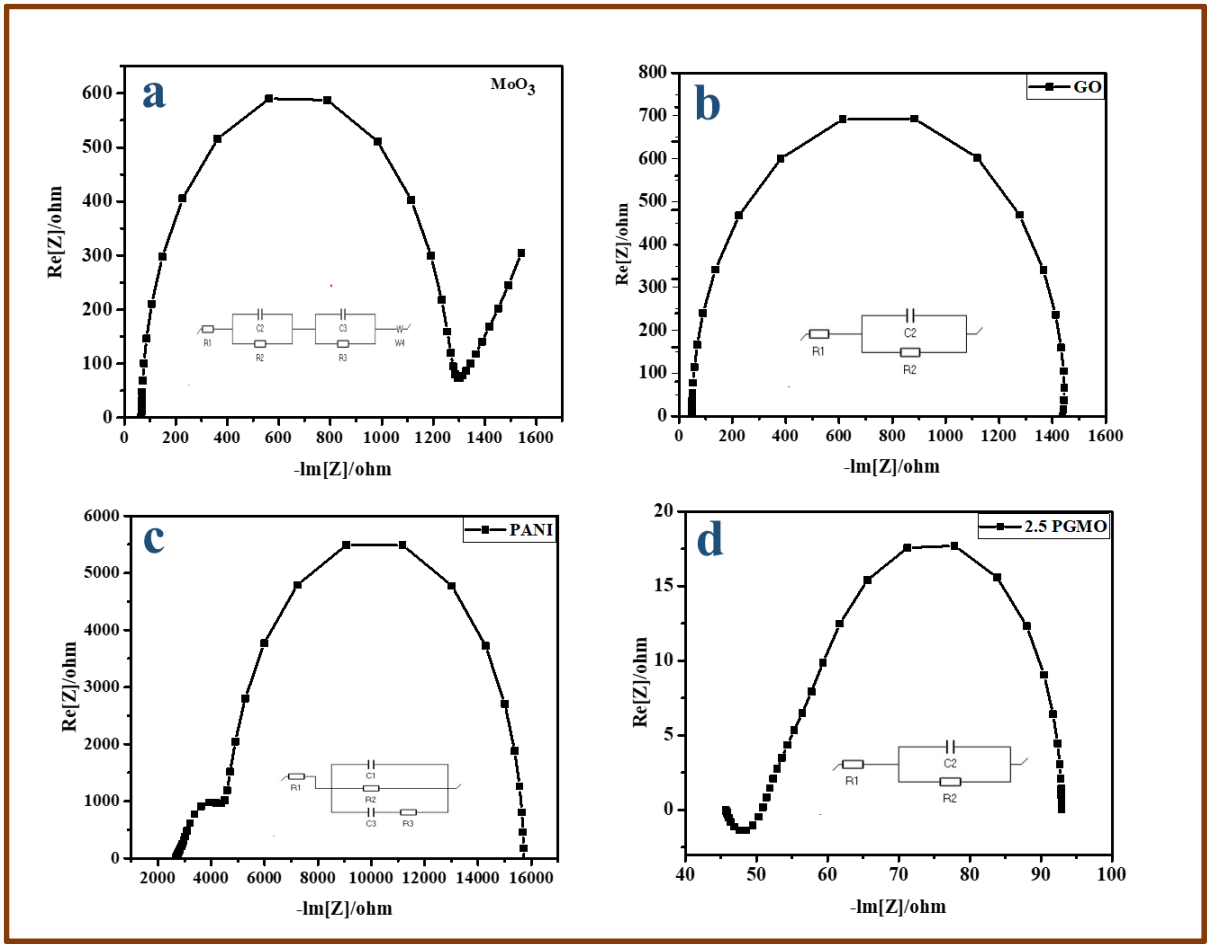

Fig 3.7: EIS plot of (a) MoO_3, (b) GO, (c) PANI, and (d) 2.5PGMO.

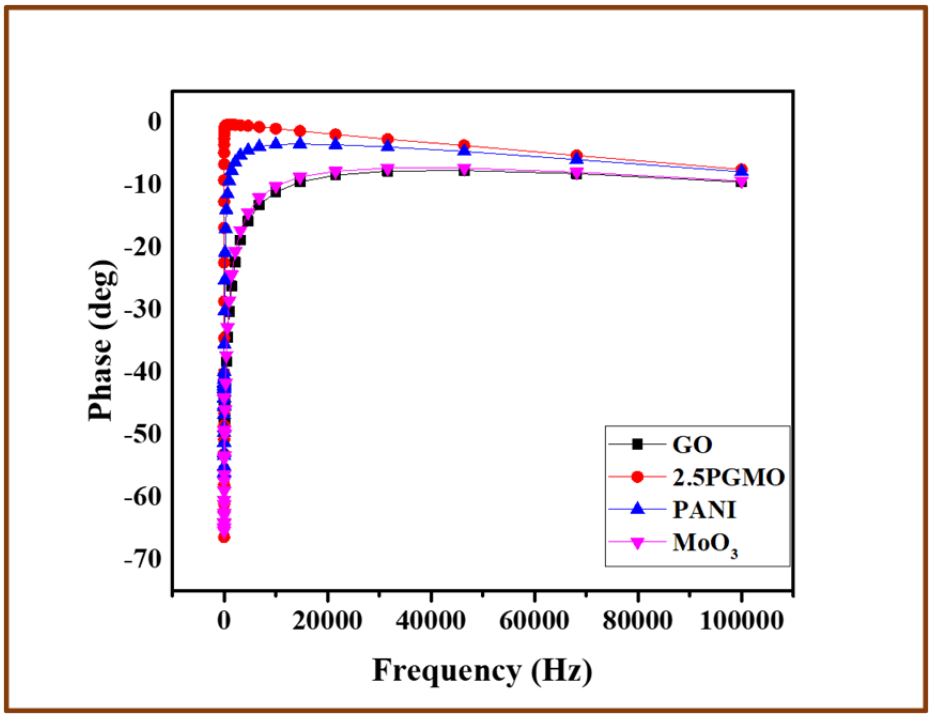

Fig 3.8: Phase angle (degree) vs. Frequency plot of (a) PANI (b) GO (c) MoO_3 (d) 2.5PGMO.

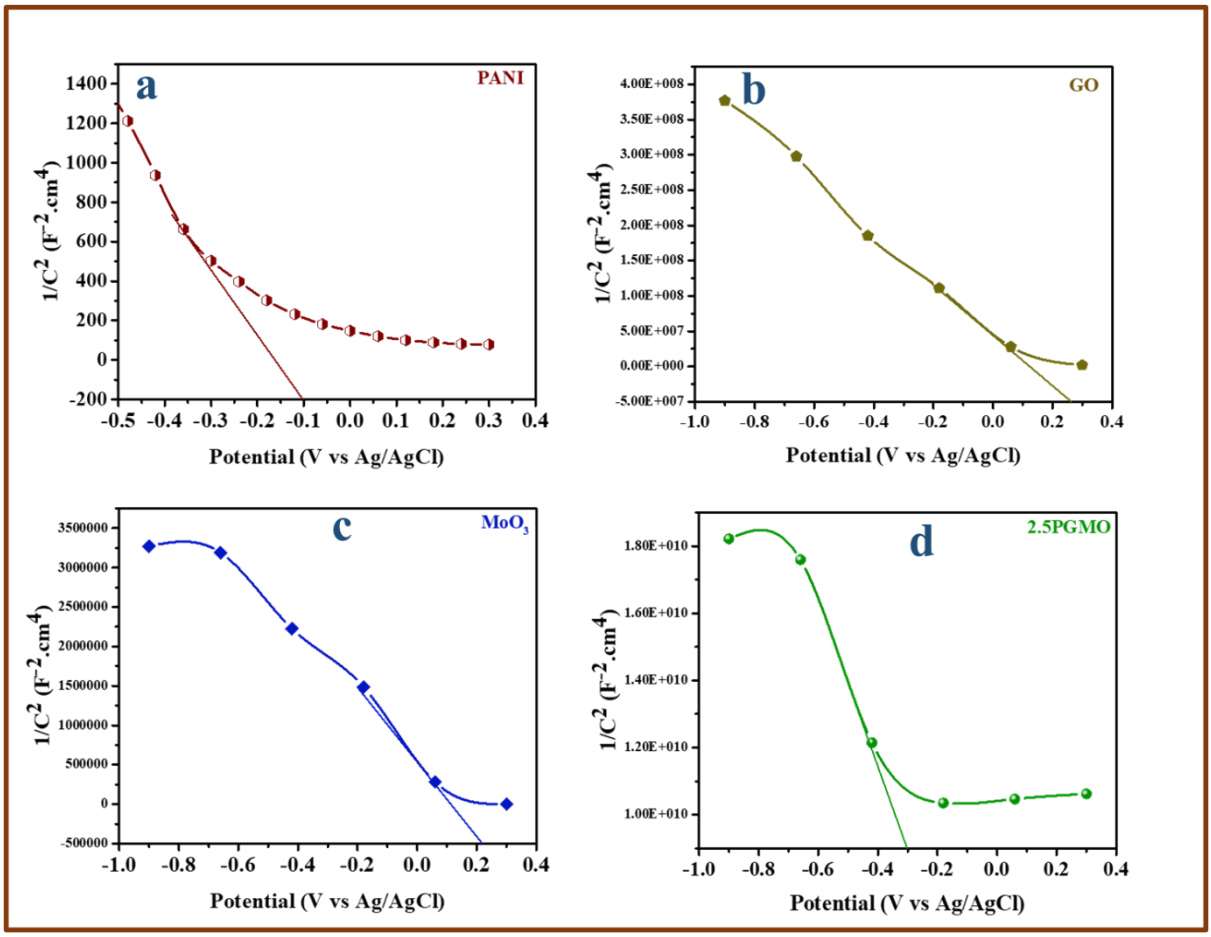

Fig 3.9: Mott-Schottky plot of (a) PANI (b) GO (c) MoO_3 (d) 2.5PGMO.

3.3.2.1.Photocatalytic removal of organic pollutant methyl orange (MO):

The efficacy of photolysis, without the presence of catalysts, in removing MO was demonstrated in **Fig 3.10a**. It showed a mere ~3% reduction in the absorbance over 120 min of LED lamp exposure. The poor ability of direct photolysis to degrade verifies the high resistance to deterioration of MO through exposure to light. Upon reaching adsorption-desorption equilibrium in the dark after 120 min, approximately 30.2% of MO molecules were adsorbed when using 2.5PGMO, however, bare PANI, GO, Molybdenum trioxide, 1PG (99 wt% of polyaniline and 1 wt% of graphene oxide), 11GMO (1:1 of graphene oxide and molybdenum trioxide), 1PMO (1 wt% of molybdenum trioxide added to 99 wt% of polyaniline),1PGMO, 4PGMO, and commercially used TiO_2 samples adsorbed 20.2, 25.5, 8.2, 12.2, 11.1, 10.7, 27.7, 28.3, and 7.1% of MO, respectively. The superior adsorption capacity of the 2.5PGMO is attributed to the increased surface area with abundant anionic azo dye methyl orange adsorption sites achieved by simultaneously incorporating 2.5 wt% of GO/MO onto the surface of PANI. To enhance removal efficacy, degradation was initiated with light illumination. After 120 min of irradiation to LED light, the catalytic efficiency associated with the prepared catalysts improved in the following manner: PANI (30.1) < GO (31.2) < Molybdenum trioxide (32.8) < TiO_2 (33.1) < 1PMO (45.6) < 1PG (50.3) < 11GMO (72.8) < 1PGMO (85.7) < 4PGMO (90.4) < 2.5PGMO (98.9%). These results demonstrate that bare MoO_3 can only decompose a finite quantity of MO due to the photo-response spectrum of the material is limited and it has an inadequate specific surface area, and rapid recombination of photo-induced e^- and h^+. The presence of PANI and GO species was discovered to enhance the performance. The photocatalytic activity of the composites 1PMO, 1PG, and 11GMO was enhanced compared to the single-component material. However, the degree of degrading was heavily influenced by the loading of GO and MoO_3. The 2.5PGMO demonstrated the most effective degrading efficiency for removing MO. However, when the amount of 11GMO was increased to 4 wt%, there was a minor decrease in the effectiveness of MO removal. This behaviour can be attributed to two factors: when the amount of inserted content from 11GMO species was reduced, the photo-generated carriers of charges in the 1PGMO composite materials were not efficiently distributed, leading to a decrease in photodegradability. In addition, the excess presence of 11GMO at a concentration

of 4 wt% can obstruct the sites of activity on the catalytic surface, hence hindering the incident irradiation and diminishing the photocatalytic capability. Hence, the inclusion of an optimal quantity of 11GMO species facilitates the attainment of maximum synergy among PANI, GO, and MoO_3, resulting in boosted photocatalytic activity. This enhancement can be credited to a shorter band gap, upgraded light absorption capacity, reduced recombination of electron-hole pairs, and increased absorbing ability. Furthermore, a quantitative examination of the photocatalytic disintegration kinetics of MO was conducted by fitting the experimental results to a pseudo-first-order rate equation:

$$\ln (C_t/C_0) = - kt \quad (3.2)$$

In this context, C_0 and C_t refer to the concentrations of MO at 0 and t minutes of irradiation, respectively. The variable k indicates the reaction rate constant (min^{-1}). Remarkably, in line with the degree of decomposition, there is a degradation rate constant k of 1PGMO (0.02283), 2.5PGMO (0.0299), 4PGMO (0.02803), 1PG (0.01063), 1PMO (0.00614), 11GMO (0.01073), PANI (0.00518), GO (0.00174), MoO_3 (0.00451), and TiO_2 (0.00385 min^{-1}), respectively.

The synergy achieved through the amalgamation of PANI, GO, and MoO_3 was quantified using the synergy factor (R), calculated through the equation:

$$R = \frac{K_{PANI+GO+MoO3}}{K_{PANI}+K_{GO}+K_{MoO3}} \quad (3.3)$$

Where, $K_{PANI+GO+MoO3}$, K_{PANI} , K_{GO} , K_{MoO3} denote the rate constants for photodegradation for the PANI/GO/MoO_3 ternary composite, as well as for PANI, GO, and MoO_3 individually. The synergy factors for 1PGMO, 2.5PGMO, 4PGMO, 1PG, 1PMO, and 11GMO were calculated as 1.84, 2.41, 2.26, 1.34, 0.49, and 1.72, respectively. Out of all of the nanocomposites, 2.5PGMO displayed the greatest synergy factor, which resulted in its superior efficacy in degrading photocatalytic substances and a maximum rate constant of 0.0299 min^{-1}.

3.3.2.2. Impact of the amount of catalyst dosage:

The effectiveness of a photocatalyst is significantly influenced by the quantity of catalyst used. To explore the impact of catalyst dosage on the degradation of MO, a set of photocatalytic experiments were conducted, varying the amount of the ternary photocatalyst (2.5PGMO) from 1 to 4 mg while maintaining a constant MO concentration of 20 ppm. When the quantity of

photocatalyst was minimal (0.1 g/L), there was limited involvement of active species in the degradation of MO, resulting in reduced photocatalytic degradation efficiency. The best degradation efficiency was achieved with 0.2 g/L (**Fig 3.10b**) of the photocatalyst, due to the greater accessibility of active sites and the efficient utilization of light energy. However, an increase in the dosage of the catalyst beyond 0.2 g/L resulted in no significant change in the degradation rate. This phenomenon can be ascribed to an excessive accumulation of the catalyst, potentially diminishing solution transparency and light penetration ability. In addition, it can deactivate some regions of the catalyst surface that would otherwise be available for the degrading process. In summary, the findings indicate that the maximum amount for MO photodegradation is 0.2 g/L of the catalyst.

3.3.2.3. Effect of the solution's pH:

The adsorption capacity of the composite is heavily controlled by the pH of the solution of dye, which in turn has a major impact on the effectiveness of degradation. [56]. To fully grasp how the pH of the solution affects the removal of MO dye, solutions with different pH levels were carefully created employing solutions of 0.1 N HCl and 0.1 N NaOH. Solutions containing catalyst-to-dye with a concentration of 0.2 g/L were prepared, and the pH values were monitored prior to and following the degradation procedure. **Fig 3.10e** illustrates that the composite 2.5PGMO possesses a point of zero charges (pzc) around pH 6.5. The degradation effectiveness gradually increases from pH 1 to 5, reaching a maximum at pH of 6.8 (**Fig 3.10f**). In basic solutions, the degradation effectiveness shows a gradual decrease. This observation underscores the crucial role of solution pH in modulating the photocatalytic degradation efficiency of the composite. The trends suggest that the surface charge of the composite, influenced by the pH conditions, significantly affects the adsorption and subsequent degradation of MO dye molecules. The optimal performance is achieved in slightly acidic conditions (pH 6.5), emphasizing the importance of considering solution pH in designing and optimizing photocatalytic processes for effective pollutant removal. The efficiency of degradation decreases gradually in highly alkaline solutions, mainly because of the creation of metal hydroxide precipitates at the surface of the catalyst.

3.3.2.4. Effect of the illuminated area:

The study effectively explored the significance of the illuminated surface area when employing the 2.5PGMO material serving as a photocatalyst in visible light conditions. A solution containing 0.2 g/L of photocatalyst was mixed with 20 ppm of MO dye. The mixture was agitated under visible light for a duration of 120 min. Vessels of varying diameters were used to alter the reaction's surface area while keeping the distance between the pollutant solution's upper surface and the lamp's bottom surface constant at 6 cm. The results demonstrated that as the surface area that was exposed to the reaction mixture increased, there was a commensurate enhancement in the degradation efficiency (**Fig 3.10c**). Increased surface area in the reaction mixture resulted in intensified exposure to light, hence enhancing the photocatalytic breakdown of contaminants and yielding the best efficiency in degradation.

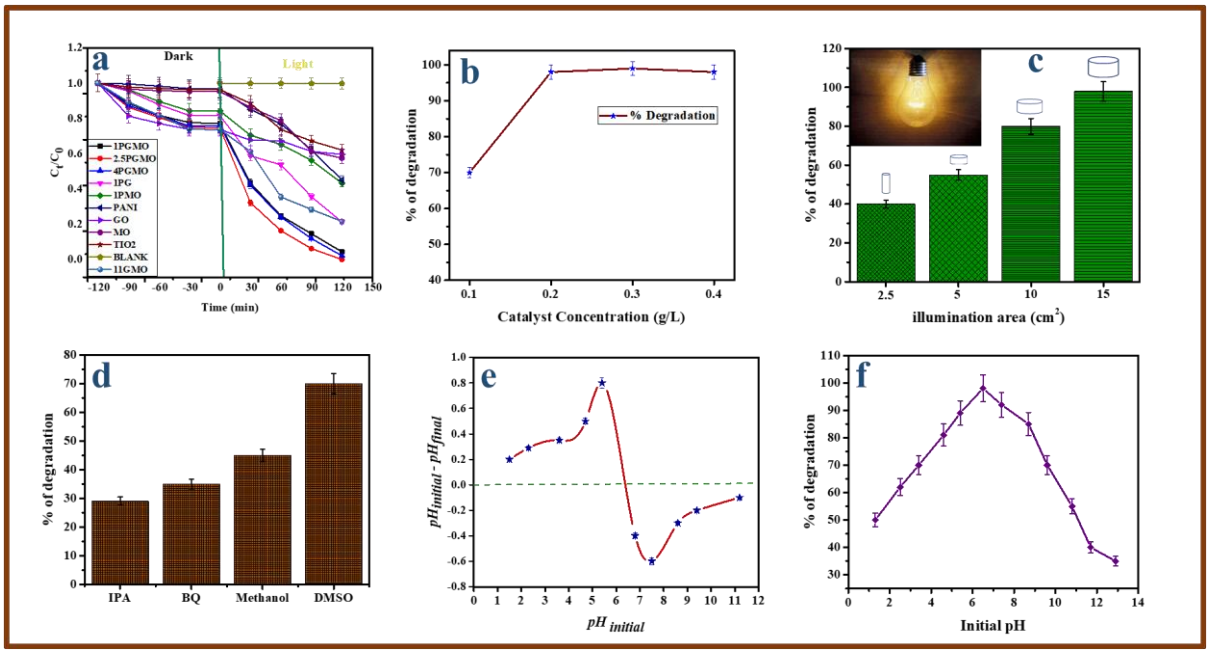

Fig 3.10: (a) Kinetic studies, (b) effect of catalyst concentration, (c) Impact of illuminated surface area, (d) scavenger studies, (e) pzc studies, and (f) effect of pH on methyl orange solution.

3.3.2.5. Probable degradation pathway of MO:

When examining the intermediates generated while decomposing organic dyes through photodegradation, it is crucial to track the TOC and COD levels in the solution as it undergoes light exposure. Following 120 min of exposure to visible light, the TOC and COD reduction efficiencies for MO are observed to be 70 and 81.1%, respectively. Examination of **Fig 3.14a** suggests that the solutions undergo nearly complete mineralization, containing intermediates

characterized by a limited mineralization potential. This observation implies a thorough breakdown of the organic dye into byproducts with diminished mineralization capacity.

GC-MS analysis was employed to identify the degradation products of MO through the use of 2.5PGMO nanocomposite. In **Fig 3.11**, the complete mass spectra of MO degradation by 2.5PGMO are presented. MO dye has a characteristic mass spectrum at m/z of 306. The mass spectrogram after 120 min of degradation (**Fig 3.11**) shows m/z peaks at 121, 136, 157, and 172, which match the intermediate products resulting from the degradation of MO. These substances include sulfanilic acid at m/z 172, which fragments into benzenesulfonic acid at m/z 157 following the removal of an amino group (NH_2). Additionally, N,N-dimethyl-p-phenylenediamine at m/z 136 fragments into N,N-dimethyl benzenenamine at m/z 121 following the removal of an amino group (NH_2). Based on the results observed, It is suggested that the degradation pathway of MO involves the even division of the azo bond (–N=N–), yielding sulfanilic acid and N, N-dimethyl-p-phenylenediamine[57]. A mechanism of the degradation path is described in **Fig 3.12**. Subsequent degradation of intermediate products may lead to further mineralization into CO_2 and H_2O.

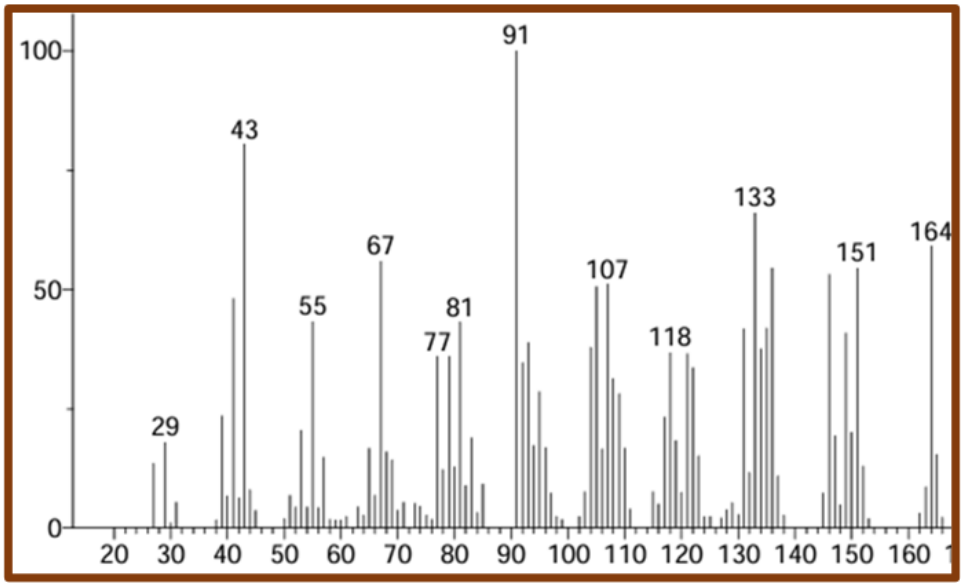

Fig 3.11: GC-MS data after degradation of methyl orange.

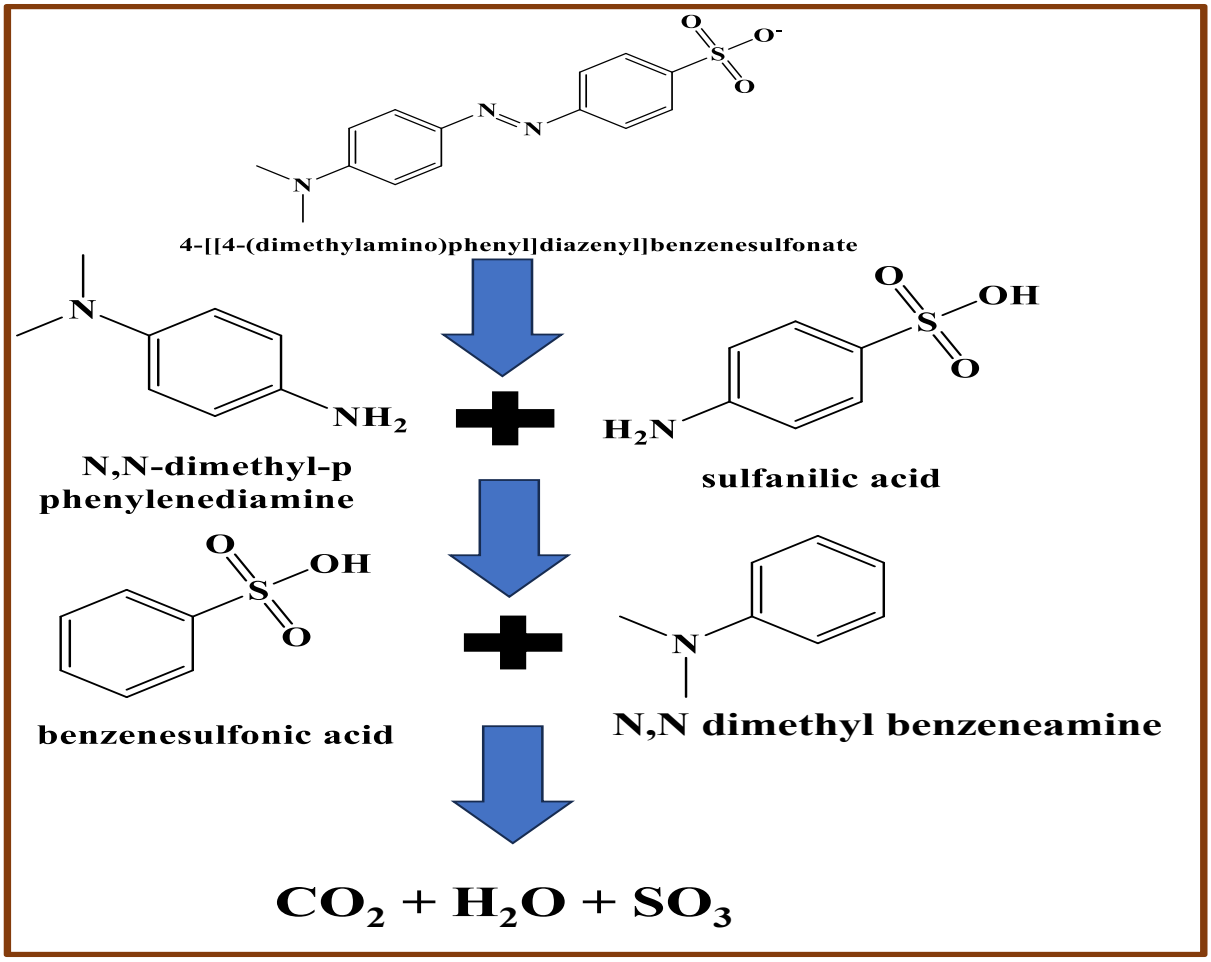

Fig 3.12: Potential pathway for photocatalytic degradation of methyl orange using the 2.5PGMO photocatalyst.

3.3.2.6. Influence of scavenger and potential mechanisms for charge transfer:

The process of degradation primarily engages electrons within the conduction band (CB), holes in the valence band (VB), superoxide radicals, and hydroxyl radicals. All of these factors play a vital function during the degradation process. An investigation into scavenging was conducted to identify the primary species involved in the degrading process. Different scavengers, including isopropyl alcohol (IPA), dimethyl sulfoxide (DMSO), benzoquinone (BQ), and methanol, were employed to capture hydroxyl radicals ($OH^{\bullet}$), electrons ($e^{\bullet}$), and superoxide radicals ($O_2^{\bullet-}$) during the degradation process. The scavenger study revealed noteworthy interactions, where the hydroxyl radicals ($OH^{\bullet}$) acted as reductive agents and interacted with benzoquinone (BQ) to generate hydroquinone. Furthermore, the participation of DMSO had the participation of DMSO, signifying the crucial role of hydroxyl radicals ($OH^{\bullet}$) in the degradation process. The presence of unpaired electrons the presence of DMSO

facilitates electron transfer involving its oxygen atoms resulting in the creation of hydrogen bonds with the hydrogen atoms from hydroxyl radicals ($OH^{\bullet}$)[58]. The results depicted in **Fig 3.10d** demonstrate that the process of degradation reaction is significantly affected by methanol, IPA, and BQ. This observation strongly suggests that holes, hydroxyl radicals, and superoxide radicals are the predominant species driving the mechanism of degradation. The comprehensive scavenger study sheds light on the intricate charge transfer mechanisms and the significant roles played by specific reactive species in the overall degradation process. The enhanced performance of the 2.5PGMO composite is attributed to the augmentation of charge separation achieved by incorporating GO and MoO_3 into the polyaniline matrix. To elucidate the mechanism underlying the heightened photocatalytic activity of the 2.5PGMO composite, a thorough examination of the investigation involved determining the relative positions of the bands of PANI, GO, and MoO_3. In **Fig 3.9**, the Mott-Schottky plots for both PANI, GO, MoO_3, and 2.5PGMO reveal their characteristic nature as typical p-type semiconductors, with overall negative slopes[59]. The determination of flat-band potentials, derived from the points where the linear region intersects the x-axis, yields values of -0.1 V for PANI, 0.26 V for GO, 0.22 V for MoO_3, and -0.3 V for 2.5PGMO, referenced against the Ag/AgCl. Significantly, the ECB of the 2.5PGMO composite displays a substantial negative shift of 0.3 V in comparison to the pure GO, and MoO_3. This observed shift can be attributed to electronic interactions involving PANI, GO, and MoO_3, leading to a pronounced lowering of the conduction band potential. This, in turn, results in occupying a conduction band at a high energy level, enhancing the reductive capacity of the 2.5PGMO composite. The detailed analysis of Mott-Schottky plots and band potential shifts sheds light on the underlying electronic interactions and contributes to the understanding of the enhanced photocatalytic properties of the 2.5PGMO composite. In the context of the two channels for the transfer of charges and analysis of energy levels under visible light illumination (**Fig 3.13**), the absorption of photons by GO, MoO_3, and PANI is instrumental in generating electrons in the conduction band (CB) of GO, MoO_3, and the lowest unoccupied molecular orbital (LUMO) of PANI. Simultaneously, this process leaves holes in the valence band (VB) of GO, MoO_3, and the highest occupied molecular orbital (HOMO) of PANI. Following the principle of energy minimization, electrons from the CB of GO and MoO_3 are more prone to move toward the HOMO of PANI, compared to their transition across the heterojunction barrier from an excited state to a ground state (VB) of GO or MoO_3. At the same time, the generated holes in the HOMO of PANI can attain a potential of $^{-}OH/^{\cdot}OH$ (+2.4 V)

[60], while the existing electrons in the CB of GO can reach the $O_2/{}^{\cdot}O^{2-}$ potentials (−0.046 V) [60]. Consequently, these holes (h^+) can efficiently oxidize OH^- to ${}^{\cdot}OH$, and the electrons (e^-) can reduce O_2 to ${}^{\cdot}O^{2-}$, both of which are energetic species capable of degrading methyl orange (MO) into by-products. However, it is noted that the existing electrons in the CB of GO and MoO_3 cannot reach the potentials of $O_2/{}^{\cdot}O^{2-}$ (−0.046 V). Therefore, these electrons directly oxidize MO into degradation products and can produce hydrogen by water splitting. Consequently, ${}^{\cdot}O^{2-}$, ${}^{\cdot}OH$, and e^- emerge as the primary active species that catalyzes the decomposition of the MO solution into products on the photocatalyst's surface. This outcome aligns with the findings of radical scavenging experiments, suggesting that the charge transfer channel of the catalyst adheres to the direct Z-scheme mechanism. The following summary encapsulates the key points:

$$\mathbf{PANI + h\nu \longrightarrow e_{LUMO}^{-}(PANI) + h_{HOMO}^{+}(PANI)} \quad \mathbf{(3.4)}$$

$$\mathbf{GO + h\nu \longrightarrow e_{CB}^{-}(GO) + h_{VB}^{+}(GO)} \quad \mathbf{(3.5)}$$

$$\mathbf{MoO_3 + h\nu \longrightarrow e_{CB}^{-}(MoO_3) + h_{VB}^{+}(MoO_3)} \quad \mathbf{(3.6)}$$

$$\mathbf{e_{LUMO}^{-}(PANI) + O_2 \longrightarrow {}^{\cdot}O^{2-}(PANI)} \quad \mathbf{(3.7)}$$

$$\mathbf{h_{VB}^{+}(PANI/GO/MoO_3) + OH^{-} \longrightarrow {}^{\cdot}OH(PANI/GO/MoO_3)} \quad \mathbf{(3.8)}$$

$$\mathbf{O^{2-}(PANI), {}^{\cdot}OH(PANI/GO/MoO_3) + MO \longrightarrow Degraded\ products} \quad \mathbf{(3.9)}$$

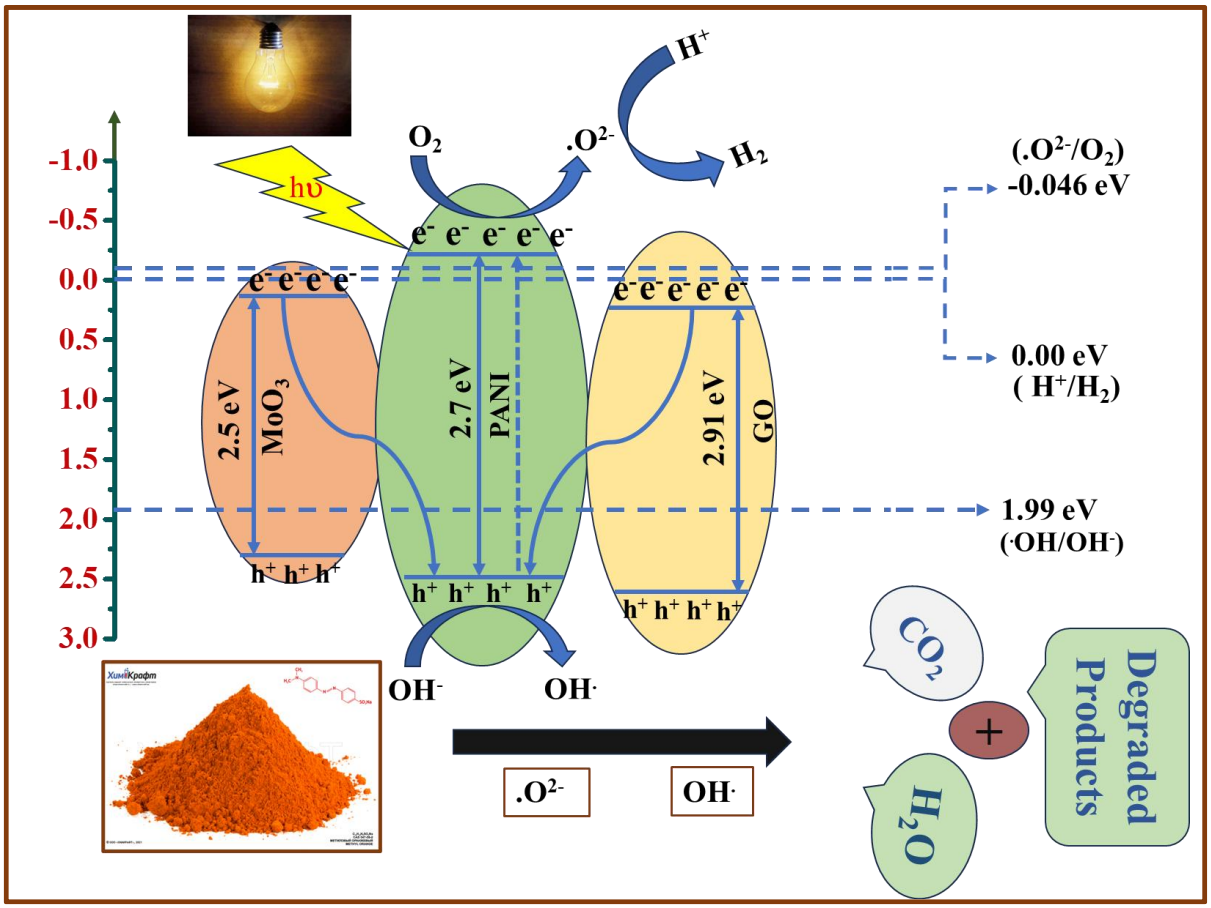

Fig 3.13: Potential mechanism for the transfer of charges in the process of photocatalytic degradation and hydrogen production.

3.3.2.7. Reusability studies:

The durability of the photocatalyst is a critical factor for the ongoing utilization of a material used in environmental remediation. Hence, it is crucial to investigate the longevity of the photocatalytic composite under multiple cycles of photodegradation. Hence, it is crucial to investigate the durability of the photocatalysis composite following numerous repetitions of photodegradation. The findings indicated that the 2.5PGMO composite demonstrated remarkable photostability, as evidenced by the high degradation efficiency of 85-98% for MO even after undergoing five cycles. This is depicted in the graphs depicting photodegradation presented in **Fig 3.14b**. After undergoing five cycles, the nanocomposite was analyzed using XRD analysis. The results indicated a slight reduction in peak intensity, likely because of the adsorption of dye molecules at the surface of the catalyst. However, there was no alteration observed in the catalyst's XRD pattern (**Fig 3.14d**). This suggests that the photocatalyst maintains its durability and integrity over time.

A comparison was conducted between the 2.5PGMO photocatalyst and other materials that have been reported in the literature for the photocatalytic purification of organic pollutants. The results have been organized in **Table 3.2**. The results of the investigation show that treating persistent organic pollutants with a lower catalyst concentration works well.

Table 3.2: Comparison of different photocatalyst materials for photocatalytic degradation.

Photocatalyst	Catalyst amount (mg)	% degradation	Time (min)	References
PANI-TiO_2	10	89.7	120	[61]
PANI/TiO_2/Cotton	-	87.7	180	[62]
PANI/TiO_2/SiO_2	-	87	120	[63]
PANI/Fe-TiO_2	-	28	150	[64]
Ag-Ag_2O/TiO_2@PPY	100	100	175	[65]
PEDOT/GO/MnO_2	20	92.7	420	[66]
RGO/mesoTiO_2/AuNP	10	-	240	[67]
PANI@GN/TiO_2	50	87	180	[68]
Ag_2O/TiO_2@PPY	50	100	240	[69]
PANI/GO/MoO_3 (2.5%)	2	98	120	Present work

3.3.2.8. Photocatalytic hydrogen generation studies:

For 24 hrs under LED light, the process of generating hydrogen through photocatalytic water splitting was conducted, employing four distinct water solutions. The starting solution comprised 1 ml of methanol (used as a sacrificial agent) mixed with 19 ml of water. The second solution entailed the process of combining 1 ml of HCl diluted with 19 ml of water, which led to the formation of an acidic solution. The third solution was prepared by combining 1 ml of

1N NaOH diluted with 19 ml of water, resulting in a basic solution. The fourth solution consisted of 20 ml of H_2O only. When methanol was present, a total of 26468.4 ppm of hydrogen gas was released (**Fig 3.14c**). Methanol acts as both a scavenger for holes and a sacrificial donor, leading to the generation of intermediate substances formed during the process like formic acid or formaldehyde[70]. During the water-splitting reaction, hydrogen ions (H^+) generated are partially involved in the photocatalytic reduction process with the aid of these intermediate products. Under acidic conditions, approximately 23901.07 ppm of hydrogen gas was produced, while under basic conditions, about 24460.4 ppm of gas consisting of hydrogen was produced. Additionally, in the presence of catalyst and water, around 23523.75 ppm of hydrogen was produced. The quantum efficiency with the sacrificial agent was approximately 30.76%, 27.78% in the acidic solution, 28.37% in the basic solution, and 27.34% in the only catalyst. The **equations 3.10-3.13** below demonstrate how the pairs of electrons and holes within the conduction band and valence band facilitate the redox reaction[71], [72].

In acidic condition:

Oxidation:

$$2H_2O\,(l) + 4h^+ \longrightarrow O_2\,(g) + 4H^+\,(aq) \qquad (3.10)$$

$E^0_{oxidation}$ = -1.23 V

Reduction

$$2H^+ + 2e^- \longrightarrow O_2\,(g) + 2H_2\,(g) \qquad (3.11)$$

$E^0_{reduction}$ = 0 V

In basic condition:

Oxidation:

$$2OH^-\,(aq) \longrightarrow \frac{1}{2}O_2\,(g) + H_2O\,(l) + 2e^- \qquad (3.12)$$

Reduction:

$$2H_2O\,(l) + 2e^- \longrightarrow H_2\,(g) + 2OH^- \qquad (3.13)$$

Observations from the scavenger study revealed that the photocatalytic activity owes its effectiveness to both electron and hole participation. Consequently, substantial hydrogen production occurred under conditions of both acidity and alkalinity.

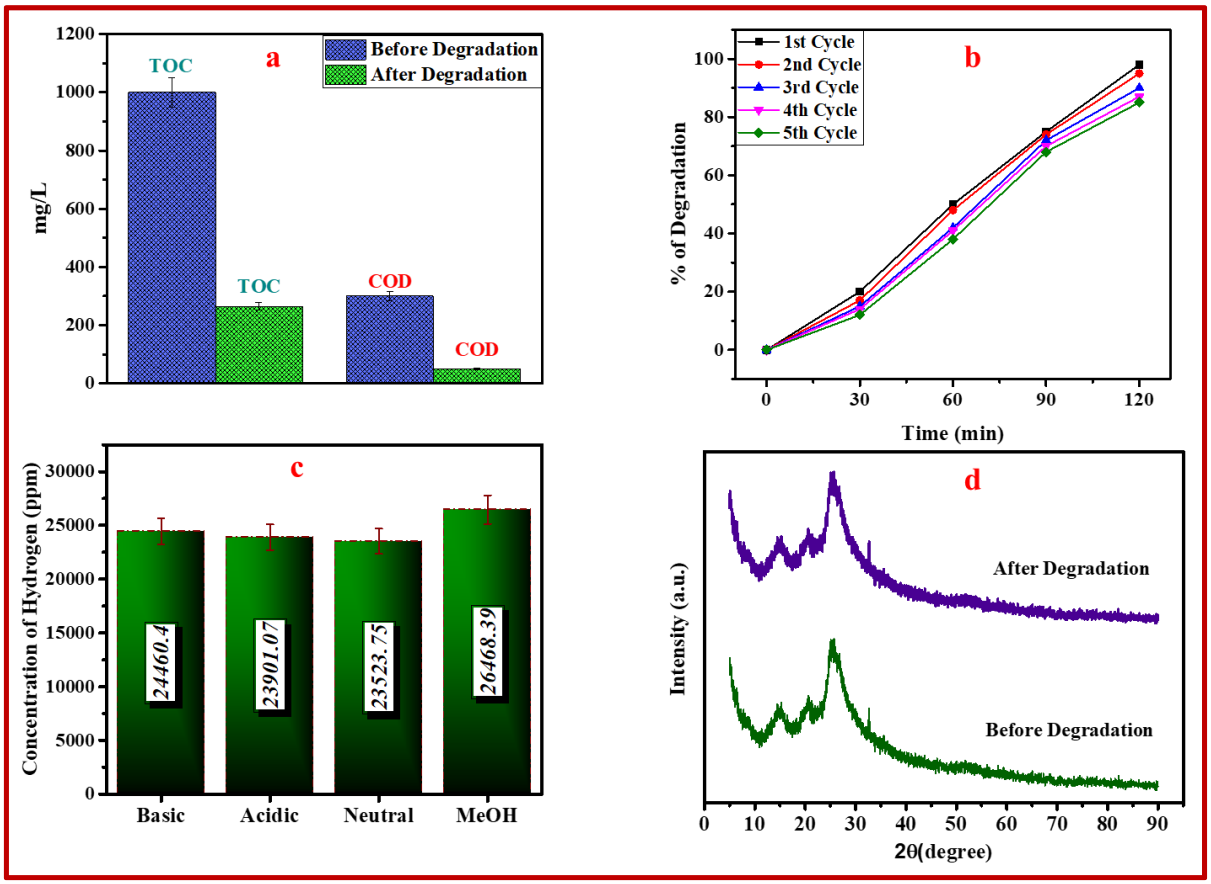

Fig 3.14: (a) TOC and COD of MO before and after degradation, (b) reusability studies, (c) hydrogen production studies, and (d) XRD of 2.5PGMO before and after degradation.

References

[1] M. N. Chong, B. Jin, C. W. K. Chow, and C. Saint, "Recent developments in photocatalytic water treatment technology: A review," *Water Res.*, vol. 44, no. 10, pp. 2997–3027, May 2010, doi: 10.1016/j.watres.2010.02.039.

[2] R. Daghrir, P. Drogui, and D. Robert, "Modified TiO_2 For Environmental Photocatalytic Applications: A Review," *Ind. Eng. Chem. Res.*, vol. 52, no. 10, pp. 3581–3599, Mar. 2013, doi: 10.1021/ie303468t.

[3] A. Mehtab *et al.*, "Hydrogen Energy as Sustainable Energy Resource for Carbon-

Neutrality Realization," *ACS Sustain. Resour. Manag.*, vol. 1, no. 4, pp. 604–620, Apr. 2024, doi: 10.1021/acssusresmgt.4c00039.

[4] R. Gupta, S. A. Ali, Upma, T. Ahmad, and R. Gupta, "Unprecedented Hydrogen Evolution Reactions Based on the Accelerating Effect of [Co–Tb]-Supramolecular Complex-Anchored CdS Heterojunctions," *ACS Appl. Mater. Interfaces*, vol. 17, no. 19, pp. 28244–28255, May 2025, doi: 10.1021/acsami.5c03322.

[5] X. Wang, W. Yang, F. Li, Y. Xue, R. Liu, and Y. Hao, "In Situ Microwave-Assisted Synthesis of Porous N-TiO_2 /g-C_3N_4 Heterojunctions with Enhanced Visible-Light Photocatalytic Properties," *Ind. Eng. Chem. Res.*, vol. 52, no. 48, pp. 17140–17150, Dec. 2013, doi: 10.1021/ie402820v.

[6] X. Chen and W. Shangguan, "Hydrogen production from water splitting on CdS-based photocatalysts using solar light," *Front. Energy*, vol. 7, no. 1, pp. 111–118, Mar. 2013, doi: 10.1007/s11708-012-0228-4.

[7] A. Kudo, K. Omori, and H. Kato, "A Novel Aqueous Process for Preparation of Crystal Form-Controlled and Highly Crystalline $BiVO_4$ Powder from Layered Vanadates at Room Temperature and Its Photocatalytic and Photophysical Properties," *J. Am. Chem. Soc.*, vol. 121, no. 49, pp. 11459–11467, Dec. 1999, doi: 10.1021/ja992541y.

[8] H. M. Braakhuis *et al.*, "Mechanism of Action of TiO_2 : Recommendations to Reduce Uncertainties Related to Carcinogenic Potential," *Annu. Rev. Pharmacol. Toxicol.*, vol. 61, no. 1, pp. 203–223, Jan. 2021, doi: 10.1146/annurev-pharmtox-101419-100049.

[9] N. Bagherlou, E. Ghasemi, P. Gharbani, M. Babazadeh, and A. Mehrizad, "Optimization and modeling of betamethasone removal from aqueous solutions using a SiO_2/g-C_3N_5@$NiFe_2O_4$ nanophotocatalyst by RSM," *npj Clean Water*, vol. 7, no. 1, p. 2, Jan. 2024, doi: 10.1038/s41545-023-00295-1.

[10] A. Mehrizad and P. Gharbani, "Novel ZnS/Carbon Nanofiber Photocatalyst for Degradation of Rhodamine 6G: Kinetics Tracking of Operational Parameters and Development of a Kinetics Model," *Photochem. Photobiol.*, vol. 93, no. 5, pp. 1178–1186, Oct. 2017, doi: 10.1111/php.12795.

[11] A. G. Khosroshahi and A. Mehrizad, "Optimization, kinetics and thermodynamics of photocatalytic degradation of Acid Red 1 by Sm-doped CdS under visible light," *J. Mol. Liq.*, vol. 275, pp. 629–637, Feb. 2019, doi: 10.1016/j.molliq.2018.11.122.

[12] X. Wang *et al.*, "A metal-free polymeric photocatalyst for hydrogen production from water under visible light," *Nat. Mater.*, vol. 8, no. 1, pp. 76–80, Jan. 2009, doi: 10.1038/nmat2317.

[13] Q. Jiang, H. Zhang, D. Rusakov, N. Yousefi, and A. Bismarck, "Additive Manufactured Carbon Nanotube/Epoxy Nanocomposites for Heavy-Duty Applications," *ACS Appl. Polym. Mater.*, vol. 3, no. 1, pp. 93–97, Jan. 2021, doi: 10.1021/acsapm.0c01011.

[14] Y. Zheng, L. Lin, B. Wang, and X. Wang, "Graphitic Carbon Nitride Polymers toward Sustainable Photoredox Catalysis," *Angew. Chemie Int. Ed.*, vol. 54, no. 44, pp. 12868–12884, Oct. 2015, doi: 10.1002/anie.201501788.

[15] G. Yu, J. Gao, J. C. Hummelen, F. Wudl, and A. J. Heeger, "Polymer Photovoltaic Cells: Enhanced Efficiencies via a Network of Internal Donor-Acceptor Heterojunctions," *Science (80-.).*, vol. 270, no. 5243, pp. 1789–1791, Dec. 1995, doi: 10.1126/science.270.5243.1789.

[16] K. Vinodgopal, D. E. Wynkoop, and P. V. Kamat, "Environmental Photochemistry on Semiconductor Surfaces: Photosensitized Degradation of a Textile Azo Dye, Acid Orange 7, on TiO_2 Particles Using Visible Light," *Environ. Sci. Technol.*, vol. 30, no. 5, pp. 1660–1666, Apr. 1996, doi: 10.1021/es950655d.

[17] G. Williams, B. Seger, and P. V. Kamat, "TiO_2 -Graphene Nanocomposites. UV-Assisted Photocatalytic Reduction of Graphene Oxide," *ACS Nano*, vol. 2, no. 7, pp. 1487–1491, Jul. 2008, doi: 10.1021/nn800251f.

[18] L. Cai, H. Jiang, and L. Wang, "Enhanced photo-stability and photocatalytic activity of Ag_3PO_4 via modification with $BiPO_4$ and polypyrrole," *Appl. Surf. Sci.*, vol. 420, pp. 43–52, Oct. 2017, doi: 10.1016/j.apsusc.2017.05.135.

[19] M. Nandi, R. Gangopadhyay, and A. Bhaumik, "Mesoporous polyaniline having high conductivity at room temperature," *Microporous Mesoporous Mater.*, vol. 109, no. 1–

3, pp. 239–247, Mar. 2008, doi: 10.1016/j.micromeso.2007.04.049.

[20] X. Ma *et al.*, "Comparison of photocatalytic reaction-induced selective corrosion with photocorrosion: Impact on morphology and stability of Ag-ZnO," *Appl. Catal. B Environ.*, vol. 201, pp. 348–358, Feb. 2017, doi: 10.1016/j.apcatb.2016.08.029.

[21] P. Hait, R. Mehta, and S. Basu, "Advancing sustainable solutions: Harnessing polyaniline/BiOCl/GO ternary nanocomposites for solar-powered degradation of organic pollutant and photocatalytic hydrogen generation," *J. Clean. Prod.*, vol. 424, p. 138851, Oct. 2023, doi: 10.1016/j.jclepro.2023.138851.

[22] Z. Zhao, Y. Zhou, F. Wang, K. Zhang, S. Yu, and K. Cao, "Polyaniline-Decorated {001} Facets of $Bi_2O_2CO_3$ Nanosheets: In Situ Oxygen Vacancy Formation and Enhanced Visible Light Photocatalytic Activity," *ACS Appl. Mater. Interfaces*, vol. 7, no. 1, pp. 730–737, Jan. 2015, doi: 10.1021/am507089x.

[23] Z. Pei *et al.*, "Synergistic Effect in Polyaniline-Hybrid Defective ZnO with Enhanced Photocatalytic Activity and Stability," *J. Phys. Chem. C*, vol. 118, no. 18, pp. 9570–9577, May 2014, doi: 10.1021/jp5020143.

[24] E. Kang, "Polyaniline: A polymer with many interesting intrinsic redox states," *Prog. Polym. Sci.*, vol. 23, no. 2, pp. 277–324, 1998, doi: 10.1016/S0079-6700(97)00030-0.

[25] H. Huang, Y. Liu, S.-T. Lee, and Z. Kang, "Polymer (polyanilines) nanoparticles: a superior catalyst for hydrocarbon selective oxidation," *J. Mater. Chem.*, vol. 22, no. 2, pp. 337–340, 2012, doi: 10.1039/C1JM15098G.

[26] S. Dong, X. Ding, T. Guo, X. Yue, X. Han, and J. Sun, "Self-assembled hollow sphere shaped Bi_2WO_6/RGO composites for efficient sunlight-driven photocatalytic degradation of organic pollutants," *Chem. Eng. J.*, vol. 316, pp. 778–789, May 2017, doi: 10.1016/j.cej.2017.02.017.

[27] H. Yang *et al.*, "Green and facile synthesis of graphene nanosheets/$K_3PW_{12}O_{40}$ nanocomposites with enhanced photocatalytic activities," *Mater. Res. Bull.*, vol. 78, pp. 112–118, Jun. 2016, doi: 10.1016/j.materresbull.2016.02.038.

[28] S. Dong *et al.*, "Designing three-dimensional acicular sheaf shaped $BiVO_4$/reduced

graphene oxide composites for efficient sunlight-driven photocatalytic degradation of dye wastewater," *Chem. Eng. J.*, vol. 249, pp. 102–110, Aug. 2014, doi: 10.1016/j.cej.2014.03.071.

[29] C. Yu, S. Dong, J. Zhao, X. Han, J. Wang, and J. Sun, "Preparation and characterization of sphere-shaped $BiVO_4$/reduced graphene oxide photocatalyst for an augmented natural sunlight photocatalytic activity," *J. Alloys Compd.*, vol. 677, pp. 219–227, Aug. 2016, doi: 10.1016/j.jallcom.2016.03.249.

[30] J. Miao, A. Xie, S. Li, F. Huang, J. Cao, and Y. Shen, "A novel reducing graphene/polyaniline/cuprous oxide composite hydrogel with unexpected photocatalytic activity for the degradation of Congo red," *Appl. Surf. Sci.*, vol. 360, pp. 594–600, Jan. 2016, doi: 10.1016/j.apsusc.2015.11.005.

[31] Y. Lin *et al.*, "Highly Efficient Photocatalytic Degradation of Organic Pollutants by PANI-Modified TiO_2 Composite," *J. Phys. Chem. C*, vol. 116, no. 9, pp. 5764–5772, Mar. 2012, doi: 10.1021/jp211222w.

[32] C. Wang *et al.*, "Probing effective photocorrosion inhibition and highly improved photocatalytic hydrogen production on monodisperse PANI@CdS core-shell nanospheres," *Appl. Catal. B Environ.*, vol. 188, pp. 351–359, Jul. 2016, doi: 10.1016/j.apcatb.2016.02.017.

[33] Y. Xu *et al.*, "Conjugated conducting polymers PANI decorated $Bi_{12}O_{17}C_{l2}$ photocatalyst with extended light response range and enhanced photoactivity," *Appl. Surf. Sci.*, vol. 464, pp. 552–561, Jan. 2019, doi: 10.1016/j.apsusc.2018.09.103.

[34] S. Zaleski *et al.*, "Investigating Nanoscale Electrochemistry with Surface- and Tip-Enhanced Raman Spectroscopy," *Acc. Chem. Res.*, vol. 49, no. 9, pp. 2023–2030, Sep. 2016, doi: 10.1021/acs.accounts.6b00327.

[35] T. He and J. Yao, "Photochromism of molybdenum oxide," *J. Photochem. Photobiol. C Photochem. Rev.*, vol. 4, no. 2, pp. 125–143, Oct. 2003, doi: 10.1016/S1389-5567(03)00025-X.

[36] Y. S. Negi and P. V. Adhyapak, "DEVELOPMENT IN POLYANILINE

CONDUCTING POLYMERS," *J. Macromol. Sci. Part C Polym. Rev.*, vol. 42, no. 1, pp. 35–53, Jan. 2002, doi: 10.1081/MC-120003094.

[37] S. A. Ali and T. Ahmad, "Ultrafast Hole Trapping in Te-$MoTe_2$-$MoSe_2$/ZnO S-Scheme Heterojunctions for Photochemical and Photo-/Electrochemical Hydrogen Production," *Small*, vol. 20, no. 48, Nov. 2024, doi: 10.1002/smll.202403401.

[38] S. A. Ali, S. Majumdar, P. K. Chowdhury, S. M. Alshehri, and T. Ahmad, "Ultrafast Charge Transfer Dynamics in Multifaceted Quaternary Te–$MoTe_2$–MoS_2 /ZnO S-Scheme Heterostructured Nanocatalysts for Efficient Green Hydrogen Energy," *ACS Appl. Energy Mater.*, vol. 7, no. 17, pp. 7325–7337, Sep. 2024, doi: 10.1021/acsaem.4c01477.

[39] A. Chithambararaj and A. C. Bose, "Hydrothermal synthesis of hexagonal and orthorhombic MoO_3 nanoparticles," *J. Alloys Compd.*, vol. 509, no. 31, pp. 8105–8110, Aug. 2011, doi: 10.1016/j.jallcom.2011.05.067.

[40] Z. B. Siddique, S. Basu, and P. Basak, "Effect of Graphene Oxide Dispersed Natural Ester Based Insulating Oil on Transformer Solid Insulation," *IEEE Trans. Dielectr. Electr. Insul.*, vol. 29, no. 2, pp. 378–385, Apr. 2022, doi: 10.1109/TDEI.2022.3157926.

[41] P. Ahuja, S. K. Ujjain, I. Arora, and M. Samim, "Hierarchically Grown NiO-Decorated Polyaniline-Reduced Graphene Oxide Composite for Ultrafast Sunlight-Driven Photocatalysis," *ACS Omega*, vol. 3, no. 7, pp. 7846–7855, Jul. 2018, doi: 10.1021/acsomega.8b00765.

[42] H. Shin *et al.*, "Efficient Reduction of Graphite Oxide by Sodium Borohydride and Its Effect on Electrical Conductance," *Adv. Funct. Mater.*, vol. 19, no. 12, pp. 1987–1992, Jun. 2009, doi: 10.1002/adfm.200900167.

[43] M. Morales-Luna, S. A. Tomás, M. A. Arvizu, M. Pérez-González, and E. Campos-Gonzalez, "The evolution of the Mo^{5+} oxidation state in the thermochromic effect of MoO_3 thin films deposited by rf magnetron sputtering," *J. Alloys Compd.*, vol. 722, pp. 938–945, Oct. 2017, doi: 10.1016/j.jallcom.2017.06.149.

[44] M. Mihalev, C. Hardalov, C. Christov, M. Michailov, B. Ranguelov, and H. Leiste,

"Structural and adhesional properties of thin MoO_3 films prepared by laser coating," *J. Phys. Conf. Ser.*, vol. 514, p. 012022, May 2014, doi: 10.1088/1742-6596/514/1/012022.

[45] H. Liu, Y. Su, Z. Chen, Z. Jin, and Y. Wang, "Graphene sheets grafted three-dimensional $BiOBr_{0.2}I_{0.8}$ microspheres with excellent photocatalytic activity under visible light," *J. Hazard. Mater.*, vol. 266, pp. 75–83, Feb. 2014, doi: 10.1016/j.jhazmat.2013.12.013.

[46] S. Shahabuddin, N. M. Sarih, F. H. Ismail, M. M. Shahid, and N. M. Huang, "Synthesis of chitosan grafted-polyaniline/Co_3O_4 nanocube nanocomposites and their photocatalytic activity toward methylene blue dye degradation," *RSC Adv.*, vol. 5, no. 102, pp. 83857–83867, 2015, doi: 10.1039/C5RA11237K.

[47] K. Zhang, L. L. Zhang, X. S. Zhao, and J. Wu, "Graphene/Polyaniline Nanofiber Composites as Supercapacitor Electrodes," *Chem. Mater.*, vol. 22, no. 4, pp. 1392–1401, Feb. 2010, doi: 10.1021/cm902876u.

[48] G. Yang *et al.*, "Facile synthesis of MoO_3 nanodots self-assembled into hollow mesoporous silica: Enhancing efficient oxidative desulfurization and investigating reaction mechanism," *J. Environ. Chem. Eng.*, vol. 9, no. 5, p. 106309, Oct. 2021, doi: 10.1016/j.jece.2021.106309.

[49] A. Abdolahi, E. Hamzah, Z. Ibrahim, and S. Hashim, "Synthesis of Uniform Polyaniline Nanofibers through Interfacial Polymerization," *Materials (Basel).*, vol. 5, no. 8, pp. 1487–1494, Aug. 2012, doi: 10.3390/ma5081487.

[50] G. Gaikwad, P. Patil, D. Patil, and J. Naik, "Synthesis and evaluation of gas sensing properties of PANI based graphene oxide nanocomposites," *Mater. Sci. Eng. B*, vol. 218, pp. 14–22, Apr. 2017, doi: 10.1016/j.mseb.2017.01.008.

[51] C.-M. Chen, Q. Zhang, M.-G. Yang, C.-H. Huang, Y.-G. Yang, and M.-Z. Wang, "Structural evolution during annealing of thermally reduced graphene nanosheets for application in supercapacitors," *Carbon N. Y.*, vol. 50, no. 10, pp. 3572–3584, Aug. 2012, doi: 10.1016/j.carbon.2012.03.029.

[52] T. Szabó, E. Tombácz, E. Illés, and I. Dékány, "Enhanced acidity and pH-dependent surface charge characterization of successively oxidized graphite oxides," *Carbon N.*

Y., vol. 44, no. 3, pp. 537–545, Mar. 2006, doi: 10.1016/j.carbon.2005.08.005.

[53] Y. Fu and X. Wang, "Magnetically Separable $ZnFe_2O_4$ –Graphene Catalyst and its High Photocatalytic Performance under Visible Light Irradiation," *Ind. Eng. Chem. Res.*, vol. 50, no. 12, pp. 7210–7218, Jun. 2011, doi: 10.1021/ie200162a.

[54] P. Wang *et al.*, "One-step synthesis of easy-recycling TiO_2-rGO nanocomposite photocatalysts with enhanced photocatalytic activity," *Appl. Catal. B Environ.*, vol. 132–133, pp. 452–459, Mar. 2013, doi: 10.1016/j.apcatb.2012.12.009.

[55] Y.-H. Choi, "Molybdenum Oxide Nanoparticle Aggregates Grown by Chemical Vapor Transport," *Materials (Basel).*, vol. 15, no. 6, p. 2182, Mar. 2022, doi: 10.3390/ma15062182.

[56] A. Kumar, R. Kumar, and G. Pandey, "Synthesis, Characterization of Titania/Polyaniline/GO Nanocomposites, and Its Photocatalytic Activity Under UV-Visible Light," *Macromol. Symp.*, vol. 379, no. 1, Jun. 2018, doi: 10.1002/masy.201600192.

[57] M. Kgatle, K. Sikhwivhilu, G. Ndlovu, and N. Moloto, "Degradation Kinetics of Methyl Orange Dye in Water Using Trimetallic Fe/Cu/Ag Nanoparticles," *Catalysts*, vol. 11, no. 4, p. 428, Mar. 2021, doi: 10.3390/catal11040428.

[58] A. Kundu, S. Sharma, and S. Basu, "Modulated BiOCl nanoplates with porous g-C_3N_4 nanosheets for photocatalytic degradation of color/colorless pollutants in natural sunlight," *J. Phys. Chem. Solids*, vol. 154, p. 110064, Jul. 2021, doi: 10.1016/j.jpcs.2021.110064.

[59] Y. Xu *et al.*, "Enhanced long-wavelength light utilization with polyaniline/bismuth-rich bismuth oxyhalide composite towards photocatalytic degradation of antibiotics," *J. Colloid Interface Sci.*, vol. 537, pp. 101–111, Mar. 2019, doi: 10.1016/j.jcis.2018.10.109.

[60] P. S. Rao and E. Hayon, "Redox potentials of free radicals. IV. Superoxide and hydroperoxy radicals $\cdot O^{2-}$ and $\cdot HO^2$," *J. Phys. Chem.*, vol. 79, no. 4, pp. 397–402, Feb. 1975, doi: 10.1021/j100571a021.

[61] H. M. El-Bery, M. R. Salah, S. M. Ahmed, and S. A. Soliman, "Efficient non-metal based conducting polymers for photocatalytic hydrogen production: comparative study between polyaniline, polypyrrole and PEDOT," *RSC Adv.*, vol. 11, no. 22, pp. 13229–13244, 2021, doi: 10.1039/D1RA01218E.

[62] J. Ma, J. Dai, Y. Duan, J. Zhang, L. Qiang, and J. Xue, "Fabrication of PANI-TiO_2/rGO hybrid composites for enhanced photocatalysis of pollutant removal and hydrogen production," *Renew. Energy*, vol. 156, pp. 1008–1018, Aug. 2020, doi: 10.1016/j.renene.2020.04.104.

[63] A. Li, W. Zhu, C. Li, T. Wang, and J. Gong, "Rational design of yolk–shell nanostructures for photocatalysis," *Chem. Soc. Rev.*, vol. 48, no. 7, pp. 1874–1907, 2019, doi: 10.1039/C8CS00711J.

[64] J. Kröger *et al.*, "Interfacial Engineering for Improved Photocatalysis in a Charge Storing 2D Carbon Nitride: Melamine Functionalized Poly(heptazine imide)," *Adv. Energy Mater.*, vol. 11, no. 6, p. 2003016, Feb. 2021, doi: 10.1002/aenm.202003016.

[65] R. Kumar, R. El-Shishtawy, and M. Barakat, "Synthesis and Characterization of Ag-Ag_2O/TiO_2@polypyrrole Heterojunction for Enhanced Photocatalytic Degradation of Methylene Blue," *Catalysts*, vol. 6, no. 6, p. 76, May 2016, doi: 10.3390/catal6060076.

[66] L. Zhang, R. Jamal, Q. Zhao, M. Wang, and T. Abdiryim, "Preparation of PEDOT/GO, PEDOT/MnO_2, and PEDOT/GO/MnO_2 nanocomposites and their application in catalytic degradation of methylene blue," *Nanoscale Res. Lett.*, vol. 10, no. 1, p. 148, Dec. 2015, doi: 10.1186/s11671-015-0859-6.

[67] Y. Yang, Z. Ma, L. Xu, H. Wang, and N. Fu, "Preparation of reduced graphene oxide/meso-TiO_2/AuNPs ternary composites and their visible-light-induced photocatalytic degradation n of methylene blue," *Appl. Surf. Sci.*, vol. 369, pp. 576–583, Apr. 2016, doi: 10.1016/j.apsusc.2016.02.078.

[68] R. Kumar *et al.*, "Facile route to a conducting ternary polyaniline@TiO_2/GN nanocomposite for environmentally benign applications: photocatalytic degradation of pollutants and biological activity," *RSC Adv.*, vol. 6, no. 112, pp. 111308–111317, 2016, doi: 10.1039/C6RA24079H.

[69] R. Kumar, "Mixed phase lamellar titania-titanate anchored with Ag_2O and polypyrrole for enhanced adsorption and photocatalytic activity," *J. Colloid Interface Sci.*, vol. 477, pp. 83–93, Sep. 2016, doi: 10.1016/j.jcis.2016.05.039.

[70] R. A. Rather, S. Singh, and B. Pal, "Core–shell morphology of Au-TiO_2 @graphene oxide nanocomposite exhibiting enhanced hydrogen production from water," *J. Ind. Eng. Chem.*, vol. 37, pp. 288–294, May 2016, doi: 10.1016/j.jiec.2016.03.039.

[71] T. Jafari, E. Moharreri, A. Amin, R. Miao, W. Song, and S. Suib, "Photocatalytic Water Splitting-The Untamed Dream: A Review of Recent Advances," *Molecules*, vol. 21, no. 7, p. 900, Jul. 2016, doi: 10.3390/molecules21070900.

[72] A. A. Murashkina, T. V. Bakiev, Y. M. Artemev, A. V. Rudakova, A. V. Emeline, and D. W. Bahnemann, "Photoelectrochemical Behavior of the Ternary Heterostructured Systems CdS/WO_3/TiO_2," *Catalysts*, vol. 9, no. 12, p. 999, Nov. 2019, doi: 10.3390/catal9120999.

Chapter 4

PANI/GO/MoS_2 Nanocomposites for Efficient Photocatalytic Pollutant Degradation and H_2 Generation

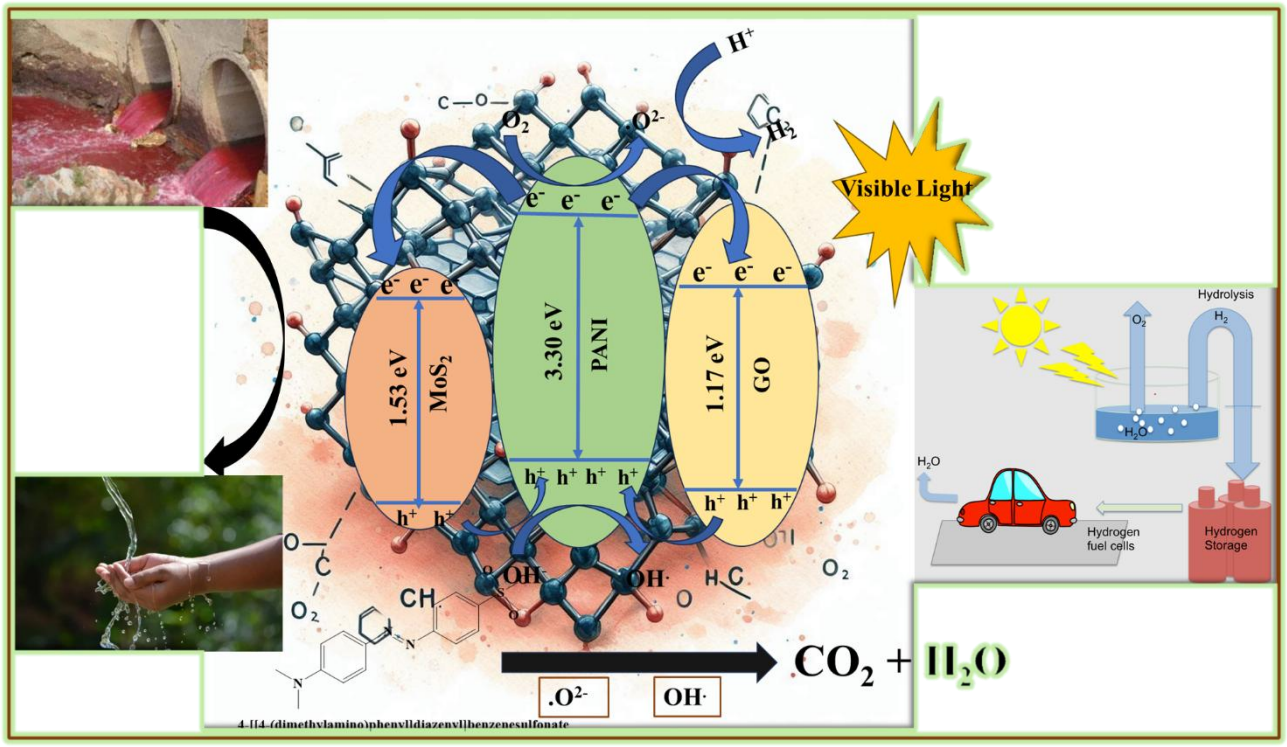

Highlights

- Fabrication of different mole ratios of Polyaniline/GO/MoS_2 ternary nanocomposite.
- Photocatalysts efficacy tested by degradation of methyl orange and H_2 production from water splitting.
- Photocatalytic elimination of methyl orange (99 %, rate constant~ 0.03 min^{-1}) was observed under LED light.
- The nanocomposite produced 1500 ppm of hydrogen gas in the presence of a sacrificial agent (MeOH) with an AQE of 26%.

4.1. Introduction:

Semiconductor-based photocatalysis has gained prominence for solar fuel production and pollutant degradation, driven by urgent energy and environmental challenges [1][2][3]. The discharge of dye waste from industries like paper, leather, and nylon production significantly affects aquatic life by causing water pollution[4]. Reducing the coloration of these dyes is a crucial step in wastewater treatment prior to environmental discharge due to their synthetic origin, intricate chemical composition, and potential toxicity, as well as their carcinogenic or explosive properties[5]. The rapid exhaustion of fossil fuels like coal, natural gas, and oil, along with rising political and environmental concerns, has heightened the need for renewable energy from sustainable sources for long-term solutions[6]. This has led to numerous efforts in investigating innovative approaches to advancing renewable energy technologies. In recent years, transforming solar energy into chemical energy as solar fuels like hydrogen, methanol, and methane has emerged as a promising solution[7] [8]. This approach aims to lessen our heavy reliance on depleting fossil resources and address future energy and environmental challenges. Hydrogen (H_2) plays a vital role as a superior energy carrier essential for promoting a low-carbon emission economy. While hydrogen (H_2) may pose challenges related to safe transportation, it possesses numerous significant advantages: (i) In addition to its environmental friendliness, hydrogen (H_2) is also non-toxic, setting it apart from most other fuel sources; (ii) With its abundant resources, hydrogen (H_2) is the most plentiful element obtainable from a diverse array of sources such as alcohol and biomass; (iii) The primary benefit of using hydrogen energy is that it produces almost no harmful emissions when burned; (iv) Hydrogen energy is a highly efficient fuel source, outperforming traditional energy sources by producing greater energy per unit of fuel [9][10][11]. Following the initial report by Honda and Fujishima on TiO_2 electrodes, significant research has focused on photocatalytic and photoelectrochemical (PEC) water splitting to enhance hydrogen fuel production and support the hydrogen economy[8]. Although TiO_2 has been the most extensively studied photocatalyst to date, its large energy gap of 3.2 eV has limited its ability to effectively utilize sunlight[8]. Given these intrinsic benefits, further research should focus on developing PANI-based composites to enhance photocatalytic materials. Polyaniline (PANI) is a conductive polymer characterized by a delocalized π-π conjugated structure[12]. Its benzenoid and quinonoid units exhibit multiple redox states along with various other intriguing properties. Furthermore, PANI is highly suitable for large-scale applications because of its excellent conductivity, outstanding

environmental stability, and ease of preparation[13]. A stable matrix can enhance the durability of the resulting composite.

On the other hand, graphene oxide, with its extensive surface area and unique optical, transport, mechanical, and electronic properties, has become a strong candidate for various applications, including hydrogen production, and catalytic activities[14]. It provides a two-dimensional (2D) surface for catalyst deposition and enhances dye adsorption capacity through π-π interactions between the dye and the aromatic regions of graphene. Moreover, PANI serves as an electron donor and a hole conductor, while graphene functions as an electron acceptor when exposed to visible or UV light[15]. Thus, integrating them with inorganic materials, particularly transition metal oxides or sulfides, enhances the degradation rate by leveraging synergistic effects that reduce recombination losses. The photocatalytic properties of various transition-metal oxides, such as NiO, BiOCl, ZnO, MnO_2, TiO_2, MoO_3, and Cu_2O, have been analyzed [16][17][18]. An RGO/PANI/Cu_2O hydrogel synthesized by Miao et al. demonstrated Congo red degradation within 20 minutes, reflecting an improvement in the composite's performance[19]. Zhang et al. showed that a composite of poly(3,4-ethylenedioxythiophene) combined with graphene and MnO_2 exhibited catalytic activity, as it successfully degraded methylene blue (MB) after 7 hours[20]. Pendiselvi et al. explored the use of graphitic carbon nitride as a mechanical support, achieving methylene blue (MB) degradation in 80 minutes[21]. Moreover, in-situ polymerizing aniline with graphene and $ZnFe_2O_4$ creates a catalyst that greatly enhances the degradation efficiency of rhodamine B [22]. Additionally, the incorporation of gold nanoparticles into a ternary composite with graphene and TiO_2 has been investigated, demonstrating complete methylene blue (MB) degradation after 250 minutes[23]. Additionally, many of these photocatalysts face challenges such as the limited photo response of TiO_2 to visible light, the high expense of Ag or Au used as key components in the composites, and prolonged degradation times. Nevertheless, MoS_2 has a layered configuration characterized by a hexagonal pattern of Mo and S atoms, resulting in S–Mo–S bonding[24]. Furthermore, the layered structure of bulk MoS_2 allows for easy intercalation of foreign atoms between its layers. Additionally, the layered arrangement of bulk MoS_2 enables the easy intercalation of foreign atoms between its layers [25]. In summary, the combined effect of the ternary composite enhances the nanocomposite's photocatalytic activity, establishing it as a leading photocatalyst.

This study focuses on developing a new ternary composite of polyaniline (PANI), molybdenum disulfide (MoS_2), and graphene oxide (GO) to evaluate its effectiveness in degrading methyl orange (MO) dye through photocatalysis under the LED light. The synthesized composites were thoroughly characterized using XRD, XPS, FTIR, FESEM, and UV-DRS techniques. Various photocatalytic factors, including catalyst dosage, illuminated area, solution pH, and the effect of scavengers, were investigated. Degradation intermediates and final products were analyzed using GC/MS, and possible mechanisms were explored for better understanding. Additionally, the photocatalyst's potential for green hydrogen generation via photocatalytic water splitting was assessed under various conditions—sacrificial agent presence, acidic, basic, and neutral environments. The apparent quantum yield (AQE%) for water splitting was also calculated, demonstrating the catalyst's ability to absorb photons and drive chemical reactions that degrade organic pollutants and dissociate water into H_2 and O_2.

4.2. Experimental section:

The following chemicals were used for the synthesis of the materials: graphite fine powder (98%, LOBA CHEMIE), aniline (99%, LOBA CHEMIE), hydrochloric acid (36%, LOBA CHEMIE), ammonium persulfate (98%, SDFCL), thiourea (99.5%-100%, LOBA CHEMIE), Ammonium Molybdate (98%, LOBA CHEMIE), potassium permanganate (99%, LOBA CHEMIE), sodium nitrite (97%, LOBA CHEMIE), and hydrogen peroxide (30% solution, RANKEM). Methyl Orange was purchased from CDH Chemical.

4.2.1. Synthesis of MoS_2 and ternary nanocomposite:

Polyaniline (PANI) and graphene oxide (GO) are synthesized by the oxidative polymerization method and modified Hummers' method, respectively, as outlined in our prior research [26]. For the synthesis of MoS_2, ammonium molybdate tetrahydrate and thiourea were initially dissolved in 20 ml of ethylene glycol; then the mixture was stirred for one hour. The mixture was then sonicated for one hour to ensure complete dispersion of the precursor. Then the prepared solution was heated for 30 min at 180°C temperature in a microwave synthesizer (Biotage initiator $^+$).

A 1:1 GO/MoS_2 (wt./wt.%) composite was first synthesized using the MoS_2 precursor through an in-situ method. Next, different weight percentages of the 1:1 GO/MoS_2 composite were used to form a ternary composite via oxidative polymerization. Initially, 1:1 GO/MoS_2 and aniline

were combined in a 2M HCl solution, stirred for one hour, and then sonicated for another hour. Next, ammonium persulfate (APS) was added gradually and the mixture was stirred overnight to facilitate polymerization. The resulting solution was rinsed with 2M HCl and water, then dried at 60°C for 24 hours. Thus, the PANI/GO/MoS_2 composites were prepared in different weight ratios (1, 2.5, 4) and were designated as 1PGMS, 2.5PGMS, and 5PGMS, respectively.

4.2.2. Techniques for characterization:

The as-prepared nanocomposites were characterized by various characterization techniques. The ultraviolet-visible absorption spectra of the synthesized materials were measured utilizing a UV-vis spectrophotometer instrument (Shimadzu UV 2600). Photoluminescence spectra were recorded utilizing a spectrofluorometer instrument (Shimadzu RF-6000). The shape of the prepared composite was analyzed using field emission scanning electron microscopy (FESEM, JEOL). The functional groups present in the materials were identified using Fourier transform infrared (FTIR) spectroscopy (Shimadzu IRTracer-100). The X-ray Photoelectron Microscopy (XPS) analysis was performed using a monochromatic aluminium source, specifically Al ka radiation, on an Omicron ESCA instrument with an energy of 1486.7 eV. Brunauere-Emmette-Teller (BET) method and Barrette-Joynere-Halenda (BJH) method were done by Belsorp Mini II instrument. The degraded products and possible Intermediate by-products of the degradation product were analysed by Gas Chromatography Mass Spectrometry (GC/MS, Bruker SHS-40). The amount of hydrogen produced by photocatalytic water splitting was measured using GC-TCD (nucon 5765).

4.2.3. Photocatalysis experiments:

4.2.3.1. Assessment of photocatalytic degradation effectiveness:

For photocatalytic degradation assessment, 4 mg of the photocatalyst was mixed with 20 mL of a 20-ppm methyl orange (MO) solution. The mixture was stored in the dark for 120 minutes to achieve equilibrium. Subsequently, the MO solution was exposed to photodegradation under illumination from a 40W LED lamp in a photocatalytic reactor, with continuous stirring. MO concentrations were monitored using a UV-vis spectrophotometer, and the degradation percentage of MO was determined using the formula of **equation 2.5 (Chapter 2)**. The degree of mineralization was calculated using the **equation 3.1 (Chapter 3)**.

A GC-MS system identified the degradation products of MO, using m/z values to deduce their chemical structures, where 'm' is the molecular mass and 'z' is the charge number. The analysis used aqueous solutions with 0.1% dichloromethane (DCM) as the mobile phase.

4.2.3.2. Hydrogen production through photocatalysis:

A 2 mg photocatalyst was mixed into 20 mL of an aqueous solution containing 1 mL of MeOH as a sacrificial agent. The experiment was performed under four varying conditions: without a sacrificial agent, in an acidic medium, in a basic medium, and with a sacrificial agent in a nitrogen-filled environment. The container was securely closed with an airtight lid. The analysis of the H_2 photoproduct was performed using gas chromatography (GC) with a thermal conductivity detector (TCD), employing nitrogen as the carrier gas. This was conducted in a photocatalytic reactor equipped with a 40 W Phillips LED lamp serving as the light source. Throughout the photocatalytic process, a magnetic stirrer was used to keep the system in constant motion. The formula form **equation 2.15 (Chapter 2)** was used to calculate the apparent quantum efficiency (AQE).

4.3. Results and discussion:

4.3.1. Characterization of the synthesized photocatalyst:

4.3.1.1. Analysis of spectral properties:

X-ray diffractograms in the 10° to 80° range were used to analyze the phase composition and crystalline structure of the prepared samples **(Fig 4.1a)**. The XRD analysis reveals peaks at 2θ = 14.92° (121), 20.48° (310), and 25.33° (003), indicating the presence of PANI[14]. The peak at 25.33° (003) particularly highlights the polymeric nature of PANI. Additionally, the presence of graphitic graphene oxide (GO) is evidenced by the peaks observed at 11.23° (002) and 42.16° (100)[27]. The diffraction peaks observed at 13.01°, and 28.1° (2θ) correspond to the lattice planes (002), and (004) of crystalline MoS_2, respectively, according to JCPDS card no. 65-0160. Analysis of the XRD patterns for the nanocomposites 1PGMS, 2.5PGMS, and 4PGMS shows that peaks attributed to MoS_2, GO, and PANI are still present. This indicates that these components have been effectively integrated into the nanocomposite structures. In the nanocomposite, the broad peak at 2θ = 14.54° could be attributed to the d(121) spacing of PANI, the d(002) spacing of GO, and the d(002) spacing of MoS_2. Using the Scherrer equation,

the crystallite sizes (D) are determined to be 40.4 nm for MoS_2, 132.21 nm for PANI, 101.6 nm for g-GO, and 108.32 nm for 2.5PGMO.

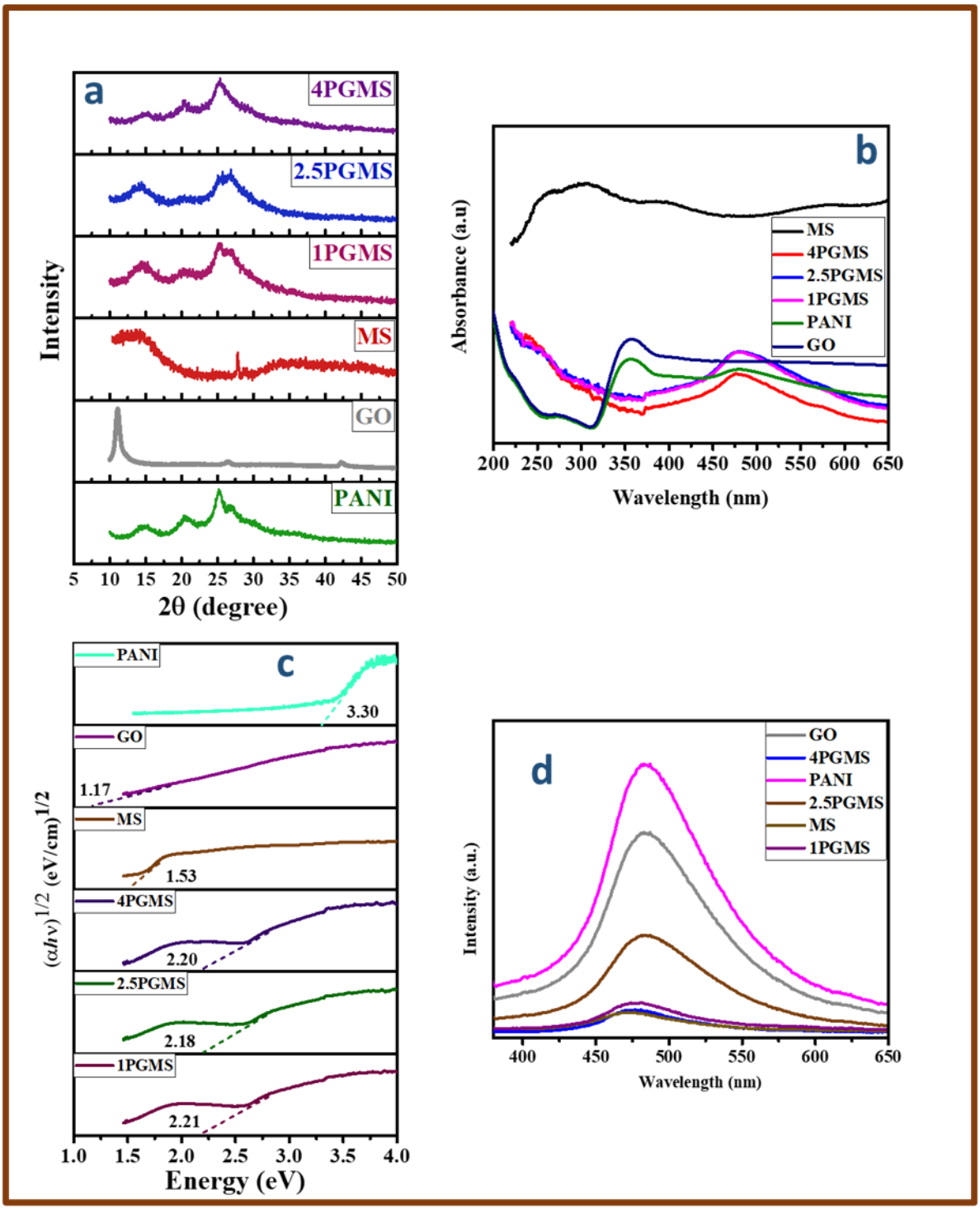

Fig 4.1: (a) XRD pattern, (b) UV-Vis DRS spectra, (c) Tauc's plot, and (d) PL spectra of GO, PANI, MS, 1PGMS, 2.5PGMS, and 4PGMS.

X-ray photoelectron spectroscopy (XPS) was used to examine the chemical composition and phase state of the synthesized ternary nanocomposite (2.5PGMS). **Fig 4.3a** of the XPS survey spectrum conclusively confirmed the presence of elements Mo, C, N, S, and O within the ternary composite. Gaussian fitting was employed to deconvolute the elemental spectra of Mo 3d, C 1s, N 1s, S 2p, and O 1s, allowing for a more detailed examination of the elemental composition and chemical states. **Fig 4.3b** shows the C 1s spectrum with four distinct binding energies. The peak at 283.90 eV corresponds to non-oxygenated carbon, including C–H and C–C bonds. The 284.7 eV peak signifies presence of graphitic carbon. The 285.5 eV peak indicates nitrogenous carbon, with bonds like C–N. The peak at 288.1 eV corresponds to the C=O bond[28]. **Fig 4.3d** displays three distinct peaks in the N 1s spectrum, each corresponding to different nitrogen environments. The peak at 398.8 eV represents quinoid amine, the 399.1 eV peak is linked to benzenoid amine, and the 399.3 eV peak indicates the presence of a nitrogen cationic radical ($N^{+\cdot}$)[29]. **Fig 4.3c** shows the O 1s spectrum with two main peaks at 531 eV and 532.3 eV. These peaks correspond to Mo–O bonds in the MoO_3 and hydroxyl groups on the composite's surface, respectively[30]. For Mo 3d spectrum, two peaks are observed at 232.2 eV and 235.6 eV **(Fig 4.3e)**. At binding energy 232.2 eV for Mo^{4+} $3d_{3/2}$ and the binding energy 235.6 is for Mo^{6+} oxidation state[31]. The S 2p spectra at 159 eV and 164 eV for $S^{2-}2p_{3/2}$ and $S^{2-}2p_{1/2}$, respectively **(Fig 4.3f)**. The peak at 159.2 eV is attributed to C-S-H, while the peak at 164.4 eV is assigned to the N-S-H bond[32]. Additionally, a peak at 168.6 eV indicates an S–O bond, indicating partial oxidation of the S edges in MoS_2[31]. From the peak of S-O bond, we can conclude the formation of bond of oxygenated graphene oxide and MoS_2. This highlights oxygen's crucial role in the composite's bonding network, contributing to interactions and structural stability.

FTIR analysis identifies distinct absorption peaks linked to specific vibrational modes and chemical groups **(Fig 4.2)**. The 1536 cm^{-1} peak corresponds to C=C stretching in the benzenoid ring, while the 1390 cm^{-1} peak indicates C-N bond stretching. The 1265 cm^{-1} signal reveals the presence of a protonated C-N group[33][34]. Additionally, a peak near 776 cm^{-1} suggests electron delocalization in the polymer matrix. In the graphene oxide (GO) spectrum, distinctive peaks appear. Around 3500 cm^{-1} peak corresponds to O-H bond stretching, while the 1717 cm^{-1} peak indicates C=O stretching in carboxylic groups. The 1615 cm^{-1} peak represents O-H bending and aromatic C=C stretching, and the 1385 cm^{-1} peak suggests the presence of tertiary

C–OH bonds[35][36][37]. Finally, the 1220 cm^{-1} peak confirms the existence of epoxy C–O groups. Broad absorption bands at 501 cm^{-1}, 695 cm^{-1}, and 1623 cm^{-1} are associated with MoS_2[38]. Peaks at 501 cm^{-1} correspond to S–S bonds[39]. Additionally, the band around 3100 cm^{-1} is associated with O–H group vibrations.

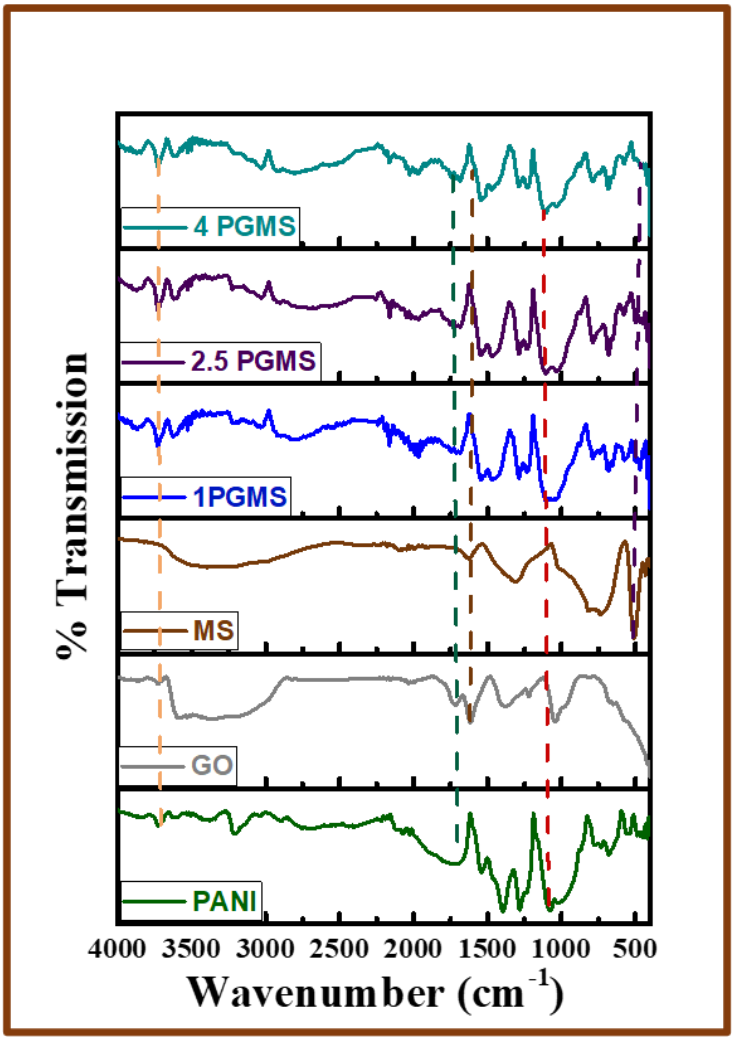

Fig 4.2: FTIR of PANI, GO, MoS_2, 1PGMS, 2.5PGMS, and 4PGMS.

A photocatalyst's light absorption capability is essential for its photocatalytic activity. **Fig 4.1b** shows the UV–vis absorption spectra of the different as-synthesized photocatalysts. MoS_2 nanospheres absorb strongly in the UV range (250−400 nm), whereas the ternary nanocomposites (PGMS) exhibit a wider absorption across visible spectra. The broader absorption is due to PANI, which sensitizes the photocatalysts to visible light. Additionally, the color change from black in MoS_2 to dark green in the ternary nanocomposites indicates successful PANI integration and enhanced visible light absorption **(Fig 4.1b)**. Tauc's formula,

$(\alpha h\nu)^{(1/n)} = A\,(h\nu - E_g)$, calculates a semiconductor's energy gap. In this formula, hν is photon energy, E_g is the bandgap, A is a constant, and α is the coefficient of light absorption. The exponent "n" reflects the electronic transition type, where n = 1/2 signifies a direct transition. In this study, the bandgap energy (Eg) was determined from plots of $(\alpha h\nu)^{1/2}$ versus Eg. As shown in **Fig 4.1c**, the Eg values are 1.53 eV for MoS_2, 2.18 eV for 2.5PGMS, 2.21 eV for 1PGMS, and 2.20 eV for 4PGMS.

Photoluminescence (PL) spectra are commonly used to evaluate processes like carrier capture, movement, transport, isolation, and recombination. **Fig 4.1d** shows the PL emission spectra for MoS_2, PANI, GO, and PGMS composites, highlighting a luminescent peak around 452 nm. Notably, the PL emission intensity of PGMS composites is significantly lower compared to pure MoS_2, PANI, and GO. This reduced fluorescence indicates the potent isolation of light-generated pairs of electrons and holes within the composite structure. Efficient management of electron-hole pairs is crucial for improving photocatalytic degradation. Effective separation of these pairs prevents recombination, allowing for better utilization in photocatalytic reactions.

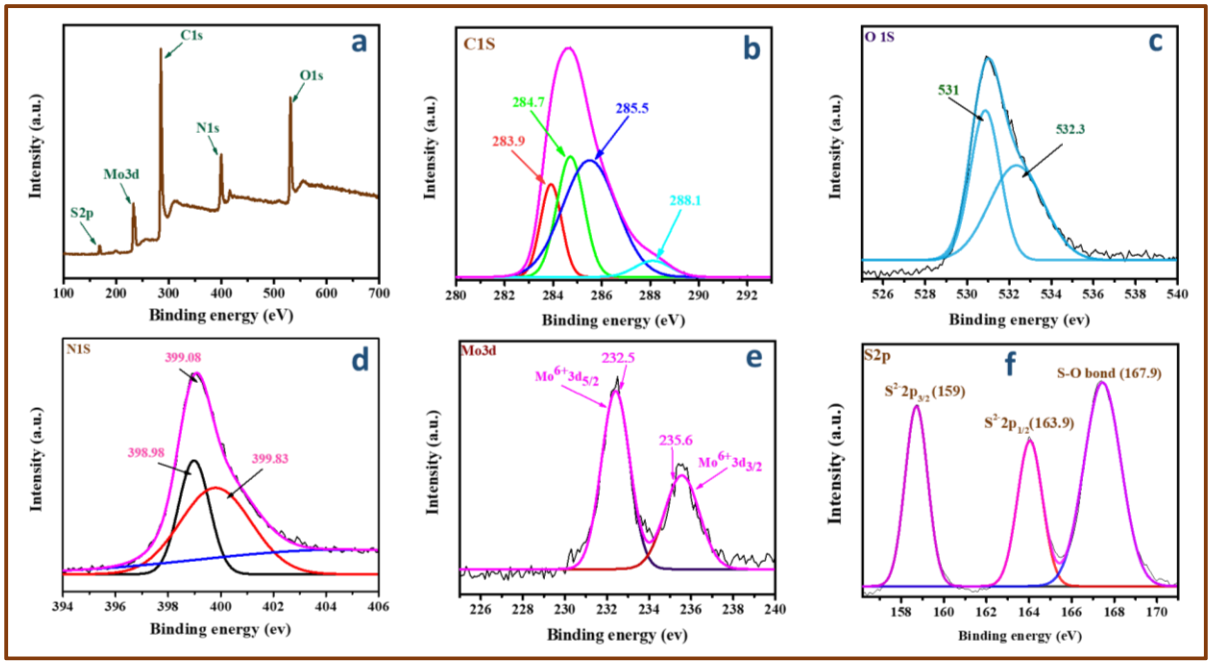

Fig 4.3: (a) XPS survey spectrum of 2.5PGMS and core level spectrum of (b) C 1s, (c) O 1s, (d) N 1s, (e) Mo 3d, and (f) S 2p.

4.3.1.2. EIS analysis:

EIS measurements were utilized to evaluate the charge transfer efficiency in PANI, GO, MS and its nanocomposite **(Fig 4.4)**. In a Nyquist plot, a smaller arc radius typically indicates improved interfacial charge transport. The incorporation of PANI, GO, and MS co-catalysts resulted in a reduced arc radius, suggesting lower electron transfer resistance and decreased recombination of electron-hole pairs, ultimately enhancing interfacial charge carrier transport. Among the tested materials, the ternary 2.5PGMS composite exhibited the smallest arc radius, demonstrating its superior conductivity, faster charge migration, and more effective separation of photo-induced carriers. These EIS results are consistent with the PL analysis, underscoring the critical role of the ternary 2.5PGMS hybrid in optimizing charge separation.

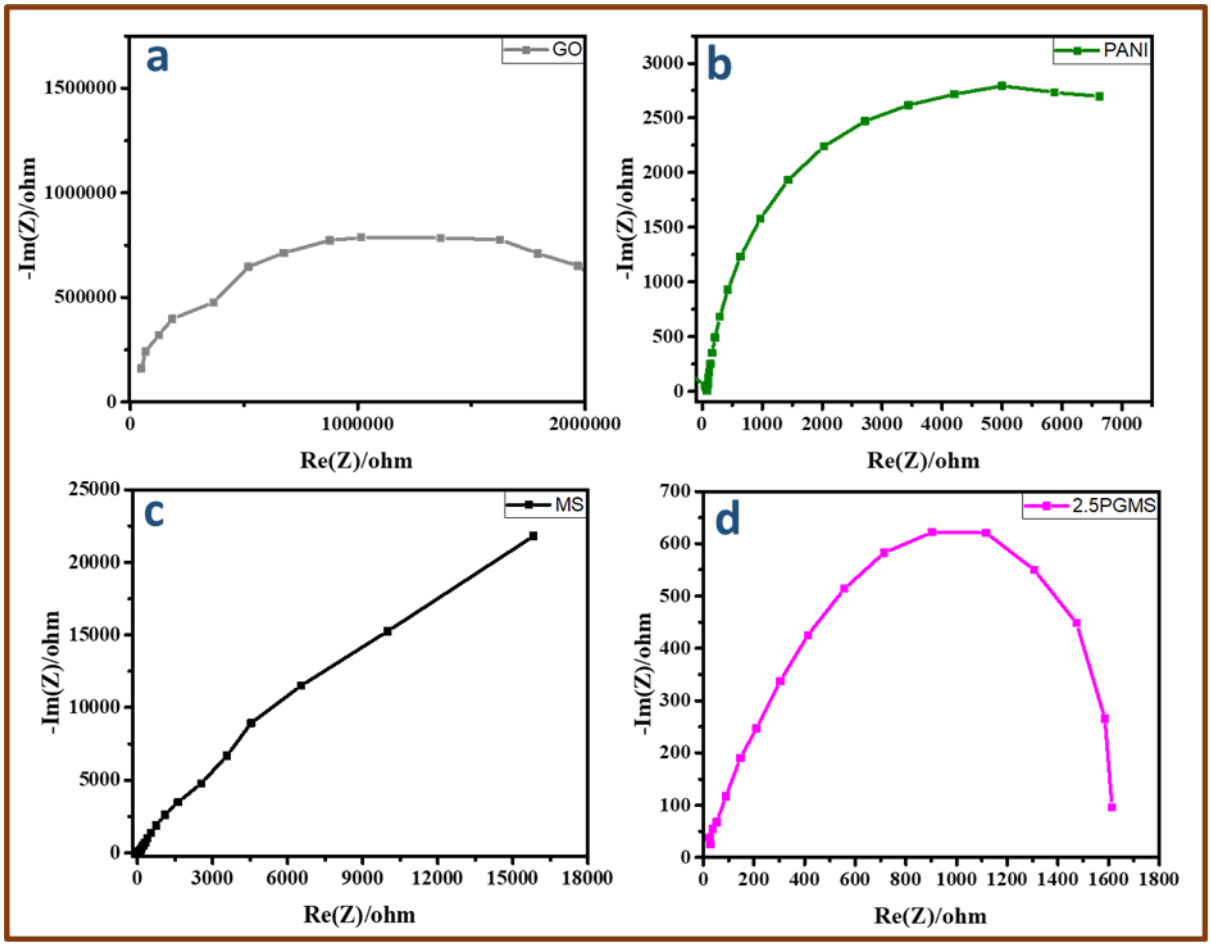

Fig 4.4: EIS plot of (a) GO, (b) PANI, (c) MS, and (d) 2.5PGMS.

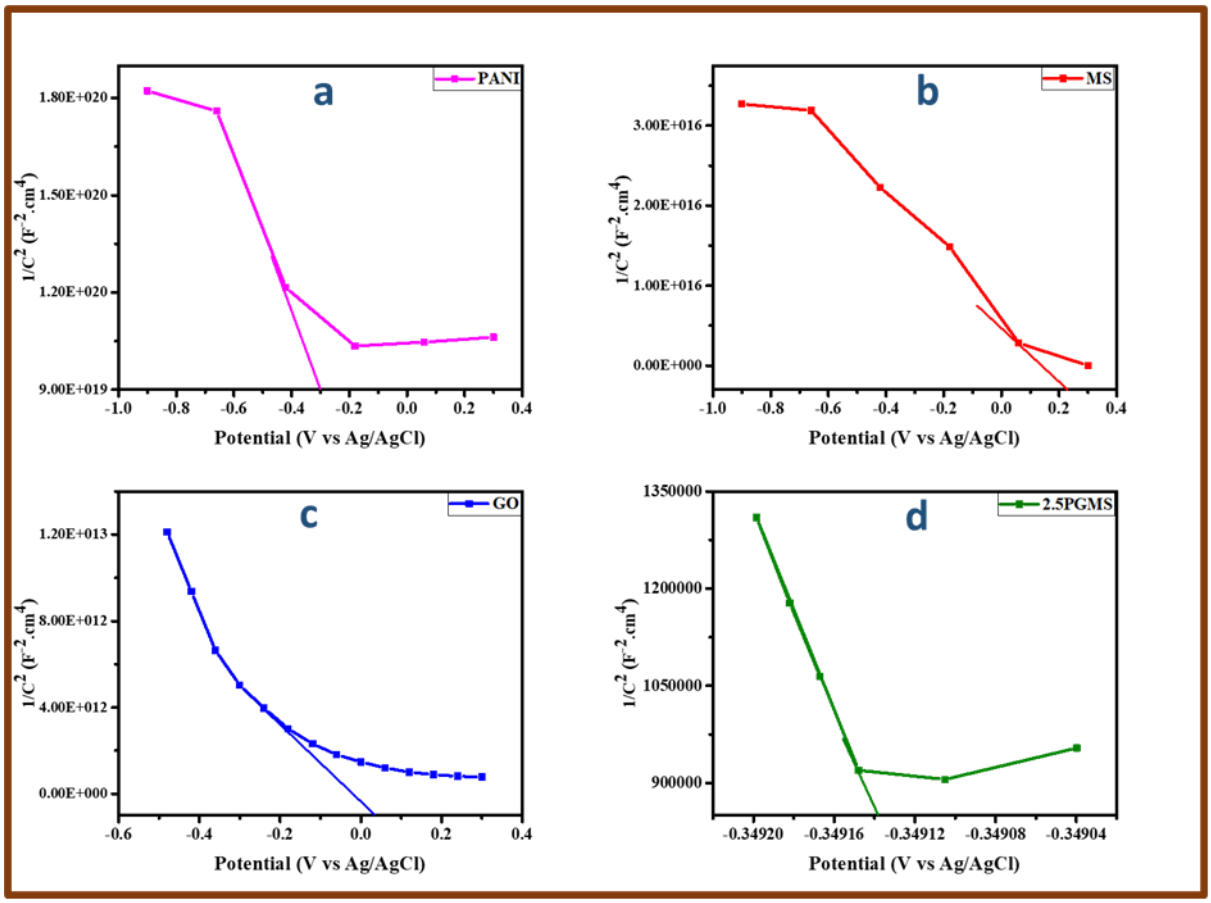

Fig 4.5: Mott-Schottky plot of (a) PANI (b) MS (c) GO (d) 2.5PGMS.

4.3.1.3. Surface properties:

FESEM investigation was conducted to understand the arrangement properties of the synthesized composite. FESEM images of MoS_2, PANI, GO, and the 1PGMS composite are depicted in **Fig 4.6 (a-d)**. The MoS_2 sample exhibited nanospheres ranging from 35 to 55 nm in diameter, while PANI displayed a fibrous, porous morphology. GO's exfoliated and well-agglomerated layers were observed, likely attributable to oxygenated surface functional groups. In the nanocomposite, GO agglomerated with PANI, and MoS_2 nanospheres were visible in the mixture **(Fig 4.6d)**. The FESEM images confirmed the existence of polyaniline, GO, and MoS_2, indicating the successful establishment of heterojunctions. Energy dispersive spectroscopy (EDS) analysis, shown in **Fig 4.7**, confirmed the presence of C, N, Mo, O, and S in the nanocomposite

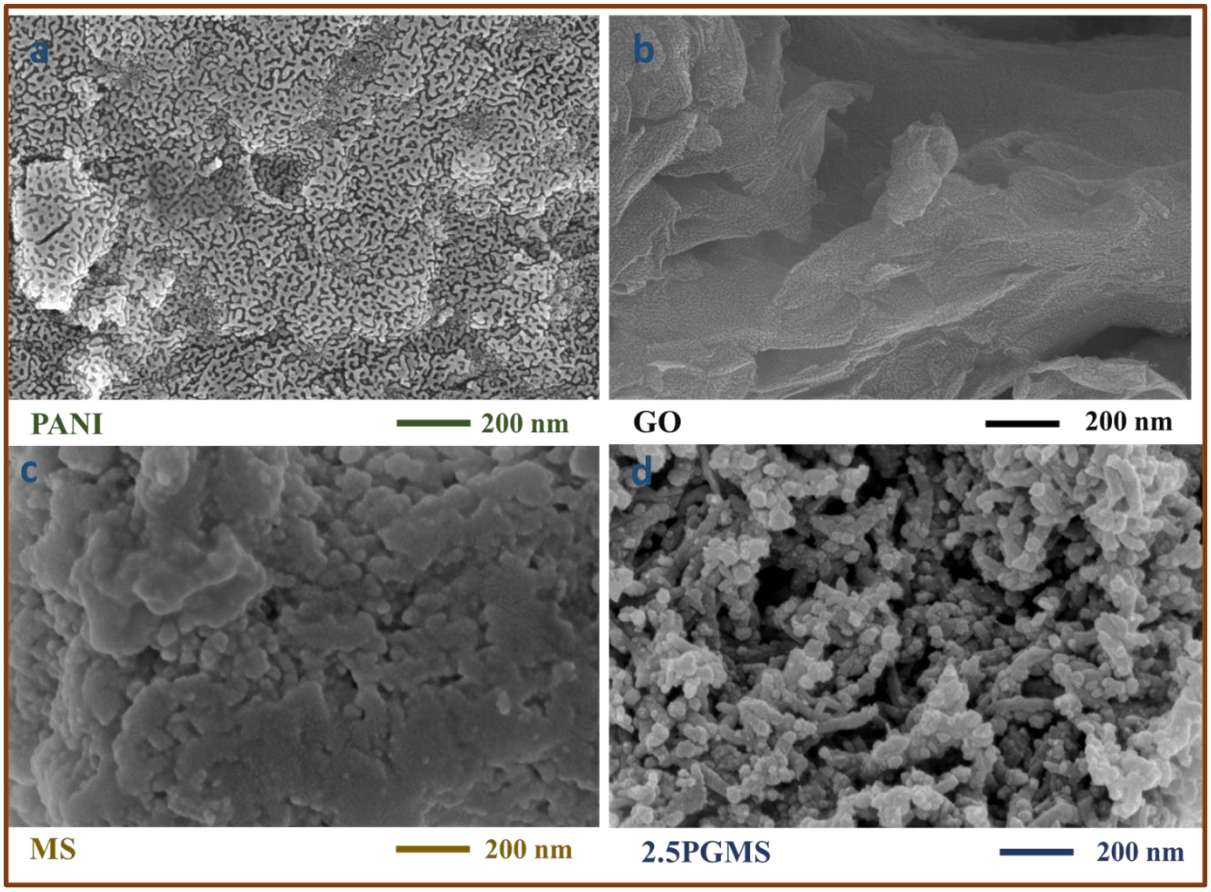

Fig 4.6: FESEM image of (a) PANI, (b) GO, (c) MS, and (d) 2.5 PGMS.

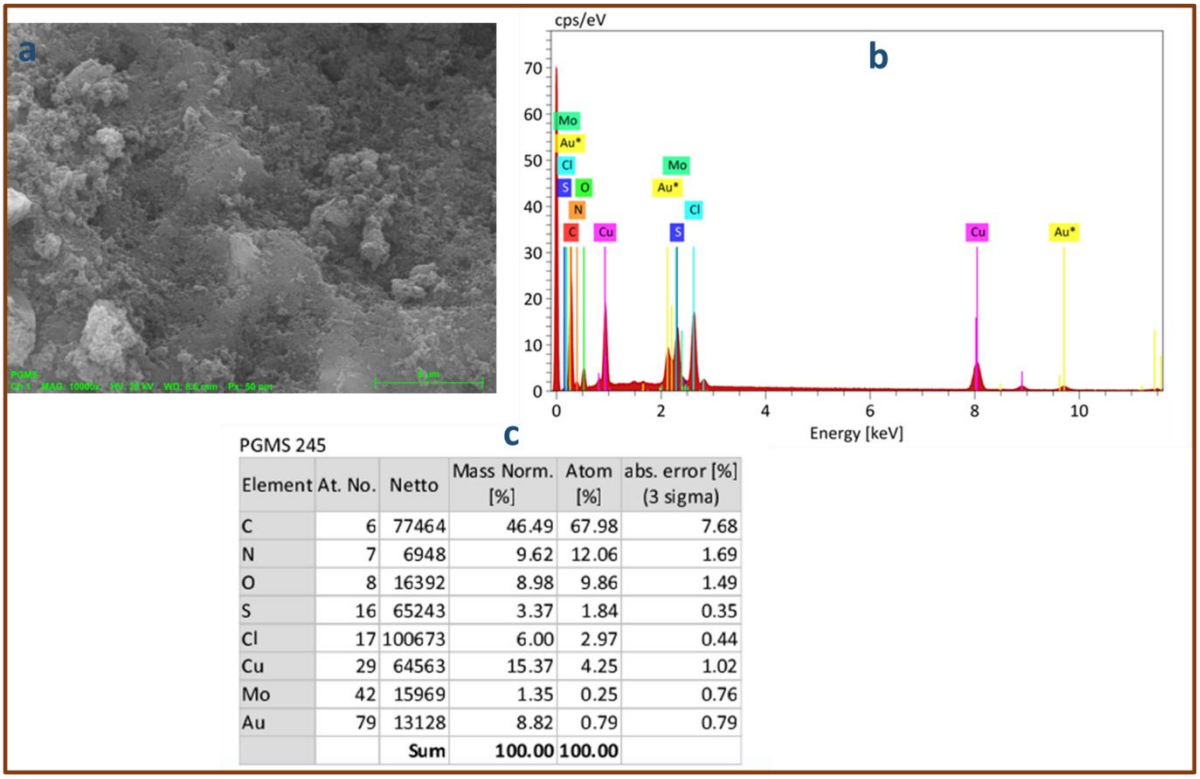

Element	At. No.	Netto	Mass Norm. [%]	Atom [%]	abs. error [%] (3 sigma)
C	6	77464	46.49	67.98	7.68
N	7	6948	9.62	12.06	1.69
O	8	16392	8.98	9.86	1.49
S	16	65243	3.37	1.84	0.35
Cl	17	100673	6.00	2.97	0.44
Cu	29	64563	15.37	4.25	1.02
Mo	42	15969	1.35	0.25	0.76
Au	79	13128	8.82	0.79	0.79
		Sum	**100.00**	**100.00**	

Fig 4.7: (a) FESEM image of 2.5PGMS (b,c) EDS spectrum of 2.5PGMS.

The specific surface area of the synthesized nanocomposites was evaluated to analyze their surface characteristics in detail. **Fig 4.8 and 4.9** present the nitrogen adsorption-desorption isotherms, which exhibit a type IV Langmuir isotherm with distinct H1 hysteresis loops for all the composites, as well as for individual components such as MoS_2, PANI, and GO. The presence of these hysteresis loops confirms the mesoporous nature of the materials, indicating well-defined pore structures.

The pore size distribution was determined using the Barrett-Joyner-Halenda (BJH) method, as depicted in **Fig 4.8 and 4.9**. **Table 4.1** provides a comparative analysis of surface area and pore volume, showing that pure PANI possesses a relatively high surface area and pore volume. However, the synthesized composites exhibit even higher surface areas than pure PANI, GO, and MoS_2, highlighting their enhanced porosity and surface characteristics.

Notably, the PGMS composites follow an increasing trend in surface area, with values recorded as 35.1 m^2/g for 1PGMS, 43 m^2/g for 4PGMS, and 52.6 m^2/g for 2.5PGMS. The superior photocatalytic performance of the 2.5PGMS composite is attributed to its higher surface area, which enhances pollutant adsorption and provides more active sites for catalytic reactions. This increased active surface area plays a crucial role in improving hydrogen production through water splitting, further confirming the composite's effectiveness in photocatalytic applications.

Table 4.1: BET-specific surface area, total pore volume, and average pore diameter.

Photocatalyst	**Specific Surface Area (m^2/g)**	**Total Pore Volume (cm^3/g)**	**Average Pore Diameter (nm)**
PANI	18.3	0.0203	4.5
GO	10.6	0.034	5.3
MS	7.3	0.0073	4.2
1PGMS	35.1	0.044	5.0
2.5PGMS	52.6	0.0841	6.4
4PGMS	43	0.052	4.8

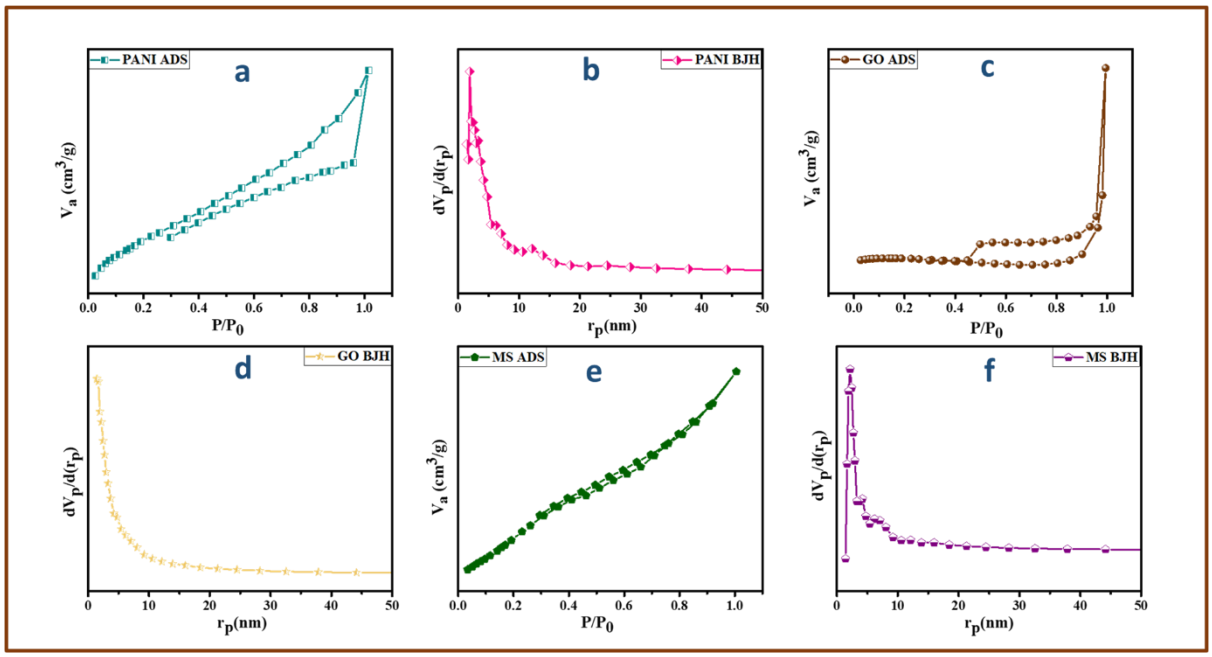

Fig 4.8: (a), (c), and (e) are adsorption-desorption curves of PANI, GO, and MS respectively, whereas (b), (d), and (f) are BJH plots of PANI, GO, and MS respectively.

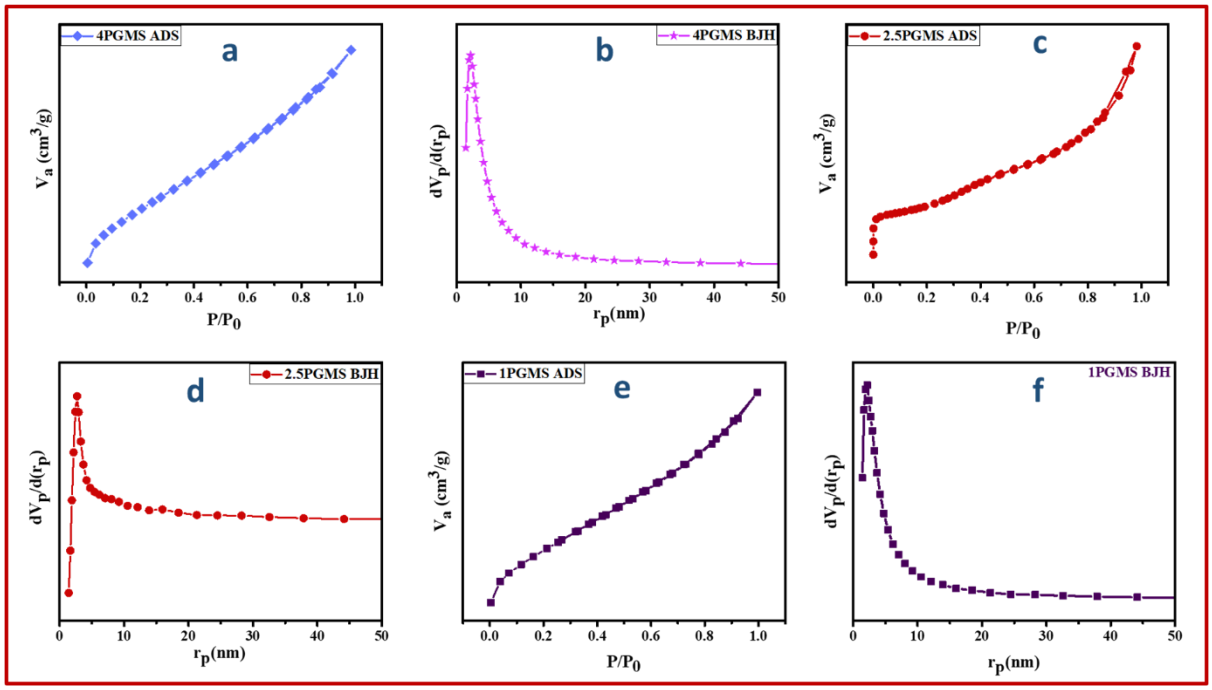

Fig 4.9: (a), (c), and (e) are adsorption-desorption curves 4PGMS, 2.5 PGMS, and 1PGMS respectively, whereas (b), (d), and (f) are BJH plots of 4PGMS, 2.5 PGMS, and 1PGMS respectively.

4.3.2. Removal of the organic pollutant methyl orange (MO) through photocatalysis:

Fig 4.10d illustrates the limited effectiveness of photolysis alone for removing methyl orange (MO), showing only about a 4% decrease in absorbance after 120 min of LED light exposure. This minimal reduction indicates that MO is highly resistant to light-induced degradation. In the dark, after 120 min of reaching adsorption-desorption equilibrium, 2.5PGMS adsorbed approximately 32% of MO. In comparison, other materials showed lower adsorption: bare PANI (21%), GO (26%), molybdenum trioxide (9%), 1PG (1 wt% of GO) (12%), 11GMS (1:1 of GO and MoS_2) (11%), 1PMS (1 wt% of MoS_2) (10 %), 1PGMS (28%), 4PGMS (29%), and TiO_2 (8%) **(Fig 4.10d)**. The enhanced adsorption capacity of 2.5PGMS is because of the increased surface area and a higher count of adsorption areas for the anionic dye, achieved by incorporating 2.5 wt% GO/MS onto PANI. Upon illumination with LED light for 120 minutes, the photocatalytic efficiency improved as follows: PANI (30%) < GO (32%) < MoS_2 (33%) < TiO_2 (34%) < 1PMS (46%) < 1PG (53%) < 11GMS (74%) < 1PGMS (87%) < 4PGMS (85%) < 2.5PGMS (99%) **(Fig 4.10d)**. This indicates that bare MoS_2's limited photodegradation capability is due to its restricted photo-response spectrum, inadequate surface area, and rapid recombination of photo-induced charge carriers. PANI and GO improve performance, with 1PMS, 1PG, and 11GMS showing enhanced photocatalytic activity compared to single-component materials. However, increasing 11GMS beyond 2.5 wt% slightly decreased MO removal efficiency. This reduction is attributed to inefficient charge distribution and potential blocking of active sites by excess 11GMS, which limits light penetration and photocatalytic efficiency. Thus, an optimal 11GMS load maximizes the synergy between PANI, GO, and MoS_2, enhancing photocatalytic activity through a smaller band gap, better light absorption, and reduced recombination of electron-hole pairs. Furthermore, the kinetics of MO photocatalytic degradation were quantitatively analyzed using a pseudo-first-order rate **equation 3.2 (Chapter 3)** on the experimental results. The degradation rate constants are as follows: 1PGMS (0.02353 min^{-1}), 2.5PGMS (0.03 min^{-1}), 4PGMS (0.02523 min^{-1}), 1PG (0.01241 min^{-1}), 1PMS (0.00512 min^{-1}), 11GMS (0.0123 min^{-1}), PANI (0.00422 min^{-1}), GO (0.00135 min^{-1}), MoS_2 (0.00472 min^{-1}), and TiO_2 (0.00324 min^{-1}). The synergy from combining PANI, GO, and MoS_2 was measured using the synergy factor (R), determined by the equation:

$$\mathbf{R} = \frac{K_{PANI+GO+MoS2}}{K_{PANI}+K_{GO}+K_{MoS2}} \qquad \textbf{(4.1)}$$

The rate constants for photodegradation of the PANI/GO/MoS_2 composite and individual components (PANI, GO, and MoS_2) are denoted as $K_{(PANI+GO+MoS2)}$, K_{PANI}, K_{GO}, and K_{MoS2}, respectively. The synergy factors calculated for 1PGMS, 2.5PGMS, 4PGMS, 1PG, 1PMS, and 11GMS are 1.9, 2.6, 2.3, 1.6, 0.5, and 1.8, respectively. Among these, 2.5PGMS exhibited the highest synergy factor, leading to its most effective photocatalytic degradation with a rate constant of 0.03 min^{-1}.

4.3.2.1. Effect of catalyst dosage amount:

The efficiency of the photocatalyst is primarily influenced by the amount of catalyst used. To examine how dosage impacts on MO degradation, experiments were conducted with varying amounts of the ternary photocatalyst (2.5PGMO) from 1 to 4 mg, keeping the MO concentration constant at 20 ppm. At the lowest dosage (0.1 g/L), fewer active species were involved in MO degradation, leading to reduced photocatalytic efficiency. The optimal degradation efficiency occurred at 0.2 g/L **(Fig 4.10a)**, where active site availability and light energy utilization were maximized. However, increasing the catalyst dosage beyond 0.2 g/L did not significantly enhance the degradation rate, likely due to catalyst accumulation, which could reduce solution transparency and light penetration, as well as deactivate some catalyst surface areas. These results suggest that 0.2 g/L is the optimal catalyst dosage for maximum MO photodegradation

4.3.2.2. Impact of the solution's pH:

The dye solution's pH notably impacts the composite's adsorption ability and thus influences the degradation efficiency [40]. To examine how pH affects the removal of MO dye, solutions with different pH levels were created using 0.1 N HCl and 0.1 N NaOH. The pH of catalyst-to-dye solutions at a concentration of 0.2 g/L was recorded before and after the degradation process. As shown in **Fig 4.10b**, the composite 2.5PGMS has a point of zero charge (pzc) around pH 7.07. Degradation efficiency increases from pH 1 to 6, peaking at pH 7.6 **(Fig 4.10c)**. In basic solutions, the efficiency decreases. These results highlight the critical role of solution pH in controlling the photocatalytic degradation efficiency of the composite. The surface charge of the composite, influenced by pH, plays a key role in the adsorption and degradation of MO dye molecules. Optimal performance is achieved under slightly basic

conditions (pH 7.6), stressing the importance of pH in designing effective photocatalytic processes. In strongly alkaline solutions, the formation of metal hydroxide precipitates on the catalyst surface leads to reduced degradation efficiency.

4.3.2.3. Impact of the lighted area:

The research examined the influence of the illuminated surface area on the photocatalytic efficiency of 2.5PGMS when exposed to visible light. A 0.2 g/L photocatalyst solution mixed with 20 ppm MO dye was agitated for 120 min under visible light. Various vessel diameters were employed to alter the reaction surface area, while keeping a consistent distance of 6 cm between the lamp and the surface of the solution. Results showed that increasing the exposed surface area improved degradation efficiency **(Fig 4.10e)**. Larger surface areas allowed for greater light exposure, enhancing photocatalytic degradation and achieving optimal efficiency.

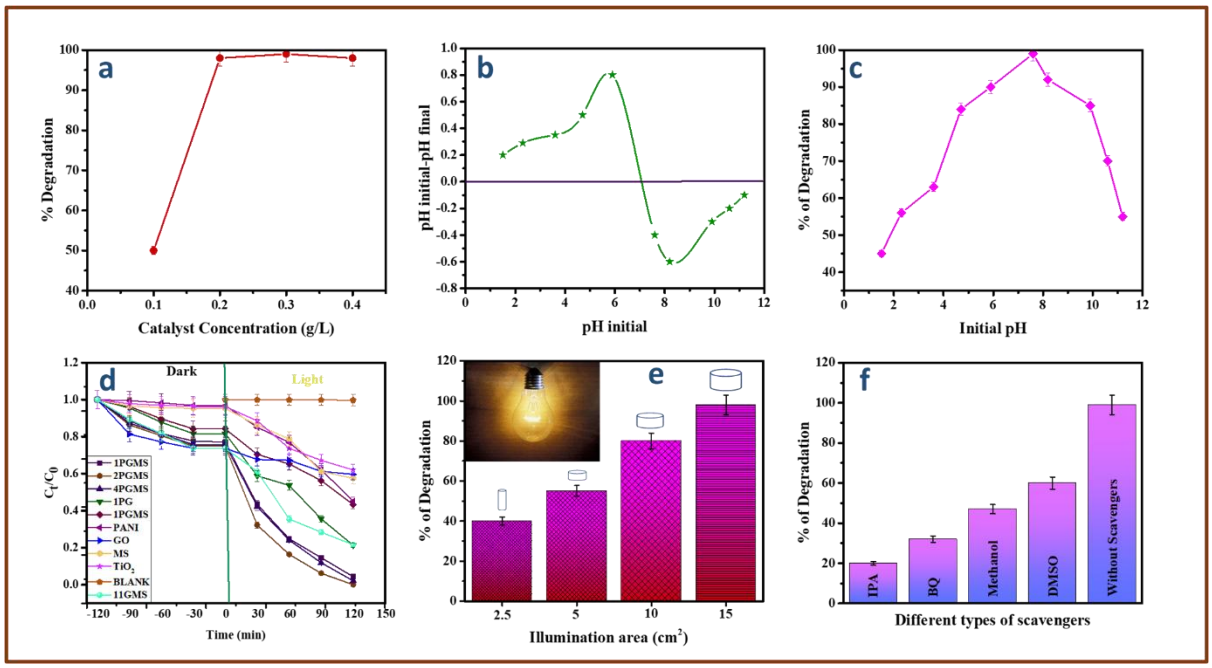

Fig 4.10: (a) Effect of catalyst concentration, (b) pzc studies, (c) effect of pH, (d) kinetic studies, (e) impact of illuminated surface area, and (f) scavenger studies.

4.3.2.4. Likely degradation route of MO:

To assess the decomposition of organic dyes via photodegradation, monitoring TOC and COD levels during light exposure is essential. After 120 min of visible light exposure, MO shows a TOC reduction of 83.21% and a COD reduction of 86.11%. **Fig 4.14a** indicates nearly complete mineralization, with intermediates having limited mineralization potential,

suggesting the organic dye is broken down into byproducts with reduced mineralization capacity.

The degradation products of MO using the 2.5PGMS nanocomposite were identified through GC-MS analysis. **Fig 4.11** presents the mass spectra for MO degradation by 2.5PGMS. The characteristic mass spectrum of MO dye is at m/z 306. After 120 min of degradation, the spectra show peaks at m/z 121, 136, 157, and 172, corresponding to intermediate products. These include sulfanilic acid at m/z 172, which breaks down into benzenesulfonic acid at m/z 157 after losing an amino group (NH_2). Similarly, N,N-dimethyl-p-phenylenediamine at m/z 136 degrades into N,N-dimethyl benzenenamine at m/z 121, also after losing an amino group. The results suggest that MO degradation involves cleavage of the azo bond (–N=N–), producing sulfanilic acid and N,N-dimethyl-p-phenylenediamine[41]. The proposed degradation mechanism is shown in **Fig 4.12**, with further breakdown potentially leading to CO_2 and H_2O.

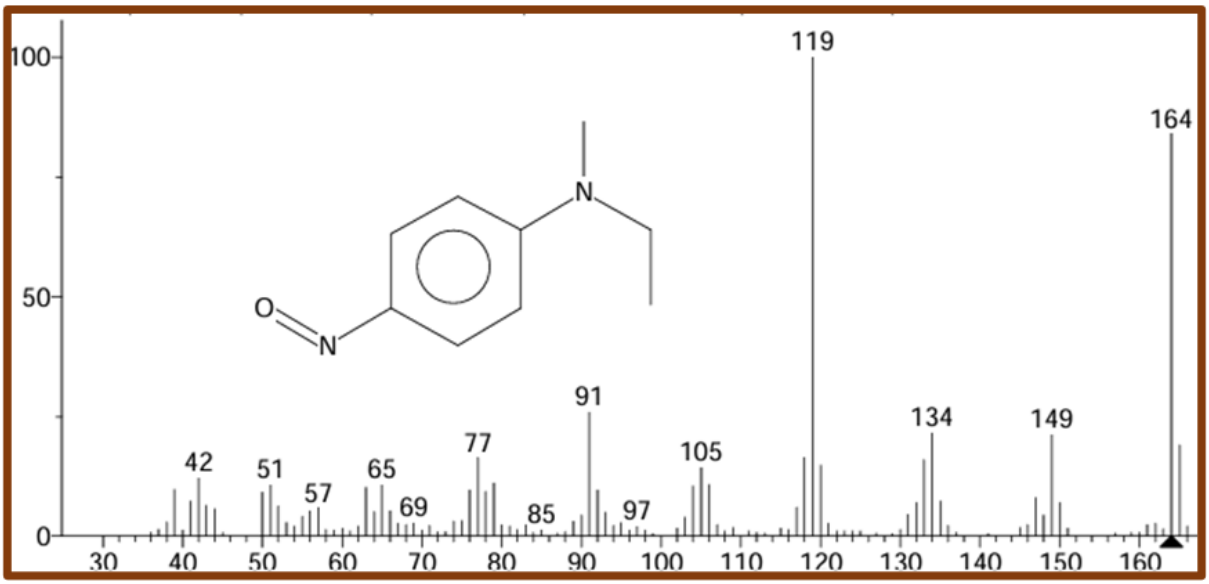

Fig 4.11: GC-MS data after degradation of methyl orange.

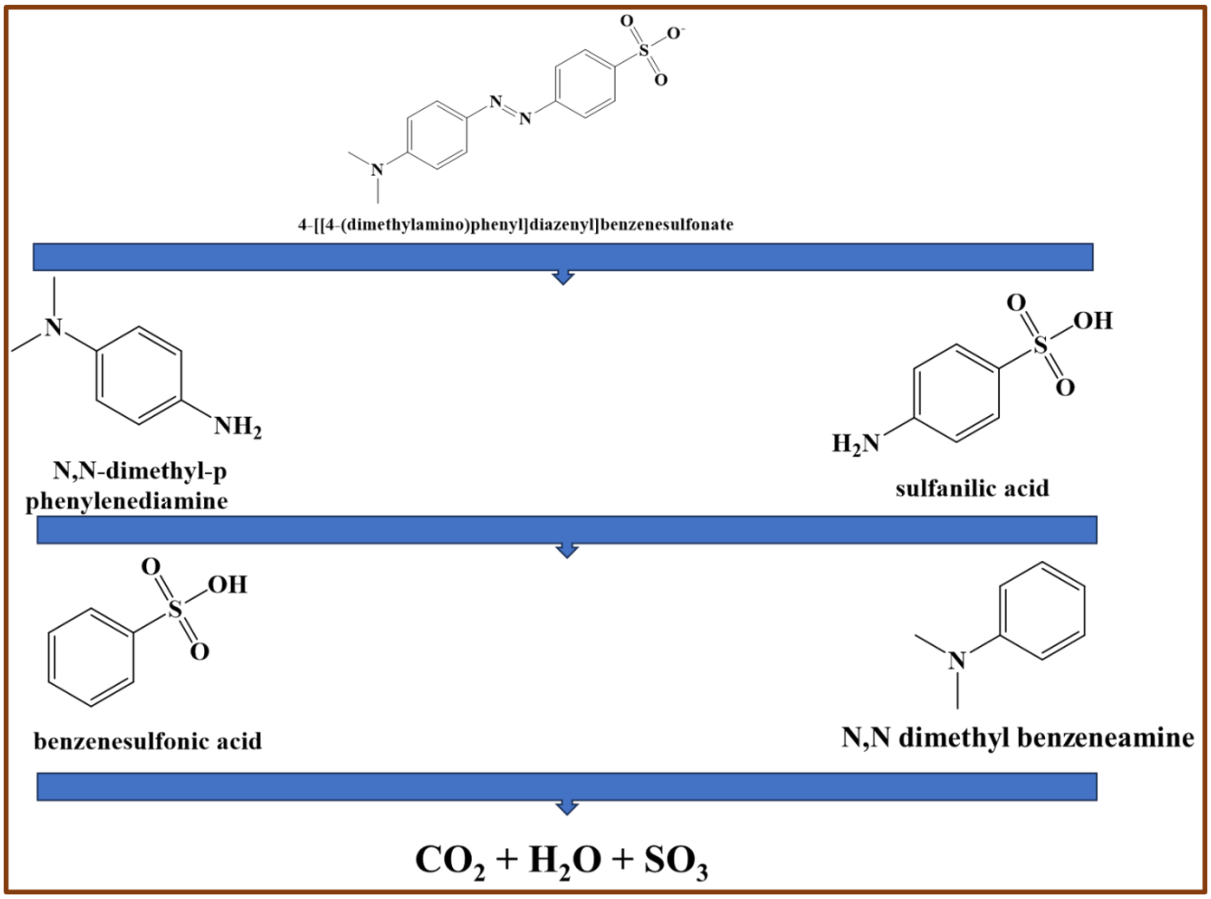

Fig 4.12: Proposed mechanism for the photocatalytic breakdown of methyl orange with 2.5PGMS catalyst.

4.3.2.5. Influence of scavengers on charge transfer mechanisms:

The degradation process mainly relies on electrons from the conduction band (CB), holes in the valence band (VB), as well as superoxide and hydroxyl radicals, which play essential roles [42]. A scavenger study was conducted to determine the primary species involved in this process. This study utilized various scavengers, including isopropyl alcohol (IPA), Dimethyl sulfoxide (DMSO), benzoquinone (BQ), and methanol, to capture hydroxyl radicals ($OH^{\bullet}$), electrons (e^-), superoxide radicals ($O_2^{\bullet-}$), and holes (h^+), respectively. The $O_2^{\bullet-}$ radical acts as a reducing agent and interacts with BQ to form hydroquinone[43]. The presence of DMSO highlights the important role of $^{\bullet}OH$ radicals. In DMSO, the unpaired electrons on oxygen atoms facilitate electron transfer and create hydrogen bonds with hydrogen in hydroxyl radicals [44]. As illustrated in **Fig 4.10f**, methanol, IPA, and BQ play a crucial role in the degradation reaction, underscoring the significance of holes, hydroxyl radicals, and superoxide in the

degradation mechanism. The enhanced photocatalytic efficiency of the 2.5PGMS composite results from improved charge separation achieved by integrating GO and MoS_2 within the polyaniline matrix. This effect was explored by analyzing the band positions of MoS_2, GO, and PANI[45][46]. **Fig 4.5** illustrates the Mott-Schottky plots for PANI, GO, MoS_2, and 2.5PGMS, confirming their characteristic behaviour as p-type semiconductors, as indicated by the overall negative slopes. The flat-band potentials, determined from the x-axis intersection points of the linear regions, are recorded as -0.349 V for 2.5PGMS, -0.30 V for PANI, 0.21 V for MoS_2, and 0.03 V for GO, all referenced against Ag/AgCl. Notably, the conduction band edge (CB) of the 2.5PGMS composite exhibits a significant negative shift of 0.349 V compared to pure GO and MoS_2. This shift suggests strong electronic interactions among PANI, GO, and MoS_2, resulting in a considerable lowering of the conduction band potential. Consequently, this modification elevates the conduction band to a higher energy level, thereby enhancing the composite's reductive capabilities. The analysis of Mott-Schottky plots and band potential variations provides valuable insights into these electronic interactions, contributing to a better understanding of the improved photocatalytic performance of 2.5PGMS. Photon absorption by GO, MoS_2, and PANI leads to the excitation of electrons into the conduction band (CB) of GO and MoS_2, as well as the lowest unoccupied molecular orbital (LUMO) of PANI. This process simultaneously generates holes in the valence band (VB) of GO and MoS_2 and the highest occupied molecular orbital (HOMO) of PANI. Due to energy minimization tendencies, electrons from the CB of GO and MoS_2 preferentially migrate toward the LUMO of PANI rather than returning to the valence band of GO or MoS_2 via the heterojunction barrier. **Fig 4.13** indicates that when the 2.5PGMS composite is exposed to visible light, PANI gets excited, producing light-induced electrons (e^-) and holes (h^+). The electrons from PANI's conduction band (CB) move to the conduction bands of GO and MoS_2, which lowers the rate of electron-hole recombination. This decreases the rate of recombination between electrons and holes. Both GO and MoS_2 exhibit higher reduction potentials compared to $O_2/O^{2-\cdot}$ (0.07 eV)[47]. Electrons located at the surface of GO and MoS_2 can react with dissolved oxygen molecules, generating superoxide radical anions (O_2/OH_2). Given that the oxidation potential of $H_2O/OH\cdot$ (+2.32 eV) is higher than the valence band of PANI[47], Water molecules can react with holes in the valence band of PANI, leading to the formation of hydroxyl radicals ($OH\cdot$). The proposed

methyl orange degradation mechanism is outlined in **Fig 4.13**, along with the corresponding **equations (4.2–4.7)**[48].

$$PANI + h\nu \longrightarrow e_{VB}^{-}(PANI) + h_{CB}^{+}(PANI) \quad (4.2)$$

$$GO + h\nu \longrightarrow e_{CB}^{-}(GO) + h_{VB}^{+}(GO) \quad (4.3)$$

$$MoS_2 + h\nu \longrightarrow e_{CB}^{-}(MoS_2) + h_{VB}^{+}(MoS_2) \quad (4.4)$$

$$e_{VB}^{-}(PANI) + O_2 \longrightarrow O^{2-}(PANI) \quad (4.5)$$

$$h_{VB} + (PANI/GO/MoS_2) + OH^{-} \longrightarrow OH\cdot(PANI/GO/MoS_2) \quad (4.6)$$

$$O^{2-}(PANI), OH\cdot(PANI/GO/MoS_2) + MO \longrightarrow \text{Degraded products} \quad (4.7)$$

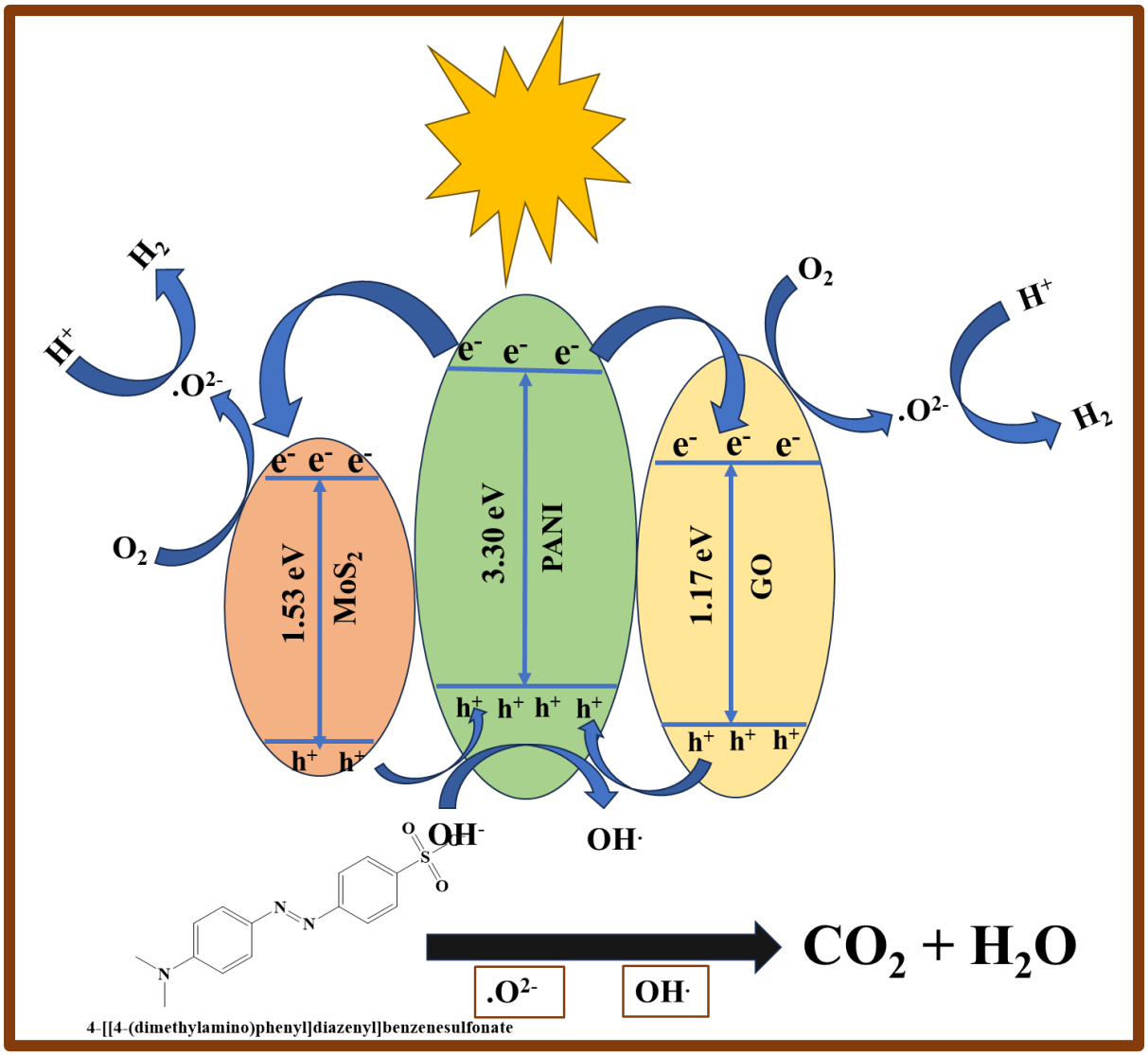

Fig 4.13: Proposed charge transfer mechanism for photocatalytic degradation and hydrogen production in the 2.5PGMS composite.

4.3.2.6. Studies on reusability:

The durability of a photocatalyst is essential for its continued application in environmental cleanup. Therefore, it's important to assess the composite's stability across multiple photodegradation cycles. The 2.5PGMS composite displayed impressive photostability, maintaining a high degradation efficiency of 85-98% for MO even after five cycles, as shown in **Fig 14b**. XRD analysis after degradation indicated only a slight reduction in peak intensity, likely caused by dye adsorption on the catalyst's surface, while the XRD pattern remained unchanged **(Fig 14c)**. These findings suggest the photocatalyst retains its durability and structural integrity over time. The 2.5PGMS photocatalyst was systematically compared with various materials documented in the literature for their efficacy in photocatalytic detoxification of organic pollutants, as detailed in **Table 4.2**. This comparative analysis reveals that 2.5PGMS not only achieves superior degradation efficiency but also does so at a lower catalyst concentration, highlighting its potential in effectively treating persistent organic pollutants with enhanced efficiency and reduced material usage.

Table 4.2: Comparison of different photocatalyst materials for photocatalytic degradation.

Photocatalyst	Catalyst amount (mg)	% degradation	Time (min)	References
PANI-TiO_2	10	89.7	120	[49]
PANI/TiO_2/Cotton	-	87.7	180	[50]
PANI/TiO_2/SiO_2	-	87	120	[51]
PANI/Fe-TiO_2	-	28	150	[52]
Ag-Ag_2O/TiO_2@PPY	100	100	175	[53]
PEDOT/GO/MnO_2	20	92.7	420	[54]
RGO/mesoTiO_2/AuNP	10	-	240	[23]
PANI@GN/TiO_2	50	87	180	[55]
Ag_2O/TiO_2@PPY	50	100	240	[56]
PANI/TiO_2	5	99	360	[57]
Ag-ZnO/PANI	200	98.6	120	[58]
PANI/GO/MoS_2 (2.5%)	2	99	120	Present work

4.3.2.7. Studies on hydrogen production via photocatalysis:

Hydrogen generation through photocatalytic water splitting was studied over 24 hrs under LED light using four different solutions. The first solution included 1 ml of methanol (sacrificial agent) in 19 ml of water. The second solution consisted of 1 ml of HCl diluted in 19 ml of water, while the third was basic, comprising 1 ml of 1N NaOH mixed with 19 ml of water. The fourth solution contained only 20 ml of water. In the presence of methanol, 1500 ppm of hydrogen gas was generated. **(Fig 14d)**. Methanol serves as a sacrificial donor and hole scavenger, leading to the formation of intermediates like formaldehyde or formic acid. In the photocatalytic reaction, hydrogen ions (H^+) partially participate in the reduction process with these intermediates. Hydrogen production reached 1000 ppm in acidic conditions, whereas under basic conditions, it yielded 800 ppm **(Fig 14d)**. With just the catalyst and water, 400 ppm of hydrogen was released **(Fig 14d)**. Quantum efficiency was about 26% with methanol, 22% in acidic solution, 19% in basic solution, and 15% with only the catalyst. **Equations 4.8-4.11** demonstrate the role of electron-hole pairs in the conduction and valence bands in facilitating redox reactions [59][60].

In acidic condition:

Oxidation: $2H_2O\ (l) + 4h^+ \longrightarrow O_2\ (g) + 4H^+\ (aq)$ **(4.8)**

E^0(oxidation) = -1.23 V

Reduction $2H^+ + 2e^- \longrightarrow O_2\ (g) + 2H_2\ (g)$ **(4.9)**

E^0reduction = 0 V

In basic condition:

Oxidation: $2OH^-\ (aq) \longrightarrow 1/2\ O_2\ (g) + H_2O\ (l) + 2e^-$ **(4.10)**

Reduction: $2H_2O\ (l) + 2e^- \longrightarrow H_2\ (g) + 2OH^-$ **(4.11)**

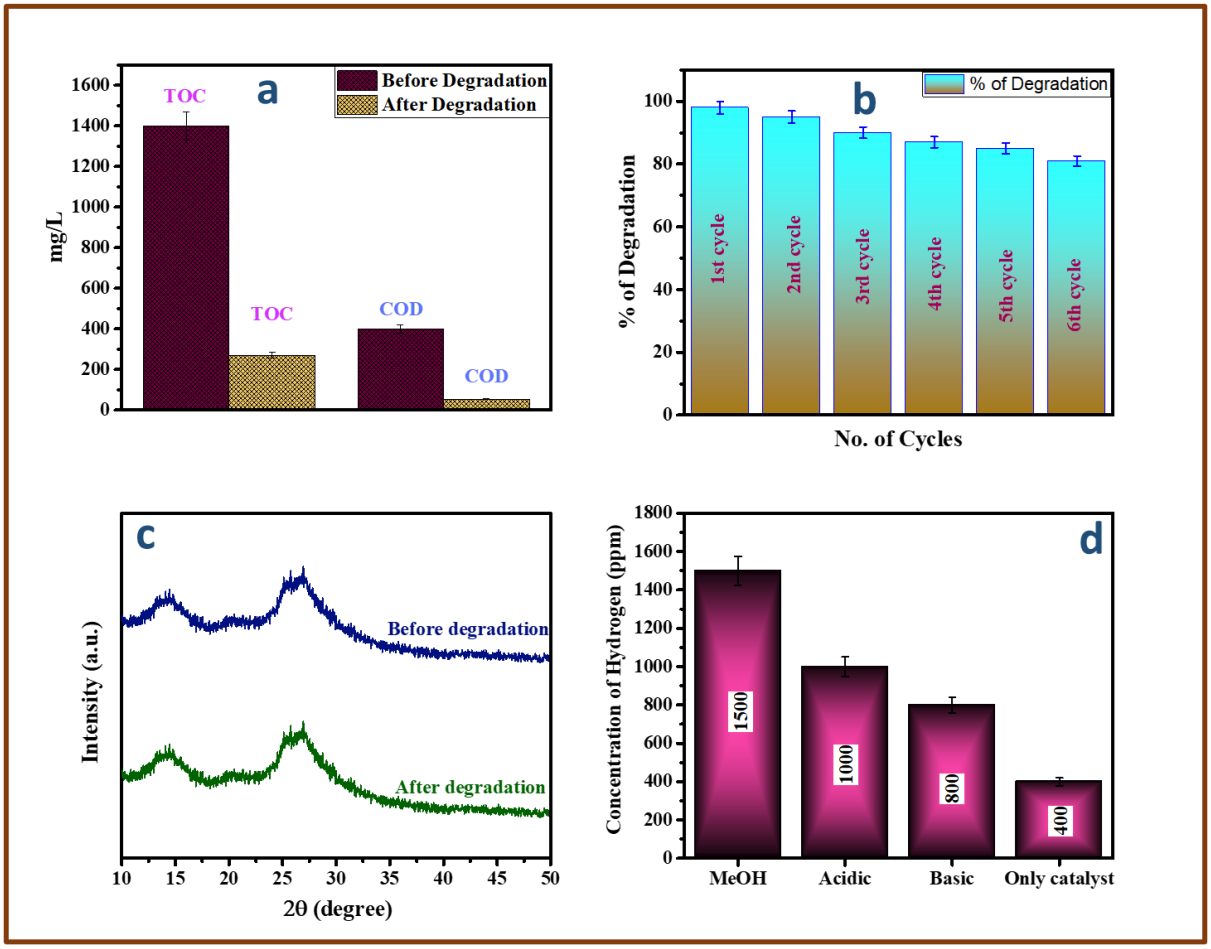

Fig 4.14: (a) TOC and COD of MO before and after degradation, (b) reusability studies, (c) XRD of 2.5PGMS before and after degradation, and (d) hydrogen production studies.

References

[1] J. Willkomm, K. L. Orchard, A. Reynal, E. Pastor, J. R. Durrant, and E. Reisner, "Dye-sensitised semiconductors modified with molecular catalysts for light-driven H_2 production," *Chem. Soc. Rev.*, vol. 45, no. 1, pp. 9–23, 2016, doi: 10.1039/C5CS00733J.

[2] S. Cao, J. Low, J. Yu, and M. Jaroniec, "Polymeric Photocatalysts Based on Graphitic Carbon Nitride," *Adv. Mater.*, vol. 27, no. 13, pp. 2150–2176, Apr. 2015, doi: 10.1002/adma.201500033.

[3] S. Wang *et al.*, "Fullerene C_{70} –TiO_2 hybrids with enhanced photocatalytic activity under visible light irradiation," *J. Mater. Chem. A*, vol. 3, no. 42, pp. 21090–21098, 2015, doi: 10.1039/C5TA03229F.

[4] E. Muratspahić, J. Schöffmann, Q. Jiang, and A. Bismarck, "Poly(acrylamide- co -styrene): A Macrosurfactant for Oil/Water Emulsion Templating toward Robust Macroporous Hydrogels," *Macromolecules*, vol. 56, no. 8, pp. 3213–3223, Apr. 2023, doi: 10.1021/acs.macromol.2c02504.

[5] J. Abdi, M. Vossoughi, N. M. Mahmoodi, and I. Alemzadeh, "Synthesis of metal-organic framework hybrid nanocomposites based on GO and CNT with high adsorption capacity for dye removal," *Chem. Eng. J.*, vol. 326, pp. 1145–1158, Oct. 2017, doi: 10.1016/j.cej.2017.06.054.

[6] M. J. Kang and Y. S. Kang, "Efficient Approaches on Photochemical CO_2 Reduction to Alcohol by Solar Light with Functional Multi-layered Membrane Catalysts," *MRS Adv.*, vol. 3, no. 55, pp. 3271–3280, Nov. 2018, doi: 10.1557/adv.2018.418.

[7] K. M. AlAqad, T. A. Kandiel, T. N. Jahangir, M. Qamar, and C. Basheer, "TiO_2 nanotubes modified with cobalt oxyphosphide spheres for efficient electrocatalytic hydrogen evolution reaction in alkaline medium," *Electrochim. Acta*, vol. 456, p. 142436, Jul. 2023, doi: 10.1016/j.electacta.2023.142436.

[8] K. Yan and G. Wu, "Titanium Dioxide Microsphere-Derived Materials for Solar Fuel Hydrogen Generation," *ACS Sustain. Chem. Eng.*, vol. 3, no. 5, pp. 779–791, May 2015, doi: 10.1021/acssuschemeng.5b00154.

[9] K. M. AlAqad, T. A. Kandiel, and C. Basheer, "Synergy between in-situ immobilized MoS_2 nanosheets and TiO_2 nanotubes for efficient electrocatalytic hydrogen evolution," *Int. J. Hydrogen Energy*, vol. 47, no. 4, pp. 2366–2377, Jan. 2022, doi: 10.1016/j.ijhydene.2021.10.159.

[10] M.-Y. Qi, M. Conte, M. Anpo, Z.-R. Tang, and Y.-J. Xu, "Cooperative Coupling of Oxidative Organic Synthesis and Hydrogen Production over Semiconductor-Based Photocatalysts," *Chem. Rev.*, vol. 121, no. 21, pp. 13051–13085, Nov. 2021, doi: 10.1021/acs.chemrev.1c00197.

[11] A. Gupta *et al.*, "Stabilizing a Ru single atom catalyst through electronic metal–support interaction with a $NiCo_2O_4$ support for overall water splitting and urea electrolysis," *J. Mater. Chem. A*, vol. 12, no. 35, pp. 23819–23836, 2024, doi:

10.1039/D4TA04284K.

[12] G. Yu, J. Gao, J. C. Hummelen, F. Wudl, and A. J. Heeger, "Polymer Photovoltaic Cells: Enhanced Efficiencies via a Network of Internal Donor-Acceptor Heterojunctions," *Science (80-.).*, vol. 270, no. 5243, pp. 1789–1791, Dec. 1995, doi: 10.1126/science.270.5243.1789.

[13] K. Vinodgopal, D. E. Wynkoop, and P. V. Kamat, "Environmental Photochemistry on Semiconductor Surfaces: Photosensitized Degradation of a Textile Azo Dye, Acid Orange 7, on TiO_2 Particles Using Visible Light," *Environ. Sci. Technol.*, vol. 30, no. 5, pp. 1660–1666, Apr. 1996, doi: 10.1021/es950655d.

[14] P. Ahuja, S. K. Ujjain, I. Arora, and M. Samim, "Hierarchically Grown NiO-Decorated Polyaniline-Reduced Graphene Oxide Composite for Ultrafast Sunlight-Driven Photocatalysis," *ACS Omega*, vol. 3, no. 7, pp. 7846–7855, Jul. 2018, doi: 10.1021/acsomega.8b00765.

[15] H. Yang *et al.*, "Green and facile synthesis of graphene nanosheets/$K_3PW_{12}O_{40}$ nanocomposites with enhanced photocatalytic activities," *Mater. Res. Bull.*, vol. 78, pp. 112–118, Jun. 2016, doi: 10.1016/j.materresbull.2016.02.038.

[16] W. Zhang *et al.*, "In situ preparation of cubic Cu_2O-RGO nanocomposites for enhanced visible-light degradation of methyl orange," *Nanotechnology*, vol. 27, no. 26, p. 265703, Jul. 2016, doi: 10.1088/0957-4484/27/26/265703.

[17] E. Pajootan, M. Arami, and M. Rahimdokht, "Application of Carbon Nanotubes Coated Electrodes and Immobilized TiO_2 for Dye Degradation in a Continuous Photocatalytic-Electro-Fenton Process," *Ind. Eng. Chem. Res.*, vol. 53, no. 42, pp. 16261–16269, Oct. 2014, doi: 10.1021/ie5024589.

[18] P. Raizada *et al.*, "Solar photocatalytic activity of nano-ZnO supported on activated carbon or brick grain particles: Role of adsorption in dye degradation," *Appl. Catal. A Gen.*, vol. 486, pp. 159–169, Sep. 2014, doi: 10.1016/j.apcata.2014.08.043.

[19] J. Miao, A. Xie, S. Li, F. Huang, J. Cao, and Y. Shen, "A novel reducing graphene/polyaniline/cuprous oxide composite hydrogel with unexpected photocatalytic activity for the degradation of Congo red," *Appl. Surf. Sci.*, vol. 360, pp.

594–600, Jan. 2016, doi: 10.1016/j.apsusc.2015.11.005.

[20] N. B. Grimm *et al.*, "Global Change and the Ecology of Cities," *Science (80-.).*, vol. 319, no. 5864, pp. 756–760, Feb. 2008, doi: 10.1126/science.1150195.

[21] K. Pandiselvi, H. Fang, X. Huang, J. Wang, X. Xu, and T. Li, "Constructing a novel carbon nitride/polyaniline/ZnO ternary heterostructure with enhanced photocatalytic performance using exfoliated carbon nitride nanosheets as supports," *J. Hazard. Mater.*, vol. 314, pp. 67–77, Aug. 2016, doi: 10.1016/j.jhazmat.2016.04.035.

[22] J. Feng *et al.*, "In-depth study on adsorption and photocatalytic performance of novel reduced graphene oxide-$ZnFe_2O_4$-polyaniline composites," *J. Alloys Compd.*, vol. 681, pp. 157–166, Oct. 2016, doi: 10.1016/j.jallcom.2016.04.146.

[23] Y. Yang, Z. Ma, L. Xu, H. Wang, and N. Fu, "Preparation of reduced graphene oxide/meso-TiO_2 /AuNPs ternary composites and their visible-light-induced photocatalytic degradation n of methylene blue," *Appl. Surf. Sci.*, vol. 369, pp. 576–583, Apr. 2016, doi: 10.1016/j.apsusc.2016.02.078.

[24] N. Huo, Y. Yang, Y.-N. Wu, X.-G. Zhang, S. T. Pantelides, and G. Konstantatos, "High carrier mobility in monolayer CVD-grown MoS_2 through phonon suppression," *Nanoscale*, vol. 10, no. 31, pp. 15071–15077, 2018, doi: 10.1039/C8NR04416C.

[25] T. H. M. Lau *et al.*, "Transition metal atom doping of the basal plane of MoS_2 monolayer nanosheets for electrochemical hydrogen evolution," *Chem. Sci.*, vol. 9, no. 21, pp. 4769–4776, 2018, doi: 10.1039/C8SC01114A.

[26] P. Hait, R. Mehta, and S. Basu, "Advancing sustainable solutions: Harnessing polyaniline/BiOCl/GO ternary nanocomposites for solar-powered degradation of organic pollutant and photocatalytic hydrogen generation," *J. Clean. Prod.*, vol. 424, p. 138851, Oct. 2023, doi: 10.1016/j.jclepro.2023.138851.

[27] H. Shin *et al.*, "Efficient Reduction of Graphite Oxide by Sodium Borohydride and Its Effect on Electrical Conductance," *Adv. Funct. Mater.*, vol. 19, no. 12, pp. 1987–1992, Jun. 2009, doi: 10.1002/adfm.200900167.

[28] H. Liu, Y. Su, Z. Chen, Z. Jin, and Y. Wang, "Graphene sheets grafted three-dimensional $BiOBr_{0.2}I_{0.8}$ microspheres with excellent photocatalytic activity under visible light," *J. Hazard. Mater.*, vol. 266, pp. 75–83, Feb. 2014, doi: 10.1016/j.jhazmat.2013.12.013.

[29] K. Zhang, L. L. Zhang, X. S. Zhao, and J. Wu, "Graphene/Polyaniline Nanofiber Composites as Supercapacitor Electrodes," *Chem. Mater.*, vol. 22, no. 4, pp. 1392–1401, Feb. 2010, doi: 10.1021/cm902876u.

[30] Z. Liu *et al.*, "Decoration of BiOI quantum size nanoparticles with reduced graphene oxide in enhanced visible-light-driven photocatalytic studies," *Appl. Surf. Sci.*, vol. 259, pp. 441–447, Oct. 2012, doi: 10.1016/j.apsusc.2012.07.063.

[31] B. Li *et al.*, "Preparation of Monolayer MoS_2 Quantum Dots using Temporally Shaped Femtosecond Laser Ablation of Bulk MoS_2 Targets in Water," *Sci. Rep.*, vol. 7, no. 1, p. 11182, Sep. 2017, doi: 10.1038/s41598-017-10632-3.

[32] H. Wang *et al.*, "Self-assembled sulphur doped carbon nitride for photocatalytic water reforming of methanol," *Chem. Eng. J.*, vol. 445, p. 136790, Oct. 2022, doi: 10.1016/j.cej.2022.136790.

[33] A. Abdolahi, E. Hamzah, Z. Ibrahim, and S. Hashim, "Synthesis of Uniform Polyaniline Nanofibers through Interfacial Polymerization," *Materials (Basel).*, vol. 5, no. 8, pp. 1487–1494, Aug. 2012, doi: 10.3390/ma5081487.

[34] G. Gaikwad, P. Patil, D. Patil, and J. Naik, "Synthesis and evaluation of gas sensing properties of PANI based graphene oxide nanocomposites," *Mater. Sci. Eng. B*, vol. 218, pp. 14–22, Apr. 2017, doi: 10.1016/j.mseb.2017.01.008.

[35] T. Szabó, E. Tombácz, E. Illés, and I. Dékány, "Enhanced acidity and pH-dependent surface charge characterization of successively oxidized graphite oxides," *Carbon N. Y.*, vol. 44, no. 3, pp. 537–545, Mar. 2006, doi: 10.1016/j.carbon.2005.08.005.

[36] Y. Fu and X. Wang, "Magnetically Separable $ZnFe_2O_4$ –Graphene Catalyst and its High Photocatalytic Performance under Visible Light Irradiation," *Ind. Eng. Chem. Res.*, vol. 50, no. 12, pp. 7210–7218, Jun. 2011, doi: 10.1021/ie200162a.

[37] Q. Wang *et al.*, "Photodegradation of methyl orange with PANI-modified BiOCl photocatalyst under visible light irradiation," *Appl. Surf. Sci.*, vol. 283, pp. 577–583, Oct. 2013, doi: 10.1016/j.apsusc.2013.06.149.

[38] W. Feng *et al.*, "Flower-like PEGylated MoS_2 nanoflakes for near-infrared photothermal cancer therapy," *Sci. Rep.*, vol. 5, no. 1, p. 17422, Dec. 2015, doi: 10.1038/srep17422.

[39] S. Reshmi, M. V Akshaya, B. Satpati, A. Roy, P. Kumar Basu, and K. Bhattacharjee, "Tailored MoS_2 nanorods: a simple microwave assisted synthesis," *Mater. Res. Express*, vol. 4, no. 11, p. 115012, Nov. 2017, doi: 10.1088/2053-1591/aa949c.

[40] A. Kumar, R. Kumar, and G. Pandey, "Synthesis, Characterization of Titania/Polyaniline/GO Nanocomposites, and Its Photocatalytic Activity Under UV-Visible Light," *Macromol. Symp.*, vol. 379, no. 1, Jun. 2018, doi: 10.1002/masy.201600192.

[41] M. Kgatle, K. Sikhwivhilu, G. Ndlovu, and N. Moloto, "Degradation Kinetics of Methyl Orange Dye in Water Using Trimetallic Fe/Cu/Ag Nanoparticles," *Catalysts*, vol. 11, no. 4, p. 428, Mar. 2021, doi: 10.3390/catal11040428.

[42] A. Kundu, S. Sharma, and S. Basu, "Modulated BiOCl nanoplates with porous g-C_3N_4 nanosheets for photocatalytic degradation of color/colorless pollutants in natural sunlight," *J. Phys. Chem. Solids*, vol. 154, p. 110064, Jul. 2021, doi: 10.1016/j.jpcs.2021.110064.

[43] S. Singla, S. Sharma, and S. Basu, "MoS_2/WO_3 heterojunction with the intensified photocatalytic performance for decomposition of organic pollutants under the broad array of solar light," *J. Clean. Prod.*, vol. 324, p. 129290, Nov. 2021, doi: 10.1016/j.jclepro.2021.129290.

[44] H. Alamgholiloo, E. Asgari, S. Nazari, A. Sheikhmohammadi, N. Noroozi Pesyan, and B. Hashemzadeh, "Architecture of bimetallic-MOF/silicate derived Co/NC@mSiO_2 as peroxymonosulfate activator for highly efficient ciprofloxacin degradation," *Sep. Purif. Technol.*, vol. 300, p. 121911, Nov. 2022, doi: 10.1016/j.seppur.2022.121911.

[45] T. Guo, L. Wang, D. G. Evans, and W. Yang, "Synthesis and Photocatalytic Properties

of a Polyaniline-Intercalated Layered Protonic Titanate Nanocomposite with a p−n Heterojunction Structure," *J. Phys. Chem. C*, vol. 114, no. 11, pp. 4765–4772, Mar. 2010, doi: 10.1021/jp9055413.

[46] T. Lv, L. Pan, X. Liu, T. Lu, G. Zhu, and Z. Sun, "Enhanced photocatalytic degradation of methylene blue by ZnO-reduced graphene oxide composite synthesized via microwave-assisted reaction," *J. Alloys Compd.*, vol. 509, no. 41, pp. 10086–10091, Oct. 2011, doi: 10.1016/j.jallcom.2011.08.045.

[47] P. S. Rao and E. Hayon, "Redox potentials of free radicals. IV. Superoxide and hydroperoxy radicals $\cdot O^{2-}$ and $\cdot HO^2$," *J. Phys. Chem.*, vol. 79, no. 4, pp. 397–402, Feb. 1975, doi: 10.1021/j100571a021.

[48] M. Mitra *et al.*, "Polyaniline/Reduced Graphene Oxide Composite-Enhanced Visible-Light-Driven Photocatalytic Activity for the Degradation of Organic Dyes," *ACS Omega*, vol. 4, no. 1, pp. 1623–1635, Jan. 2019, doi: 10.1021/acsomega.8b02941.

[49] H. M. El-Bery, M. R. Salah, S. M. Ahmed, and S. A. Soliman, "Efficient non-metal based conducting polymers for photocatalytic hydrogen production: comparative study between polyaniline, polypyrrole and PEDOT," *RSC Adv.*, vol. 11, no. 22, pp. 13229–13244, 2021, doi: 10.1039/D1RA01218E.

[50] J. Ma, J. Dai, Y. Duan, J. Zhang, L. Qiang, and J. Xue, "Fabrication of PANI-TiO_2/rGO hybrid composites for enhanced photocatalysis of pollutant removal and hydrogen production," *Renew. Energy*, vol. 156, pp. 1008–1018, Aug. 2020, doi: 10.1016/j.renene.2020.04.104.

[51] A. Li, W. Zhu, C. Li, T. Wang, and J. Gong, "Rational design of yolk–shell nanostructures for photocatalysis," *Chem. Soc. Rev.*, vol. 48, no. 7, pp. 1874–1907, 2019, doi: 10.1039/C8CS00711J.

[52] J. Kröger *et al.*, "Interfacial Engineering for Improved Photocatalysis in a Charge Storing 2D Carbon Nitride: Melamine Functionalized Poly(heptazine imide)," *Adv. Energy Mater.*, vol. 11, no. 6, p. 2003016, Feb. 2021, doi: 10.1002/aenm.202003016.

[53] R. Kumar, R. El-Shishtawy, and M. Barakat, "Synthesis and Characterization of Ag-Ag_2O/TiO_2@polypyrrole Heterojunction for Enhanced Photocatalytic Degradation of

Methylene Blue," *Catalysts*, vol. 6, no. 6, p. 76, May 2016, doi: 10.3390/catal6060076.

[54] L. Zhang, R. Jamal, Q. Zhao, M. Wang, and T. Abdiryim, "Preparation of PEDOT/GO, PEDOT/MnO_2, and PEDOT/GO/MnO_2 nanocomposites and their application in catalytic degradation of methylene blue," *Nanoscale Res. Lett.*, vol. 10, no. 1, p. 148, Dec. 2015, doi: 10.1186/s11671-015-0859-6.

[55] R. Kumar *et al.*, "Facile route to a conducting ternary polyaniline@TiO_2 /GN nanocomposite for environmentally benign applications: photocatalytic degradation of pollutants and biological activity," *RSC Adv.*, vol. 6, no. 112, pp. 111308–111317, 2016, doi: 10.1039/C6RA24079H.

[56] R. Kumar, "Mixed phase lamellar titania-titanate anchored with Ag_2O and polypyrrole for enhanced adsorption and photocatalytic activity," *J. Colloid Interface Sci.*, vol. 477, pp. 83–93, Sep. 2016, doi: 10.1016/j.jcis.2016.05.039.

[57] Y.-J. Lee *et al.*, "Application of PANI/TiO_2 Composite for Photocatalytic Degradation of Contaminants from Aqueous Solution," *Appl. Sci.*, vol. 10, no. 19, p. 6710, Sep. 2020, doi: 10.3390/app10196710.

[58] F. Habtamu, S. Berhanu, and T. Mender, "Polyaniline Supported Ag-Doped ZnO Nanocomposite: Synthesis, Characterization, and Kinetics Study for Photocatalytic Degradation of Malachite Green," *J. Chem.*, vol. 2021, pp. 1–12, Sep. 2021, doi: 10.1155/2021/2451836.

[59] T. Jafari, E. Moharreri, A. Amin, R. Miao, W. Song, and S. Suib, "Photocatalytic Water Splitting—The Untamed Dream: A Review of Recent Advances," *Molecules*, vol. 21, no. 7, p. 900, Jul. 2016, doi: 10.3390/molecules21070900.

[60] A. A. Murashkina, T. V. Bakiev, Y. M. Artemev, A. V. Rudakova, A. V. Emeline, and D. W. Bahnemann, "Photoelectrochemical Behavior of the Ternary Heterostructured Systems CdS/WO_3/TiO_2," *Catalysts*, vol. 9, no. 12, p. 999, Nov. 2019, doi: 10.3390/catal9120999.

Chapter 5

Multifunctional PANI–LDH for Dye Mineralization and Hydrogen Production

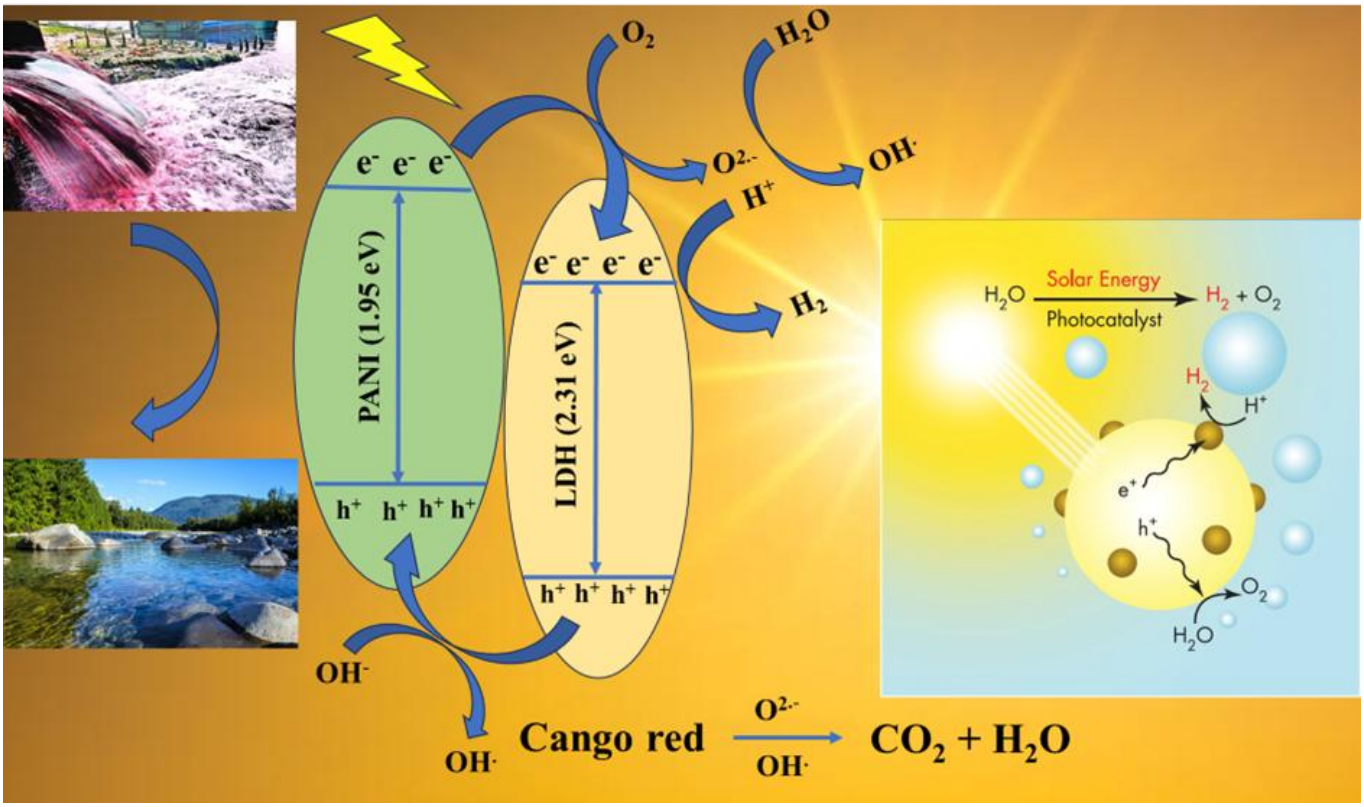

Highlights

- Fabrication of different mole ratios of Polyaniline-LDH nanocomposite.
- Photocatalysts efficacy tested by degradation of Cango red and H_2 production from water splitting.
- Photocatalytic elimination of Cango red (98 %, rate constant~ 0.037 min^{-1}) was observed under LED light.
- The nanocomposite produced 10475 ppm of hydrogen gas in the presence of a sacrificial agent (MeOH) with an AQE of 20%.

5.1. Introduction:

Environmental pollution remains a critical challenge faced daily by both developed and emerging nations across the globe. Both fossil fuel and anthropogenies pollution of air, water, and solid waste plays a major role in disrupting environmental balance[1]. The quick evolution of current human society and the exhaustion of fossil energy sources highlight the urgent need to create energy sources that are clean, affordable, and environmentally sustainable[2]. Producing clean, carbon-free hydrogen through light-driven water decomposition via photocatalysis offers a highly optimistic method for transforming solar power into stored chemical energy [3][4][5]. Light-assisted catalytic splitting of water using semiconductor compounds subjected to sunlight is a promising and eco-friendly approach to transform solar power into hydrogen fuel[6][7]. Organic pollutants in water exist in various forms and can be classified into several categories, including pesticides, pharmaceuticals, phenolic compounds, surface-active agents, organohalides, dyes, and hydrocarbons[8]. A large number of these pollutants are chemically stable, difficult to break down, toxic, and even carcinogenic[9][10][11]. Both the solar energy conversion efficiency and photo-catalytic degradation of individual semiconducting materials remain limited caused due to the fast recombination of e^--h^+ pairs generated by photo excitation. Building a heterojunction structure is an effective approach to address this problem[12]. Compared to this, PANI, being one of the most extensively researched conductive polymers, has a wide range of uses within both the catalytic and light-assisted catalytic (photocatalytic) sectors. Polyaniline (PANI), a polymer with a long π-conjugated backbone, demonstrates remarkably high electrical conductivity when treated with a protonic acid dopant. Polyaniline (PANI) can be found in three distinct oxidation states: the leucoemeraldine base, the emeraldine base, and the pernigraniline base. Of the three forms, the leucoemeraldine base shows limited reducing capability, primarily because the benzene rings are connected by −NH− linkages. The interface between polyaniline (PANI) and an n-type semiconductor Induces self-established potential gradient across the junction of the p- and n-type materials[13]. This electric field promotes the swift migration of photogenerated holes into the polyaniline (PANI) layer, where they oxidize nearby materials, while photogenerated electrons are quickly directed to reduction reactions occurring on the surface of the n-type semiconductor composite[14]. Due to their distinctive structure and functional properties, two-dimensional layered double hydroxides (LDHs) have attracted

considerable attention for use in photocatalytic applications. Layered double hydroxides (LDHs) are a category of inorganic compounds, commonly represented by the formula $[M^{2+}_{1-x}M^{3+}_{x}(OH)_2]X^{+}[A_{x/n}]^{n-}.mH_2O$, where M^{2+} denotes divalent metal cations, and M^{3+} refers to trivalent metal cations. The structure is composed of octahedral units that share edges, where each metal ion is surrounded by six hydroxyl (OH) groups. Partially replacing Ni^{2+}cations with Al^{3+} via isomorphic substitution yields a positively charged Ni Al-LDH. Furthermore, the anion $[A^{n-}]$, which balances the charge, is located in the spaces between the layers[15][16][17]. Applications of LDHs span adsorption, electrochemical technologies, energy storage solutions, pharmaceutical delivery, and catalysis[18]. Their widespread use is due to factors such as natural abundance, affordability, excellent chemical stability, broad redox capabilities, non-toxicity, and an extensive surface area [19]. The versatility of the matrix components and the configuration of the intercalated anions contribute to improving the photocatalytic efficiency of LDHs. To address these challenges and raise the photocatalytic efficiency of unmodified LDHs, researchers have turned to constructing heterojunctions with various two-dimensional materials[20][21][22]. In recent times, numerous nanocomposites based on heterojunctions have been effectively synthesized, such as g-C_3N_4/Ni Al LDH[23], Ag/Zn Ti LDH[24], Au-loaded $CaFe_2O_4$/Co Al LDH[21], Ni Al LDH/Fe_2O_4/RGO[25], Au-Pd/Ni Al LDH[26], Ga_2O_3-modified Mg Al LDH[27], g-C_3N_4/Mg Fe LDH[28], g-C_3N_4/Ni Fe LDH[29], r-GO/$La_2Ti_2O_7$/ Ni Fe LDH[30], MgO/$MgCr_2O_4$[31], and Co Mn LDH/g-C_3N_4[32]. All studies either involved the use of expensive noble metals or required a relatively long time for degradation to be completed. Huang et al. synthesized a C_3N_4/$MgAl_{0.80}Ce_{0.20}$-LDH composite, which degraded Rhodamine B dye (50 mg/L catalyst concentration) within 180 min, achieving 90% efficiency[33]. Similarly, Chen et al. reported a CuS/UiO-66 composite that degraded methylene blue dye (150 mg/L catalyst concentration) in 60 min, also with 90% efficiency[2]. Notably, both studies required relatively high catalyst concentrations and longer reaction times to achieve 90% degradation. In contrast, our synthesized PANI/Ni-Al LDH composite achieved 99% Congo red dye degradation within 120 min using comparatively lower catalyst concentration. Furthermore, we have also explored the photocatalytic water splitting performance of our composite, which demonstrates its multifunctionality. The integration of Ni-Al LDH with PANI in a two-dimensional heterojunction considerably lowers electron–hole recombination and improves the material's ability to absorb light. This study aims to develop a novel binary nanocomposite consisting of polyaniline (PANI), Ni-Al LDH, and to assess its

efficacy in degrading Cango red (CR) dye via photocatalysis under visible light. Comprehensive analyses of the synthesized composites implemented using FTIR, XPS, UV-DRS, XRD, HRTEM, and FESEM techniques. Various factors influencing photocatalysis were evaluated, such as solution pH, catalyst concentration, light-exposed area, and the role of scavengers. To gain a more comprehensive understanding, HRMS was utilized to examine both the intermediate and final degradation products, and the underlying mechanisms were investigated. To assess its potential for sustainable hydrogen generation, the photocatalyst was tested for photocatalytic water splitting under diverse scenarios, including the presence of a sacrificial agent and different pH values. By analyzing AQE%, the photocatalyst exhibited strong photon-harvesting abilities, contributing simultaneously to pollutant degradation and H_2/O_2 evolution.

5.2. Methodology:

The following chemicals were used for the synthesis of the materials: aluminium nitrate (98%, LOBA CHEMIE), aniline (99%, LOBA CHEMIE), hydrochloric acid (36%, LOBA CHEMIE), ammonium persulfate (98%, SDFCL), urea (99.5%-100%, LOBA CHEMIE), nickel nitrate (98%, LOBA CHEMIE), ammonium fluoride (99%, LOBA CHEMIE). Cango red was purchased from LOBA CHEMIE.

5.2.1. Methodology for synthesizing PANI, LDH, and the binary nanocomposite:

The synthesis of PANI was carried out using the oxidative polymerization technique, as described in our previous study.

A hydrothermal technique was employed to synthesize the Ni-Al layered double hydroxide (LDH). Initially, 0.435 g of nickel nitrate and 0.188 g of aluminium nitrate were mixed into 50 mL of distilled water and agitated steadily for 30 min. Afterward, 0.296 g of ammonium fluoride along with 1.20 g of urea was introduced, followed by an additional 30 min of stirring. After mixing, to initiate the hydrothermal reaction, the solution was sealed in a 50 mL Teflon-lined autoclave and maintained at 120 °C for a duration of 24 hrs. Once the solution naturally returned to room temperature, the product was separated via centrifugation and washed several times with ethanol and distilled water. To complete the process, the powder was placed in an oven at 60 °C and dried for 12 hrs.

As illustrated in **Scheme 5.1**, the binary nanocomposite was synthesized by initially dispersing a precise amount of polyaniline (PANI) in 50 mL of water, followed by ultrasonic treatment to achieve a homogeneous suspension. Subsequently, specific quantities of nickel nitrate and aluminium nitrate were dissolved into the PANI dispersion. After adding ammonium fluoride and urea, the solution was stirred steadily for 60 min. Hydrothermal synthesis was carried out by sealing the solution in a 50 mL Teflon-lined autoclave and heating it at 120°C for 24 hrs. Upon completion, the autoclave was cooled gradually to ambient temperature without external intervention. The resultant material was recovered by centrifugation and extensively rinsed several times using distilled water and ethanol. The powder was ultimately dried in an oven set to 60 °C for 12 hrs. Three different compositions of binary nanocomposites were prepared with varying LDH contents-2, 5 , and 7 wt% - with the remaining portion consisting of PANI. These samples were designated as 2PL, 5PL, and 7PL, respectively.

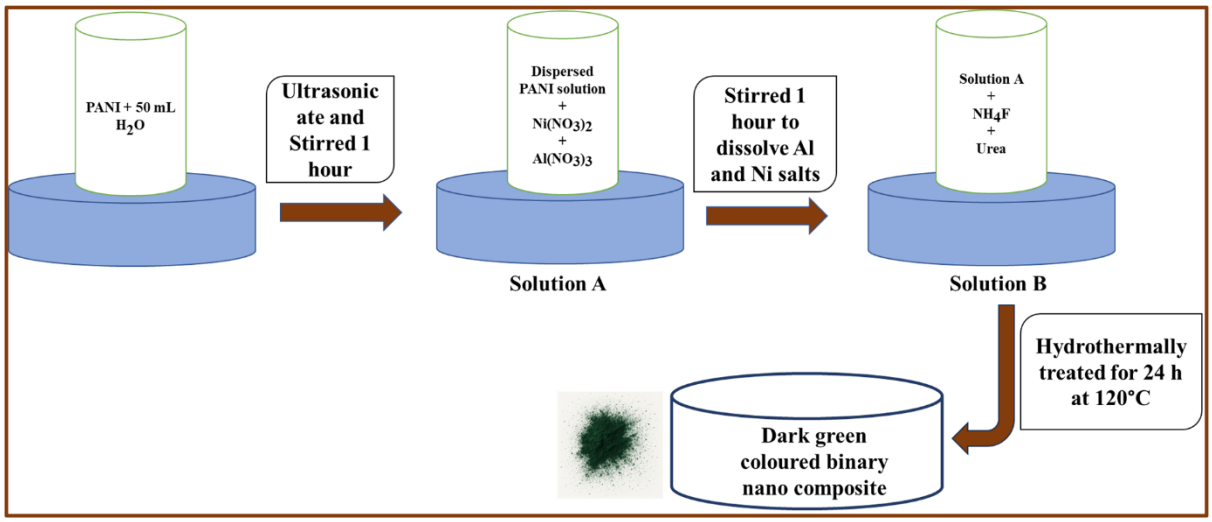

Scheme 5.1: Synthesis procedure of PL nanocomposite.

5.2.2. Techniques for characterization:

The as-prepared nanocomposites were characterized by various characterization techniques. The ultraviolet-visible absorption spectra of the synthesized materials were measured utilizing a UV-vis spectrophotometer instrument (Shimadzu UV 2600). Photoluminescence spectra were recorded utilizing a spectrofluorometer instrument (Shimadzu RF-6000). The shape of the prepared composite was analyzed using field emission scanning electron microscopy (FESEM, JEOL). The functional groups present in the materials were identified using Fourier transform infrared (FTIR) spectroscopy (Shimadzu IRTracer-100). The X-ray Photoelectron Microscopy (XPS) analysis was performed using a monochromatic aluminium source, specifically Al ka

radiation, on an Omicron ESCA instrument with an energy of 1486.7 eV. Brunauere-Emmette-Teller (BET) method and Barrette-Joynere-Halenda (BJH) method were done by Belsorp Mini II instrument. The degraded products and possible Intermediate by-products of the degradation product were analysed by High Resolution Mass Spectrometry (HRMS, Bruker SHS-40). The amount of hydrogen produced by photocatalytic water splitting was measured using GC-TCD (nucon 5765).

5.2.3. Photocatalytic activity experiments:

5.2.3.1. Examining the performance of photocatalytic degradation:

To evaluate the degradation activity, 4 mg of catalyst was mixed with 20 mL of Congo Red dye solution (25 ppm). The system was maintained under dark conditions for 2 hrs to enable the establishment of adsorption–desorption balance. Under constant agitation, the solution underwent photodegradation within the photocatalytic setup illuminated by a 40 W LED lamp (637 W/m^2). Using a UV–vis spectrophotometer, the CR concentration was measured, and its degradation efficiency was computed using the formula of **equation 2.5 (Chapter 2)**. The degree of mineralization was calculated using the **equation 3.1 (Chapter 3)**.

The HRMS technique was applied to detect CR degradation products, where their m/z values served to infer structural information. Within this framework, 'm' indicates the mass of the molecule, and 'z' represents its charge state. For the analysis, the mobile phase consisted of HPLC-grade water.

5.2.3.2. Photocatalysis-driven hydrogen generation:

The photocatalyst (2 mg) was suspended in 20 mL of water with 1 mL of methanol added as a sacrificial reagent. Photocatalytic tests were conducted under four scenarios: no sacrificial agent, acidic solution, basic solution, using a sacrificial reagent under inert nitrogen conditions. An airtight lid was used to tightly seal the vessel, and hydrogen produced through photocatalysis was analyzed using gas GC equipped with a TCD, with nitrogen serving as the transporting gas. The experiment was carried out in a photocatalytic setup, utilizing a 40 W Philips LED bulb as the illumination source. A magnetic stirrer was employed during the photocatalytic reaction to ensure continuous mixing of the system. To determine the apparent quantum efficiency (AQE), the formula was applied form **equation 2.15 (Chapter 2).**

5.3. Results and discussion:

5.3.1. Evaluation of the structural and functional properties of the prepared photocatalyst:

5.3.1.1. Assessment of spectral behaviour:

X-ray diffraction patterns collected between 10° and 50° were used to investigate the phase composition and crystallinity of the synthesized samples **(Fig 5.1a)**. XRD data show specific peaks located at 2θ angles of 14.59° (121), 19.26° (310), and 25.69° (003), confirming the successful inclusion of PANI. The distinct peak observed at 25.69° (003) specifically demonstrates the structural polymeric features of PANI [34]. The diffraction peaks observed at 11.44°, 23.12°, 34.80°, 39.34, and 46.59°, respectively the observed reflections for pure Ni-Al LDH correspond to the (003), (006), (012), (015), and (018) planes in order. These peaks match the hexagonal symmetry of LDH, as identified by JCPDS reference 15-0087[35][36]. For the PANI/LDH composites, the peak corresponding to pure PANI (19.15°, 16.17°) was observed alongside the peaks of LDH (23.58°) with some amount of shifting, confirming its presence in the composites. The intensity of the LDH peaks increased as the weight percentage of LDH (ranging from 2 to 7%) in the PANI/LDH samples rose, indicating successful formation of the composite. According to the Scherrer equation, the crystallite dimensions were calculated as 80.25 nm for LDH, 135.54 nm for PANI, and 104.23 nm for the 5PL material.

The light absorption ability of a photocatalyst significantly contributes to enhancing its photocatalytic activity. The optical absorption characteristics of the prepared photocatalysts, as revealed by UV–vis spectroscopy, are shown in **Fig 5.1b**. Although LDH exhibits strong absorption in the UV range (250–400 nm), the PL binary nanocomposites show enhanced absorption spanning into the visible region. PANI is responsible for the enhanced visible light absorption, acting as a sensitizer that activates the photocatalyst under visible light. **Scheme 5.1** demonstrates that the change in color from LDH's light green to the darker hue of the nanocomposites signifies efficient PANI loading and boosted visible-light sensitivity. The energy band gap of a semiconductor can be determined using Tauc's equation: $(\alpha h\nu)^{1/2} = A(h\nu - Eg)$. In the given equation, hν signifies the energy of the incident photons, Eg refers to the band gap energy, A is a proportionality constant, and α stands for the absorption coefficient of light. Here, n is used to describe the type of electronic transition; when n=0.5, it indicates that

the transition is direct and allowed. In this work, the band gap energy (E_g) was estimated using plots of $(\alpha h\nu)^{0.5}$ versus photon energy. As illustrated in **Fig 5.1c**, the calculated band gap values are 2.31 eV for LDH, 1.95 eV for PANI, 1.82 eV for 2PL, 1.74 eV for 5PL, and 1.77 eV for 7PL. Photoluminescence spectroscopy is widely employed to assess key processes such as carrier trapping, migration, transport, separation, and recombination. The photoluminescence

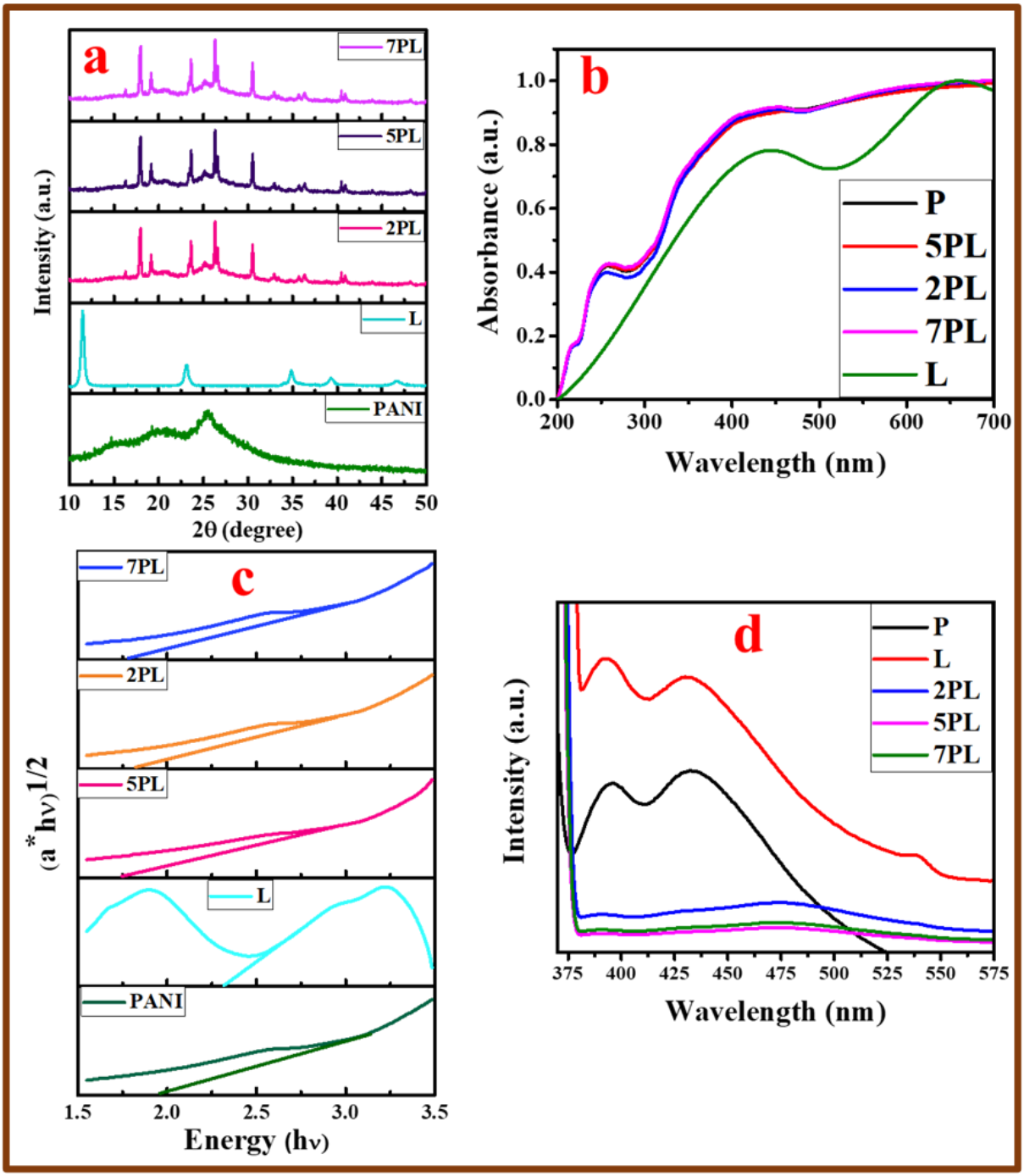

Fig 5.1: (a) XRD pattern, (b) UV-Vis DRS spectra, (c) Tauc's plot, and (d) PL spectra of PANI, L, 2PL, 5PL, and 7PL.

emission spectra of PANI, LDH, and PL composites are shown in **Fig 5.1d**, with all samples exhibiting a dominant peak at approximately 452 nm. It is noteworthy that the photoluminescence emission intensity of the PL composites is considerably reduced in comparison to that of pure PANI, and LDH. The diminished fluorescence intensity suggests successful division of photoinduced e^--h^+ pairs throughout the composite material. Effective control of e^--h^+ pair dynamics is a key factor in advancing the effectiveness of photocatalytic degradation. Enhancing the division of e^--h^+ pairs reduce their recombination rate, thus improving their involvement in photocatalytic processes. Also, from Electrochemical Impedance Spectroscopy (EIS) **(Fig 5.2)**, the 5PL composite exhibits superior charge separation compared to parent PANI and LDH, as indicated by its smaller arc radius.

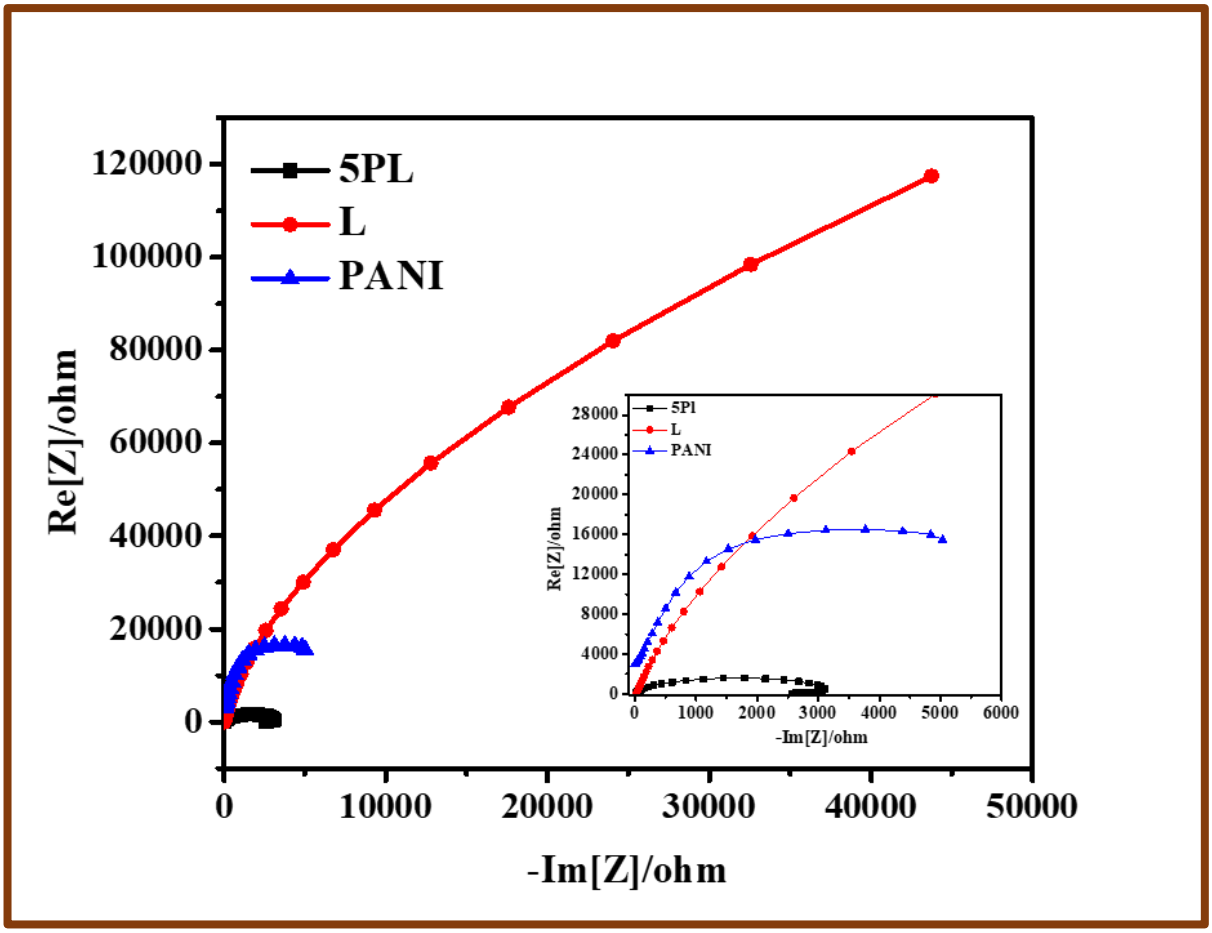

Fig 5.2: EIS spectra of 5PL, L, and PANI.

The chemical composition and phase state of the synthesized binary nanocomposite (5PL) were analyzed using X-ray photoelectron spectroscopy (XPS). As shown in **Fig 5.3a**, the XPS broad scan spectrum clearly indicates the manifestation of lithium (Li), Aluminium (Al), carbon (C), nitrogen (N), and oxygen (O) within the composite material. A more refined analysis of the elements and their chemical environments was performed by applying Gaussian deconvolution to the Ni 2p, Al 2p, C 1s, N 1s, and O 1s spectra. As depicted in **Fig 5.3b**, four separate binding energy peaks are evident in the C 1s spectral profile. The peak located at 284.23 eV is indicative of C–C and C–H bonds, which are free of oxygen functionalities. Graphitic carbon is represented by the 285.12 eV peak, whereas the 286.48 eV peak corresponds to nitrogen-functionalized carbon, such as C–N bonds[37][38]. **Fig 5.3c** displays the N 1s spectrum, which features three distinct peaks associated with various nitrogen coordination states. The peak observed at 399.18 eV is indicative of quinoid amine species. while the adjacent peak at 399.84 eV indicates benzenoid amine species. A binding energy of 401.06 eV corresponds to the nitrogen cationic radical (N^{+}•)[39]. The O 1s spectrum **(Fig 5.3d)** shows binding energy peaks at 529.10 eV and 531.73 eV, linked to M–O–H and M–O–M bonding environments, respectively[40]. As depicted in **Fig 5.3e**, the Ni 2p spectrum exhibits key peaks at 856.29 eV and 873.94 eV, which are indicative of the spin-orbit splitting for Ni^{2+}, allotted to Ni $2p_{3/2}$ and Ni $2p_{1/2}$, respectively. In addition, satellite features emerge at 861.96 eV and 879.68 eV in the

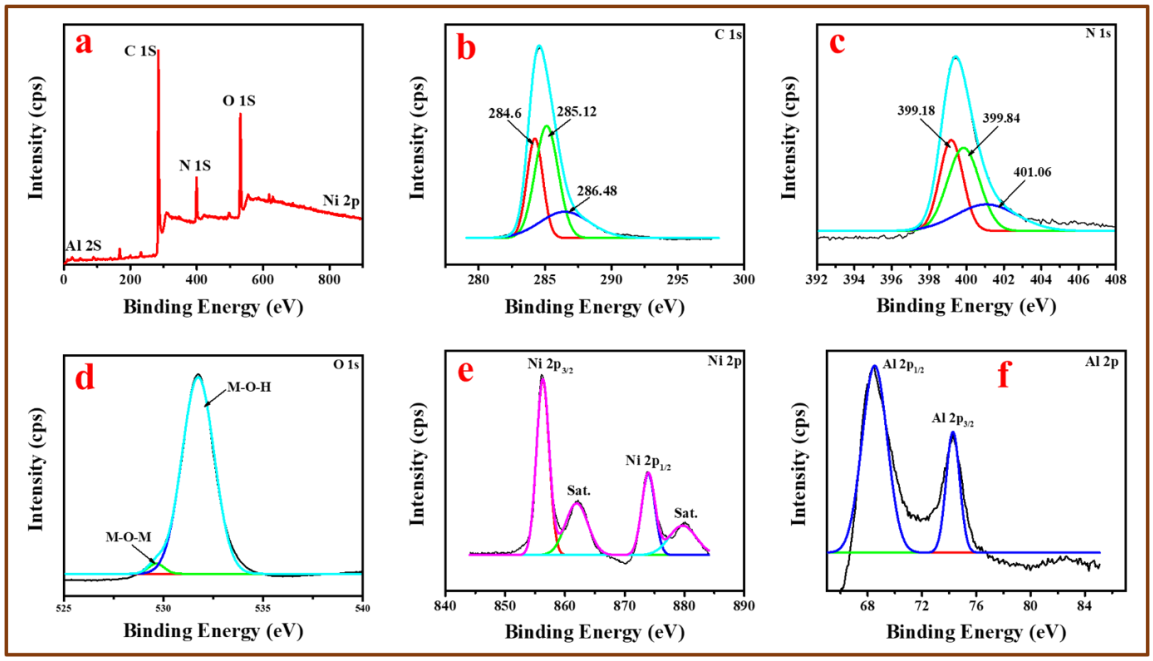

Fig 5.3: presents the XPS analysis of the 5PL sample, including (a) the survey spectrum and high-resolution core-level spectra of (b) C 1s, (c) N 1s, (d) O 1s, (e) Ni 2p, and (f) Al 2p.

binding energy spectrum. Likewise, peaks at 68.49 and 74.25 eV appear in the Al 2p spectrum **(Fig 5.3f)**, representing the Al $2p_{1/2}$ and Al $2p_{3/2}$ states, respectively[23][41].

As depicted in **Fig 5.4**, Fourier-transform infrared (FTIR) spectroscopy identified distinct absorption bands associated with distinct functional groups and their characteristic vibrational modes. A distinct peak at 1536 cm^{-1} indicates the occurrence of C=C stretching in benzenoid structures, whereas the absorption at 1390 cm^{-1} arises from C–N stretching vibrations. Moreover, the spectral peak at 1265 cm^{-1} signifies the existence of a protonated C–N functional group. The signal at approximately 776 cm^{-1} also indicates the delocalization of electrons within the polymer network[42][43]. **Fig 5.4** displays broad absorption features near 3480 cm^{-1} and 1630 cm^{-1}. The band at ~3480 cm^{-1} arises from the symmetric and asymmetric stretching of brucite-like Ni/Al–OH layers, whereas the signal at ~1630 cm^{-1} corresponds to the bending vibration of water molecules confined in the LDH interlayer space. The intense vibrational band at approximately 1370 cm^{-1} corresponds to the antisymmetric ν_3 mode of interlayer carbonate anions, while the peak at 2150 cm^{-1} is associated with the presence of CO_2 in the Ni-Al LDH samples. The bands observed under 800 cm^{-1} are due to lattice vibrations involving Ni–O and Al–O bonds, as well as Ni–O–Al bridges in the LDH layers[44]. The appearance of signature peaks from individual PANI and LDH phases within the nanocomposite confirms their effective integration into a heterojunction.

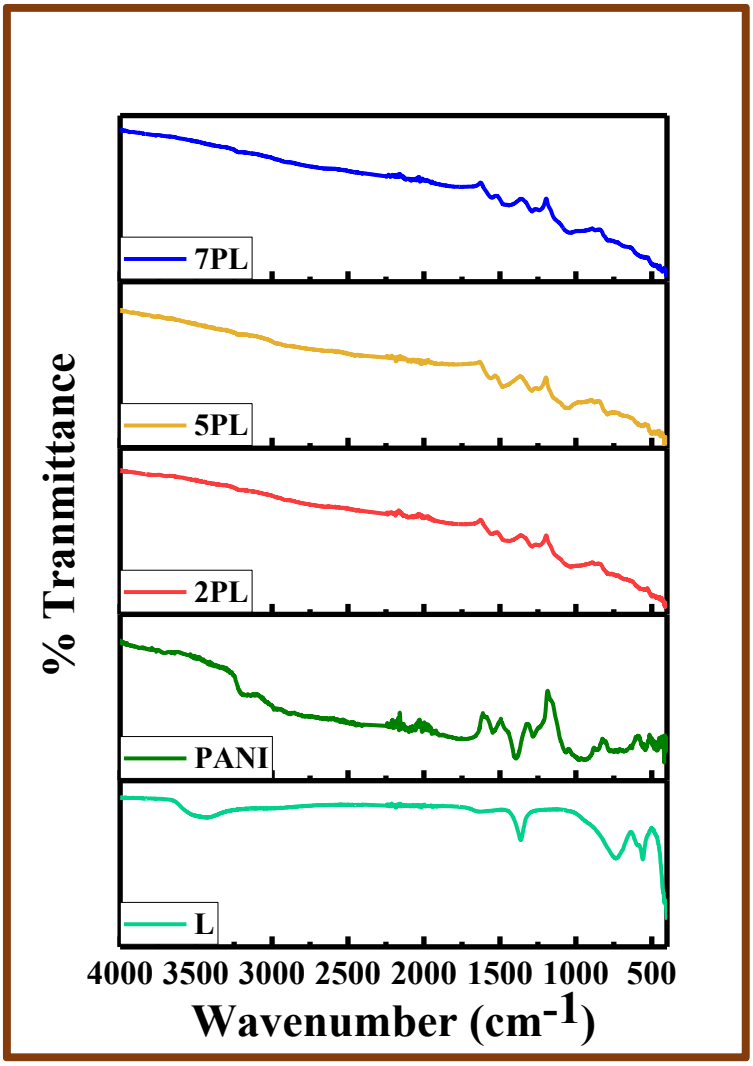

Fig 5.4: FTIR of L, PANI, 2PL, 5PL, and 7PL.

5.3.1.2. properties of the material's surface:

FESEM was utilized to characterize the microstructural features of the synthesized composite material. **Fig 5.5(a–c)** depicts the FESEM surface morphologies of LDH, PANI, and the 5PL composite. The FESEM image of the pristine LDH, shown in **Fig 5.5b**, clearly reveals flower like particles with nanoscale thickness of the plates. A notable morphological difference is observed in the 5PL nanocomposite compared to the pristine LDH, as depicted in **Fig 5.5c**, where fibrous PANI structures are observed covering the LDH surface. The FESEM analysis revealed distinct features of polyaniline and LDH, supporting the effective formation of heterojunctions. As depicted in **Fig 5.6**, EDS analysis provided evidence of the nanocomposite's elemental constituents, which include C, N, O, Ni, and Al.

A more comprehensive examination of the 5PL nanocomposite's surface and internal structure was performed using high-resolution TEM. The fibrous morphology of PANI surrounding LDH plates in the HRTEM visualization **(Fig 5.5d)** confirms the establishment of a PANI–LDH 2D/2D heterojunction. As illustrated by **Fig 5.5e**, the HRTEM image highlights the boundary between LDH and PANI, with measured spacings of 0.760 nm and 0.350 nm matching the (003) planes of LDH and PANI.

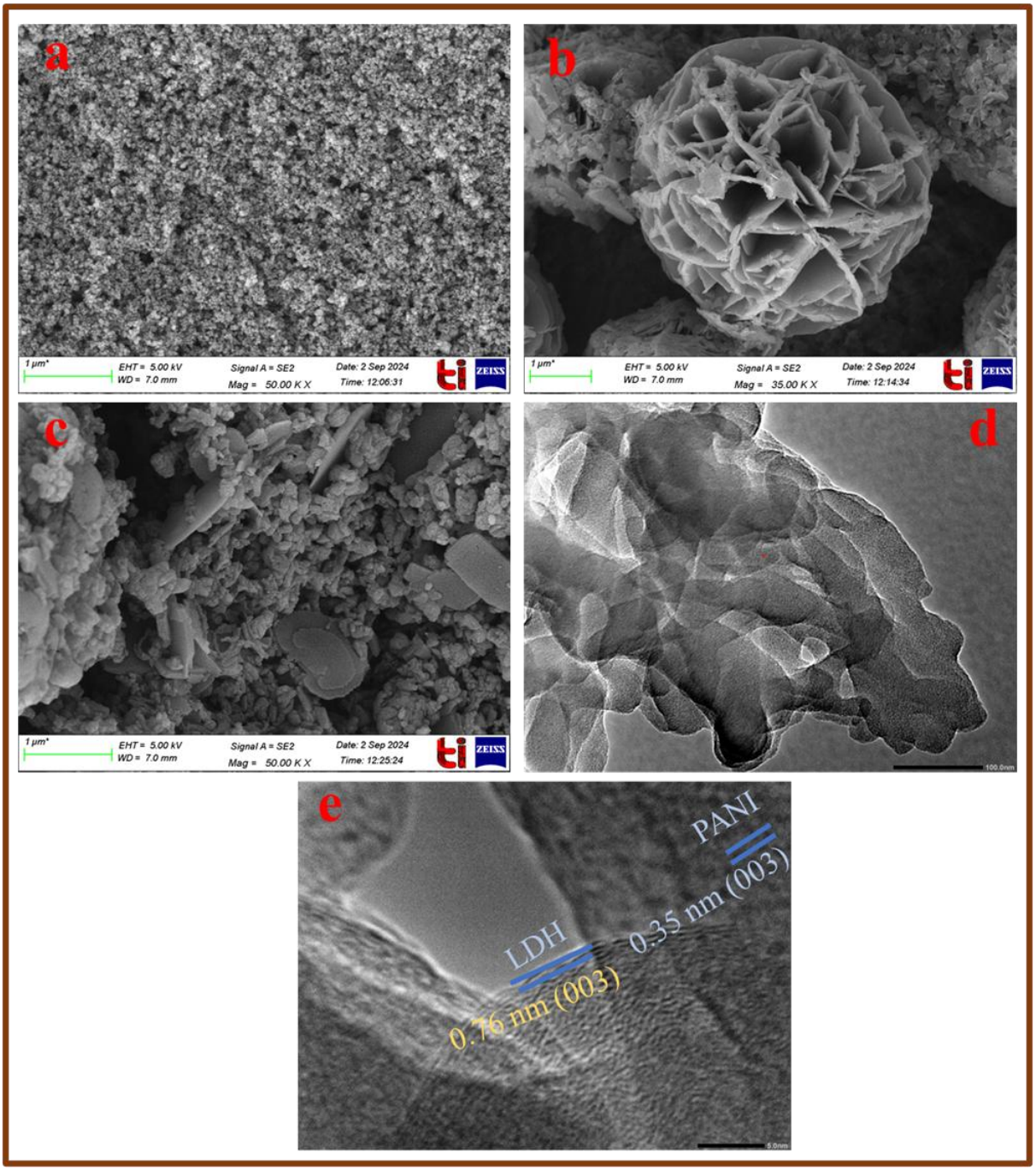

Fig 5.5: FESEM image of (a) PANI, (b) LDH, (c) 5PL, and HRTEM images (d-e) of 5PL.

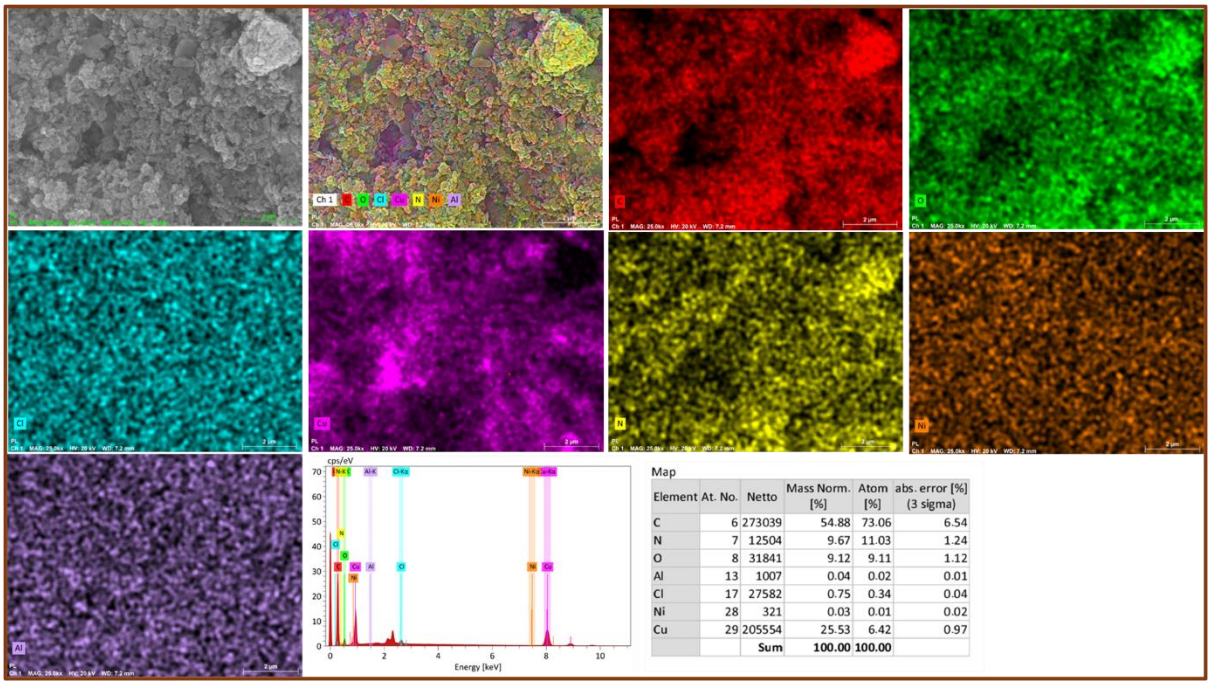

Fig 5.6: Elemental mapping, EDS spectrum of 5PL.

The synthesized nanocomposites' surface features were analyzed through specific surface area measurements. **Fig 5.7-5.8** displays a type IV Langmuir isotherm for all composites, as well as for bare PANI, and LDH, confirming their mesoporous characteristics. The pore size distribution was analyzed using the BJH method, as shown in **Fig 5.8**. As shown in **Table 5.1**, PANI is characterized by a notably large surface area and porous volume. The surface areas of all the composites are higher than those of pure PANI, and LDH. The surface area of the PL composites follows an increasing trend in the order of: 2PL (38.4 m^2/g) < 7PL (44.2 m^2/g) < 5PL (53.6 m^2/g). Enhanced pollutant adsorption and an expanded active surface area endow the 5PL composite with superior photocatalytic performance, thereby enabling more efficient hydrogen generation via water splitting.

Table 5.1: BET-specific surface area, total pore volume, and average pore diameter.

Photocatalyst	Specific Surface Area (m^2/g)	Total Pore Volume (cm^3/g)	Average Pore Diameter (nm)
PANI	18.3	0.0073	4.2
LDH	30.5	0.0203	4.5
2PL	38.4	0.044	5.0
5PL	53.6	0.0841	6.4
7PL	44.2	0.052	4.8

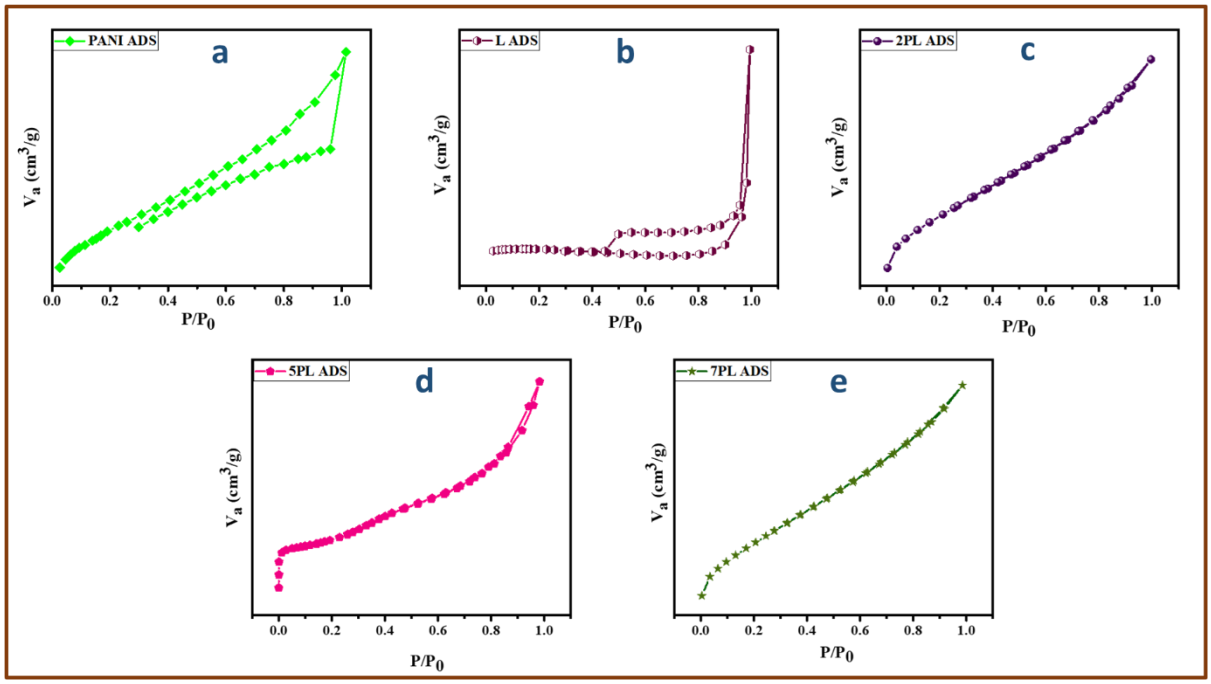

Fig 5.7: (a), (b), (c), (d), and (e) adsorption-desorption curves of PANI, L, 2PL,5PL, and 7PL respectively.

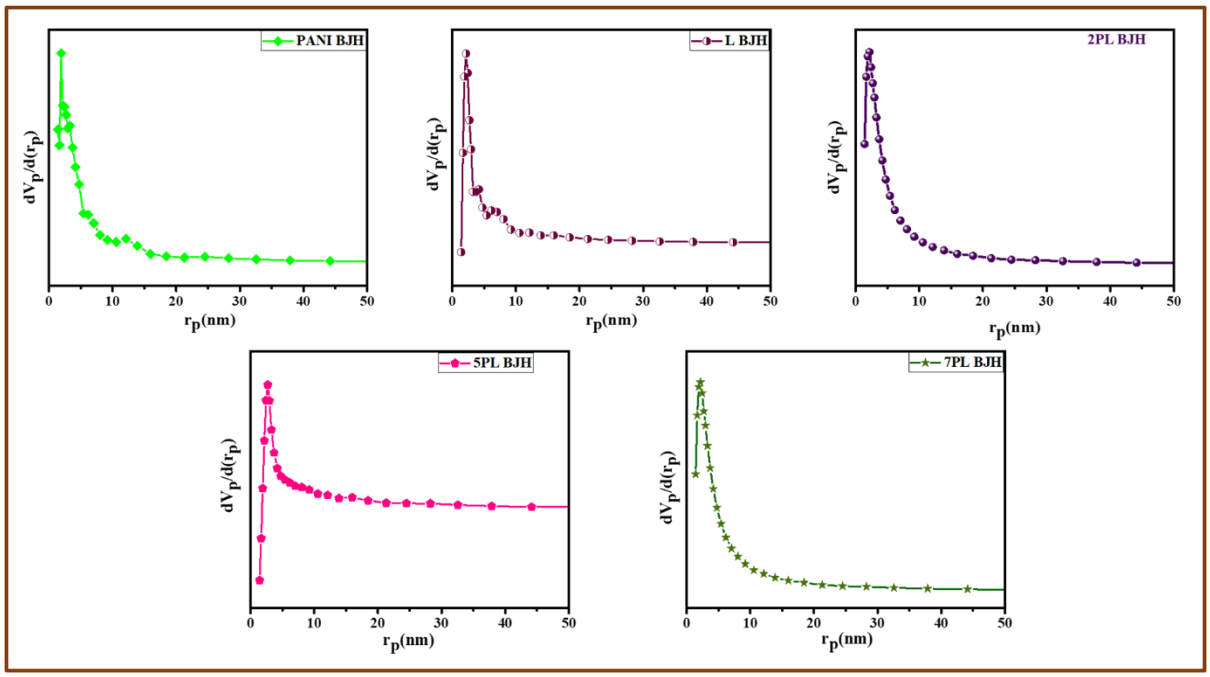

Fig 5.8: (a), (b), (c), (d), and (e) BJH plots of PANI, L, 2PL, 5PL, and 7PL respectively.

5.3.2. Photocatalytic degradation of the organic dye Cango red (CR):

As depicted in Fig. 4(d), exposure to LED light alone (photolysis) results in minimal degradation of Congo red (CR), with absorbance decreasing by merely 2% after 120 min. This slight decrease suggests that CR exhibits strong resistance to degradation under light exposure. After 120 min in the absence of light, allowing for adsorption-desorption equilibrium, the 5PL composite demonstrated the highest adsorption capacity for CR, removing approximately 54%. In contrast, lower adsorption efficiencies were observed for other materials: PANI (3.27%), L (25.87%), 2PL (49%), 7PL (52%), and TiO_2 (3.8%) as shown in **Fig 5.9**. The improved adsorption capacity of 5PL can be attributed to its increased surface area and a larger number of sites available for the negative dye, which resulted from the addition of L onto PANI. An ideal L load optimizes the interaction between PANI, and L, improving photocatalytic performance by narrowing the band gap energy, increasing light absorption, and minimizing the recombination of e^--h^+ pairs. To quantify the degradation kinetics of CR, the experimental data were modelled with a pseudo–first-order rate **equation 3.2 (Chapter 3)**. The calculated degradation rate constants for the different samples are: PANI (0.006 min^{-1}), L (0.00458 min^{-1}), 2PL (0.027 min^{-1}), 5PL (0.037 min^{-1}), 7PL (0.032 min^{-1}), and TiO_2 (0.0038 min^{-1}). A synergy factor (R) was used to quantify the interactive effect of PANI and L, calculated using the equation below:

$$\mathbf{R} = \frac{K_{PANI+L}}{K_{PANI}+K_L} \quad \textbf{(5.1)}$$

Photodegradation kinetics for the PANI/L composite and for PANI and L on their own are represented by $K_{(PANI+L)}$, $K_{(PANI)}$, and $K_{(L)}$, respectively. The calculated synergy factors for 2PL, 5PL, and 7PL are 2.55, 3.5, and 3.02, respectively. Among all the samples, 5PL demonstrated the greatest synergy factor, consequently, it achieved the maximum efficiency in photocatalytic degradation with a corresponding rate constant of 0.037 min^{-1}.

5.3.2.1. Influence of varying catalyst dosage levels:

Photocatalytic performance is highly dependent on the dosage of the catalyst applied. To investigate the effect of catalyst dosage on CR degradation, a range of experiments was conducted using varying amounts (1 to 6 mg) of the 5PL ternary photocatalyst. while maintaining a constant CR concentration of 25 ppm. A low photocatalyst loading of 0.1 g/L yielded fewer reactive species for CR degradation, which in turn decreased the photocatalytic performance. The highest degradation efficiency was achieved at a dosage of 0.4 g/L **(Fig 5.9a)**, where both the availability of active sites and the utilization of light energy reached their peak. Despite the higher catalyst loading above 0.4 g/L, there was no substantial improvement observed in the degradation efficiency. This may be attributed to the aggregation of catalyst particles, which can lower the transparency of the solution, hinder light penetration, and potentially block or deactivate portions of the catalyst surface. It was observed that using 0.4 g/L of catalyst provides the best outcome for attaining superior CR degradation performance.

5.3.2.2. Influence of Solution pH on the Reaction:

Variations in solution pH significantly affect the composite's ability to adsorb the dye, thereby determining its degradation performance[45]. To assess the effect of pH on CR removal, pH variation in the solutions was attained by carefully titrating with either 0.1 N hydrochloric acid or 0.1 N sodium hydroxide. Prior to and after degradation, the pH of the catalyst (0.4 g/L) and dye mixtures was measured. **Fig 5.9b** demonstrates that the pzc of the 5PL composite lies near pH 6.7. As illustrated in **Fig 5.9c**, removal efficiency climbs from pH 1 to 6, peaks at pH 7.2, and then diminishes under alkaline conditions. This outcome demonstrates how solution pH directly affects the degradation capability of the photocatalyst. Varying pH changes the composite's surface charge, which in turn significantly governs CR dye adsorption and

decomposition. A pH of 7.2 yielded the most effective photocatalytic results, underscoring the importance of maintaining suitable pH levels for maximum performance. Specifically, hydroxyl radicals (·OH) are the primary oxidizing species in photocatalysis. In basic medium, the higher OH^- concentration provides more precursors for ·OH generation, thereby enhancing degradation efficiency. In contrast, under acidic conditions, ·OH generation is suppressed and many reactive oxygen species (ROS) are less stable, leading to reduced degradation performance. The presence of excess hydroxide ions in highly basic solutions promotes the deposition of metal hydroxides on the catalyst, thereby lowering its degradation performance.

5.3.2.3. Impact of the exposed light area:

An evaluation was conducted to determine how different light exposure areas influence the photocatalytic efficiency of the 5PL nanocomposite under visible light[46]. The photocatalytic experiment involved stirring a 0.4 g/L suspension of the catalyst with 25 ppm CR dye under visible light for two hours. To control the area exposed to light, reaction vessels with different diameters were used, ensuring that the lamp remained fixed at 6 cm above the liquid surface. An enhancement in degradation performance was observed with the expansion of the region exposed to visible light as depicted in **Fig 5.9e**. Increased illuminated area intensified light absorption, which in turn enhanced the degradation performance and optimized efficiency.

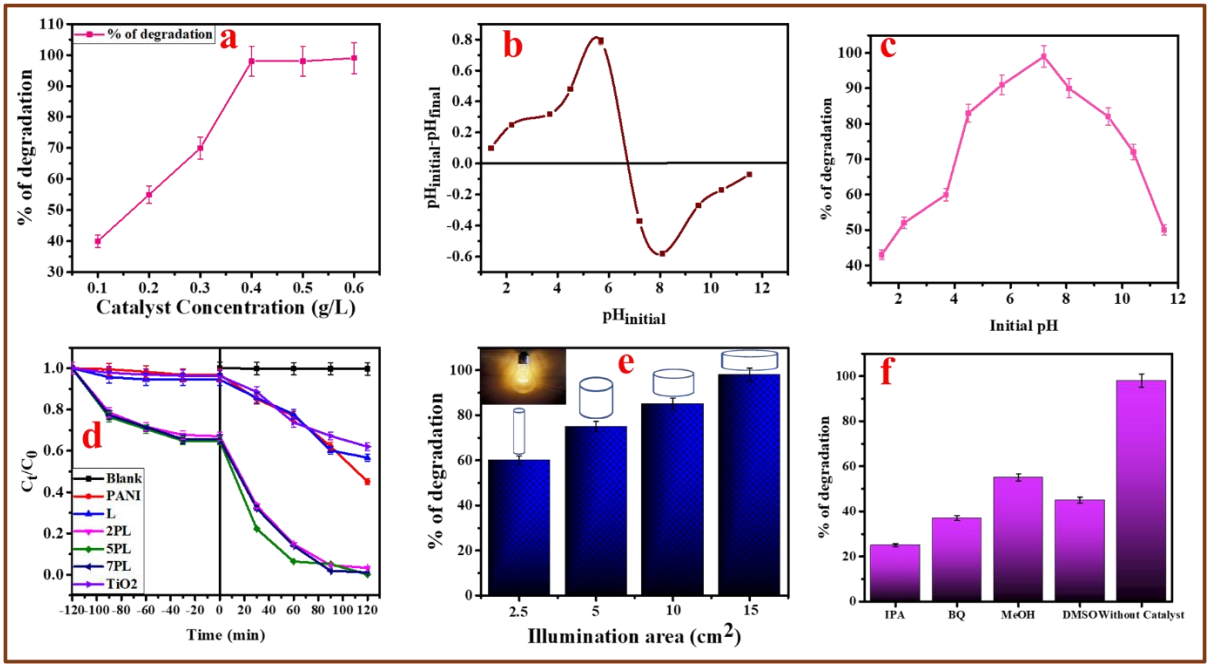

Fig 5.9: (a) Effect of catalyst concentration, (b) pzc studies, (c) effect of pH, (d) kinetic studies, (e) impact of illuminated surface area, and (f) scavenger studies.

5.3.2.4. The anticipated degradation mechanism of CR:

Evaluating the photodegradation of organic dyes involves tracking change in Total Organic Carbon (TOC) under light exposure. After 120 min of illumination with visible light, CR exhibits a significant decrease in TOC levels, by 50%. As shown in **Fig 5.13a**, this suggests that the dye undergoes 50% mineralization. The intermediates formed exhibit low potential for complete mineralization, implying that the original dye is degraded into less mineralizable compounds. To verify the degradation process and identify intermediate products, an HRMS analysis was conducted on the CR dye. The resulting mass spectra obtained at 120 min is presented in **Fig 5.10**. According to literature, the degradation of CR can proceed through several pathways: (i) disruption of the carbon–sulfur bond within the aromatic structure, (ii) cleavage of the azo (─N═N─) linkage, (iii) fragmentation of the benzene aromatic core, and (iv) breaking of multiple carbon–nitrogen and carbon–carbon linkages. Breaking of the ─N═N─, C─N, and C─C bonds results leading to the generation of various low-molecular-weight intermediate species characterized by m/z values of 395.9, 351.13, 294.18, 174.995 as shown in **Fig 5.10**. These intermediates can subsequently undergo further mineralization, leading to the generation of CO_2, H_2O. **Fig 5.11** presents the potential structures of intermediate compounds generated during the breakdown of the CR dye[47][48][49].

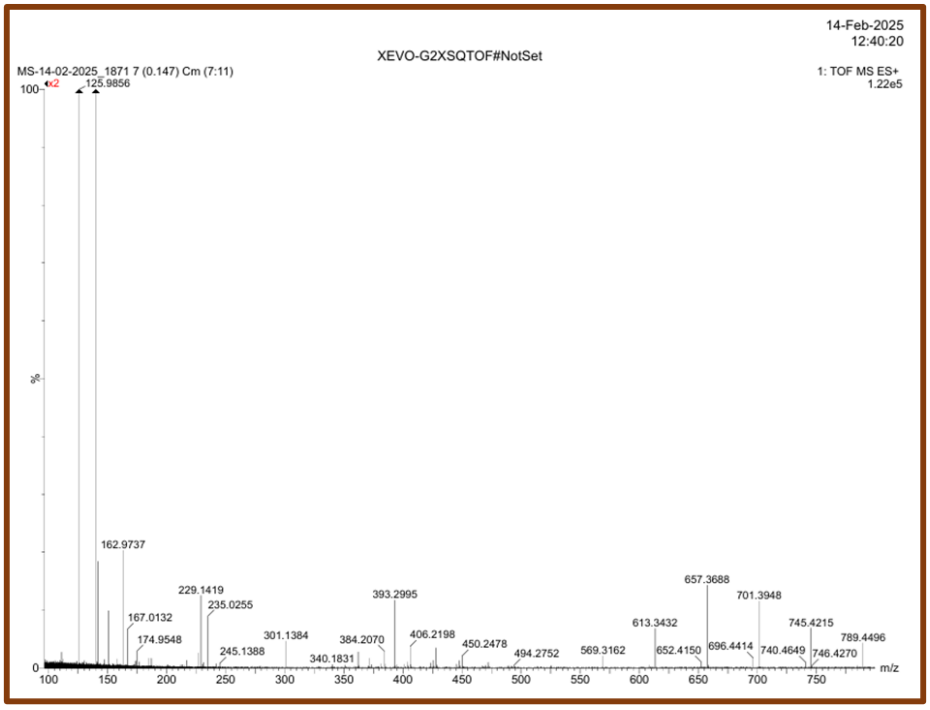

Fig 5.10: GC-MS data after degradation of Cango red.

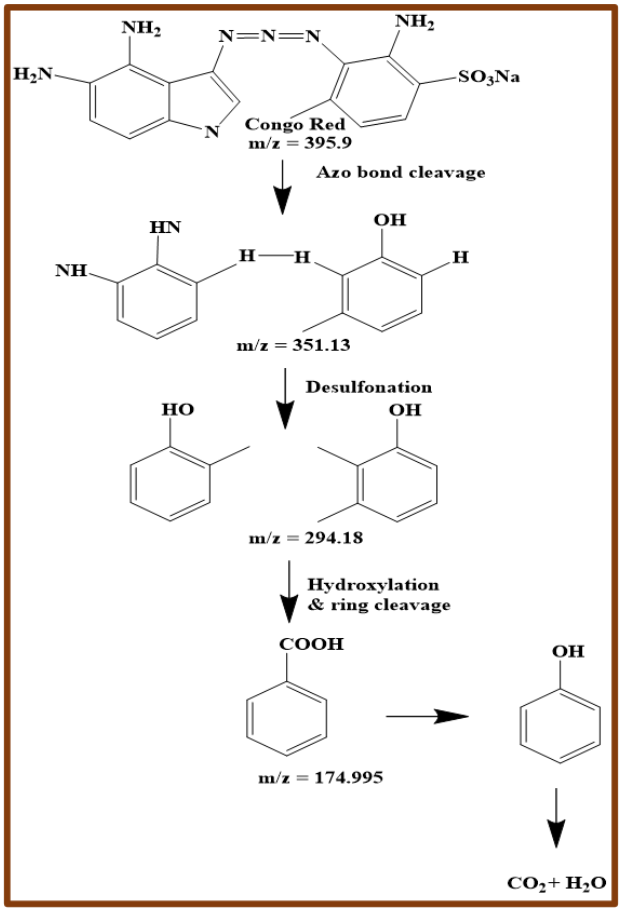

Fig 5.11: Suggested mechanism for degrading Congo Red (CR) via photocatalysis with the 5PL catalyst.

5.3.2.5. Effect of scavenging agents on charge carrier transfer processes:

The pathway by which degradation occurs is primarily driven by conduction band electrons, valence band holes, and contribution from reactive intermediates including hydroxyl and superoxide radicals, all of which are crucial to the process[50]. To identify the key reactive species participating in the process, a scavenger experiment was performed using different agents: isopropyl alcohol (IPA) for trapping hydroxyl radicals ($OH^{\bullet}$), dimethyl sulfoxide (DMSO) for electrons (e^{-}), benzoquinone (BQ) for superoxide radicals ($O_2^{\bullet-}$), and methanol for capturing holes (h^{+})[51]. Acting as a reducing species, the superoxide radical ($O_2^{\bullet-}$) reacts with benzoquinone (BQ) to produce hydroquinone. The use of DMSO emphasizes the significance of $^{\bullet}OH$ in the reaction. DMSO's oxygen atom donates lone-pair electrons to facilitate electron movement and form hydrogen bonds with the hydrogen atom of $^{\bullet}OH$ [52]. **Fig 5.9f** highlights the vital involvement of DMSO, methanol, IPA, and BQ in the degradation process, indicating the key roles of h^{+}, $OH^{\bullet}$, and $O_2^{\bullet-}$ in the underlying mechanism. The

integration of LDH into the PANI framework leads to better charge separation, resulting in heightened photocatalytic efficiency of the 5PL composite. The band diagrams of LDH and PANI were investigated to shed light on this phenomenon. As shown in **Fig 5.12**, When exposed to visible light, PANI becomes photoexcited, generating e^- and holes h^+. By moving from the CB of PANI to the VB of LDH, the energized electrons hinder the recombination process of charge carriers. This mechanism effectively reduces the rate at which electrons and holes recombine. LDH possess reduction potentials greater than that of the O_2/O_2^- couple (0.07 eV). LDH surface electrons facilitate the reduction of dissolved oxygen into superoxide species (O_2^-/OH_2). Since the oxidation potential required to convert H_2O into $OH^{\cdot}$ (+2.32 eV) is greater than the VB energy

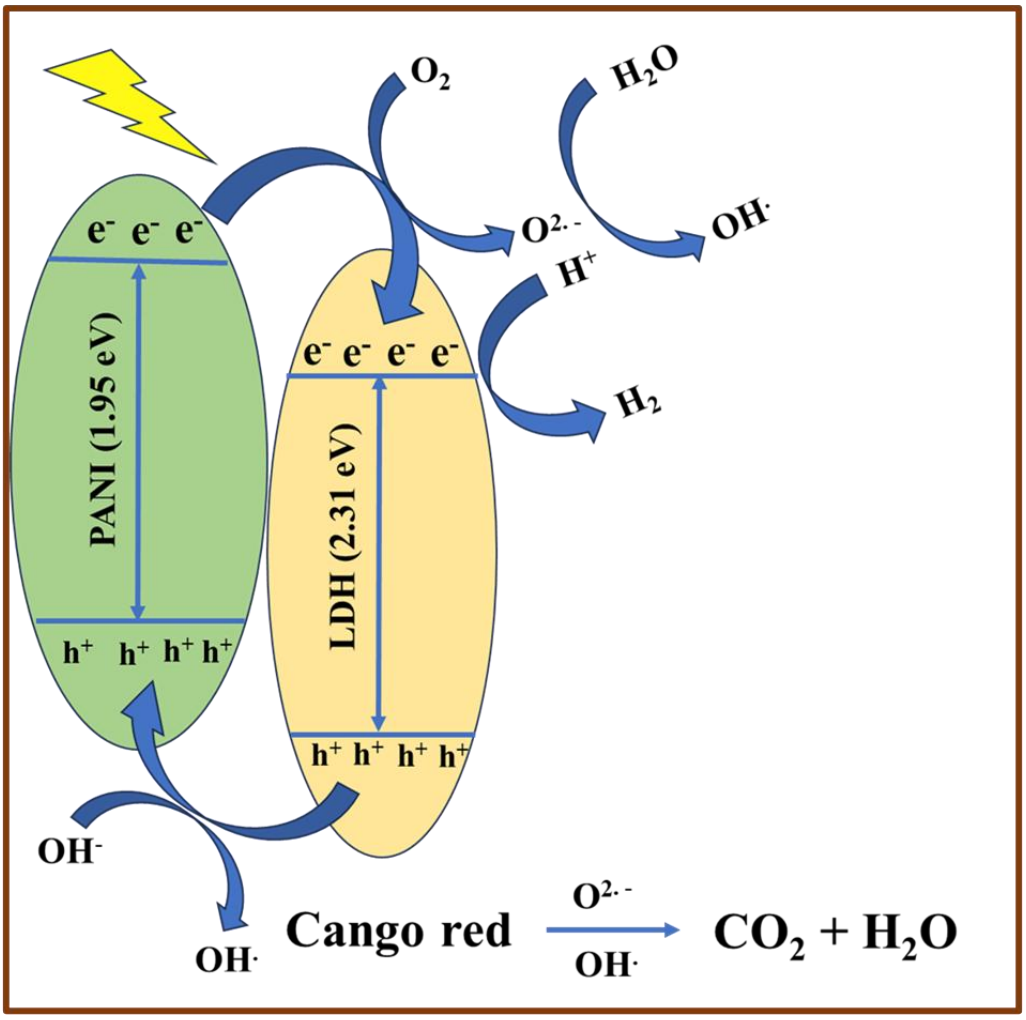

Fig 5.12: Mechanistic insight into charge migration during photocatalytic degradation and H_2 generation in the 5PL nanocomposite.

of PANI, the holes in PANI can effectively oxidize water, producing hydroxyl radicals[53]. **Fig 5.12** presents the suggested mechanism for CR degradation.

5.3.2.6. Studies on reusability:

Ensuring long-term effectiveness in environmental remediation requires a photocatalyst with strong durability. Thus, evaluating the stability of the composite over repeated photodegradation cycles is crucial. As illustrated in **Fig 5.13b**, the 5PL composite demonstrated remarkable photostability, retaining a degradation efficiency between 99 and 70% for CR over five consecutive cycles. Post-degradation XRD analysis revealed that the overall pattern remained consistent **(Fig 5.13c)**, with only a minor decrease in peak intensity, which is likely attributed to dye molecules adhering to the surface of the catalyst. The results indicate that the photocatalyst maintains both its structural stability and long-term durability. A comparative evaluation, presented in **Table 5.2**, was carried out to assess the performance of the 5PL photocatalyst against various other materials previously reported for the photocatalytic removal of organic pollutants. The comparison demonstrates that 5PL delivers higher degradation performance even at a reduced catalyst dosage, emphasizing its capability to efficiently remove persistent organic pollutants while minimizing material consumption.

Table 5.2: Comparison of different photocatalyst materials for photocatalytic degradation.

Photocatalyst	Catalyst amount (mg)	% degradation	Time (min)	References
PANI-TiO_2	10	89.7	120	[54]
PANI/TiO_2/Cotton	-	87.7	180	[55]
PANI/TiO_2/SiO_2	-	87	120	[56]
PANI/Fe-TiO_2	-	28	150	[57]
Ag-Ag_2O/TiO_2@PPY	100	100	175	[58]
PEDOT/GO/MnO_2	20	92.7	420	[59]
RGO/mesoTiO_2/AuNP	10	-	240	[60]
PANI@GN/TiO_2	50	87	180	[61]
Ag_2O/TiO_2@PPY	50	100	240	[62]
PANI/TiO2	5	99	360	[63]
Ag-ZnO/PANI	200	98.6	120	[64]
C_3N_4/$MgAl_{0.80}Ce_{0.20}$-LDH	50	90	180	[33]
CuS/UiO-66	150	90	60	[65]
5PL	4	99	120	Present work

5.3.2.7. Investigations into hydrogen generation through photocatalytic processes:

Hydrogen generation through the process of photocatalytic water decomposition was investigated over *a* 24 hr period under LED bulb illumination, utilizing four distinct

solutions configurations. The initial solution was composed of 19 ml of water mixed with 1 ml of methanol, which acted as a sacrificial agent. In the second setup, 1 mL of hydrochloric acid was combined with 19 mL of distilled water. To create the third solution, 1 mL of 1 N NaOH was diluted in 19 mL of water, yielding an alkaline medium. The final setup was composed entirely of 20 mL of distilled water. As shown in **Fig 5.13d**, the use of methanol led to the generation of 11227 ppm of hydrogen gas. By serving as both an electron donor and a h^+ scavenger, methanol facilitates the generation of intermediates such as formaldehyde and formic acid[66]. H^+ ions take part in reducing intermediate products throughout the photocatalytic cycle. Under acidic conditions, H_2 production was recorded at 9675 ppm, while basic conditions resulted in a yield of 10475 ppm. In contrast, using only water and the photocatalyst produced 8505 ppm of hydrogen, as also depicted in **Fig 5.13d**. The AQE achieved was approximately 20% when methanol was used, followed by 18% in a low pH setting, 21% under high pH conditions, and 16% with the catalyst alone. As illustrated in **Equations 5.2-5.5**, e^--h^+ pairs generated in the CB and VB serve a key function in promoting redox reactions[67][68].

In acidic condition:

Oxidation: $2H_2O\ (l) + 4h^+ \longrightarrow O_2\ (g) + 4H^+\ (aq)$ **(5.2)**

E^0(oxidation) = -1.23 V

Reduction $2H^+ + 2e^- \longrightarrow O_2\ (g) + 2H_2\ (g)$ **(5.3)**

E^0reduction = 0 V

In basic condition:

Oxidation: $2OH^-\ (aq) \longrightarrow 1/2\ O_2\ (g) + H_2O\ (l) + 2e^-$ **(5.4)**

Reduction: $2H_2O\ (l) + 2e^- \longrightarrow H_2\ (g) + 2OH^-$ **(5.5)**

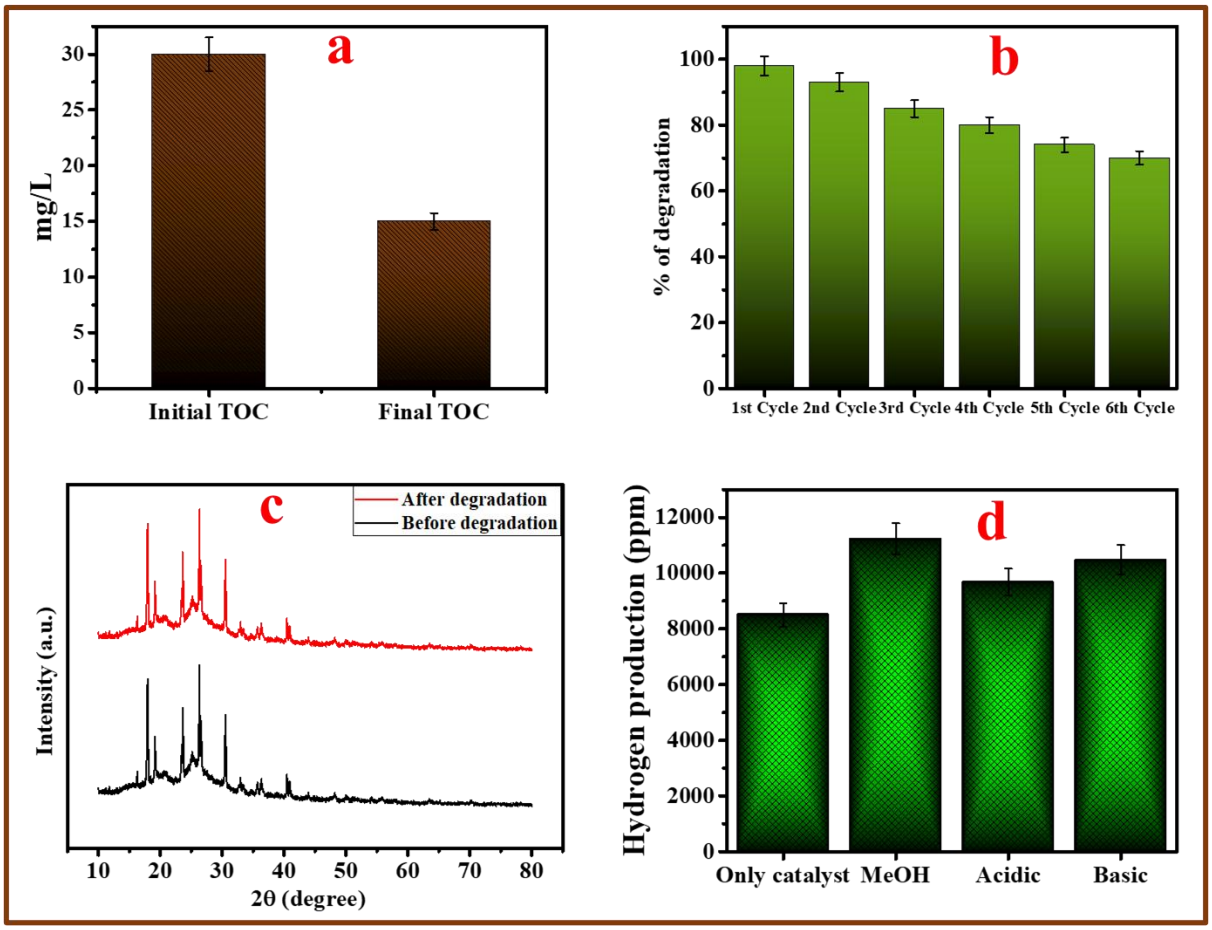

Fig 5.13: (a) TOC of CR before and after degradation, (b) reusability studies, (c) XRD of 5PL before and after degradation, and (d) hydrogen production studies.

References

[1] Z. Fan *et al.*, "Green recycling of waste poly(ethylene terephthalate) into <scp>Ni-MOF</scp> nanorod for simultaneous interfacial solar evaporation and photocatalytic degradation of organic pollutants," *EcoMat*, vol. 6, no. 1, Jan. 2024, doi: 10.1002/eom2.12422.

[2] B. Chen *et al.*, "Functional upcycling of waste polyester into Cr-MOF towards synergistic interfacial solar evaporation and organic pollutant degradation," *Mater. Today Sustain.*, vol. 24, p. 100561, Dec. 2023, doi: 10.1016/j.mtsust.2023.100561.

[3] Z. Cao *et al.*, "Amorphous Co–Pi anchored on CdSe/TiO_2 nanowire arrays for efficient photoelectrochemical hydrogen production," *J. Mater. Sci.*, vol. 54, no. 4, pp. 3284–3293, Feb. 2019, doi: 10.1007/s10853-018-3079-5.

[4] S. Nayak and K. M. Parida, "Deciphering Z-scheme Charge Transfer Dynamics in Heterostructure NiFe-LDH/N-rGO/g-C_3N_4 Nanocomposite for Photocatalytic Pollutant Removal and Water Splitting Reactions," *Sci. Rep.*, vol. 9, no. 1, p. 2458, Feb. 2019, doi: 10.1038/s41598-019-39009-4.

[5] G. Ge, X. Guo, C. Song, and Z. Zhao, "Reconstructing Supramolecular Aggregates to Nitrogen-Deficient g-C_3N_4 Bunchy Tubes with Enhanced Photocatalysis for H 2 Production," *ACS Appl. Mater. Interfaces*, vol. 10, no. 22, pp. 18746–18753, Jun. 2018, doi: 10.1021/acsami.8b04227.

[6] J. Aiswarya *et al.*, "Design of Two Homoleptic Co(III) Complexes Derived from Flexible Salicylamine and Bulky 3,5-Di- tert -butylsalicylaldehyde Ligands as Efficient Electrocatalysts for Oxygen Evolution Reaction," *ACS Appl. Energy Mater.*, vol. 9, no. 1, pp. 412–422, Jan. 2026, doi: 10.1021/acsaem.5c03152.

[7] X. Li, J. Yu, J. Low, Y. Fang, J. Xiao, and X. Chen, "Engineering heterogeneous semiconductors for solar water splitting," *J. Mater. Chem. A*, vol. 3, no. 6, pp. 2485–2534, 2015, doi: 10.1039/C4TA04461D.

[8] H. Bai *et al.*, "Waste-treating-waste: Upcycling discarded polyester into metal–organic framework nanorod for synergistic interfacial solar evaporation and sulfate-based advanced oxidation process," *Chem. Eng. J.*, vol. 456, p. 140994, Jan. 2023, doi: 10.1016/j.cej.2022.140994.

[9] S. Chaturvedi and P. N. Dave, "Environmental Application of Photocatalysis," *Mater. Sci. Forum*, vol. 734, pp. 273–294, Dec. 2012, doi: 10.4028/www.scientific.net/MSF.734.273.

[10] G. Ren *et al.*, "Recent Advances of Photocatalytic Application in Water Treatment: A Review," *Nanomaterials*, vol. 11, no. 7, p. 1804, Jul. 2021, doi: 10.3390/nano11071804.

[11] S. Bao, Y. Wang, Z. Wei, W. Yang, and Y. Yu, "Highly efficient recovery of heavy rare earth elements by using an amino-functionalized magnetic graphene oxide with acid and base resistance," *J. Hazard. Mater.*, vol. 424, p. 127370, Feb. 2022, doi: 10.1016/j.jhazmat.2021.127370.

[12] J. Fu, Q. Xu, J. Low, C. Jiang, and J. Yu, "Ultrathin 2D/2D WO_3/g-C_3N_4 step-scheme H_2-production photocatalyst," *Appl. Catal. B Environ.*, vol. 243, pp. 556–565, Apr. 2019, doi: 10.1016/j.apcatb.2018.11.011.

[13] U. Riaz and S. M. Ashraf, "Synergistic effect of microwave irradiation and conjugated polymeric catalyst in the facile degradation of dyes," *RSC Adv.*, vol. 4, no. 88, pp. 47153–47162, 2014, doi: 10.1039/C4RA06698G.

[14] G. Yu, J. Gao, J. C. Hummelen, F. Wudl, and A. J. Heeger, "Polymer Photovoltaic Cells: Enhanced Efficiencies via a Network of Internal Donor-Acceptor Heterojunctions," *Science (80-.).*, vol. 270, no. 5243, pp. 1789–1791, Dec. 1995, doi: 10.1126/science.270.5243.1789.

[15] G. Salehi, R. Abazari, and A. R. Mahjoub, "Visible-Light-Induced Graphitic–C_3N_4 @Nickel–Aluminum Layered Double Hydroxide Nanocomposites with Enhanced Photocatalytic Activity for Removal of Dyes in Water," *Inorg. Chem.*, vol. 57, no. 14, pp. 8681–8691, Jul. 2018, doi: 10.1021/acs.inorgchem.8b01636.

[16] S. Iguchi, K. Teramura, S. Hosokawa, and T. Tanaka, "Effect of the chloride ion as a hole scavenger on the photocatalytic conversion of CO_2 in an aqueous solution over Ni–Al layered double hydroxides," *Phys. Chem. Chem. Phys.*, vol. 17, no. 27, pp. 17995–18003, 2015, doi: 10.1039/C5CP02724A.

[17] M. Suárez-Quezada, G. Romero-Ortiz, J. E. Samaniego-Benítez, V. Suárez, and A. Mantilla, "H_2 production by the water splitting reaction using photocatalysts derived from calcined ZnAl LDH," *Fuel*, vol. 240, pp. 262–269, Mar. 2019, doi: 10.1016/j.fuel.2018.11.155.

[18] A. Karmakar *et al.*, "Unveiling the significance of working electrode substrates in electrocatalytic water splitting for sustainable hydrogen energy production," *J. Mater. Chem. A*, vol. 13, no. 25, pp. 19252–19281, 2025, doi: 10.1039/D5TA02980E.

[19] Y. Wang, L. Dou, and H. Zhang, "Nanosheet Array-Like Palladium-Catalysts Pdx /rGO@CoAl-LDH via Lattice Atomic-Confined in Situ Reduction for Highly Efficient Heck Coupling Reaction," *ACS Appl. Mater. Interfaces*, vol. 9, no. 44, pp. 38784–38795, Nov. 2017, doi: 10.1021/acsami.7b11695.

[20] H. Lee *et al.*, "Drastic Improvement of 1D-CdS Solar-Driven Photocatalytic Hydrogen Evolution Rate by Integrating with NiFe Layered Double Hydroxide Nanosheets Synthesized by Liquid-Phase Pulsed-Laser Ablation," *ACS Sustain. Chem. Eng.*, vol. 6, no. 12, pp. 16734–16743, Dec. 2018, doi: 10.1021/acssuschemeng.8b04000.

[21] S. Das, S. Patnaik, and K. M. Parida, "Fabrication of a Au-loaded $CaFe_2O_4$ /CoAl LDH p–n junction based architecture with stoichiometric H_2 & O_2 generation and Cr(vi) reduction under visible light," *Inorg. Chem. Front.*, vol. 6, no. 1, pp. 94–109, Dec. 2019, doi: 10.1039/C8QI00952J.

[22] W.-J. Ong, L.-L. Tan, S.-P. Chai, S.-T. Yong, and A. R. Mohamed, "Surface charge modification via protonation of graphitic carbon nitride (g-C_3N_4) for electrostatic self-assembly construction of 2D/2D reduced graphene oxide (rGO)/g-C_3N_4 nanostructures toward enhanced photocatalytic reduction of carbon dioxide to methane," *Nano Energy*, vol. 13, pp. 757–770, Apr. 2015, doi: 10.1016/j.nanoen.2015.03.014.

[23] S. Tonda, S. Kumar, M. Bhardwaj, P. Yadav, and S. Ogale, "g-C_3N_4 /NiAl-LDH 2D/2D Hybrid Heterojunction for High-Performance Photocatalytic Reduction of CO_2 into Renewable Fuels," *ACS Appl. Mater. Interfaces*, vol. 10, no. 3, pp. 2667–2678, Jan. 2018, doi: 10.1021/acsami.7b18835.

[24] Y. Zhu *et al.*, "Plasmonic Ag coated Zn/Ti-LDH with excellent photocatalytic activity," *Appl. Surf. Sci.*, vol. 433, pp. 458–467, Mar. 2018, doi: 10.1016/j.apsusc.2017.09.236.

[25] J. Ni, J. Xue, L. Xie, J. Shen, G. He, and H. Chen, "Construction of magnetically separable NiAl LDH/Fe_3O_4 –RGO nanocomposites with enhanced photocatalytic performance under visible light," *Phys. Chem. Chem. Phys.*, vol. 20, no. 1, pp. 414–421, 2018, doi: 10.1039/C7CP06682A.

[26] Z. Wang, Y. Song, J. Zou, L. Li, Y. Yu, and L. Wu, "The cooperation effect in the Au–Pd/LDH for promoting photocatalytic selective oxidation of benzyl alcohol," *Catal. Sci. Technol.*, vol. 8, no. 1, pp. 268–275, 2018, doi: 10.1039/C7CY02006F.

[27] S. Iguchi *et al.*, "Drastic improvement in the photocatalytic activity of Ga_2O_3

modified with Mg–Al layered double hydroxide for the conversion of CO_2 in water," *Sustain. Energy Fuels*, vol. 1, no. 8, pp. 1740–1747, 2017, doi: 10.1039/C7SE00204A.

[28] J. Shi *et al.*, "2D/2D g-C_3N_4/MgFe MMO nanosheet heterojunctions with enhanced visible-light photocatalytic H_2 production," *J. Alloys Compd.*, vol. 769, pp. 611–619, Nov. 2018, doi: 10.1016/j.jallcom.2018.08.028.

[29] S. Nayak, L. Mohapatra, and K. Parida, "Visible light-driven novel g-C_3N_4 /NiFe-LDH composite photocatalyst with enhanced photocatalytic activity towards water oxidation and reduction reaction," *J. Mater. Chem. A*, vol. 3, no. 36, pp. 18622–18635, 2015, doi: 10.1039/C5TA05002B.

[30] R. Boppella, C. H. Choi, J. Moon, and D. Ha Kim, "Spatial charge separation on strongly coupled 2D-hybrid of rGO/$La_2Ti_2O_7$/NiFe-LDH heterostructures for highly efficient noble metal free photocatalytic hydrogen generation," *Appl. Catal. B Environ.*, vol. 239, pp. 178–186, Dec. 2018, doi: 10.1016/j.apcatb.2018.07.063.

[31] S. Nayak, A. C. Pradhan, and K. M. Parida, "Topotactic Transformation of Solvated MgCr-LDH Nanosheets to Highly Efficient Porous MgO/$MgCr_2O_4$ Nanocomposite for Photocatalytic H_2 Evolution," *Inorg. Chem.*, vol. 57, no. 14, pp. 8646–8661, Jul. 2018, doi: 10.1021/acs.inorgchem.8b01517.

[32] M. Arif *et al.*, "Coupling of Bifunctional CoMn-Layered Double Hydroxide@Graphitic C_3N_4 Nanohybrids towards Efficient Photoelectrochemical Overall Water Splitting," *Chem. – An Asian J.*, vol. 13, no. 8, pp. 1045–1052, Apr. 2018, doi: 10.1002/asia.201800016.

[33] X. Huang, X. Xu, R. Yang, and X. Fu, "Synergetic adsorption and photocatalysis performance of g-C_3N_4/Ce-doped MgAl-LDH in degradation of organic dye under LED visible light," *Colloids Surfaces A Physicochem. Eng. Asp.*, vol. 643, p. 128738, Jun. 2022, doi: 10.1016/j.colsurfa.2022.128738.

[34] P. Ahuja, S. K. Ujjain, I. Arora, and M. Samim, "Hierarchically Grown NiO-Decorated Polyaniline-Reduced Graphene Oxide Composite for Ultrafast Sunlight-Driven Photocatalysis," *ACS Omega*, vol. 3, no. 7, pp. 7846–7855, Jul. 2018, doi: 10.1021/acsomega.8b00765.

[35] W. Zheng, S. Sun, Y. Xu, R. Yu, and H. Li, "Facile synthesis of NiAl-LDH/MnO_2 and NiFe-LDH/MnO_2 composites for high-performance asymmetric supercapacitors," *J. Alloys Compd.*, vol. 768, pp. 240–248, Nov. 2018, doi: 10.1016/j.jallcom.2018.07.168.

[36] R. Xie, G. Fan, Q. Ma, L. Yang, and F. Li, "Facile synthesis and enhanced catalytic performance of graphene-supported Ni nanocatalyst from a layered double hydroxide-based composite precursor," *J. Mater. Chem. A*, vol. 2, no. 21, p. 7880, 2014, doi: 10.1039/c4ta00395k.

[37] H. Liu, Y. Su, Z. Chen, Z. Jin, and Y. Wang, "Graphene sheets grafted three-dimensional $BiOBr_{0.2}I_{0.8}$ microspheres with excellent photocatalytic activity under visible light," *J. Hazard. Mater.*, vol. 266, pp. 75–83, Feb. 2014, doi: 10.1016/j.jhazmat.2013.12.013.

[38] S. Shahabuddin, N. M. Sarih, F. H. Ismail, M. M. Shahid, and N. M. Huang, "Synthesis of chitosan grafted-polyaniline/Co_3O_4 nanocube nanocomposites and their photocatalytic activity toward methylene blue dye degradation," *RSC Adv.*, vol. 5, no. 102, pp. 83857–83867, 2015, doi: 10.1039/C5RA11237K.

[39] K. Zhang, L. L. Zhang, X. S. Zhao, and J. Wu, "Graphene/Polyaniline Nanofiber Composites as Supercapacitor Electrodes," *Chem. Mater.*, vol. 22, no. 4, pp. 1392–1401, Feb. 2010, doi: 10.1021/cm902876u.

[40] H. Lu, J. Chen, and Q. Tian, "Wearable high-performance supercapacitors based on Ni-coated cotton textile with low-crystalline Ni-Al layered double hydroxide nanoparticles," *J. Colloid Interface Sci.*, vol. 513, pp. 342–348, Mar. 2018, doi: 10.1016/j.jcis.2017.11.046.

[41] X. Cui, W. Li, P. Ryabchuk, K. Junge, and M. Beller, "Bridging homogeneous and heterogeneous catalysis by heterogeneous single-metal-site catalysts," *Nat. Catal.*, vol. 1, no. 6, pp. 385–397, Jun. 2018, doi: 10.1038/s41929-018-0090-9.

[42] A. Abdolahi, E. Hamzah, Z. Ibrahim, and S. Hashim, "Synthesis of Uniform Polyaniline Nanofibers through Interfacial Polymerization," *Materials (Basel).*, vol. 5, no. 8, pp. 1487–1494, Aug. 2012, doi: 10.3390/ma5081487.

[43] G. Gaikwad, P. Patil, D. Patil, and J. Naik, "Synthesis and evaluation of gas sensing properties of PANI based graphene oxide nanocomposites," *Mater. Sci. Eng. B*, vol. 218, pp. 14–22, Apr. 2017, doi: 10.1016/j.mseb.2017.01.008.

[44] S. PALMER, R. FROST, and T. NGUYEN, "Hydrotalcites and their role in coordination of anions in Bayer liquors: Anion binding in layered double hydroxides," *Coord. Chem. Rev.*, vol. 253, no. 1–2, pp. 250–267, Jan. 2009, doi: 10.1016/j.ccr.2008.01.012.

[45] A. Kumar, R. Kumar, and G. Pandey, "Synthesis, Characterization of Titania/Polyaniline/GO Nanocomposites, and Its Photocatalytic Activity Under UV-Visible Light," *Macromol. Symp.*, vol. 379, no. 1, Jun. 2018, doi: 10.1002/masy.201600192.

[46] S. Sharma and S. Basu, "Fabrication of centimeter-sized Sb_2S_3/SiO_2 monolithic mimosa pudica nanoflowers for remediation of hazardous pollutants from industrial wastewater," *J. Clean. Prod.*, vol. 280, p. 124525, Jan. 2021, doi: 10.1016/j.jclepro.2020.124525.

[47] B. Chakravarthi, V. Mathkala, and U. M. D. Palempalli, "Degradation and Detoxification of Congo Red azo dye by Immobilized Laccase of Streptomyces sviceus," *J. Pure Appl. Microbiol.*, vol. 15, no. 2, pp. 864–876, Jun. 2021, doi: 10.22207/JPAM.15.2.41.

[48] N. Asses, L. Ayed, N. Hkiri, and M. Hamdi, "Congo Red Decolorization and Detoxification by Aspergillus niger : Removal Mechanisms and Dye Degradation Pathway," *Biomed Res. Int.*, vol. 2018, pp. 1–9, Aug. 2018, doi: 10.1155/2018/3049686.

[49] F. Aounallah, N. Hkiri, K. Fouzai, A. Elaoud, L. Ayed, and N. Asses, "Biodegradation Pathway of Congo Red azo dye by Geotrichum candidum and Toxicity Assessment of Metabolites," *Catal. Letters*, vol. 154, no. 11, pp. 6064–6079, Nov. 2024, doi: 10.1007/s10562-024-04777-w.

[50] A. Kundu, S. Sharma, and S. Basu, "Modulated BiOCl nanoplates with porous g-

C_3N_4 nanosheets for photocatalytic degradation of color/colorless pollutants in natural sunlight," *J. Phys. Chem. Solids*, vol. 154, p. 110064, Jul. 2021, doi: 10.1016/j.jpcs.2021.110064.

[51] S. Singla, S. Sharma, and S. Basu, "MoS_2/WO_3 heterojunction with the intensified photocatalytic performance for decomposition of organic pollutants under the broad array of solar light," *J. Clean. Prod.*, vol. 324, p. 129290, Nov. 2021, doi: 10.1016/j.jclepro.2021.129290.

[52] H. Alamgholiloo, E. Asgari, S. Nazari, A. Sheikhmohammadi, N. Noroozi Pesyan, and B. Hashemzadeh, "Architecture of bimetallic-MOF/silicate derived Co/NC@$mSiO_2$ as peroxymonosulfate activator for highly efficient ciprofloxacin degradation," *Sep. Purif. Technol.*, vol. 300, p. 121911, Nov. 2022, doi: 10.1016/j.seppur.2022.121911.

[53] P. S. Rao and E. Hayon, "Redox potentials of free radicals. IV. Superoxide and hydroperoxy radicals $\cdot O^{2-}$ and $\cdot HO^2$," *J. Phys. Chem.*, vol. 79, no. 4, pp. 397–402, Feb. 1975, doi: 10.1021/j100571a021.

[54] H. M. El-Bery, M. R. Salah, S. M. Ahmed, and S. A. Soliman, "Efficient non-metal based conducting polymers for photocatalytic hydrogen production: comparative study between polyaniline, polypyrrole and PEDOT," *RSC Adv.*, vol. 11, no. 22, pp. 13229–13244, 2021, doi: 10.1039/D1RA01218E.

[55] J. Ma, J. Dai, Y. Duan, J. Zhang, L. Qiang, and J. Xue, "Fabrication of PANI-TiO_2/rGO hybrid composites for enhanced photocatalysis of pollutant removal and hydrogen production," *Renew. Energy*, vol. 156, pp. 1008–1018, Aug. 2020, doi: 10.1016/j.renene.2020.04.104.

[56] A. Li, W. Zhu, C. Li, T. Wang, and J. Gong, "Rational design of yolk–shell nanostructures for photocatalysis," *Chem. Soc. Rev.*, vol. 48, no. 7, pp. 1874–1907, 2019, doi: 10.1039/C8CS00711J.

[57] J. Kröger *et al.*, "Interfacial Engineering for Improved Photocatalysis in a Charge Storing 2D Carbon Nitride: Melamine Functionalized Poly(heptazine imide)," *Adv. Energy Mater.*, vol. 11, no. 6, p. 2003016, Feb. 2021, doi: 10.1002/aenm.202003016.

[58] R. Kumar, R. El-Shishtawy, and M. Barakat, "Synthesis and Characterization of Ag-Ag_2O/TiO_2@polypyrrole Heterojunction for Enhanced Photocatalytic Degradation of Methylene Blue," *Catalysts*, vol. 6, no. 6, p. 76, May 2016, doi: 10.3390/catal6060076.

[59] L. Zhang, R. Jamal, Q. Zhao, M. Wang, and T. Abdiryim, "Preparation of PEDOT/GO, PEDOT/MnO_2, and PEDOT/GO/MnO_2 nanocomposites and their application in catalytic degradation of methylene blue," *Nanoscale Res. Lett.*, vol. 10, no. 1, p. 148, Dec. 2015, doi: 10.1186/s11671-015-0859-6.

[60] Y. Yang, Z. Ma, L. Xu, H. Wang, and N. Fu, "Preparation of reduced graphene oxide/meso-TiO_2 /AuNPs ternary composites and their visible-light-induced photocatalytic degradation n of methylene blue," *Appl. Surf. Sci.*, vol. 369, pp. 576–583, Apr. 2016, doi: 10.1016/j.apsusc.2016.02.078.

[61] R. Kumar *et al.*, "Facile route to a conducting ternary polyaniline@TiO_2/GN nanocomposite for environmentally benign applications: photocatalytic degradation of pollutants and biological activity," *RSC Adv.*, vol. 6, no. 112, pp. 111308–111317, 2016, doi: 10.1039/C6RA24079H.

[62] R. Kumar, "Mixed phase lamellar titania-titanate anchored with Ag_2O and polypyrrole for enhanced adsorption and photocatalytic activity," *J. Colloid Interface Sci.*, vol. 477, pp. 83–93, Sep. 2016, doi: 10.1016/j.jcis.2016.05.039.

[63] Y.-J. Lee *et al.*, "Application of PANI/TiO_2 Composite for Photocatalytic Degradation of Contaminants from Aqueous Solution," *Appl. Sci.*, vol. 10, no. 19, p. 6710, Sep. 2020, doi: 10.3390/app10196710.

[64] F. Habtamu, S. Berhanu, and T. Mender, "Polyaniline Supported Ag-Doped ZnO Nanocomposite: Synthesis, Characterization, and Kinetics Study for Photocatalytic Degradation of Malachite Green," *J. Chem.*, vol. 2021, pp. 1–12, Sep. 2021, doi: 10.1155/2021/2451836.

[65] J. Chen *et al.*, "Synthesis of flower-like CuS/UiO-66 composites with enhanced visible-light photocatalytic performance," *Inorg. Chem. Commun.*, vol. 104, pp. 223–228, Jun. 2019, doi: 10.1016/j.inoche.2019.04.022.

[66] R. A. Rather, S. Singh, and B. Pal, "Core–shell morphology of Au-TiO_2@graphene oxide nanocomposite exhibiting enhanced hydrogen production from water," *J. Ind. Eng. Chem.*, vol. 37, pp. 288–294, May 2016, doi: 10.1016/j.jiec.2016.03.039.

[67] T. Jafari, E. Moharreri, A. Amin, R. Miao, W. Song, and S. Suib, "Photocatalytic Water Splitting—The Untamed Dream: A Review of Recent Advances," *Molecules*, vol. 21, no. 7, p. 900, Jul. 2016, doi: 10.3390/molecules21070900.

[68] A. A. Murashkina, T. V. Bakiev, Y. M. Artemev, A. V. Rudakova, A. V. Emeline, and D. W. Bahnemann, "Photoelectrochemical Behavior of the Ternary Heterostructured Systems CdS/WO_3/TiO_2," *Catalysts*, vol. 9, no. 12, p. 999, Nov. 2019, doi: 10.3390/catal9120999.

Chapter 6

Conclusions and Future Perspectives

6.1. Chapter 2:

A ternary nanocomposite, PANI/BiOCl/GO with varying GO/BiOCl contents have been prepared using the in situ oxidative polymerization process. The formation of PANI, GO, BiOCl, and the different composites was confirmed through various characterization techniques. These materials were used for the mineralization of Rhb and for photocatalytic water splitting in the presence of a sacrificial agent, under acidic and basic conditions. The synergistic effect of BiOCl, PANI, and GO in the composite significantly improves photocatalytic degradation efficiency under sunlight. Among the different composites, 1PBG exhibits the best photocatalytic activity, with a first-order rate constant (0.015 min^{-1}) of which is 7.25 times, 3.8 times, 3.9 times, and 4.7 times higher than that of PANI, GO, BiOCl, and TiO_2-P25, respectively. The impact of the concentration of the catalyst, illumination area, and solution pH on the photodegradation was also investigated. This indicates that holes (h^+), hydroxyl radicals ($OH\cdot$), and electrons (e^-) are the superior species in the degradation mechanism. The results indicate complete detoxification of the Rhb solution with a small amount of photocatalyst (0.6 g/L). The AQE for photocatalytic water splitting was found to be 17.97% in the presence of CH_3OH as a sacrificial agent, 9.69% in acidic medium, and 11.63% in basic medium. This work presents PANI/BiOCl/GO as a novel ternary composite which may be used in various solar-driven applications.

6.2. Chapter 3:

Ternary nanocomposites, PANI/GO/MoO_3, featuring varied GO-MoO_3 ratios, were synthesized through an in-situ oxidative polymerization process. Characterization techniques confirmed the synthesis of PANI, GO, MoO_3, and their unique composites. The aforementioned components were utilized for the purpose of MO mineralization and photocatalytic water splitting, while a sacrificial agent was present. These processes were carried out under both acidic and basic conditions, as well as with the catalyst alone. The electron lifetime of the 2.5PGMO composite stands at 0.612 ms, marking a significant increase compared to PANI, which has a lifetime of 0.0495 ms, GO with 0.023 ms, and MoO_3 with 0.022 ms. Specifically, the electron lifetime of 2.5PGMO is 12 times longer than PANI, 25 times longer than GO, and

28 times longer than MoO_3. The composite's synergistic effect involving MoO_3, PANI, and GO significantly enhanced the efficiency of photocatalytic degradation when exposed to LED light. Notably, among the various composites, 2.5PGMO demonstrated the most promising catalytic activity under light exposure, boasting a first-order rate constant (0.0299 min^{-1}) that surpassed PANI, GO, MoO_3, and TiO_2-P25 by 4.87 times, 17.18 times, 6.63 times, and 7.77 times, respectively. Investigation into how catalyst concentration, size of the illuminated area, and solution acidity affect photodegradation was a focal point of the study. This underscores the pivotal role of h^+, $OH^{\cdot}$, and e^- in the degradation mechanism. The findings demonstrated that using a small quantity of photocatalyst (0.2 g/L) achieved a 70% mineralization of the MO solution. Moreover, the apparent quantum efficiency (AQE) for photocatalytic hydrogen production was found to be 30.76% using CH_3OH as the sacrificial agent, 27.78% in acidic conditions, 28.37% in basic conditions, and 27.34% using only the catalyst. The rod-shaped MoO_3 enhances 2D GO dispersion, reducing its stacked layers and synergistically improving electron lifetime in the PANI/GO/MoO_3 composite. This increased electron lifetime boosts dye degradation efficiency and solar-driven hydrogen production via water splitting. This study introduces PANI/GO/MoO_3 as a novel ternary composite with potential applications in diverse solar-powered systems.

6.3. Chapter 4:

Ternary nanocomposites (PANI/GO/MoS_2) were prepared through in-situ oxidative polymerization, varying the ratios of GO to MoS_2. Characterization validated the successful synthesis of pure PANI, GO, MoS_2, and their corresponding composites. These materials were utilized for the mineralization of MO and photocatalytic water splitting, employing a sacrificial agent under acidic and basic conditions, as well as with the catalyst on its own. The composite's photocatalytic efficiency under visible light was significantly enhanced by the synergistic interaction among MoS_2, PANI, and GO, with 2.5PGMS exhibiting the greatest catalytic activity. Its first-order rate constant (0.03 min^{-1}) was 7.1 times higher than PANI, 22 times higher than GO, 6.35 times higher than MoS_2, and 9.26 times higher than TiO_2-P25. Key parameters like catalyst concentration (0.2 g/L), illuminated area (15 cm^2), and solution pH (7.6) were investigated for their impact on photodegradation, highlighting the importance of h^+, $OH^{\cdot}$, and $O^{2\cdot}$ in the process. The findings demonstrate that a small amount of photocatalyst (0.2 g/L) achieves 83.21% detoxification of the MO solution. The apparent quantum efficiency (AQE) for hydrogen production was 26% with CH_3OH as the sacrificial agent, 22% in acidic

conditions, 19% in basic conditions, and 15% using only the catalyst. This research showcases PANI/GO/MoS_2 as a potential ternary composite suitable for a range of solar-powered applications.

6.4. Chapter 5:

Binary nanocomposites (PANI/LDH) were synthesized via oxidative polymerization carried out in situ, with different ratios of LDH (2 wt%, 5 wt%, and 7wt%). Analytical techniques validated the proper formation of pristine PANI, LDH, and their respective composite materials. These samples were applied to mineralize Congo Red and to split water photo catalytically using a sacrificial agent at different pH levels and also under catalyst-only conditions. Enhanced photocatalytic activity under visible light was observed in the composite as a result of the synergistic effect between PANI and LDH, with 5PL exhibiting the most superior performance. The reaction conformed to first-order kinetics, demonstrating a rate constant that exceeded pure PANI by sixfold, LDH by eightfold, and TiO_2-P25 by ninefold. The impact of critical factors including catalyst dosage (0.4 g/L), light-exposed surface expanse (15 cm^2), and solution pH (7.2) on the photodegradation process was examined, prominence the involvement of h^+, OH^-, and O_2 species in driving the reaction. The results indicate that a low concentration of photocatalyst (0.4 g/L) is sufficient to achieve 98% degradation of the CR solution. The AQE for H_2 production was 19% when CH_3OH was used as the sacrificial agent, 18% under low pH conditions, 21% in high pH conditions, and 15% with the catalyst alone. This study highlights the potential of the PANI/LDH binary nanocomposite for various solar energy-driven applications. Characterization verified the efficacious preparation of pristine PANI, LDH, and their respective composites.

6.5. Overall conclusion:

Overall, hybrid structures combining conducting polymer (PANI) with metal oxide/chalcogenides appear to be highly promising candidates for photocatalytic applications under visible as well as solar light exposure. Many studies have indicated that reducing the likelihood of charge-carrier recombination is one of the simplest and most effective strategies for improving photocatalytic performance. Thus, metal oxide/chalcogenides nanohybrids incorporating PANI offer an excellent option, as their bandgap falls within the visible range, enabling them to capture as much as ~53% of incoming solar radiation. This thesis highlights how PANI and their evolving roles have been utilized to significantly improve the

efficiency of metal oxide/chalcogenides-based nanohybrid photocatalysts in breaking down hazardous chemicals, toxic pollutants, and hydrogen production via water splitting. When coupled with metal oxide/chalcogenides, PANI further promote the separation of photogenerated charge carriers by broadening light absorption from the UV into the visible range, thereby boosting the photocatalytic activity under visible illumination. The enhanced photocatalytic degradation efficiency can also be attributed to the synergistic interaction that forms between PANI and metal oxide/chalcogenides. Since polymers naturally inhibit particle aggregation, incorporating conducting polymer in higher concentrations during synthesis effectively minimizes extensive clustering, thereby improving photocatalytic performance. The π-conjugated backbones of conducting polymers readily capture photoinduced holes, which helps prevent self-oxidation of the photocatalyst, suppresses photo-corrosion, and ultimately enhances overall photostability.

This thesis focuses on the fabrication of four different visible light-driven heterojunction photocatalysts i.e PANI/BiOCl/GO, PANI/GO/MoO_3, PANI/GO/MoS_2, and PANI/Ni-Al LDH prepared in various weight ratios using the in-situ polymerization method. The resulting composites exhibited superior properties compared to their pristine counterparts, including larger surface area, narrower band gap, reduced electron–hole recombination, and enhanced charge transport ability. A noteworthy feature of these photocatalysts is their excellent reusability and long-term stability, enabling repeated use without significant loss of activity. These characteristics highlight their potential for practical applications in photocatalysis.

Table 6.1: Comparison of different photocatalyst materials for photocatalytic degradation and hydrogen production.

Photocatalysis	**Pollutant (% degradation)**	**H_2 produced with sacrificial agent (CH_3OH)**
PANI/BiOCl/GO	Rhodamine-b (96%)	1000 ppm, AQE is 17.97%
PANI/GO/MoO_3	Methyl orange (98%)	26468.4 ppm, AQE is 30.76%
PANI/GO/MoS_2	Methyl orange (99%)	1500 ppm, AQE is 26%
PANI/Ni-Al LDH	Cango red (98%)	10475 ppm, AQE is 20%

6.6. Challenges and future perspectives:

Most studies on photocatalysis using conducting polymer/metal oxides/chalcogenides nanohybrids, as well as other similar nanocomposites, have been carried out in static laboratory setups. However, such systems are difficult to translate to real-world water treatment, where catalysts must remain stable in continuous flow conditions and where even minor metal leaching from the nanohybrids becomes a concern. Future investigations should focus on removing key contaminants from actual water sources by replicating real environmental conditions and gradually transitioning studies from controlled laboratory settings to field applications. Emphasis should be placed on developing efficient post-treatment recovery methods for the nanohybrids to enable their large-scale application. Implementing magnetic separation techniques could play a crucial role in post-treatment recovery of these nanohybrids, allowing their easy extraction through the application of an external magnetic field. Photocatalysis holds significant potential to create new avenues in solar energy harvesting and storage, and the field still offers substantial room for further advancement. Additionally, photocatalysis can serve as a vital tool in environmental remediation, providing effective pathways to eliminate diverse organic and inorganic pollutants including toxic metals like arsenic, chromium, and mercury from freshwater systems, while also aiding in the reduction and recovery of copper and noble metals. Future research should prioritize exploring the environmental and energy sustainability aspects of these hybrid systems. To achieve long-term sustainability, advancements in eco-friendly synthesis methods and their application in renewable energy production and environmental clean-up will be essential. Overall, PANI/metal oxides/chalcogenides based photocatalytic systems have demonstrated strong potential for removing organic pollutants at the laboratory scale; however, successful real-world implementation will require overcoming several existing challenges that should be prioritised in future research.

List of Publication

1.1. Related to Ph.D. work (Objectives)

i) **Hait, P**., Mehta, R., Basu, S., 2023. Advancing sustainable solutions: Harnessing polyaniline/BiOCl/GO ternary nanocomposites for solar-powered degradation of organic pollutant and photocatalytic hydrogen generation. J. Clean. Prod. 424, 138851. https://doi.org/10.1016/j.jclepro.2023.138851. (I.F 10.7)

ii) **Hait, P**., Mehta, R., Basu, S., 2025. Ultrafast charge separation and photostability in PANI/GO/MoO_3 ternary nanocomposites for dual-function solar photocatalysis: enhanced dye degradation and hydrogen evolution under visible light. New J. Chem. https://doi.org/10.1039/D5NJ02247A. (I.F 2.6)

iii) **Hait, P**., Mehta, R., Basu, S., 2025b. Design and synthesis of PANI/GO/MoS_2 nanocomposites via oxidative polymerization for efficient photocatalytic applications: organic pollutant degradation and hydrogen generation. Mater. Adv. 6, 2811–2822. https://doi.org/10.1039/D4MA01249F. (I.F 5.8)

iv) **Hait, P**., Mehta, R., Basu, S., 2025. Multifunctional PANI-LDH nanocomposites: from efficient cango red mineralization to high-yield solar hydrogen generation. Sol. Energy 302, 114012. https://doi.org/10.1016/j.solener.2025.114012. (I.F 7.9)

1.2. Other publications

i) Garg, B., **Hait, P**., Basu, S., 2024. Unlocking solar energy's potential: Dual photocatalytic activities of g-C_3N_4/Sb_2S_3 for hydrogen evolution and tetracycline degradation in sunlight. J. Environ. Manage. 370, 122403. https://doi.org/10.1016/j.jenvman.2024.122403. (I.F 9.2)

ii) Singla, G., Kansay, V., Sharma, S., Gupta, S., Kaushal, A., **Hait, P**., Basu, S., Pahwa, C., Lallar, I., Yogi, A.K., Chakrabarti, S., Bera, M.K., 2025. Nanocomposite bio-sponge air-electrode biogenically derived from Plantago ovata for applications in wearable and biodegradable zinc-air batteries. Sustain. Mater. Technol. 45, e01558. https://doi.org/10.1016/j.susmat.2025.e01558. (I.F 9.7)

iii) Singla, G., Bera, M.K., **Hait, P**., Basu, S., Isha, Yogi, A.K., Kumar, N., Selvaraj, M., Assiri, M.A., Chakrabarti, S., 2025. Impact of biosynthesized heteroatom-doped α-MnO_2 nanocatalyst loading on the performance of nanocomposite bio-sponge air electrode for wearable and biodegradable zinc-air batteries. J. Energy Storage 134, 118110. https://doi.org/10.1016/j.est.2025.118110. (I.F 10.7).

iv) Samanta, K.K., Kumar, M., Mamgain, H.P., **Hait, P**., Manna, S., Bhunia, B., Basu, S., Pandey, J.K., 2025. Nature-inspired ZnO nanoparticles: unlocking the biomedical potential of Glycyrrhiza glabra -mediated green synthesis through in vitro and in silico approaches. RSC Adv. 15, 35598–35616. https://doi.org/10.1039/D5RA05670E. (I.F 6.1).

v) Kaur, M., **Hait, P**., Basu, S., 2025. Flower-like NiAl-LDH/$BiVO_4$ Z-scheme photocatalysts for sunlight-driven degradation of azo dye: performance and mechanistic insights. RSC Adv. 15, 37166–37182. https://doi.org/10.1039/D5RA06146F. (I.F 6.1).

vi) Monika, Bera, M.K., Singla, G., **Hait, P**., Basu, S., Kumar, N., Siddeeg, S.M., Selvaraj, M., Singh, G., Chakrabarti, S., 2026. Harnessing the synergistic effects of green-synthesized Sn_2ZnO_4 nanoparticles in biodegradable PVA nanocomposites for high-output triboelectric nanogenerators enabling sustainable energy harvesting. J. Alloys Compd. 1060, 187339. https://doi.org/10.1016/j.jallcom.2026.187339 . (I.F 6.7)

Conferences and Workshops

i) Oral presentation on the topic “Advancing Sustainable Solutions: Harnessing

Polyaniline/BiOCl/GO Ternary Nanocomposites for Solar-Powered Degradation of Organic Pollutant and Photocatalytic Hydrogen Generation” SDCEE-2024 International Conference on “Sustainable Development in Chemical and Environmental Engineering” February 22-24,2024, organized by Department of Chemical Engineering, Thapar Institute of Engineering and Technology, Patiala, Punjab.

ii) 2nd best Poster presentation on the topic “Advancing Sustainable Solutions:

Harnessing Polyaniline/BiOCl/GO Ternary Nanocomposites for Solar-Powered Degradation of Organic Pollutant and Photocatalytic Hydrogen Generation” DST SERB Sponsored International Conference on “Emerging Trends in Green Energy and Environment Sustainability” September 26-27, 2024, organized by Department of Biotechnology, Chandigarh Group of Colleges, Mohali, Punjab.

iii) Poster presentation on the topic “Advancing Sustainable Solutions: Harnessing

Polyaniline/BiOCl/GO Ternary Nanocomposites for Solar-Powered Degradation of Organic Pollutant and Photocatalytic Hydrogen Generation” 24th National Symposium on Catalysis (CATSYMP-24) “Catalysis for Sustainable Chemicals, Materials & Energy” (CSCME-2025) Golden Jubilee celebrations of the Catalysis Society of India (CSI), 24-26 February, 2025, organized by Department of Chemistry and Biochemistry, TIET, Patiala, Punjab, 147004.

iv) Poster presentation on the topic “Ultrafast charge separation and photostability in

PANI/GO/MoO_3 ternary nanocomposites for dual-function solar photocatalysis: enhanced dye degradation and hydrogen evolution under visible light.” INTERNATIONAL CONFERENCE ON ENERGY AND WATER FOR SUSTAINABLE ENVIRONMENT - ICEWSE 2025 - 30 September & 01 October, 2025, Jointly Organised by UNESCO MADANJEET SINGH CENTRE FOR SOUTH ASIA WATER MANAGEMENT (UMCSAWM) DEPARTMENT OF CIVIL ENGINEERING, UNIVERSITY OF MORATUWA (UOM), Moratuwa- Sri Lanka and UNESCO MADANJEET SINGH SCHOOL OF GREEN ENERGY TECHNOLOGIES

(UMSGET) DEPARTMENT OF GREEN ENERGY TECHNOLOGY, PONDICHERRY UNIVERSITY, Puducherry- India.

14% Overall Similarity

The combined total of all matches, including overlapping sources, for each database.

Filtered from the Report

- Bibliography
- Quoted Text
- Cited Text
- Small Matches (less than 8 words)

Exclusions

- 13 Excluded Sources

Match Groups

- 397 Not Cited or Quoted 14%
  Matches with neither in-text citation nor quotation marks
- 0 Missing Quotations 0%
  Matches that are still very similar to source material
- 0 Missing Citation 0%
  Matches that have quotation marks, but no in-text citation
- 0 Cited and Quoted 0%
  Matches with in-text citation present, but no quotation marks

Top Sources

8% Internet sources
9% Publications
9% Submitted works (Student Papers)

Integrity Flags

0 Integrity Flags for Review

Our system's algorithms look deeply at a document for any inconsistencies that would set it apart from a normal submission. If we notice something strange, we flag it for you to review.

A Flag is not necessarily an indicator of a problem. However, we'd recommend you focus your attention there for further review.

Match Groups

397 Not Cited or Quoted 14%
Matches with neither in-text citation nor quotation marks

0 Missing Quotations 0%
Matches that are still very similar to source material

0 Missing Citation 0%
Matches that have quotation marks, but no in-text citation

0 Cited and Quoted 0%
Matches with in-text citation present, but no quotation marks

Top Sources

8% Internet sources
9% Publications
9% Submitted works (Student Papers)

Top Sources

The sources with the highest number of matches within the submission. Overlapping sources will not be displayed.

1	Internet pubs.rsc.org	<1%
2	Publication Karthikeyan Sekar, Ashil Augustin, Manova Santhosh Yesupatham, Rajini Muruge...	<1%
3	Internet coek.info	<1%
4	Internet www2.mdpi.com	<1%
5	Publication Bhavika Garg, Palkaran Sethi, Soumen Basu. "Strategic innovation in CuBTC/PANI...	<1%
6	Student papers Dayalbag Educational Institute on 2014-04-30	<1%
7	Publication Surbhi Sharma, Soumen Basu. "Fabrication of centimeter-sized Sb2S3/SiO2 monol...	<1%
8	Student papers University of the Western Cape on 2024-10-31	<1%
9	Publication Wee-Jun Ong, Lling-Lling Tan, Yun Hau Ng, Siek-Ting Yong, Siang-Piao Chai. " Gra...	<1%
10	Publication Bao Sun, Yanzhong Hao, Fen Guo, Yinhu Cao, Yanhui Zhang, Yingpin Li, Dongshen...	<1%

S Basu 19/01/26